# 論文 / 著書情報
# Article / Book Information

| | |
|---|---|
| 題目(和文) | |
| Title(English) | Development of Sulfur Electrode Technologies for Practical Lithium/Sulfur Rechargeable Cells |
| 著者(和文) | 川瀬綾子 |
| Author(English) | Ayako Kawase |
| 出典(和文) | 学位:博士(工学),<br>学位授与機関:東京工業大学,<br>報告番号:乙第4173号,<br>授与年月日:2019年3月31日,<br>学位の種別:論文博士,<br>審査員:高田 十志和,伊原 学,山口 猛央,谷口 泉,稲木 信介 |
| Citation(English) | Degree:Doctor (Engineering),<br>Conferring organization: Tokyo Institute of Technology,<br>Report number:乙第4173号,<br>Conferred date:2019/3/31,<br>Degree Type:Thesis doctor,<br>Examiner:,,,, |
| 学位種別(和文) | 博士論文 |
| Type(English) | Doctoral Thesis |

Doctoral Thesis

# Development of Sulfur Electrode Technologies for Practical Lithium/Sulfur Rechargeable Cells

Ayako Kawase

NexTech Batteries

# Content

**Chapter 1.** Introduction … 1

1.1 Why lithium/sulfur cells? … 2

1.2 Principles and cell components of lithium/sulfur cells … 9

1.3 Development of lithium/sulfur cells … 10

1.4 Purpose of this work … 21

1.5 References … 24

**Chapter 2.** Electrochemical reactions of lithium/sulfur cells: an analytical study using the organic conversion technique

2.1 Introduction … 29

2.2 Results and discussion

2.2.1 LC/MS analysis … 31

2.2.2 NMR analysis … 40

2.2.3 UV-Vis analysis … 43

2.3 Summary … 48

2.4 Experimental section

2.4.1 Experimental detail … 48

2.4.2 Computational detail … 52

2.5 References … 52

**Chapter 3.** Detailed study of sulfur deposition onto graphene oxide for lithium/sulfur cells

3.1 Introduction

3.1.1 Sulfur active materials … 57

3.1.2 S-GO composite … 57

3.2 Results and discussion

3.2.1 Sulfur deposition reactions … 58

3.2.2 Synthesis Process … 59
3.2.3 Alkaline deposition process … 60
3.2.4 Acidic deposition process … 64
3.2.5 SEM for the samples prepared by alkaline deposition … 67
3.2.6 SEM for the samples prepared by both alkaline and acidic deposition … 70
3.2.7 SEM for the samples prepared by different acidic deposition temperature … 72
3.2.8 SEM for the samples after the heat treatment … 74
3.2.9 Cell performance for the samples prepared by different alkaline deposition time … 75
3.2.10 Cell performance for the samples prepared by different acidic deposition temperature … 77
3.2.11 Relationship between the morphology and the cell performance … 80
3.2.12 Acidic deposition without Alkaline deposition … 80
3.2.13 Addition of conductivity to the sample prepared by acidic deposition … 85
3.2.14 Cell performance of the sample prepared by acidic deposition … 86
3.3 Summary … 89
3.4 Experimental section
3.4.1 Synthesis … 89
3.4.2 Material characterization … 91
3.4.3 Electrochemical characterization … 91
3.5 References … 92

**Chapter 4.** The function of cetyltrimethyl ammonium bromide in lithium/sulfur cells
4.1 Introduction
4.1.1 Introduction of CTAB (cetyltrimethyl ammonium bromide) … 95
4.1.2 Analysis of S-GO composite … 95
4.2 Results and discussion
4.2.1 Synthesis process … 96
4.2.2 TGA analysis … 99

4.2.3 ESI-MS spectrometry and NMR … 102
4.2.4 TGA analysis 2 … 109
4.2.5 Raman spectroscopy … 110
4.2.6 ESI-Mass spectrometry … 113
4.2.7 Computational analysis for Raman spectroscopy … 116
4.2.8 XAS analysis … 118
4.2.9 SEM observation … 125
4.2.10 Electrochemical Test … 126
4.3 Summary … 131
4.4 Experimental section
4.4.1 Synthesis … 131
4.4.2 Material characterization … 133
4.4.3 Theoretical calculation … 134
4.4.4 Electrochemical characterization … 135
4.5 References … 135

**Chapter 5.** Electrostatic polysulfides confinement to inhibit redox shuttle process in the lithium/sulfur batteries
5.1 Introduction … 139
5.2 Results and discussion
5.2.1 Theoretical calculation … 140
5.2.2 UV-vis spectroscopy … 141
5.2.3 Electrochemical test … 142
5.2.4 Electrochemical analysis … 145
5.2.5 SEM observation … 147
5.3 Summary … 150
5.4 Experimental section
5.4.1 Computational detail … 151
5.4.2 Experimental detail … 151
5.5 References … 153

**Chapter 6.** Degradation mechanism of lithium/sulfur cells using X-ray Absorption Spectroscopy

6.1 Introduction

6.1.1 Degradation during cycling … 156

6.1.2 Introduction of X-Ray Absorption Tools … 157

6.2 Results and discussion

6.2.1 Characterization of cycled cathode materials … 158

6.3 Summary … 161

6.4 Experimental section

6.4.1 Sample preparation … 162

6.4.2 Analysis … 162

6.5 References … 163

**Chapter 7.** Conclusion … 165

**Supporting information** … 171

**List of Measurement Equipment and Chemical Reagents** … 176

**List of Publications** … 178

**Acknowledgement** … 182

CHAPTER 1

# Introduction

## 1.1) Why lithium/sulfur cells?

Sustainable and clean energy technologies are highly desirable due to the increasing global energy consumption. The research and development of rechargeable batteries with sufficient energy storage is becoming one of the most active aspects of the automobile and the power industry, due to the rapidly increasing demands for environmentally-friendly electric vehicles and load leveling systems. Especially for development of electric vehicles, they require rechargeable batteries having significantly high specific energy and high energy density in order to deliver a range comparable with that of combustion-engine vehicles. Figure 1-1 shows the calculated weight and volume of batteries required for electronic vehicles with a range of 500 km using 150 Wh/km as the running energy.

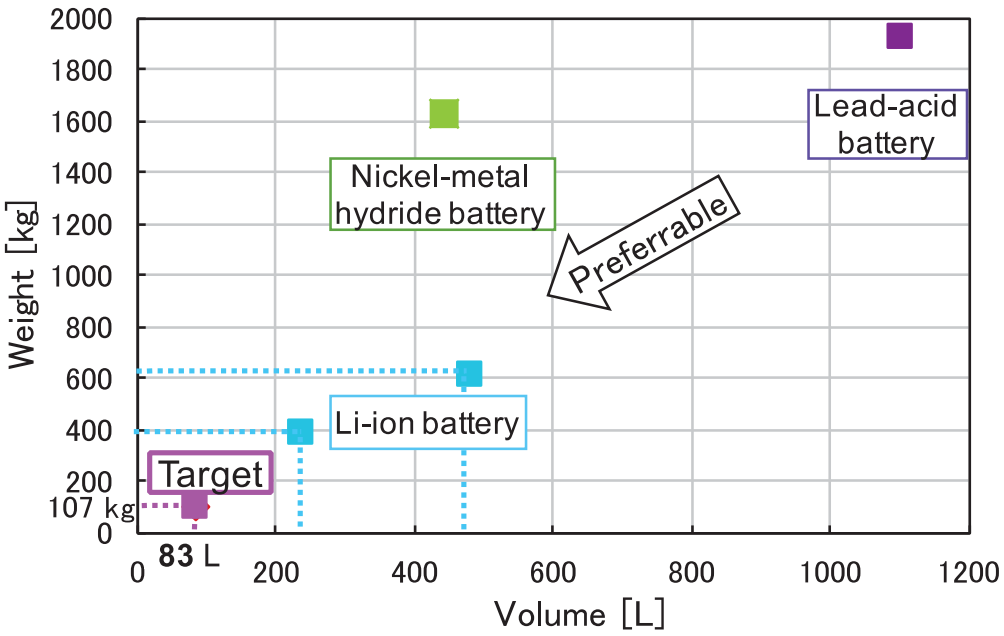


Figure 1-1. Weight and volume of batteries required for electronic vehicles with a range of 500 km based on the calculation using 150 Wh/km as the running energy.

Although huge improvement has been achieved in the past about 30 years commercializing Nickel-metal hydride batteries and Li-ion batteries supplying much larger energy density

than lead-acid batteries, those cells do not meet the demand judging from the fact that an electronic vehicle still needs a battery weighing over 400 kg even using decent Li-ion batteries to run 500 km without charging. Not only electric vehicles but also aerospace applications and aircraft applications are requiring batteries having much higher specific energy than Li-ion batteries. In order to meet those demands, scientists are actively seeking new cell chemistries which can offer capabilities beyond the current best-performing Li-ion cells in the marketplace.

### ◆ Theoretical screening of the active materials

To seek a new cell system to comply with such a requirement, potential specific energies of cells were compared theoretically. To compose a cell, a set of two materials, one is for the negative electrode and the other is for the positive electrode, should be chosen. The energy of the cell is determined by the capacity and the voltage of the cell.

$$\text{Energy [Wh]} = \text{Capacity [Ah]} \times \text{Voltage [V]} \quad \dots (1)$$

The cell voltage is the difference of the electrode potentials E of the negative electrode and the positive electrode.

$$\text{Voltage} = E\,(\text{positive electrode}) - E\,(\text{negative electrode}) \quad \dots (2)$$

The electrode potential E of a material is defined as

$$E = -\Delta G/nF \quad \dots (3)$$

where $\Delta G$ is the standard Gibbs energy for the cell reaction, n is the number of electrons transferred in the cell reaction, F is the Faraday constant. The theoretical capacity [Ah] of an active material is calculated by

$$\text{Capacity} = nF/(3600M) \quad \dots (4)$$

where n is the number of electrons transferred in the half-cell reaction, F is the Faraday

constant, M is molecular weight of the active material.

### ◆ Lithium as the negative electrode active material

According to the calculations using from Equation 1 to Equation 4, it is easily noticed that lithium is the ideal material for an negative electrode because of the lowest electrode potential, i.e. -3.04 V versus standard hydrogen electrode, and the highest theoretical capacity, i.e. 3861 mAh/g. The research for the practical use of lithium metal for battery electrode had been active since 1970s affected by increase in demand for batteries applied for electric devices. [1, 2] However, the cells using lithium metal electrode failed to be on the market due to some fire accidents despite the efforts of commercialization. The fire accident can be caused by the nature of lithium metal to crystalize with a branching, treelike structure, i.e. dendrites, which penetrate the separator to reach to the positive electrode resulting in an electrical shorting of the cell. [3] The heat produced by the cell short can cause a fire by igniting the organic electrolyte solvents in the cell. Meanwhile, carbonaceous materials were discovered to store lithium in between the graphite layers forming $LiC_6$ in the 1980s [4] and successfully applied this to a new cell concept, the Li-ion cell, synchronizing to another discovery of $LiCoO_2$ as the positive electrode active material for the new concept. [5] Thus, the Li-ion battery was introduced to the market without using lithium metal electrodes. After the 2000s, with the demand for higher energy storage devices responding to the serious environmental issues, research on lithium metals electrode was rekindled. [3, 6] The main improvements for the application of lithium metal so far have been about the electrolyte components such as solid electrolytes, ionic liquids and electrolyte additives. In this study, aiming at the battery application, lithium metal has been adopted as the negative electrode active material. Based on this adoption, research is focused on positive electrode active materials.

## ◆ Selection of the positive electrode active material

To search for a promising candidate for the positive electrode active material, theoretical capacities and voltages versus the lithium electrode for substances of which the standard Gibbs energy data can be obtained in the Handbook of Electrochemistry were calculated using Equation 1 to 4. [7] Then the theoretical specific energies and energy densities were evaluated by using those values. For the calculation of energy density, density of the elemental substances was used. Figure 1-2 shows a scatter plot of the calculated specific energies and energy densities.

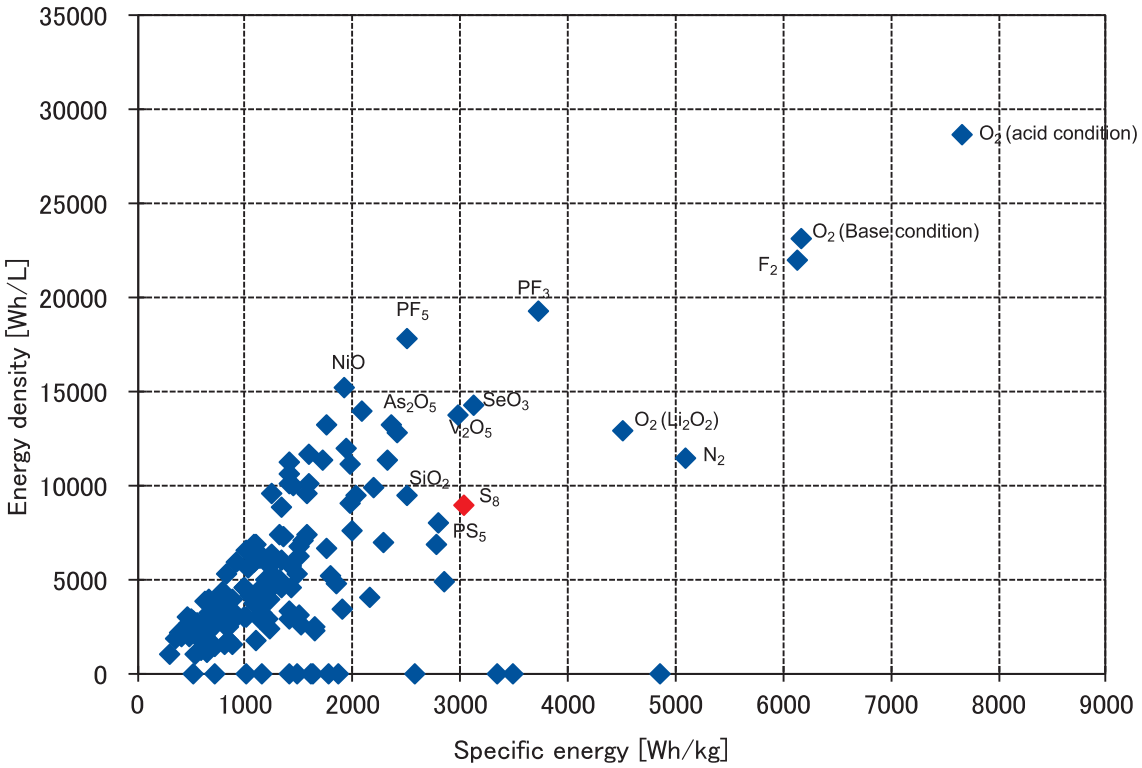


Figure 1-2. Scatter plot of the specific energy and the energy density of substances which have the standard Gibbs energy data when the negative electrode is lithium metal. The energy densities were calculated based on the density of the bulk crystal of the substances.

When the substances is gas, the density of the product compounds of the reaction with lithium were used for the calculation.

Some gaseous substances such as oxygen, fluorine and nitrogen showed high energy density because those consist of light elements. Since oxygen and nitrogen are components of the air, cells using those gases as the positive electrode active materials have been investigated as lithium/air batteries. [8] Lithium/air batteries are attractive because the theoretical specific energy is high. However, the whole system will be complicated and bulky due to installation of compressors, filters and so on in order to use the air as the active material. $PF_3$ and $PF_5$ are highly toxic gases. It is notable that sulfur has the highest specific energy among the solid substances in this calculation. While $SeO_3$ and $V_2O_5$ have higher energy densities than sulfur, the specific energies are slightly less than the one for sulfur. Although these values are just potentials for substances, these are important information in order to screen a promising candidate for future batteries. This importance is emphasized by the fact that Li-ion batteries are almost hitting the ceiling of the theoretical limitation, which prevent them from exceeding the theoretical values. Figure 1-3 shows the theoretical capacities and electrode potentials of major active materials for Li-ion cells and cells under research. The theoretical capacity of sulfur is more than six times as much as that of Li-ion cells based on $LiCoO_2$. The asymptotic line shows the guideline of specific energy which is the product of capacity and voltage on the assumption that the negative electrode is lithium. As the result of taking into account the higher voltage of Li-ion cells than lithium/sulfur cells, the specific energy of lithium/sulfur cells are supposed to have potentially four times as much specific energy as Li-ion cells.

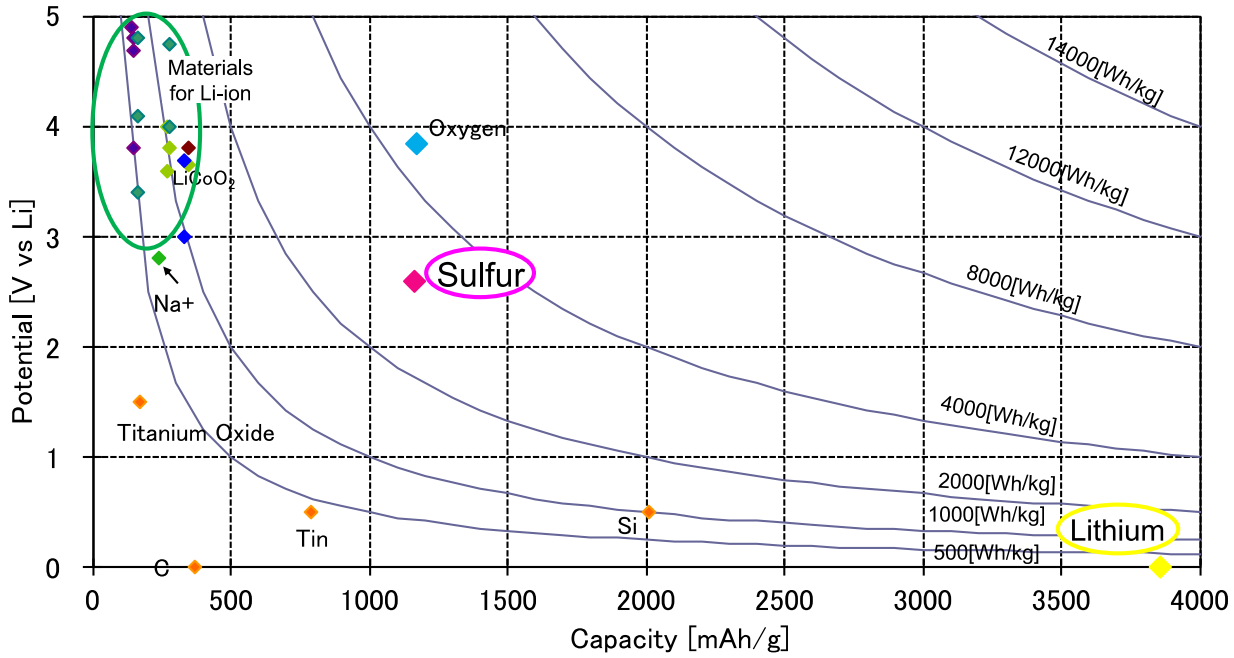


Figure 1-3. Plots of theoretical capacities and electrode potentials of battery material candidates.

### ◆ Sulfur as the positive electrode active material

Sulfur is a plentiful natural resource and thus is low in cost. Almost all elemental sulfur is produced as a byproduct of removing sulfur-containing contaminants from natural gas and petroleum. Compared to the lithium/air cell, lithium/sulfur cells can be compactly packaged and thus can be used to replace currently-used lithium ion battery systems with less difficulty. Due to these favorable features of sulfur as an electrode material for high-energy batteries, sulfur had been researched since the late 1960s responding to the demand for energy storage. [9] The chronological table about Li-ion cells, lithium/sulfur cells and sodium/sulfur cells is shown in Figure 1-4.

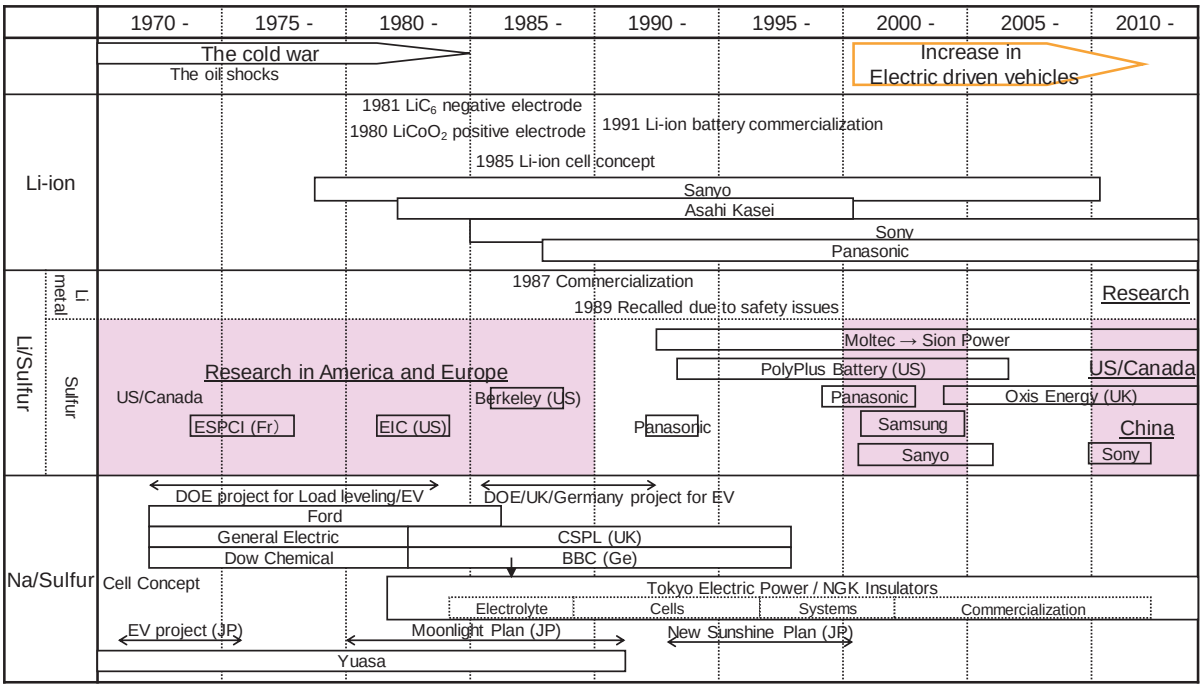


Figure 1-4. Chronological table about Li-ion cells, lithium/sulfur cells and sodium/sulfur cells.

One of them adopted sodium as the negative electrode material, called sodium/sulfur cells, and it was finally commercialized by NGK insulators in 2000 utilizing alumina as the solid electrolyte after a long struggle while many other government-supported projects had given up. [10] Although research of sulfur cells with lithium metal as the negative electrode started in the 1960s as well [9], it did not thrive after the lithium metal electrode was discovered to be unsafe, and Li-ion cells were commercialized. Around the year 2000, research on lithium/sulfur cells using liquid electrolyte was rekindled responding to the demand for energy storage devices having higher energy than Li-ion cells in order to meet the requirement for electric vehicles. [6]

## 1.2) Principles and cell components for lithium/sulfur cells

The reactions on lithium negative electrode and sulfur positive electrode and the overall reaction are shown as the following equations.

Negative electrode: $2Li \rightarrow 2Li^{+} + 2e^{-}$ … (5)

Positive electrode: $S + 2e^{-} \rightarrow S^{2-}$ … (6)

Overall: $2Li + S \rightarrow Li_2S$ … (7)

During discharging, the electrons released at the lithium negative electrode by its oxidation are transported through the external electrical circuit to the sulfur electrode. At the positive electrode, sulfur is reduced by combining with the electrons to produce a series of polysulfides, and finally lithium sulfide.

A lithium/sulfur cell consists of a lithium metal as the negative electrode, a separator, electrolyte and sulfur as the positive electrode. When the electrolyte is solid, the solid electrolyte acts as a separator. An illustration of cell components of a lithium/sulfur cell is shown in Figure 1-5.

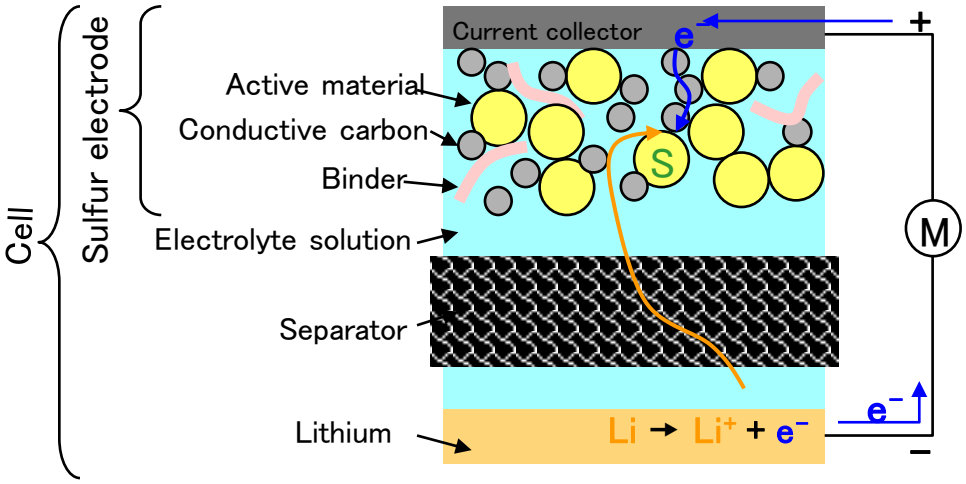


Figure 1-5. Illustration of cell components of a lithium/sulfur cell.

## 1.3) Development of lithium/sulfur cells

### ◆ The beginning of lithium/sulfur cells

Research on lithium/sulfur cells started from the late 1960s. Cairns et al. presented the actual cell data using LiF-LiCI-LiI electrolyte at 475 °C in 1969. [9] It was noted that the main issue of the cells was the increase of the internal resistance caused by the accumulation of lithium sulfide as the reaction product as presented in Equation 7. Sulfur and lithium sulfide are insulators. In order for them to be reduced or oxidized, a conductive network should exist to carry the electrons to the reaction sites. When the cell is operated at a temperature below the melting point of sulfur (115 °C) or lithium sulfide (938 °C), accumulation of the insulating deposition will interfere with the further reactions. In the 1970s, basic understanding of the phase transition of sulfur, polysulfide and lithium sulfide and behavior of polysulfides in various solutions were intensively studied. The redox profiles of sulfur in cyclic voltammetry and chronopotentiometry were presented by Merrit et al in1970. [11] This study showed the two distinctive reduction peaks in the profiles like that is shown in Figure 1-6. Elemental sulfur is known to have an eight-member ring structure. A number of studies have been conducted to know why it shows the two distinctive peaks and how the eight-member ring of sulfur is reduced. Still it has not been fully unveiled.

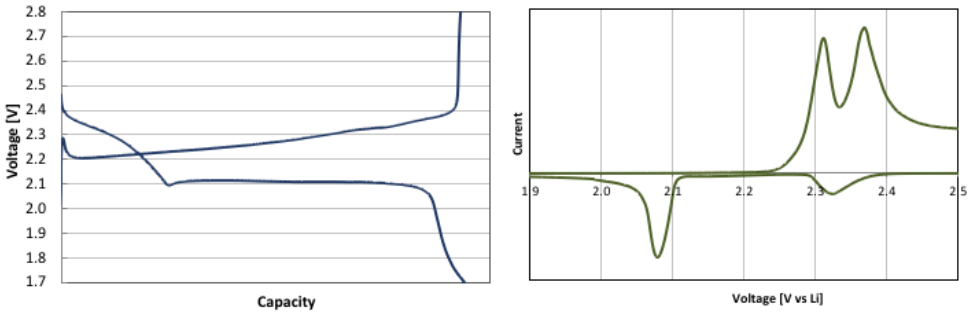


Figure 1-6. The redox profiles of sulfur in chronopotentiometry (left) and in cyclic voltammetry (right).

Cunningham et al. summarized the phase diagram of the lithium/sulfur system in 1972. [12] This study revealed that there was no solid state other than $Li_2S$ as isolated compounds of lithium and sulfur. This means that when eight-member ring elemental sulfur, $S_8$, is reduced in a cell, the intermediate, polysulfide $Li_2S_x$, cannot form a solid phase so that polysulfide should be dissolved in the electrolyte solution or take another form in a solid state. This fact would be one of the critical issues for lithium/sulfur cells. On the other hand, in solution, sulfur, polysulfide and lithium sulfide have very different solubilities from one another. Sulfur is soluble in non-polar solvents, lithium sulfide is soluble in polar solvents, and polysulfides are soluble in both. This difference causes changes in the physical state of sulfur species if the cell is operated using a liquid electrolyte. Sulfur and lithium sulfide are not maintained perfectly in the conductive network due to the volumetric and morphology changes caused by dissolution and precipitation cycles of sulfur species, even if the original active materials are well designed to have sulfur in a conductive network. [13, 14] As more and more sulfur species become isolated from the electrochemical reactions, the results is loss of the specific capacity.

### ◆ Understanding of polysulfide species

Giggenbach, Chivers et al. and Seel et al. studied polysulfide species in aqueous and organic solutions in the early 1970s. [15-21] They tried to reveal the origin of unique colors in polysulfide solutions utilizing UV-vis spectroscopy. The important finding was that $S_3^-$ radical was very stable in some organic solvents, which was the origin of the blue color of the polysulfide solutions. [16-21] From the late 1970s, the electrochemical behaviors of polysulfide species in various organic solvent such as dimethyl sulfoxide (DMSO), dimethylformamide (DMF), tetrahydrofuran (THF) started to be studied. [22-25] In these studies, the big difference in solubilities and behaviors of polysulfides in different solvent systems were emphasized. Despite the intense efforts to understand the reactions among polysulfides, however, the obtained knowledge was limited because the analysis depended mainly on UV-vis spectroscopy in which polysulfide species showed overlapping peaks in

the spectra. In the late 1980s, the kinetics of polysulfides in aqueous solutions were studied intensively by Lessner et al. [26-28] In the 1990s, fundamental research became scarce. [29]

### ◆ Redox shuttle of polysulfide

In 1981, Rao et al. found an important phenomenon for lithium/sulfur cells in the study of lithium/$TiS_2$ cells, which is the so-called redox shuttle phenomenon of polysulfide. [36] In the redox shuttle phenomenon, the dissolved polysulfides migrate to the lithium metal electrode and react to form shorter polysulfides that diffuse back to the sulfur electrode (Figure 1-8). This phenomenon has a consequence that the polysulfides corrode the lithium electrode and contribute to self-discharge and lower the coulombic efficiency. [36, 37] This problem has become one of the most critical challenges for lithium/sulfur cells.

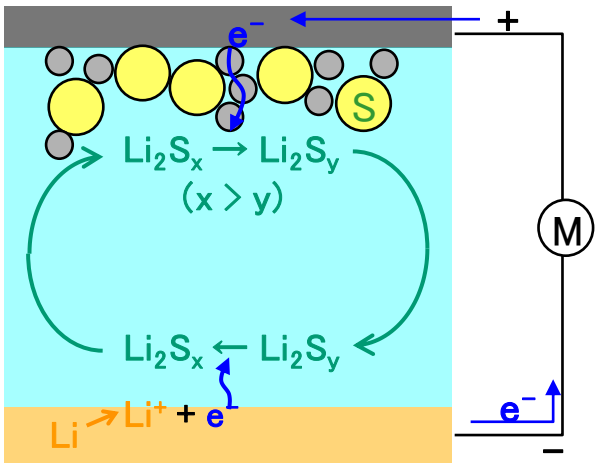


Figure 1-8. Illustration of mechanism of redox shuttle phenomenon of polysulfide in lithium/sulfur cells.

## ◆ Liquid electrolyte development #1 - Introduction of DOL -

Rauh et al. tried to use a polysulfide solution as a catholyte using THF solvent with $LiAsF_6$ salt in the late 1970s. [30, 31] This was one of the first trials from an industrial laboratory. The cell using polysulfide solutions as a catholyte can ideally enhance the rate capability because electronic and ionic conductivity can be higher than for solid electrode having insulating elemental sulfur and lithium sulfide. Also, cycling stability can be enhanced because precipitation and dissolution of sulfur and lithium sulfide can be avoided, in which active sulfur species can be lost from the conductive network. However, it was extremely difficult to avoid the precipitation of lithium sulfide completely. In the 1980s, Yamin et al. presented cell data using polysulfide solutions as a catholyte and fundamental studies of the electrochemical reactions of sulfur and polysulfide. [32, 33] In 1989, Peled et al. in the same group introduced 1,3-dioxolane (DOL) as the electrolyte solvent for the lithium/sulfur cell. [34] Until this point, THF had been the popular solvent for polysulfide catholyte. DOL was known to have a low viscosity and a compatibility with lithium. The reason for the high compatibility with lithium was revealed by Aurbach et al in 1990. [35] They claimed that the cyclic structure of DOL can stabilize the surface of Li metal by deposition of a protective layer that comes from a ring-opening reaction (Figure 1-7). DOL has become an important solvent in lithium/sulfur cells in the later studies.

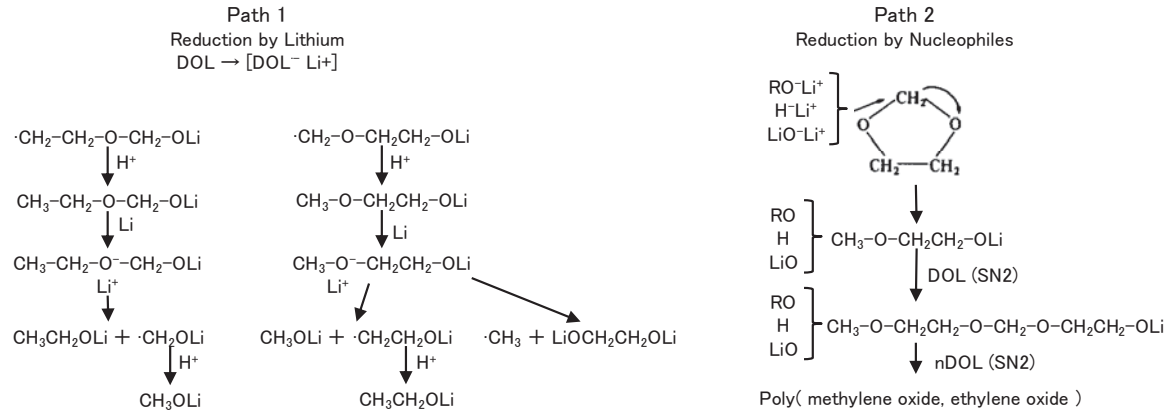


Figure 1-7. Reduction patterns of DOL on lithium metal from the literature 35.

## ◆ Liquid Electrolyte development #2 - Introduction of LiTFSI and DME –

PolyPlus Battery introduced polyethylene oxide (PEO) polymer with lithium trifluoromethanesulfonimide (LiTFSI) salt as a solid electrolyte to the lithium/sulfur cell in the late 1990s. [40] Polymer electrolytes can enhance the cycling stability because the polymer can prevent the migration of polysulfide from the positive electrode to the negative electrode which results in the redox shuttle phenomenon. However, if the density of the polymer is high enough to prevent the migration of polysulfide, the ion conductivity turns out not to be enough. In the early 2000s, a number of studies for the electrolyte components using the similar cell design to that of Li-ion cells started to be reported. In 2000, Marmostein et al. introduced polyethyleneglycol dimethylether (PEGDME) with LiTFSI as the polymer electrolyte. [41] In 2002, Chang et al. presented a study using a binary electrolyte based on tetra (ethylene glycol) dimethylether (TEGDME) and DOL. [42] This study noted that a solvent with low viscosity such as DOL was necessary in the electrolyte because the electrolyte became viscous when the concentration of polysulfide in the electrolyte was high, resulting low ionic conductivity. Also, they claimed that the creation of a passivation layer of lithium sulfide was critical for capacity decay. In 2004, Kim et al. proposed a binary electrolyte based on dimethoxyethane (DME) and DOL with LiTFSI salt. [43] DME is known to be one of the best solvents to dissolve polysulfide. It was found that the capacity could be increased by introducing DME as the electrolyte solvent because the more polysulfides could be dissolved, the more sulfur utilization could be obtained. At the same time, DOL worked to stabilize the lithium metal electrode surface. Later on, a combination of DME and DOL at 1:1 ratio became the most popular formulation of the electrolyte solvents for lithium/sulfur cells.

## ◆ Liquid Electrolyte development #3 - Introduction of $LiNO_3$ –

Although some cells showed promising initial capacity, over 1200mAh/g (sulfur) i.e. 70% sulfur utilization, they encountered a serious capacity degradation after just several cycles due to the redox shuttle phenomenon of polysulfide. In 2004, Mikhaylik at the Sion Power corporation filed a patent of a big invention for lithium/sulfur cells. [44] The invention was that an additive, $LiNO_3$, to the liquid electrolyte in lithium/sulfur cells drastically alleviated redox shuttle problems. The effect of $LiNO_3$ was to produce protection layers on the lithium surface (Figure 1-9), which was studied in detail later by Aurbach et al. [45] Mikhaylik et al. analyzed the details of redox shuttle phenomenon using both experimental and calculational methods [37] Later on, co-solvent of DME and DOL with LiTFSI and $LiNO_3$ as the salts became the most popular formulation of the electrolyte. After a while, since researchers were encouraged by experiencing a significant improvement of cycling performance with adoption of $LiNO_3$ additive, research of lithium/sulfur cells increased gradually after 2010. [6]

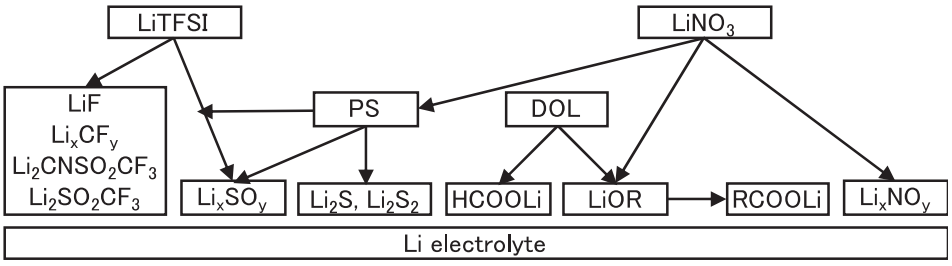


Figure 1-9. A schematic presentation of the contribution of the various components in DOL/LiTFSI/$Li_2S_6$/$LiNO_3$ solutions to the surface chemistry of Li electrodes from literature 45.

## ◆ Liquid Electrolyte development #4 - Introduction of Ionic liquids –

In 2008, Shin et al. introduced N-methyl-(n-butyl)pyrrolidinium bis(trifluoromethanesulfonyl)imide (PYR14TFSI) with LiTFSI salt to a lithium/sulfur cell. [48] PYR14TFSI is one of the ionic liquids which are couples of ions that exist as a liquid at room temperature. They claimed that having PYR14TFSI in the electrolyte enhanced compatibility with Li metal. Also, they emphasized that mixing with TEGDME increased the ion conductivity at low temperature. Ionic liquid was receiving attentions in the research of Li-ion cells because of its low flammability at first. Later, the effect for stabilization of Li metal attracted more attentions. Basile et al. revealed that just immersing Li metal in a ionic liquid, N- methyl-(n-propyl)pyrrolidinium bis(fluorosulfonyl)imide (PYR13FSI), in advance of assembly of the cell enabled longer cycling stability of Li metal electrode in 2016. [49] The functions of various ionic liquid electrolyte for lithium/sulfur cells were summarized by Park et al. in 2013. [50] They claimed that the higher donor number of TFSI anion had polysulfide dissolved more than the other anions among the popular ionic liquids. Also, the low viscosity of TFSI anion was preferable in the electrolyte. N-methyl-(n-propyl)pyrrolidinium bis(trifluoromethanesulfonyl)imide (PYR13TFSI) and PYR14TFSI have been used in many studies of lithium/sulfur cells. [51] Although the protection layers produced by those ionic liquids on the lithium metal electrode enhance the cycling stability of the cells, capacity can be sacrificed due to the lower ion conductivity and lower permeability than organic solvents if solely ionic liquid is used as the solvents of the electrolyte. Therefore, the ionic liquids are introduced at a certain ratio to the common formulation, co-solvent of DME and DOL with LiTFSI and $LiNO_3$, when cycling stability is emphasized. The more ionic liquid is introduced, the more cycling stability and the less capacity are supposed.

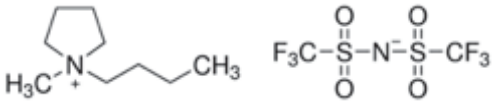

N-methyl-(n-butyl)pyrrolidinium bis(trifluoromethanesulfonyl)imide
PYR14TFSI

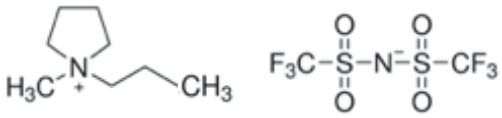

N-methyl-(n-propyl)pyrrolidinium bis(trifluoromethanesulfonyl)imide
PYR13TFSI

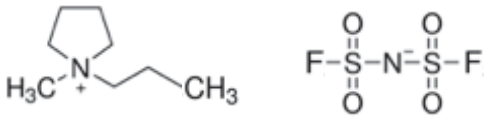

N-methyl-(n-propyl)pyrrolidinium bis(fluorosulfonyl)imide
PYR13FSI

Figure 1-11. Molecular structures of ionic liquids.

## ◆ Solid Electrolyte

In 2004, the idea of using a ceramic-based solid electrolyte with the sulfur electrode was proposed. Hayashi et al. introduced the $Li_2S$-$P_2S_5$ glass-ceramic electrolyte to sulfur cells. [46] In the case of the ceramic solid electrolyte, reduction of sulfur takes place in a different way than the case of liquid electrolyte because polysulfide cannot exist as a solid phase. A benefit of liquid electrolytes is high Li ion conductivity so that high current density can be obtained. A disadvantage of liquid electrolytes specifically for sulfur cells is inducing dissolution and precipitation of sulfur species causing associated problems as mentioned above. As for the lithium electrode, liquid electrolyte allows lithium metal to grow dendrites which can cause safety issues. Potentially, organic solvents are flammable, which can also be a safety problem. Solid electrolytes can prevent those potential hazards associated with liquid electrolyte so that the cycling stability can be higher and potentially safer than liquid electrolytes. However, the relatively poor ionic conductivity of solid electrolytes hinder high current applications. [47] Moreover, the solid-solid interface

between the positive electrode active material and the solid electrolyte also sacrifice the rate capability. The illustration of a cell using a solid electrolyte is shown in Figure 1-10.

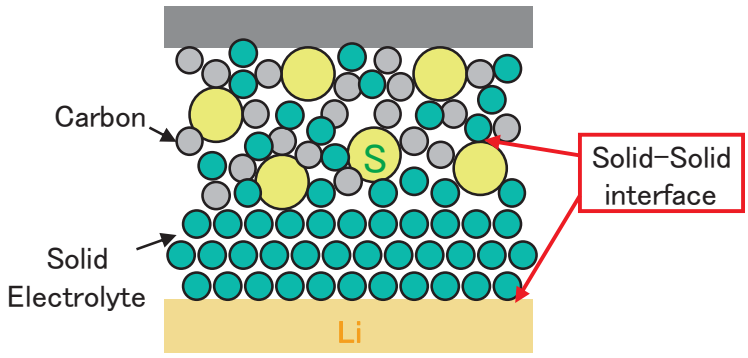


Figure 1-10. Illustration of a cell using a solid electrolyte.

### ◆ Sulfur active material development #1 - Organosulfur compounds –

From the late 1990s, practical cell designs were introduced to lithium/sulfur cells, influenced by the commercialization of Li-ion batteries (Figure 1-4), such as the electrodes prepared from a slurry of sulfur and carbon powders. Panasonic filed some patents using lithium thiolate compounds and disulfide compounds as the positive electrode active materials in 1990s. [38] Moltec Corporation filed some patents using organosulfide polymer compounds as the positive electrode active materials at the same time. [39] Since sulfur is an insulator, combining with a conductive material is necessary to be used as an electrode active material. The idea of using organosulfide compounds is to add conductivity and to immobilize the sulfur species in the electrode to prevent redox shuttle phenomenon. The positive electrode using organosulfide compounds can show better cycling stability than an electrode using elemental sulfur because the loss of sulfur species from the conductive network and redox shuttle phenomenon can be avoided. The drawback is that the cells lose the specific energy because the organic moiety adds significant weight and volume other than active sulfur species.

## ◆ Sulfur active material development #2 - Sulfur/carbon Composites -

Since the late 2000s, research on sulfur electrode active materials became predominant. Many studies have revealed that using composites of sulfur and conductive materials as the active material in the positive electrode is an effective way to obtain high sulfur utilization. [14] In 2009, Ji et al. in a group at University of Waterloo presented a composite of CMK-3 mesoporous carbon with infiltrated sulfur in the matrix as the positive electrode active material. [52] Zheng et al. at a group of Stanford University proposed a composite of carbon nanofibers with encapsulated sulfur in 2011. [53] Seh et al. in the same group at Stanford University presented sulfur nanoparticles encapsulated in a $TiO_2$ yolk shell structure and Liang et al. reported $TiO_2$ inverse opal structure. [54,55] These studies used a concept of infiltrating or encapsulating sulfur in a conductive matrix with a well-controlled design in order to prevent diffusion of sulfur species during electrochemical reactions. Sulfur is known to have the lowest viscosity in the liquid phase at 155 °C. Therefore, infiltration by heating up the precursor of sulfur with matrices were a popular method. It was possible to encapsulate sulfur in the pores of such conductive matrices as the initial structure. However, it was still challenging to maintain the structure after cycling. Also, the complicated synthesis process was not suitable for scaling up for practical applications. More and more studies about material development for the active materials have been reported since then. As the conductive substrate for the sulfur electrode, a variety of carbon materials have been used, such as graphene oxide (GO), carbon nanotubes and carbon nanofibers. In 2011, Ji et al. presented a composite of sulfur and GO with decent cell performance and Song et al. improved the cell performance based on the same composite in 2013. [56, 57] The composite of sulfur and GO received attentions because of not only the high cell performance but also the water-based synthesis process which can be scaled-up practically.

## ◆ Positive electrode sheet development

In order for an active material to work in a cell, electron access and lithium ion access should be given to each particle of the active material. For this purpose, a functional electronically-conductive sheet is indispensable. Binders are used to provide the integrity to sulfur active materials and conductive additives, and a current collector with a certain porosity. In 2002, Cheon et al. investigated the effect of the preparation method of the positive electrode sheet on the cell performance using PEO binder. It was verified that in order to create lithium ion access to sulfur species, a moderate porosity must be maintained so that the electrolyte solution is distributed through the pores. Although some research was conducted on new binders, there had not been very many studies on components for positive electrode sheets until the 2010s, because similar components to those of Li-ion cells could be introduced to lithium/sulfur cells without significant issues. Mainly PEO, poly-(tetrafluoroethylene) (PTFE), poly-(vinylidene fluoride) (PVdF), styrene-butadiene rubber (SBR) and carboxymethyl cellulose (CMC) have been used as the binder of sulfur electrode. In 2010, Elazari et al. realized a binder free electrode by using microporous activated carbon fibers as the substrate to host sulfur, forming carbon fiber cloth as the electrode. [59] Thus, carbon fibers have been known to be able to reduce or eliminate binders from the electrode. In 2013, Seh et al. presented a concept of bifunctional binders which worked as the binder and the immobilizer of sulfur species to prevent the redox shuttle in the cell. [60] Then, research using strong affinity of polymer binders with sulfur species have been intensive. All the components are influential to the cell performance. Also, all the engineering processes to fabricate electrodes and cells significantly affects the cell performance, too.

## 1.4) Purpose of this work

Decades of research have contributed to the improvement of the cell performance of lithium/sulfur cells. Especially, a significant improvement has been achieved by inventions of liquid electrolyte components. Nowadays, most of investigations have been using the usual components for the liquid electrolyte, which contains DME and DOL as the solvents and LiTFSI and $LiNO_3$ as the salts with or without some ionic liquid. The reason why those inventions succeeded are the fact that the procedure to make the liquid electrolyte is relatively straightforward, which is almost just to mix and stir all the components, so that the products and the results are highly reproducible. On the other hand, inventions about sulfur electrode active materials and sulfur electrode sheet components have not been fruitful despite a number of efforts. Even inventions of state-of-the-art technologies for sulfur electrode active materials hardly have worked for practical applications mainly due to poor reproducibility and/or difficulty of scaling-up. In contrast to preparation of liquid electrolyte, fabrication of sulfur electrode active materials is not straightforward. As for sulfur electrode sheet fabrication, if only a little sulfur is loaded, the ratio of the other components to sulfur in a cell, such as casing materials, becomes significant, resulting low specific capacity as a whole cell. However, it is challenging to produce a sulfur electrode sheet with high sulfur loading sustaining decent electron conductivity and ion conductivity to obtain high sulfur utilization.

The purpose of this thesis is to develop technologies for the sulfur electrode active material and the sulfur electrode sheet components to realize a practical lithium/sulfur cell. The sulfur electrode active material technology should be “reproducible” and “easy to be scaled-up” with high performance. In order for the technology to be qualified to meet these requirements, it should be adequately understood from a chemical point of view, because otherwise the important parameters and conditions in the synthesis process which affect the cell performance can be overlooked. The sulfur electrode sheet technology should be able to hold “high sulfur loading” maintaining high capacity.

If the day comes when a practical lithium/sulfur cell is completed and commercialized, much of our modern-day technologies leading social development, such as transportation, energy distribution, aircrafts and aerospace, will progress dramatically. There is currently a real need for innovations to battery cells in order to overcome challenges in energy generation and storage.

In Chapter 2 in this thesis, the electrochemical reactions of sulfur in the cell are focused on understand the complicated polysulfide reactions and the associate redox shuttle phenomenon. In Chapter 3, the focus is on the details of the sulfur deposition process in the fabrication of the sulfur- GO composite as a sulfur electrode active material. The relationship between the process and the resulting morphology which affects the cell performance is revealed. In Chapter 4, the reaction of sulfur with cetyltrimethyl ammonium bromide (CTAB) during the synthesis process of sulfur-GO composite is intensively researched to understand the resulting surface modification of the materials which has significant influence to the cell performance. In Chapter 5, the function of PQ polymer as a binder is investigated in detail to achieve a sulfur electrode with high sulfur loading. In Chapter 6, the degradation mechanism of the sulfur-GO composite is the focus to overcome the challenge of long lifetime of the cell.

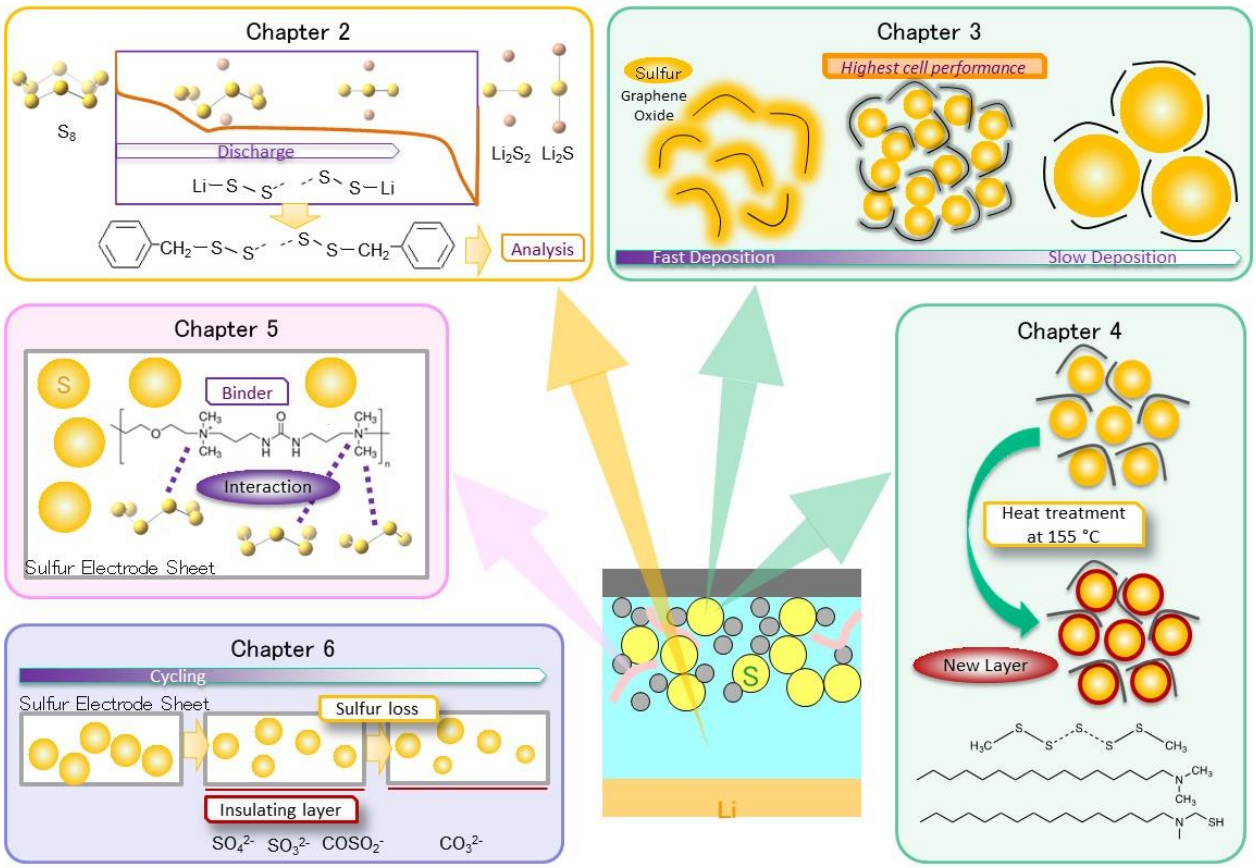


Figure 1-11. Strategy chart of this work.

## 1.5) References

[1] J. -M. Tarascon, M. Armand, *Nature* **2001**, *414*, 359−367.

[2] M. S. Whittingham, *Science* **1976**, *192*, 1226.

[3] X.-B. Cheng, R. Zhang, C.-Z. Zhao, Q. Zhang, *Chem. Rev.* **2017**, *117*, 10403−10473.

[4] M. Mohri, et al. *J. Power Sources* **1989**, *26*, 545–551.

[5] K. Mizushima, P. C. Jones, P. J. Wiseman, J. B. Goodenough, *Mat. Res. Bull*. **1980**, *15*, 783–789.

[6] X.-B. Cheng, J.-Q. Huang, Q. Zhang, *J. Electrochem. Soc*. **2018**, *165*, A6058-A6072.

[7] Handbook of Electrochemistry, *Maruzen*, **2013**, ISBN-13: 978-4621084137.

[8] P. G. Bruce, S. A. Freunberger, L. J. Hardwick, J.-M. Tarascon, *Nat. Mater*., **2012**, *11*, 19-29.

[9] E. J. Cairns and H. Shimotake, *Science*, **1969**, *164*, 3886

[10] E. Fukushima, Case study project for Okochi prize in COE program for 21st Century at Hitotsubashi University, **2008**, Case#08-02.

[11] M. V. Merritt, D. T. Sawyer, *Inorg. Chem.* **1970,** *9*, 211-215

[12] P. T. Cunningham, S. A. Johnson, E. J. Cairns, *J. Electrochem. Soc*. **1972**, *119*, 1448-1450.

[13] S.-E. Cheon, K.-S. Ko, J.-H. Cho, S.-W. Kim, E.Y. Chin, H.-T. Kim, *J. Electrochem. Soc*. **2003**, 150, *6*, A800-A805.

[14] Q. Pang, X. Liang, C. Y. Kwok. L. F. Nazar, *Nat. Energy*, DOI:10.1038/NENERGY.2016.132

[15] A. Teder *Acta Chem. Scand.* **1971**, *25*, 1722-1728

[16] T. Chivers, I. Drummond, *Inorg. Chem.* **1972**, *11*, 2525-2527

[17] W. Giggenbach, *Inorg. Chem.* **1972**, *11*, 1201

[18] W. Giggenbach *J. Chem. Soc.* **1973**, (D) 729-731

[19] F. Seel H.-J. Guttler *Angew. Chem. Internat. Edit.* **1973**, *12*, 420-421

[20] T. Chivers I. Drummond *J. Chem. Soc.* **1974**, (D) 631-633

[21] Robin J. H. CLARK, Inorg. Chem. **1978**, *17*, 3169-3174

[22] M. Delamar J.-c. Marchon *J. Electroanal. Chem*. **1975**, *63*, 351-357

[23] J. Badoz-Lambling, R. Bonnaterre, G. Cauquis, M. Delaamar, Georgette Demange, *Electrochim. Acta*, **1976**, *21*, 119-131

[24] T. Fujinaga, T. Kuwamoto, S. Okazaki, M. Hojo, *Bull. Chem. Soc. Jpn.* **1980**, *53*, 2851-2855

[25] J. Paris, V. Plichon *Electrochim. Acta*, **1981**, *26*, 1823-1829

[26] P. Lessner, J. Winnick, F. R. McLarnon, E. J. Cairns, *J. Electrochem. Soc.*, **1986**, *133*, 2510-2516.

[27] P. Lessner, J. Winnick, F. R. McLarnon, E. J. Cairns, *J. Electrochem. Soc.*, **1986**, *133*, 2517-2522.

[28] P. Lessner, J. Winnick, F. R. McLarnon, E. J. Cairns, *J. Electrochem. Soc.*, **1987**, *134*, 2669-2676.

[29] S. Tobishima, H. Yamamoto, M. Matsuda, *Electrochim. Acta*, **1997**, *42*, 1019-1029.

[30] R. D. Rauh, F. S. Shuker, J. M. Marston, S. B. Brummer, *Inorg. Nucl. Chem*. **1977**, (39). 1761-1766

[31] R. D. Rauh, K. M. Abraham, G. F. Pearson, J. K. Surprenant, S. B. Brummer *J. Electrochem. Soc.* **1979**, *126*, No. 4, 523-527

[2832] H. Yamin, J. Penciner, A. Gorenshtain, M. Elam, E. Peled *J. Power Sources*, **1985**, *14*, 129-134

[33] H. Yamin, A. Gorenshtein, J. Penciner, Y. Sternberg, E. Peled *J. Electrochem. Soc.*, **1988**, *135,* 1045-1048

[34] E. Peled, Y. Sternberg, A. Gorenshtein, Y. Lavi *J. Electrochem. Soc.*, **1989**, *136*, 1621-1625

[35] D. Aurbach, O. Youngman, Y. Gofer, A. Meitav, *Electrochim. Acta*. **1990**, *35*, 625-638.

[36] B. M. L. Rao J. A. Shropshire *J. Electrochem. Soc*. **1981**, *128*, 942-945

[37] Y. V. Mikhaylik, J. R. Akridge, *J. Electrochem. Soc*., **2004**, *151,* A1969-A1976.

[38] M. Sotomura, Y. Sato, H. Uemachi, JP Patent **1992**, 28403

[39] S. Zhang, S. Cheng, WO97/44840 **1997**

[40] M. -Y. Chu US Patent **1998,** 5789108.

[41] D. Marmorstein, T.H. Yu, K.A. Striebel, F.R. McLarnon, J. Hou, E. J. Cairns, *J. Power Sources* **2000**, *89*, 219–226

[42] D. Chang, S.-H. Lee, S.-W. Kim, H.-T. Kim *J. Power Sources*, **2002**, *112*, 452-460.

[43] S. Kim, Y. Jung, H. S. Lim, *Electrochimica Acta* **2004**, *50*, 889–892

[44] Y. Mikhaylik, US Patents 7,354,680; 7,358,012; 7,553,590.

[45] D. Aurbach, E. Pollak, R. Elazari, G. Salitra C. S. Kelley, J. Affinito, *J. Electrochem. Society*, **2009**, *156*, A694-A702

[46] A. Hayashi, T. Ohtomo, F. Mizuno, K. Tadanaga, M. Tatsumisago *Electrochim. Acta* **2004**, *50*, 893–897

[47] T. Hakari, A. Hayashi, and M. Tatsumisago, *Adv. Sustainable Syst.* **2017**, 1700017.

[48] J. H. Shin, E. J. Cairns, *J. Power Sources* **2008**, *177*, 537–545.

[49] A. Basile, A.I. Bhatt, A.P. O'Mullane, *Nat. Commun*. **2016**, DOI:10.1038/ncomms11794

[50] J.-W. Park, K. Ueno , N. Tachikawa , K. Dokko , M. Watanabe *J. Phys. Chem. C*, **2013**, *117*, 20531–20541.

[51] S, Zhang , K, Ueno , K, Dokko, M. Watanabe, *Adv. Energy Mater*., **2015**, 1500117.

[52] X. Ji, K. T. Lee, L. F. Nazar, *Nat. Mater*., **2009**, *8*, 500-506.

[53] G. Zheng, Y. Yang, J. J. Cha, S. S. Hong, Y. Cui, *Nano Lett.*, **2011**, *11*, 4462–4467.

[54] Z. W. Seh, W. Li, J. J. Cha, G. Zheng, Y. Yang, M. T. McDowell, P.-C. Hsu, Y. Cui *Nat. Commun*. **2012**, DOI: 10.1038/ncomms232

[55] Z. Liang, G. Zheng, W. Li, Z. W. Seh, H. Yao, K. Yan, D. Kong, Y. Cui *ACS nano*, **2014**, *8*, 5249–5256

[56] L. Ji, M. Rao, H. Zheng, L. Zhang, Y. Li, W. Duan, J. Guo, E. J. Cairns, Y. Zhang, *J. Am. Chem. Soc*. **2011**, *133*, 18522–18525.

[57] M.-K. Song, Y. Zhang, E. J. Cairns, *Nano Lett.* **2013**, *13*, 5891–5899.

[58] S.-E. Cheon, J.-H. Cho, K.-S. Ko, C.-W. Kwon, D.-R. Chang, H.-T. Kim, S.-W.

Kim, *J. Electrochem. Soc*. **2002**, *149*, A1437-A1441.

[59] R. Elazari, G. Salitra, A. Garsuch, A. Panchenko, D. Aurbach, *Adv. Mater*. **2011**, *23*, 5641–5644.

[60] Z. W. Seh, Q. Zhang, W. Li, G. Zheng, H. Yao, Y. Cui, *Chem. Sci*. **2013**, *4*, 3673-3677.

# CHAPTER 2

## Electrochemical reactions of lithium/sulfur cells: an analytical study using the organic conversion technique

## 2.1) Introduction

The polysulfide compounds produced in a lithium/sulfur cell have been investigated for over a half century. It is because identification of the reactants, intermediates and products in the cell is a indispensable step in understanding the electrochemical reactions. [1-22] The following reaction scheme has been suggested in the previous studies by using ultraviolet-visible absorption (UV-Vis) spectroscopic studies. [1, 2]

$S_8 + 2e^- \rightarrow S_8^{2-}$ (1)

$S_8^{2-} + 2e^- \rightarrow 2S_4^{2-}$ (2)

$S_8^{2-} \rightleftarrows S_6^{2-} + ¼\ S_8$ (3)

$S_6^{2-} \rightarrow 2S_3^-$ (4)

However, the details of these reactions are still unclear because the UV-Vis absorption bands of some polysulfides including unidentified species overlap. The absence of reference spectra for isolated polysulfide compounds further hinder the identification.

Eqn (5) through (8) with eqn (1) and (2) are also widely accepted. [23]

$3S_8^{2-} + 2e^- \rightarrow 4S_6^{2-}$ (5)

$2S_6^{2-} + 2e^- \rightarrow 3S_4^{2-}$ (6)

$S_4^{2-} + 2e^- \rightarrow 2S_2^{2-}$ (7)

$S_2^{2-} + 2e^- \rightarrow 2S^{2-}$ (8)

These equations are based on the hypothesis that elemental sulfur having eight-membered ring structure is reduced with respect to an even number of sulfur atoms. The hypothesis has not been authenticated by experimental studies.

Since some polysulfide molecules readily transform in solution, in situ measurements of reactions within a cell are difficult. IR and Raman spectroscopic studies have been conducted, however, these analyses have faced difficulties in peak assignments as well as UV-Vis. [3-6] In particular, IR and Raman peak assignments for polysulfide species having more than four sulfur atoms have hardly been reported. Although the number of sulfur atoms in a polysulfide molecule can be determined by mass spectrometry (MS) in principle, some polysulfide molecules can transform even during the injection and ionization process due to their high reactivity. The sensitivity of $^{33}S$ nuclear magnetic resonance spectrometry (NMR) is insufficient for identification of the structures of polysulfides. Thus, ingenious methods of analysis are necessary to overcome these difficulties and to obtain additional insights into the detailed reaction mechanism.

Recently, it has been reported that sodium polysulfide species ($Na_2S_x$) can be converted to benzylized polysulfide ($Bz_2S_x$) molecules without changing the number of S atoms. The $Bz_2S_x$ species can be analyzed via proton NMR ($^1H$ NMR). [24, 25] Also, in order to investigate the distribution of polysulfide species, polysulfides in aqueous solution were determined by using methylation and following identification using High-performance liquid chromatography (HPLC). [26-28]

Ths organic conversion technique can be applied to lithium polysulfide ($Li_2S_x$) species. Therefore, it enables us to follow electrochemical reactions in battery cells using $^1H$ NMR. Furthermore, liquid chromatography-mass spectrometry (LC/MS) becomes applicable, since the benzylized or methylized polysulfide species are stable sufficiently in the LC/MS environment. [29] Since, $^1H$ NMR spectra of isolated benzylized polysulfide species are rarely available, ab initio molecular orbital (MO) calculations are utilized for peak assignments. Ab initio MO calculations can also be useful in peak assignment and interpretation of UV-Vis spectra. [30]

In this chapter, the polysulfide species within a lithium/sulfur cell have been identified

utilizing LC/MS and NMR following application of the organic conversion technique, in order to elucidate the electrochemical reactions in detail. UV-Vis spectra were also obtained to confirm consistency of the results of this work with those of previous studies.

## 2.2) Results and Discussion

### 2.2.1) LC/MS analysis

The charge–discharge profile of the lithium/sulfur cell during the first cycle with the specific measurement points is presented in Figure 2-1. Distinctive two plateaus appeared at approximately 2.3 and 2.1 V. The slope between 2.3 and 2.1 V is regarded as the transition state. It is notable that, while the voltage is almost constant in the second plateau, the voltage varies with the capacity in the first plateau and the transition state.

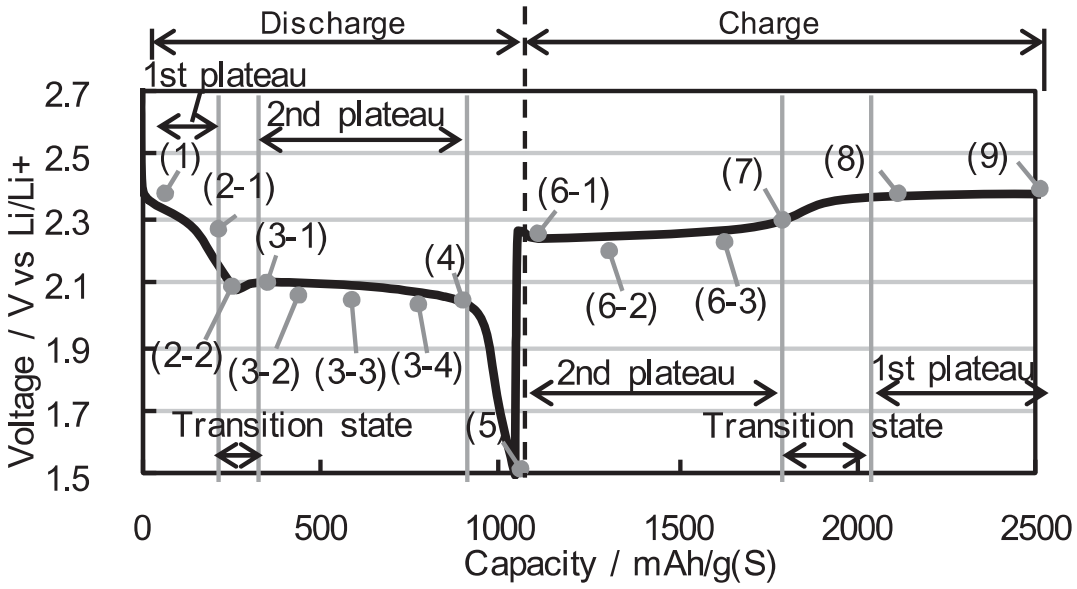


Figure 2-1. Discharge–charge profile of the lithium/sulfur cell during the first cycle with observation points.

The LC data associated with the discharge process along with reference data for $Bz_2S$, $Bz_2S_2$ and $S_8$ are shown in Figure 2-2. LC peaks for $Bz_2S_x$ were successfully identified by MS as shown in Figure 2-3. The peak for $S_8$ was identified by reference.

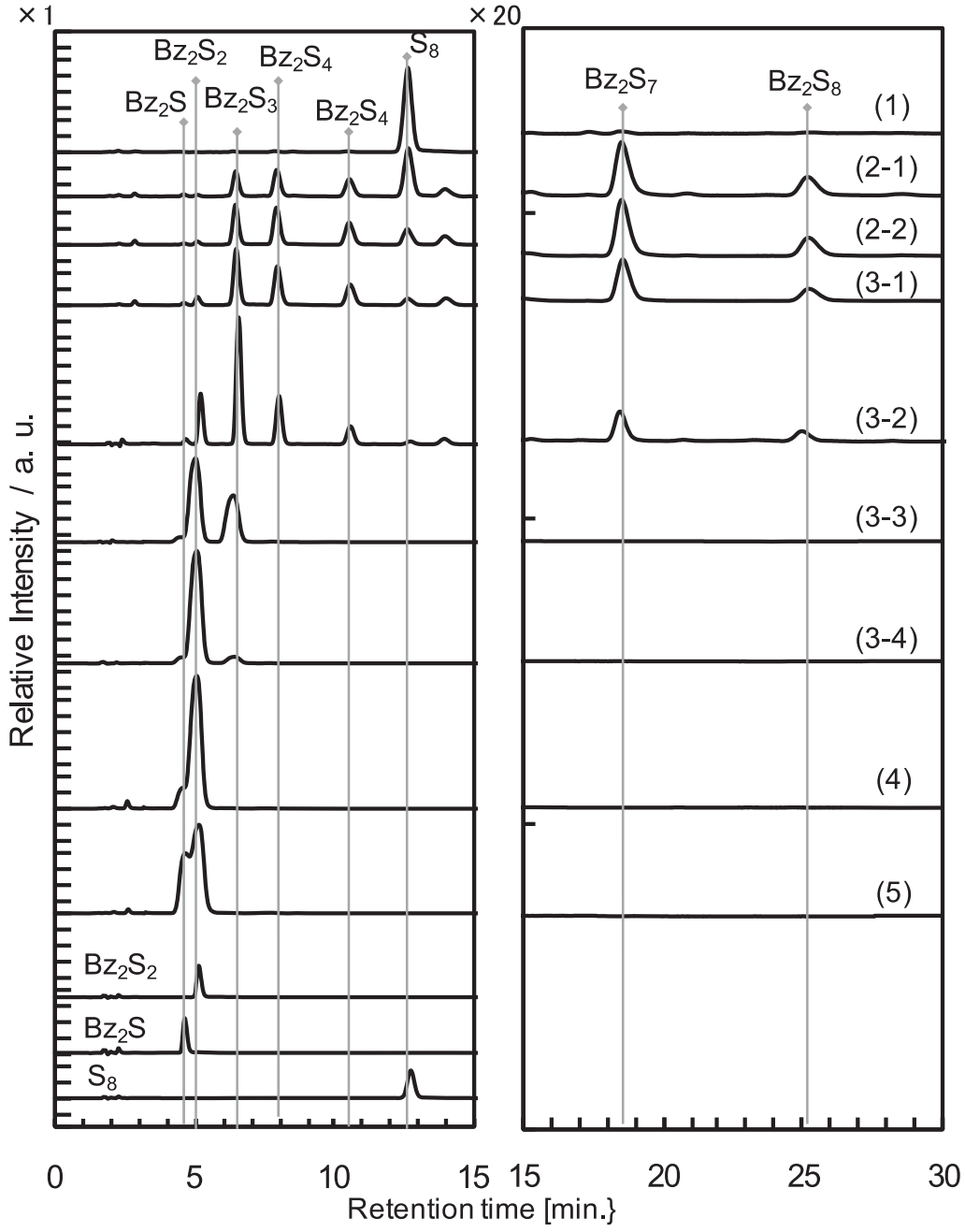


Figure 2-2. LC data for points 1 to 5, including $Bz_2S$, $Bz_2S_2$ and $S_8$ as references.

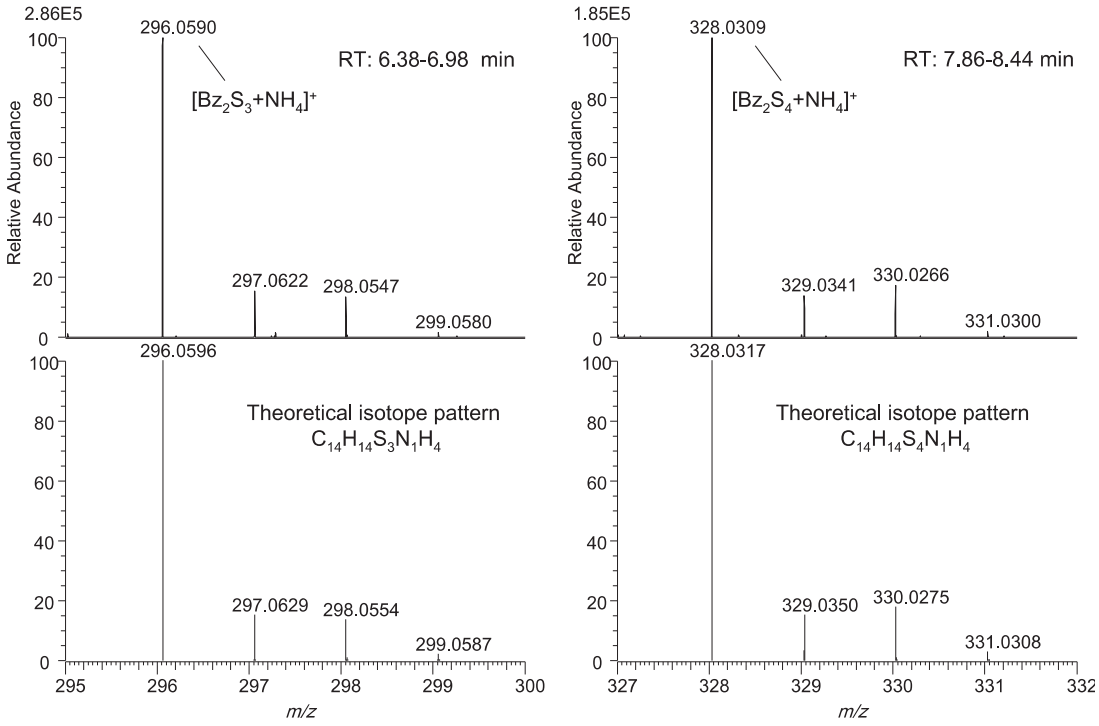


Figure 2-3. Experimental mass spectra and the corresponding theoretical isotope patterns for ammonium adducts of benzylized polysulfides $Bz_2S_3$ (left) and $Bz_2S_4$ (right).

The amount of each species relative to its original concentration at each point is estimated from the peak area. The results are summarized in Table 1. The amount change of $Bz_2S_x$ (x = 1 to 6) is shown in Figure 2-4.

Table 2-1. LC peak identification by MS and the relative remaining quantity of species as estimated from LC data.

| | | $S_8$ | $Li_2S_8$ | $Li_2S_7$ | $Li_2S_6$ | $Li_2S_5$ | $Li_2S_4$ | $Li_2S_3$ | $Li_2S_2$ | $Li_2S$ |
|---|---|---|---|---|---|---|---|---|---|---|
| m/z ($[Bz_2S_x+NH_4]^+$) | | - | 456 | 424 | 392 | 360 | 328 | 296 | 264 | - |
| Retention time [min.] | | 12.6 | 25.2 | 18.6 | 14.0 | 10.6 | 8.0 | 6.5 | 5.1 | 4.6 |
| Relative amount [ / mol ] at observation points | 1 | 184 | 0 | 0 | 0 | 0 | 0 | 0 | 0 | 0 |
| | 2-1 | 103 | 6 | 10 | 27 | 109 | 86 | 68 | 4 | 14 |
| | 2-2 | 32 | 6 | 11 | 33 | 135 | 112 | 97 | 8 | 8 |
| | 3-1 | 14 | 4 | 7 | 27 | 129 | 126 | 144 | 21 | 15 |
| | 3-2 | 4 | 1 | 3 | 15 | 80 | 116 | 242 | 101 | 25 |
| | 3-3 | 0 | 0 | 0 | 0 | 0 | 9 | 264 | 163 | 23 |
| | 3-4 | 0 | 0 | 0 | 0 | 0 | 8 | 100 | 392 | 29 |
| | 4 | 0 | 0 | 0 | 0 | 0 | 0 | 12 | 501 | 60 |
| | 5 | 0 | 0 | 0 | 0 | 0 | 0 | 10 | 448 | 87 |
| | 6-1 | 0 | 0 | 0 | 0 | 0 | 5 | 145 | 271 | 27 |
| | 6-2 | 0 | 0 | 1 | 3 | 31 | 68 | 216 | 169 | 30 |
| | 7 | 2 | 1 | 2 | 11 | 73 | 104 | 231 | 61 | 20 |
| | 8 | 35 | 5 | 10 | 29 | 115 | 100 | 83 | 5 | 11 |
| | 9 | 44 | 7 | 14 | 36 | 134 | 108 | 80 | 6 | 4 |

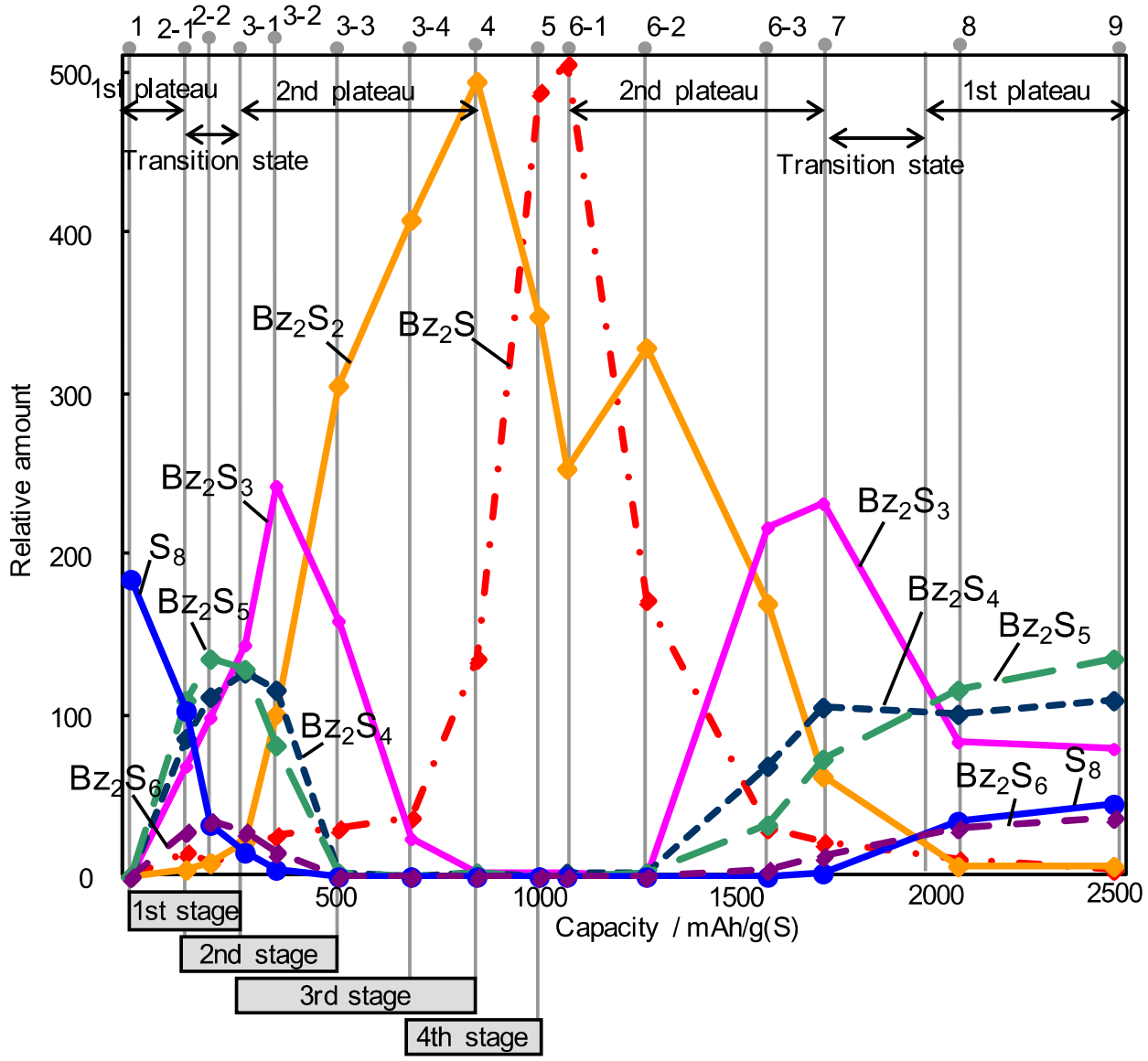


Figure 2-4. Relative remaining quantity of $Bz_2S_x$ (x = 1 to 6) at points 1 to 9 as estimated from LC data.

It is evident that the concentration of $S_8$ decreases between points 1 and 3–2. All possible species produced by the decomposition of $S_8$, including $Li_2S_7$, $Li_2S_5$, $Li_2S_3$, $Li_2S_2$ and $Li_2S$, are detected. These species had been undetected in previous studies. [3-23] $Li_2S_5$, $Li_2S_4$ and $Li_2S_3$ are major, while $Li_2S_8$ is minor at point 2–1. The increasing rate of $Li_2S_x$ (x = 4 to 8) makes a downward turn between points 2–1 and 3–1. These species completely

disappear at point 3–3. $Li_2S_3$, which is dominant at point 3–2, gradually decreases up to point 4. $Li_2S$ and $Li_2S_2$ increase over this same span. Beginning at point 3–4, while the increasing rate of $Li_2S_2$ is reduced, $Li_2S$ increases at an accelerated rate.

The results suggest that the overall electrochemical reaction can be divided into four major stages as follows.

The first stage: between points 1 and 3–1 (in the first plateau and the transition state).

The second stage: between points 2–1 and 3–3 (in the transition state and the beginning of the second plateau).

The third stage: from points 3–1 to 4 (in the second plateau).

The fourth stage: from points 3–4 to 5 (in the latter half of the second plateau and after the plateau).

In the first stage, $S_8$ is either reduced to $Li_2S_8$ or smaller species directly. This decomposition of $S_8$ continues up to point 3–1. The first stage (from point 1 to point 3–1) is described by equation (9) through (13).

$$S_8 + 2e^- \rightarrow S_8^{2-} \quad (9)$$

$$S_8 + 4e^- \rightarrow S_7^{2-} + S^{2-} \quad (10)$$

$$S_8 + 4e^- \rightarrow S_6^{2-} + S_2^{2-} \quad (11)$$

$$S_8 + 4e^- \rightarrow S_5^{2-} + S_3^{2-} \quad (12)$$

$$S_8 + 4e^- \rightarrow 2S_4^{2-} \quad (13)$$

The increase in $Li_2S_x$ (x = 1 to 3), concurrent decline of $Li_2S_y$ (y = 4 to 8) and disappearance at point 3–3 suggest that $Li_2S_y$ (y = 4 to 8) is reduced to $Li_2S_x$ (x = 1 to 3) in the second stage.

The second stage (from point 2–1 to point 3–3) is noted by equation (14) through (20).

$$S_8^{2-} + 2e^- \rightarrow S_6^{2-} + S_2^{2-} \quad (14)$$

$S_8^{2-} + 2e^- \rightarrow S_5^{2-} + S_3^{2-}$ (15)

$S_8^{2-} + 2e^- \rightarrow 2S_4^{2-}$ (16)

$S_7^{2-} + 2e^- \rightarrow S_4^{2-} + S_3^{2-}$ (17)

$Li_2S_3$ produced in the first and second stage is reduced to $Li_2S_2$ and $Li_2S$ subsequently in the third stage. The third stage (from point 3–1 to point 4) is represented by equatin (21).

$S_3^{2-} + 2e^- \rightarrow S_2^{2-} + S^{2-}$ (21)

$Li_2S_2$ is partly reduced to $Li_2S$ in the fourth stage in the latter half of the second plateau and subsequent plateau. Judging from the observation that most of the $Li_2S_2$ remains intact, the fourth stage does not complete,. The fourth stage (from point 3–4 to point 5) is represented by equation (22).

$S_2^{2-} + 2e^- \rightarrow 2S^{2-}$ (22)

It is worth noting that the second plateau with a constant voltage is associated with the simple reaction, i.e. the reduction of $Li_2S_3$. On the other hand, multiple reactions occur simultaneously in the first plateau and the transition state in which the voltage changes drastically. The quantities of polysulfides in the regions in which multiple reactions overlap can be considered as the sum total generated by the simultaneous reactions.

Equation (9), (16), (20) and (22) correspond to the reactions proposed previously, which are shown above as equation (1), (2), (7) and (8) respectively. [1,2,23] The other reactions are newly presented in this study.

Reverse reactions occur in the charging process. LC data in the charge process is shown in Figure 2-5. The amount change of $Bz_2S_x$ (x = 1 to 6) is shown in Figure 2-4.

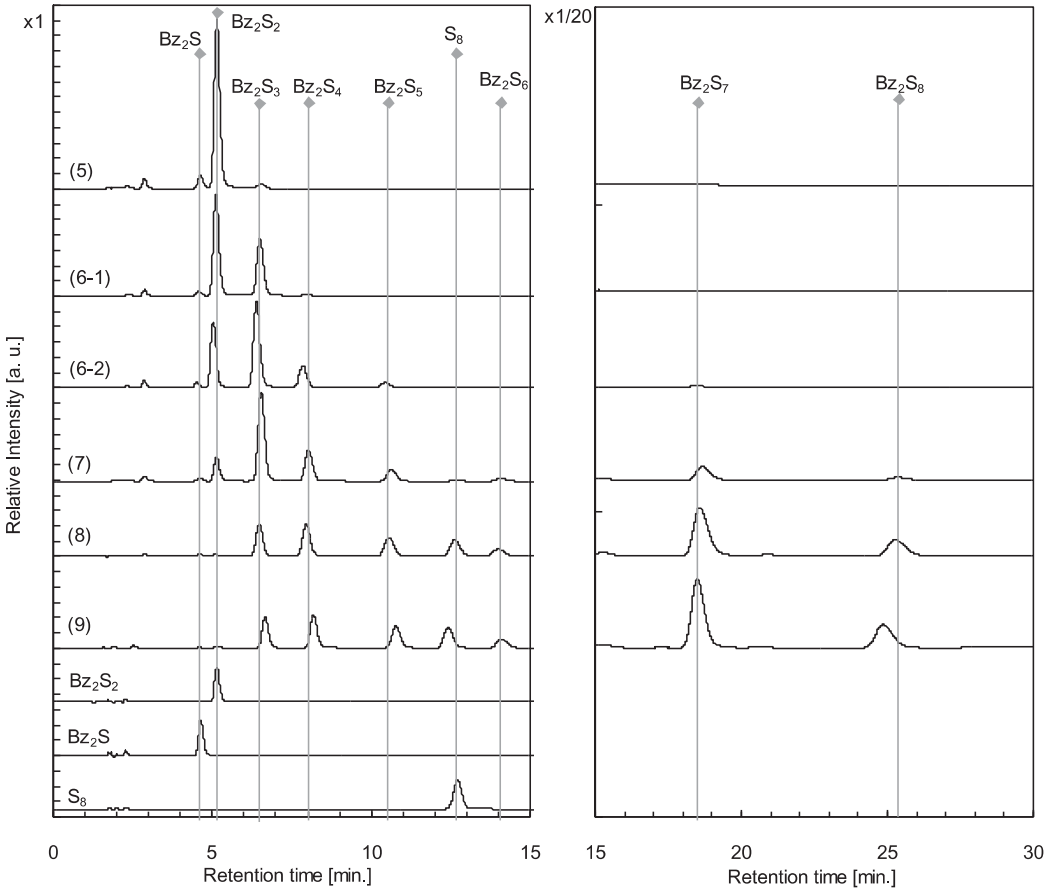


Figure 2-5. LC data resulting from the charge process. LC data at retention times < 15 min for points 5 to 9 with $Bz_2S$, $Bz_2S_2$ and $S_8$ as references (left). LC data at retention times > 15 min at 1:20 vertical scale (right).

The relationship between the voltage profile and the reactions is examined. Nernst equation shown as Equation (23) is used at the basic input.

$$U = U^0 - \frac{RT}{zF}\ln\frac{a_{Red}}{a_{Ox}} \quad (23)$$

where U is the potential, $U^0$ is the standard potential, R is the universal gas constant: 8.31 J $K^{-1}$ $mol^{-1}$, T is the temperature in kelvins, z is the number of electrons transferred in the cell reaction, F is the Faraday constant, a is the chemical activity for the relevant species.

The voltage is determined as the summary of the potentials calculated using Nernst equation with input of the chemical activity of the each specie in the each electrochemical reaction. The point is that the solubilities of $S_8$, $Li_2S_2$ and $Li_2S$ to the electrolyte solution are very low so that the concentration of those species in the electrolyte solution is kept constant by the solubility equilibrium as long as the solid state exists.

In the first plateau, the concentration of $S_8$ in the electrolyte is maintained by the solubility equilibria because the solid $S_8$ exists, resulting the small voltage change. Once all the solid $S_8$ are dissolved in the electrolyte as the dissolved $S_8$ is reduced to polysulfide, the profile moves to the transition state. In the transition state, the voltage decreases as the concentration of the shorter polysulfide increase. The voltage reaches to the minimal point under the oversaturation of $S_2^{2-}$ and $S^{2-}$. Once $Li_2S_2$ and/or $Li_2S$ nucleate, the voltage profile moves to the second plateau. The voltage is stable because the concentration of $S_3^{2-}$, $S_2^{2-}$ and $S^{2-}$ are constant. The concentration of $S_3^{2-}$ keeps constant because $S_3^{2-}$ is produced by the reduction reactions of the longer polysulfides. The concentration of $S_2^{2-}$ and $S^{2-}$ are managed by the solubility equilibrium. After all the longer polysulfides are consumed in the second stage, the concentration of $S_3^{2-}$starts to decreases resulting the slight voltage decline. Once all $S_3^{2-}$ is consumed in the third stage, Nernst equation for the reaction in the forth stage becomes dominant. As the concentration of $S_2^{2-}$ decrease to zero, the voltage drops down to zero.

It can be noticed that $Li_2S_x$ (x = 4 to 8) increase and $Li_2S_3$ keeps its amount from points 8 to 9. This phenomenon is attributed to the redox shuttle phenomenon. In this phenomenon, the polysulfides migrate onto the Li anode and reduced on the spot, resulting in the endless charge of such cells. [31-33] It is notable that the shuttle phenomenon occurs between points 8 and 9 (in the first plateau in the charging process), in which longer $Li_2S_y$ (y = 6 to 8) appear. The results suggest that longer $Li_2S_y$ (y = 6 to 8) are responsible for the shuttle phenomenon. They are reduced to shorter $Li_2S_z$ (z = 3 to 5) on the Li anode. The shuttle phenomenon can be suppressed by electrolyte additives and/or protection layers of the Li anode. [31-33]

### 2.2.2) NMR analysis

The $^{1}$H NMR spectra of benzylized polysulfides in the electrolyte solutions are shown in Figure 2-6, along with spectra of $Bz_2S$ and $Bz_2S_2$ as reference.

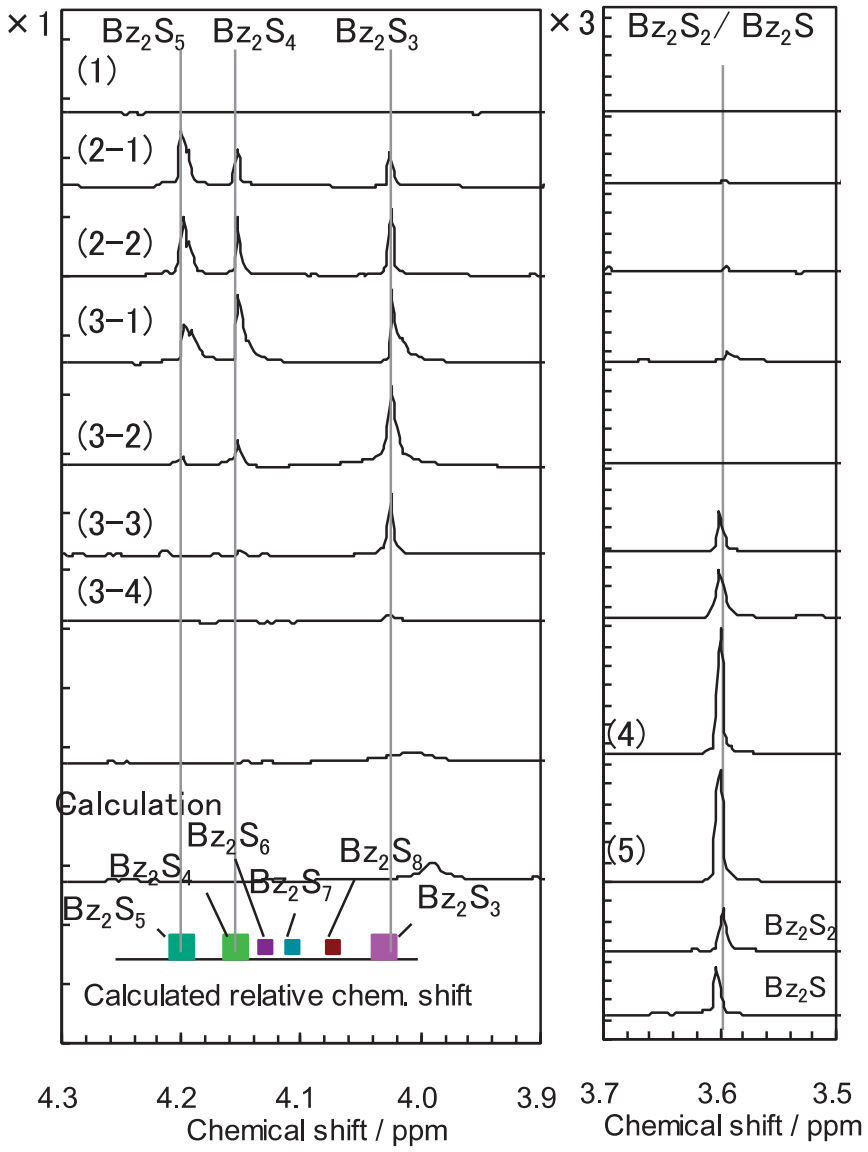


Figure 2-6. $^{1}$H NMR spectra at chemical shift for points 1 to 5, along with data for $Bz_2S$, $Bz_2S_2$ and calculated relative chemical shifts for $Bz_2S_x$ (x = 3 to 8) as references.

The peaks appearing in the region from 3 to 5 ppm correspond to methylene H of the benzylized polysulfides. The peak at 3.60 ppm, which can be assigned to either $Bz_2S$ or $Bz_2S_2$, is the most prominent at point 5. It is observed at all points except point 1. Three major peaks at 4.02, 4.15 and 4.20 ppm can be assigned to either of $Bz_2S_3$, $Bz_2S_4$ and $Bz_2S_5$ according to the LC/MS results. The calculated relative chemical shifts for $Bz_2S_y$ (y = 3 to 8) are summarized in Figure 2-5. The results suggest the following peak assignments: 4.02 ppm to $Bz_2S_3$, 4.15 ppm to $Bz_2S_4$, and 4.20 ppm to $Bz_2S_5$.

The relative concentrations of the species estimated from peak areas are shown in Figure 2-7.

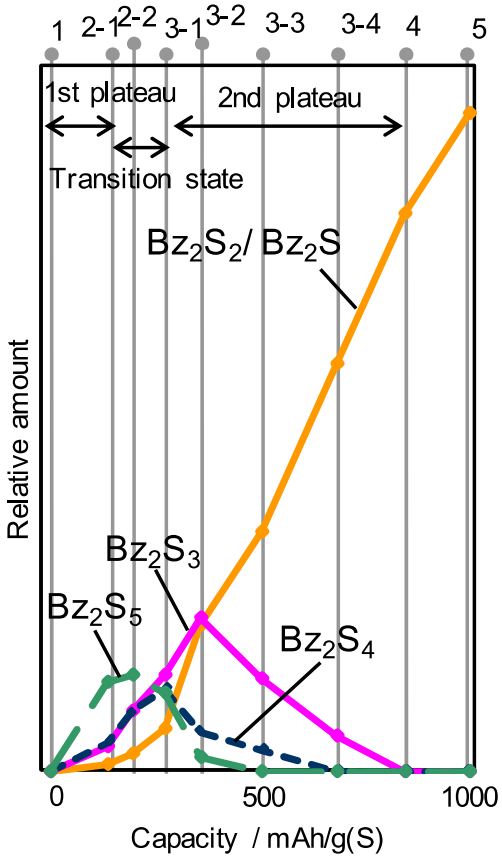


Figure 2-7. Relative remaining quantity of species as estimated from $^1$H NMR spectra.

These results demonstrate that $Li_2S_5$, $Li_2S_4$, $Li_2S_3$, along with small amounts of $Li_2S_2$ and/ or $Li_2S$, were generated between points 1 and 2–1. Both $Li_2S_5$ and $Li_2S_4$ have disappeared by point 3–4. $Li_2S_3$ is the dominant species at point 3–2. Then is fragments into $Li_2S_2$ and/or $Li_2S$ from point 3–1 to point 5. These findings are qualitatively consistent with the LC/MS results.

In the case of $Bz_2S_x$ (x = 1 to 5), the calculated chemical shift increases with the number of S atoms. This is a result of withdrawal of the electrons from the benzyl group by the polysulfur moieties (due to the high electronegativity of S). The electron withdrawing strength of the polysulfur moiety increases with an increasing number of sulfur atoms since the negative charge can be more widely distributed and thus stabilized throughout the expanded orbitals. However, the chemical shift decreases in the order of $Bz_2S_5$ > $Bz_2S_6$ > $Bz_2S_7$ > $Bz_2S_8$ conversely. In the optimized $Bz_2S_5$ geometry, one of the methylene H is located close to the fifth S atom, resulting in a H bonding-type interaction as shown in Figure 2-8. It has been shown that the chemical shift of the H closest to the S atom in $Bz_2S_5$ is remarkably high because of the deshielding by S atoms with the electron withdrawing property. In the case of $Bz_2S_x$ (x = 6 to 8), the methylene H is further removed from the sulfur atom, resulting in the lower chemical shift.

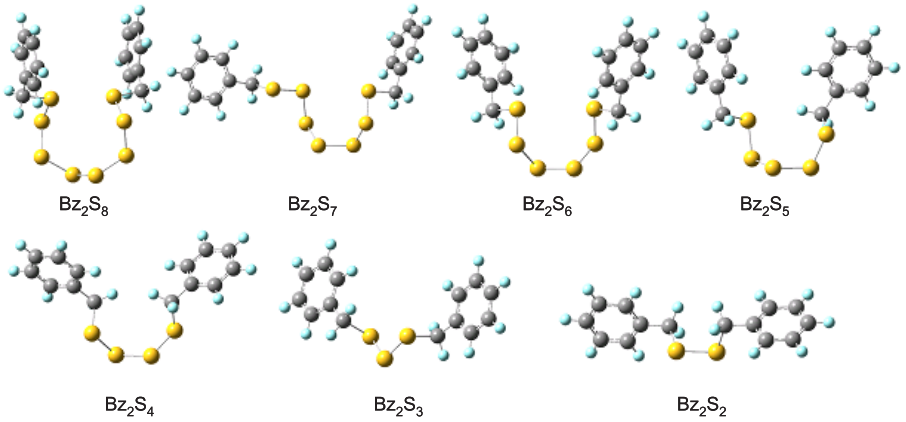


Figure 2-8. Benzylized polysulfide models for calculation of $^1$H NMR chemical shifts. (yellow, S; gray, C; and light blue, H)

### 2.2.3) UV-Vis analysis

The UV-Vis spectra of the electrolytes in the cell are shown in Figure 2-9.

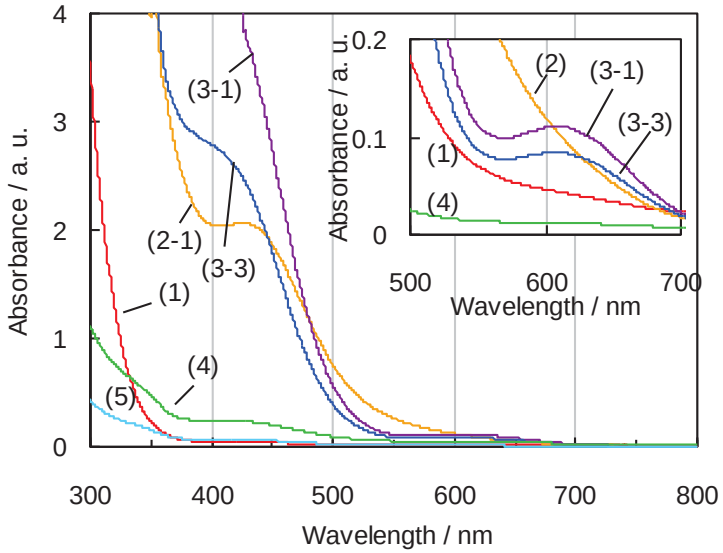


Figure 2-9. UV-Vis spectra of electrolyte solutions over the discharge process.

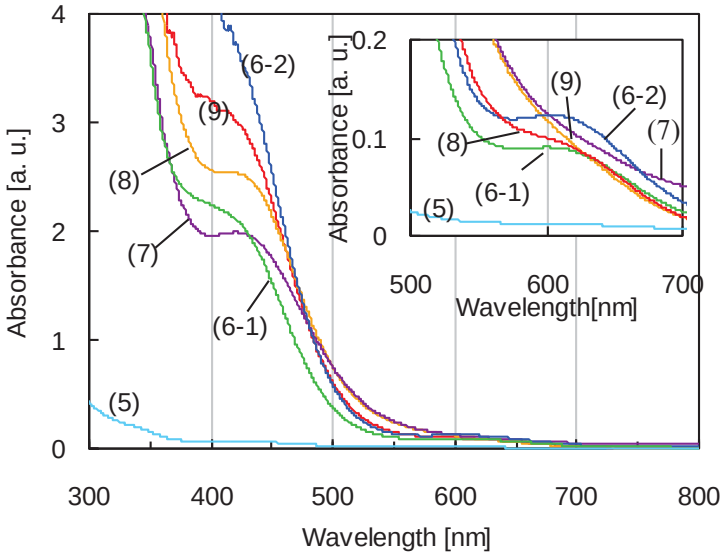


Figure 2-10. UV-Vis spectra of electrolyte solutions over the charge process.

No peaks are observed in the region above 300 nm at point 1. A peak appears at 430 nm at point 2–1. A prominent peak at 400 nm along with a smaller peak at 610 nm are both observed at point 3–1. Both the peaks at 400 and 610 nm gradually decrease during the second plateau (from points 3–1 to 5). In the charging process, reverse reactions are observed except for point 9 as shown in Figure 2-10. It corresponds to LC/MS results.

The calculated UV-Vis spectra incorporating the solvent effect of dimethoxyethane (DME) are shown in Figure 2-11. The models used for the calculation are presented in Figure 2-12.

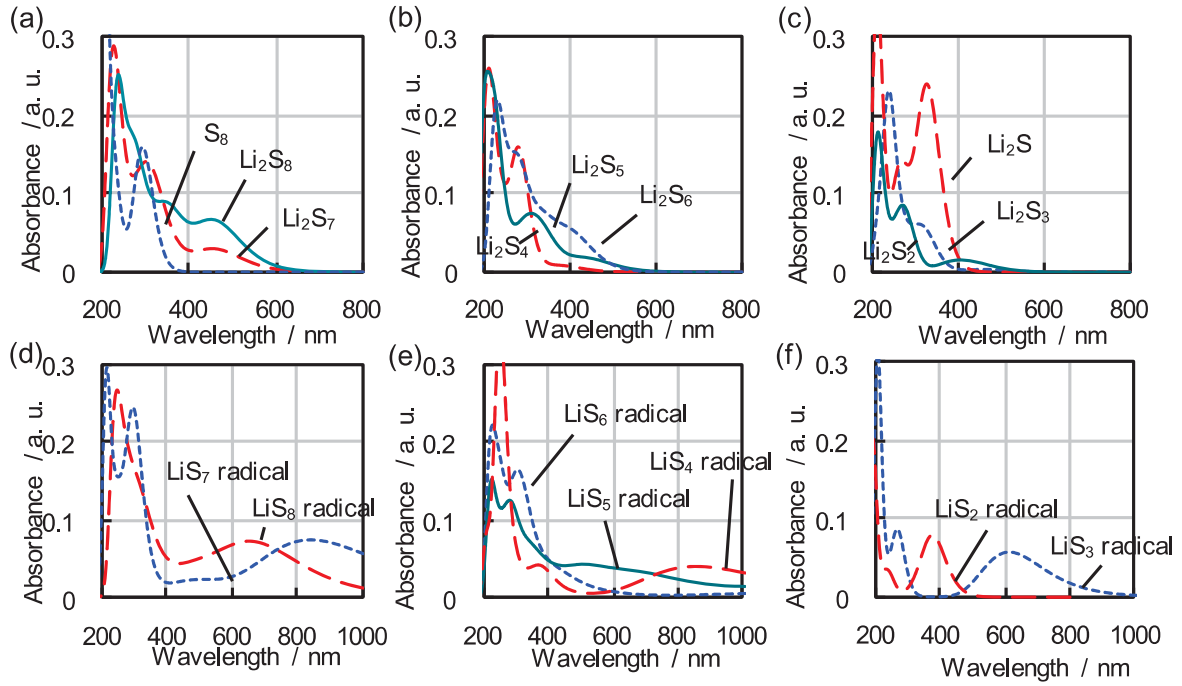


Figure 2-11. Calculated spectra with the DME solvent effect for: (a) $S_8$, $Li_2S_8$ and $Li_2S_7$; (b) $Li_2S_6$, $Li_2S_5$ and $Li_2S_4$; (c) $Li_2S_3$, $Li_2S_2$ and $Li_2S$; (d) $LiS_8$ and $LiS_7$ radicals; (e) $LiS_6$, $LiS_5$ and $LiS_4$ radicals; and (f) $LiS_3$ and $LiS_2$ radicals.

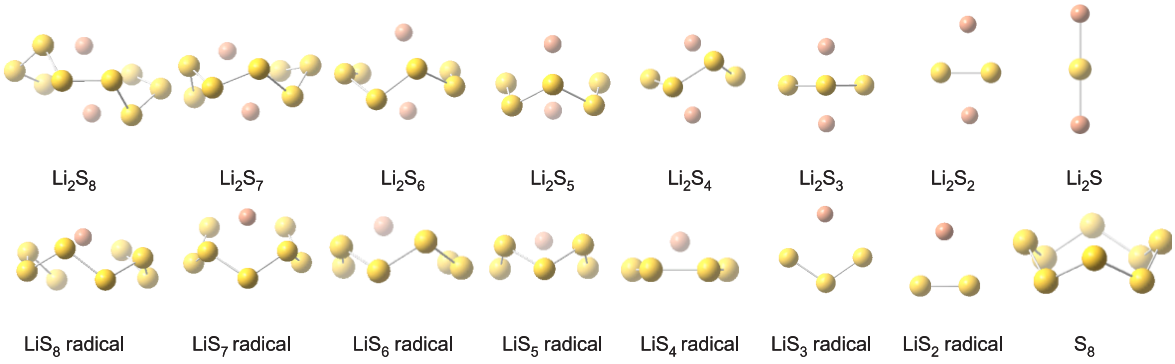


Figure 2-12. Lithium-polysulfide, lithium-polysulfide radical and sulfur models used for the calculation of UV-Vis spectra (yellow, S; and red, Li).

The calculated spectra indicate that some of the polysulfide species produce characteristic peaks in the region above 300 nm. Both $Li_2S_8$ and $Li_2S_7$ have absorption bands at 430 nm and $Li_2S_6$ has a band at 400 nm. Most radical species show significantly red-shifted peaks. The $LiS_3$ radical has a peak at 610 nm. These calculated results suggest that $Li_2S_8$ and/or $Li_2S_7$ are produced at point 2–1. $Li_2S_6$ and the $LiS_3$ radical is generated at point 3–1. The large absorption band which appears between 300 and 400 nm can be assigned to a mixture of $Li_2S_x$ (x = 1 to 8) and/or radicals. The results of this analysis are consistent with LC/MS and NMR results.

The absorbance obtained in both experimental and calculated results incorporating the solvent effects of DME and dimethylformamide (DMF) are compared in Table 2-2. This comparison shows that these calculation results are mostly consistent with both present and previous experimental results.

The calculation results suggest that the reaction products $Li_2S_7$, $Li_2S_5$ and $Li_2S_3$ have gone undetected in previous studies because their absorption bands overlap one another. Thus, it can be said that these species are hardly determined by conventional UV-Vis.

A detailed analysis of the calculation results reveals that the absorbance of polysulfides above 300 nm results from HOMO–LUMO single electron transitions. The

HOMO and LUMO energies in $Li_2S_x$ are listed in Table 2-3.

Table 2-2. Comparison of UV-Vis absorption bands between experimental and calculation results with solvent effect of DME and DMF.

| Solvent effect | method | $Li_2S_8$ | $Li_2S_6$ | $LiS_3$ radical |
|---|---|---|---|---|
| DME | Experiment | 430 | 400 | 610 |
| | Calculation | 453 | 413 | 613 |
| DMF | Experiment [12] | 505 | 460 | 618 |
| | Calculation | 492 | 436 | 648 |

Table 2-3. Energies of HOMO, LUMO and the HOMO-LUMO gap (**Δ**HOMO-LUMO) in $Li_2S_x$ and $LiS_x$ radicals.

Closed-shell species

| | $Li_2S$ | $Li_2S_2$ | $Li_2S_3$ | $Li_2S_4$ | $Li_2S_5$ | $Li_2S_6$ | $Li_2S_7$ | $Li_2S_8$ | $S_8$ |
|---|---|---|---|---|---|---|---|---|---|
| LUMO [eV] | -0.25 | -0.69 | -1.13 | -1.40 | -2.16 | -1.90 | -2.80 | -2.69 | -2.75 |
| HOMO [eV] | -4.77 | -4.66 | -4.91 | -5.47 | -5.78 | -5.68 | -6.24 | -6.02 | -7.40 |
| **Δ**HOMO-LUMO [eV] | 4.52 | 3.97 | 3.78 | 4.07 | 3.63 | 3.78 | 3.43 | 3.34 | 4.65 |

Radical species

| | $LiS_2\cdot$ | $LiS_3\cdot$ | $LiS_4\cdot$ | $LiS_5\cdot$ | $LiS_6\cdot$ | $LiS_7\cdot$ | $LiS_8\cdot$ |
|---|---|---|---|---|---|---|---|
| β-LUMO [eV] | -3.28 | -3.52 | -3.65 | -4.07 | -2.26 | -4.06 | -3.85 |
| β-HOMO [eV] | -5.27 | -6.32 | -5.78 | -5.82 | -5.70 | -6.01 | -6.33 |
| **Δ**HOMO-LUMO [eV] | 1.99 | 2.80 | 2.13 | 1.75 | 3.44 | 1.95 | 2.48 |

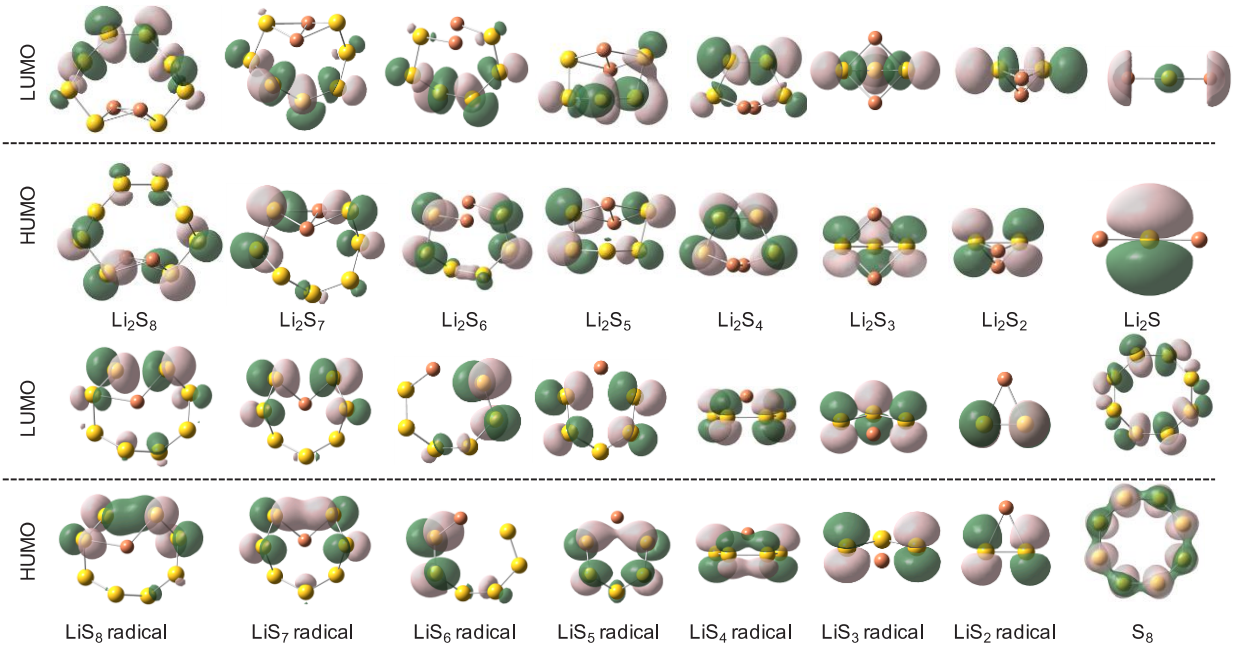


Figure 2-13. HOMO and LUMO visualizations based on model calculations for lithium–polysulfide and sulfur (yellow, S; and red, Li).

As shown in Figure 2-13, in the larger $Li_2S_x$ (x = 4 to 8), the HOMOs are mainly distributed to those S atoms which are close to Li atoms and the LUMOs distribute around the centers of the molecules. Therefore, the HOMO–LUMO transition can be considered as an intramolecular charge transfer from the edges to the center of the molecule. The HOMOs mainly consist of S 3p orbitals. The LUMOs consist of S 4s and/or 4p orbitals. The HOMO–LUMO transition energy decreases with the number of S atoms because the LUMO can be stabilized by S atoms due to their high electronegativity. In contrast, the HOMOs are destabilized by Li atoms as a result of their strong electron-donating abilities. The absorptions of the radical species can be attributed to the transition from β-HOMO to β-LUMO. A very small energy gap between β-HOMO and β-LUMO is responsible for the long absorption wavelength. The LUMO of $S_8$ distributes uniformly to each S atom. This result supports the LC/MS result that $S_8$ is reduced to all possible species produced by the decomposition of $S_8$ including $Li_2S_7$, $Li_2S_5$, $Li_2S_3$ and $Li_2S$, since all bonds of $S_8$ can be

split by delocalized LUMO. The theoretical result that LUMOs are localized around the centers of the $Li_2S_x$ (x = 4 to 8) molecules supports the experimental result which $Li_2S_x$ (x = 4 to 8) are split around the centers of the molecules.

The reason why only $S_3$ radicals notably appear in the reaction path was examined. Considering the low concentration of $S_8^{2-}$, it is assumable that $S_4$ radical is not observed. However, it is surprising that $S_2$ radical which can be produced from $S_4^{2-}$ is not observed at all, despite the analytical results showing that concentration of $S_4^{2-}$ is higher than the concentration of $S_6^{2-}$. There is a calculation result that explains the reason in a recent publication. [34] Although the formation of $S_2$ radical and $S_3$ radical are both slightly energetically favorable from a thermodynamics standpoint, the dissociation of $S_4^{2-}$ need to overcome an energy barrier which is five times as high as the case of $S_6^{2-}$. As the result, $S_2$ radical is not observed like $S_3$ radical.

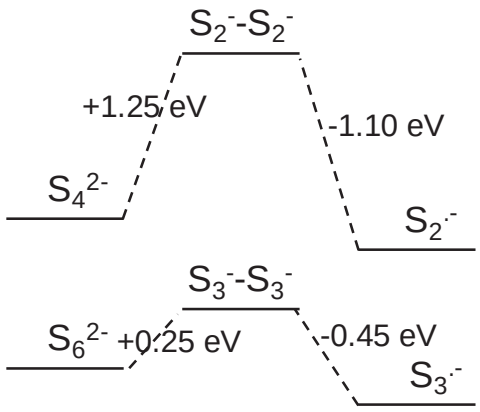


Figure 2-14. Energy barrier of dissociation reaction to produce $S_2$ free radical and $S_3$ free radical from the reference 34.

## 2.3) Summary

The lithium polysulfide species produced in a lithium/sulfur cell were analyzed by LC/MS and NMR combined with an organic conversion technique. All of the results suggest that electrochemical reactions in the cell proceed through four distinct stages. It is

of particular interest that the second plateau in the discharge profile is dominated by the reduction of $Li_2S_3$. The second plateau is the most important reaction state in practical use because of its constant voltage. Meanwhile, the first plateau and the transition state, in which the voltage varies with the capacity, are associated with multiple reactions. It also revealed that longer polysulfides, $Li_2S_x$ (x = 6 to 8), are responsible for the redox shuttle phenomenon. This phenomenon causes serious capacity degradation. This analytical method is also useful in the study of sulfur based redox flow cells and catholyte cells. [35, 36] This work is the first step of understanding the influence of current density and electrolyte components on the reaction scheme, which is connected with cell performances.

## 2.4) Experimental section

### 2.4.1) Experimental detail

Cathodes were composed of 60 wt% sulfur, 30 wt% carbon (Ketjenblack EC-600 JD), 8 wt% polytetrafluoroethylene binder and 2 wt% carboxymethylcellulose thickener. A slurry made from these cathode materials mixed with water was applied to etched Al foil and then dried, after which the cathode sheets were cut into disks (j = 10 mm) and pressed. The finished sulfur cathodes (80 mm thickness, 8 g $cm^2$) were assembled in coin-type cells (CR2032) along with polyethylene separators (S6722, Asahi Kasei), Li foil (150 mm thickness) and electrolyte solutions (60 ml) consisting of 1.5 M lithium bis(trifluoromethanesulfonyl) imide in DME and dioxolane. The discharge–charge profiles were obtained using a current density of 0.8 mA/$cm^2$ and voltages between 1.5 and 2.7 V at 25 °C.

All the subsequent sample preparation procedures were conducted under an Ar atmosphere. During the discharge–charge reaction, the cathodes were removed from the cells at various points within the process. The cathode, still wet with electrolytes, was immersed in l ml of DME and the resulting solution was transferred into a 1 mm path length quartz cell and examined by UV-Vis spectroscopy using a Shimadzu UV-3100PC.

For LC/MS and $^1$H NMR measurements, cathodes taken from cells in the same manner were instead immersed in a mixture of DME and benzyl chloride, after which the cathode was pulverized by ultrasonication. Each sample was then allowed to sit for three hours to convert the lithium polysulfide ($Li_2S_x$) to benzylized polysulfide ($Bz_2S_x$). The conversion of $Li_2S_x$ (x = 3 to 8) is almost complete with in three hours (see Figure 2-14). On the other hand, three-hour conversion is supposed to be insufficient for $Li_2S_x$ (x = 1 to 2) because of those pour solubility. Therefore, the half of each sample was allowed to sit for four days to get the highest conversion rate for $Li_2S$ (see Figure 2-16). The conversion ratio of $Li_2S_x$ (x = 1 to 2) is supposed to be higher than 66%. Though the chain length of $Bz_2S_x$ (x = 6 to 8) can be shortened during the long-time conversion, $Bz_2S_x$ (x = 3 to 8) obtained by three-hour conversion should reflect the relative amounts of $Li_2S_x$ in cathodes (see Figure 2-15). $S_8$ dissolved in the solution remains unreacted during that time. The residual carbon matrix and the current collector were subsequently removed by filtration, after which the solvent was evaporated. Sulfur and $Bz_2S_x$ were dissolved in either tetrahydrofuran (THF) or deuterated chloroform. Sulfur and $Bz_2S_x$ samples that were dissolved in THF were analyzed via LC/MS, and the samples that were dissolved in deuterated chloroform were analyzed using $^1$H NMR. LC/MS experiments were carried out on a Thermo Scientific Exactive mass spectrometer, equipped with an atmospheric pressure chemical ionization (APCI) source, and interfaced to a Dionex Ultimate 3000 LC system with a 254 nm UV detector. Samples were first diluted with methanol and then injected into an Intersil ODS-3 (150 × 2.1 mm, 5 μm) column, using a mobile phase composed of 10% aqueous ammonium acetate (5 mM) and 90% methanol at a constant flow rate of 200 mL/min. MS data were collected in positive ion mode, and $Bz_2S_x$ species were detected as the ammonium adducts. To allow quantitative analysis, LC peak area for $S_8$, $Bz_2S$ and $Bz_2S_2$ was converted to a relative analyte amount using calibration curves derived from standard solutions, and peak area for $Bz_2S_x$ (x = 3 to 8) was converted based on the calculated relative absorbance at 254 nm. NMR data were recorded on a JEOL AL-400 spectrometer.

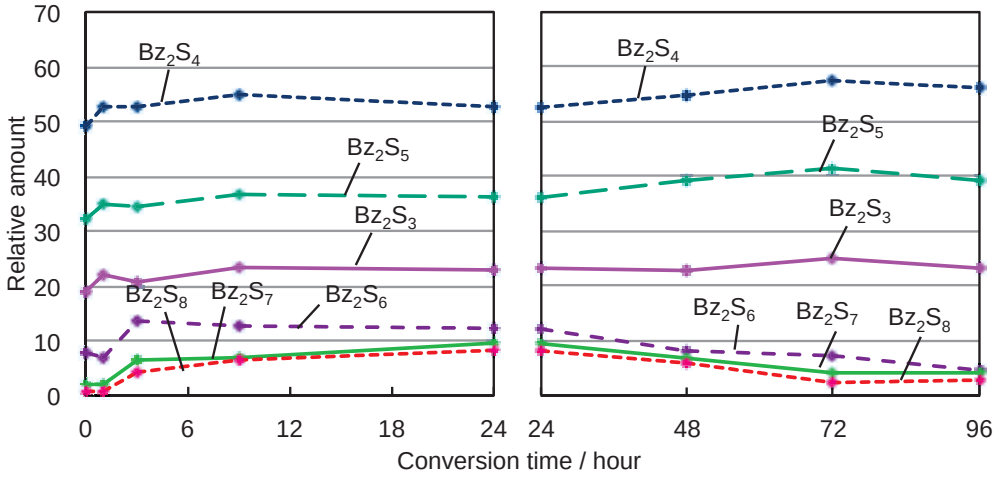


Figure 2-15. Relative amounts of $Bz_2S_x$ from $Li_2S_x$ (x=3 to 8) against conversion time. The benzyl chloride was added at zero hour. $Li_2S_x$ mixture was prepared by reaction of $S_8$ and $Li_2S$ ($S_8$:$Li_2S$ = 7:8 molar ratio) in DME and filtration. Relative amounts were estimated from LC peak area using the calculated relative absorbance at 254 nm. The conversion of $Li_2S_x$ (x=3 to 8) is almost complete within three hours (left). The longer $Li_2S_i$ (i = 6 to 8) are split to shorter $Li_2S_j$ (j = 3 to 5) after 24 hours (one day) (right).

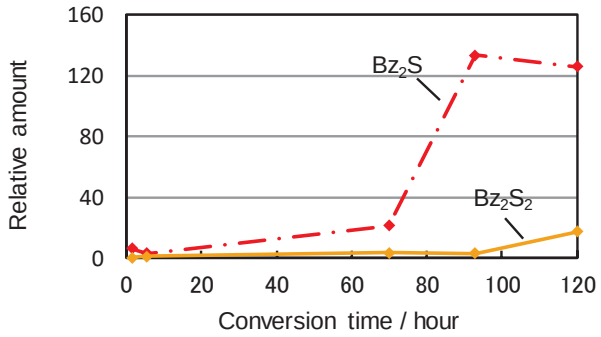


Figure 2-16. Relative amounts of $Bz_2S$ and $Bz_2S_2$ converted from $Li_2S$ against conversion time. The benzyl chloride was added at zero hour and the solvent was DME. Relative amounts were estimated from LC peak area, using calibration curves. The $Bz_2S$ maximum is around 96 hours (four days). After the $Bz_2S$ maximum, $Bz_2S_2$ appears, indicating $Li_2S$ coalesces to $Li_2S_2$.

### 2.4.2) Computational detail

Lithium–polysulfide molecules, which can be generated in the electrochemical reactions within the lithium–sulfur cell, were prepared. The closed-shell species were $S_8$, $Li_2S_8$, $Li_2S_7$, $Li_2S_6$, $Li_2S_5$, $Li_2S_4$, $Li_2S_3$, $Li_2S_2$ and $Li_2S$, while the open-shell radical species were $LiS_8$, $LiS_7$, $LiS_6$, $LiS_5$, $LiS_4$, $LiS_3$ and $LiS_2$. $Bz_2S_x$ models were prepared by replacing the Li atoms in these species with a benzyl group ($C_6H_5CH_2$).

The molecular geometries were first optimized using density function theory (DFT) calculations. The $^1$H NMR chemical shifts for $Bz_2S_x$ were calculated using DFT combined with the gauge-independent atomic orbital (GIAO) technique. [37-41] The shielding constant of tetramethylsilane (TMS) was calculated to be 31.7947 ppm using the same theoretical approach and this was employed as the standard. The calculated chemical shifts for the four methylene H were represented by the average of their individual values. The excited states of polysulfide compounds were calculated using time dependent DFT (TD-DFT) calculations [42] in order to simulate their UV-Vis spectra, and each peak was represented by a Gaussian function with a maximum height proportional to the oscillator strength, using a full width at half maximum (FWHM) value of 0.73 eV. The solvent effect of methanol, DME and DMF on UV-Vis spectra was accounted for by utilizing a polarizable continuum model with the integral equation formalism variant (IEFPCM). The B3LYP exchange–correlation functional [43, 44] was utilized for both DFT and TD-DFT and the 6-311+G(2d,p) [45, 46] basis sets were employed for the calculation of $^1$H NMR chemical shifts, while 6-31+G(d) for all other calculations. [47-49] All calculations were performed using the Gaussian03 program. [50]

## 2.5) References

[1] J. Paris and V. Plichon, *Electrochim. Acta* **1981**, *26*, 1823.

[2] T. Fujinaga, T. Kuwamoto, S. Okazaki and M. Hojo, Bull. *Chem. Soc. Jpn.* **1980**, *53*, 2851.

[3] S. Tobishima, H. Yamamoto and M. Matsuda, *Electrochim. Acta* **1997**, *42*, 1019.

[4] R. J. H. Clark and D. G. Cobbold, *Inorg. Chem*. **1978**, *17*, 3169.

[5] T. Chivers and I. Drummond, *Inorg. Chem*. **1972**, *11*, 2525.

[6] T. Chivers and I. Drummond, *J. Chem. Soc. Dalton Trans.* **1974**, 631.

[7] W. F. Giggenbach, *J. Chem. Soc. Dalton Trans.* **1973**, 729.

[8] F. Seel and H.-J. Guttler, *Angew. Chem., Int. Ed. Engl.* **1973**, *12*, 420.

[9] F. Seel, H.-J. Guttler, G. Simon and A. Wieckowski, *Pure Appl. Chem.,* **1977**, *49*, 45.

[10] J. Badoz-Lambling, R. Bonnaterre, G. Cauquis, M. Delaamar and G. Demange, *Electrochim. Acta,* **1976**, *21*, 119.

[11] M. V. Merritt and D. T. Sawyer, *Inorg. Chem.* **1970**, *9*, 211.

[12] R. P. Martin, W. H. Doub, J. L. Roberts Jr. and D. T. Sawyer, *Inorg. Chem.* **1973**, *12,* 1921

[13] M. Delamar and J.-C. Marchon, *J. Electroanal. Chem.* **1975**, *63*, 351.

[14] M. Delamar, *J. Electroanal. Chem.* **1975**, *63*, 339.

[15] R. D. Rauh, F. S. Shuker, J. M. Marston and S. B. Brummer, *J. Inorg. Nucl. Chem.* **1977**, *39*, 1761.

[16] K. M. Abraham, R. D. Rauh and S. B. Brummer, *Electrochim. Acta* **1978**, *23*, 501.

[17] J. C. Dobson, F. R. McLarnon and E. J. Cairns, *J. Electrochem. Soc.* **1986**, *133*, 1549.

[18] J. C. Dobson, F. R. McLarnon and E. J. Cairns, *J. Electrochem. Soc.* **1986**, *133*, 2069.

[19] P. Lessner, J. Winnick, F. R. McLarnon and E. J. Cairns, *J. Electrochem. Soc.* **1986**, *133*, 2510.

[20] P. Lessner, J. Winnick, F. R. McLarnon and E. J. Cairns, *J. Electrochem. Soc.* **1986**, *133*, 2517.

[21] P. Lessner, J. Winnick, F. R. McLarnon and E. J. Cairns, *J. Electrochem. Soc.* **1987**, *134*, 2669.

[22] P. T. Cunningham, S. A. Johnson and E. J. Cairns, *J. Electrochem. Soc.* **1972**, *119*, 1448.

[23] K. Kumaresan, Y. Mikhaylik and R. E. White, J. Electrochem. Soc., 2008, 155, A576.

[24] N. Yamada, M. Furukawa, M. Nishi and T. Takata, *Chem. Lett.* **2002**, 454

[25] T. Takata, D. Saeki, Y. Makita, N. Yamada and N. Kihara, *Inorg. chem.* **2003**, *42*, 3712.

[26] A. Kamyshny, Jr., J. Gun, D. Rizkov, T. Voitsekovski, O. Lev, *Environ. Sci. Technol.* **2004**, *38*, 6633-6644.

[27] D. Rozkov, O. Lev, J. Gun, B. Anisimov, I. Kuselman, *Environ. Sci. Technol*. **2004**, *38*, 6633-6644.

[28] D. Rizkov, O. Lev, J. Gun, B. Anisimov, I. Kuselman, *Accred Qual Assur* **2004,** *9,* 399–403.

[29] Y. W. Park, Y. Na and D.-J. Baek, *Bull. Korean Chem. Soc.* **2006**, *27*, 2023.

[30] J. A. Tossell, *Geochem. Trans.* **2003**, *4*, 28.

[31] Y. V. Mikhaylik and J. R. Akridge, *J. Electrochem. Soc*. **2004**, *151*, A1969.

[32] D. Aurbach, E. Pollak, R. Elazari, G. Salitra, C. S. Kelley and J. Affinito, *J. Electrochem. Soc.* **2009**, *156*, A694.

[33] Y. Mikhaylik, I. Kovalev, R. Schock, K. Kumaresan, J. Xu and J. Affinito, *ECS Trans.* **2010**, *25*, 23.

[34] M. Vijayakumar, N. Govind, E. Walter, S. D. Burton, A. Shukla, A. Devaraj, J. Xiao, J. Liu, C. Wang, A. Karim and S. Thevuthasan, *Phys. Chem. Chem. Phys*. **2014**, *16*, 10923.

[35] R. Demir-Cakan, M. Morcrette, Gangulibabu, A. Gu´eguen, R. Dedryv`ere and J.-M. Tarascon, *Energy Environ. Sci.* **2013**, *6*, 176.

[36] R. D. Rauh, K. M. Abraham, G. F. Pearson, J. K. Surprenant and S. B. Brummer, *J. Electrochem. Soc.* **1979**, *126*, 523.

[37] F. London, *J. Phys. Radium*, **1937**, *8*, 397.

[38] R. McWeeny, *Phys. Rev.* **1962**, *126*, 1028.

[39] R. Ditchfield, *Mol. Phys.* **1974**, *27*, 789.

[40] K. Wolinski, J. F. Hinton and P. Pulay, *J. Am. Chem. Soc.* **1990**, *112*, 8251.

[41] J. R. Cheeseman, G. W. Trucks, T. A. Keith and M. J. Frisch, *J. Chem. Phys.* **1996**, *104*, 5497.

[42] M. E. Casida, *Recent Advances In Density Functional Methods, Recent Advances In Computational Chemistry, World Scientific, Singapore*, **1995**, 155.

[43] A. D. Becke, *J. Chem. Phys.* **1993**, *98*, 5648.

[44] C. Lee, W. Yang and R. G. Parr, *Phys. Rev. B: Condens. Matter Mater. Phys.* **1988**, *37*, 785.

[45] R. Krishnan, J. S. Binkley, R. Seeger and J. A. Pople, *J. Chem. Phys.* **1980**, *72*, 650.

[46] A. D. McLean and G. S. Chandler, *J. Chem. Phys.* **1980**, *72*, 5639.

[47] W. J. Hehre, R. Ditchfield and J. A. Pople, *J. Chem. Phys.* **1972**, *56*, 2257.

[48] J. D. Dill and J. A. Pople, *J. Chem. Phys.* **1975**, *62*, 2921.

[49] M. M. Francl, W. J. Pietro, W. J. Hehre, J. S. Binkley, M. S. Gordon, D. J. DeFrees and J. A. Pople, *J. Chem. Phys.* **1982**, *77*, 3654.

[50] M. J. Frisch, et al., *Gaussian 03, Revision E.01, Gaussian Inc., Wallingford, CT,* **2004**.

# CHAPTER 3

# Detailed study of sulfur deposition for lithium/sulfur cells

## 3.1) Introduction

### 3.1.1) Sulfur active materials

Fabrication of the sulfur active materials is one of the main subjects in research of lithium/sulfur cells. In order to address the primary issue of sulfur cells, which is insulating property of sulfur, a wide variety of materials comprised of sulfur and various conductive materials have been proposed. Carbon materials having various structures, such as carbon spheres, carbon fibers, carbon sheets, have been introduced into the composites. [1-8] This strategy has also worked to limit polysulfide dissolution by immobilizing sulfur species with some interactions or embedding sulfur species into porous structures. Although a number of methodologies have been researched, one major method to make such sulfur-carbon composites is to infiltrate molten sulfur into cavities of the conductive material by heating the mixture above 155 °C. [1] Another significant technique is chemical deposition of sulfur on conductive materials. [2-8] Since the chemical deposition of sulfur mostly takes place in the solution phase, the conductive matrix should be dispersed in the solution in advance. An aqueous system is preferable from an environmental point of view for a scaled-up system.

Graphene oxide (GO) is one of the effective carbon materials as a component of sulfur cathode. [9-16]. GO is the results from the chemical exfoliation of graphite and can be regarded as a large, disordered, but two-dimensional polymerfunctionalized with a range of oxygen-containing groups. While it has high surface area, it can be easily dispersed in aqueous solution thanks to the oxygen-containing groups on the surface. Then sulfur can deposit on the surface in the aqueous solution creating fine structure of composite.

### 3.1.2) SGO composite

Research about sulfur deposited onto GO have been conducted. [10-16] It is called SGO (sulfur-graphene oxide) composite in this chapter. The cell performance using SGO

composite has demonstrated a high initial discharge capacity of 1440 mA·h/g (sulfur) at 0.2C (1C=1675 mAh/g), and excellent rate capability up to 6C for discharge and 3C for charge, while it still maintaining high specific capacity (e.g., 800mA·h/g (sulfur) at 6C). [10] The cells demonstrated cycling performance up to 1500 cycles with a low capacity decay rate of 0.039% per cycle. [10] This is one of the best performance reported so far for lithium/sulfur cells. Li/SGO cell meets most of the requirements for the development of clean engine vehicles with zero emission.

The synthesis of the material consists of chemical deposition of sulfur onto GO by acidification of a polysulfide solution and subsequent heat treatment. A detailed investigation of the sulfur deposition process has not been conducted. Not only for improvement of the cell performance of the sulfur/GO materials, but also for reproducibility of the high performance, a deep understanding of the deposition process of sulfur is indispensable. Controlling the process of sulfur deposition is necessary for designing the scale-up of active material preparation and optimization of cell performance and lifetime.

In this chapter, the sulfur deposition process is investigated including the mixing process of polysulfide and GO and the acidification process. The influence of each step and the conditions on the composite morphology and the cell performance have been clarified by using elemental analysis (EA), i.e. CHNS analysis, scanning electron microscopy (SEM), and electrochemical characterization.

## 3.2) Results and Discussion

### 3.2.1) Sulfur deposition reactions

Chemical deposition of elemental sulfur, $S_8$, takes place from a $S_x^{2-}$ precursor under acid conditions. The reaction occurs because the equilibrium of polysulfide and sulfur shifts toward sulfur when the pH decreases. The equilibrium between sulfur and polysulfide under acid conditions is written as:

$$S_iS^{2-} + H^+ \Leftrightarrow iS_{(s)} + HS^- \quad (1)$$

The equilibrium in alkaline condition can be written as Equation (2) as well [17].

$$S_iS^{2-} + H_2O \Leftrightarrow iS_{(s)} + HS^- + OH^- \quad (2)$$

### 3.2.2) Synthesis Process

In the preparation of the SGO composites, acidification with formic acid was introduced in order to obtain elemental sulfur deposited on GO. The preparation of the SGO composites is shown graphically in Figure 3-1. The first step is the mixing process of the $Na_2S_x$ solution and the suspension of GO. After mixing the $Na_2S_x$ solution and the GO suspension, the mixture is added dropwise into the formic acid solution.

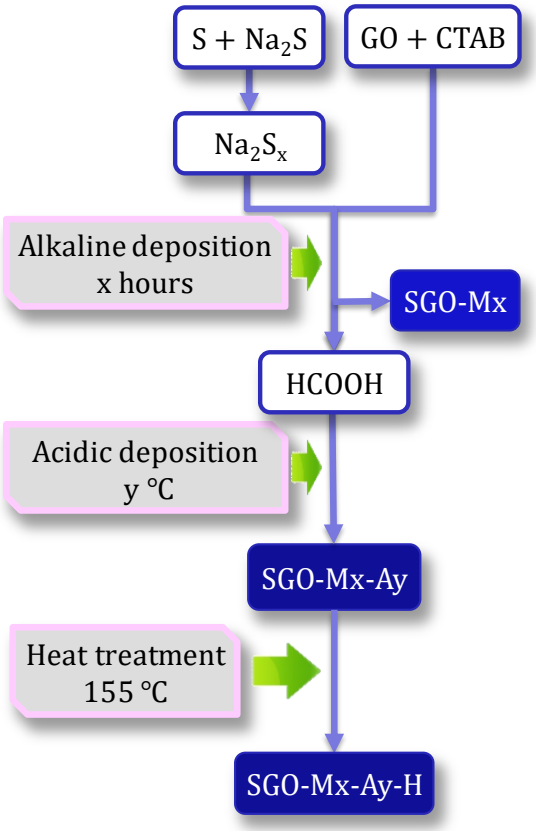


Figure 3-1. Diagram of the preparation of the sulfur/GO composite.

During the acidification process, polysulfide is supposed to deposit on GO as elemental sulfur. In the earlier understanding, it had been assumed that the mixing process of $Na_2S_x$ and GO was just mixing of $Na_2S_x$ and GO to make a homogeneous mixture. It was found, however, that some chemical reactions were taking place during the mixing process.

### 3.2.3) Alkaline deposition process

Powder samples were taken from the suspension at different times of mixing $Na_2S_x$ and GO. The powders prepared by mixing $Na_2S_x$ and GO for 1 hour, 3 hours, 6 hours, 16 hours, 28 hours and 52 hours are labeled as SGO-M1, SGO-M3, SGO-M6, SGO-M16, SGO-M28 and SGO-M52 respectively. All the samples used in this chapter are listed in Table 3-1.

Table 3-1. List of samples prepared in different synthesis condition.

| | Alkaline deposition time | Acidic deposition temperature | Heat Treatment |
|---|---|---|---|
| SGO-M1 | 1 hour | None | None |
| SGO-M3 | 3 hours | None | None |
| SGO-M6 | 6 hours | None | None |
| SGO-M16 | 16 hours | None | None |
| SGO-M28 | 28 hours | None | None |
| SGO-M52 | 52 hours | None | None |
| SGO-M1-A15 | 1 hour | 15 °C | None |
| SGO-M3-A15 | 3 hours | 15 °C | None |
| SGO-M6-A15 | 6 hours | 15 °C | None |
| SGO-M16-A5 | 16 hours | 5 °C | None |
| SGO-M16-A15 | 16 hours | 15 °C | None |
| SGO-M16-A20 | 16 hours | 20 °C | None |
| SGO-M16-A25 | 16 hours | 25 °C | None |
| SGO-M28-A15 | 28 hours | 15 °C | None |
| SGO-M1-A15-H | 1 hour | 15 °C | 155 °C 18 hours |
| SGO-M3-A15-H | 3 hours | 15 °C | 155 °C 18 hours |
| SGO-M6-A15-H | 6 hours | 15 °C | 155 °C 18 hours |
| SGO-M16-A5-H | 16 hours | 5 °C | 155 °C 18 hours |
| SGO-M16-A15-H | 16 hours | 15 °C | 155 °C 18 hours |
| SGO-M16-A20-H | 16 hours | 20 °C | 155 °C 18 hours |
| SGO-M16-A25-H | 16 hours | 25 °C | 155 °C 18 hours |
| SGO-M28-A15-H | 28 hours | 15 °C | 155 °C 18 hours |

| | | | |
|---|---|---|---|
| SGO-M52-H | 52 hours | None | 155 °C 18 hours |
| SGO-A | 0 | 20 °C | None |
| SGO-A-G | 0 | 5 °C | None |
| SGO-A-G-H | 0 | 5 °C | 155 °C 18 hours |

Each sample was analyzed to check the contents of sulfur, carbon, hydrogen and nitrogen by CHNS elemental analysis as shown in Figure 3-2. The content of oxygen was estimated by the difference of 100% and the sum total of the contents of sulfur, carbon, hydrogen and nitrogen based on the assumption that there was no other element than sulfur, carbon, hydrogen, nitrogen and oxygen comprising the composition of the starting materials. The sodium in $Na_2S$ should have been washed out when the powder samples were washed by water.

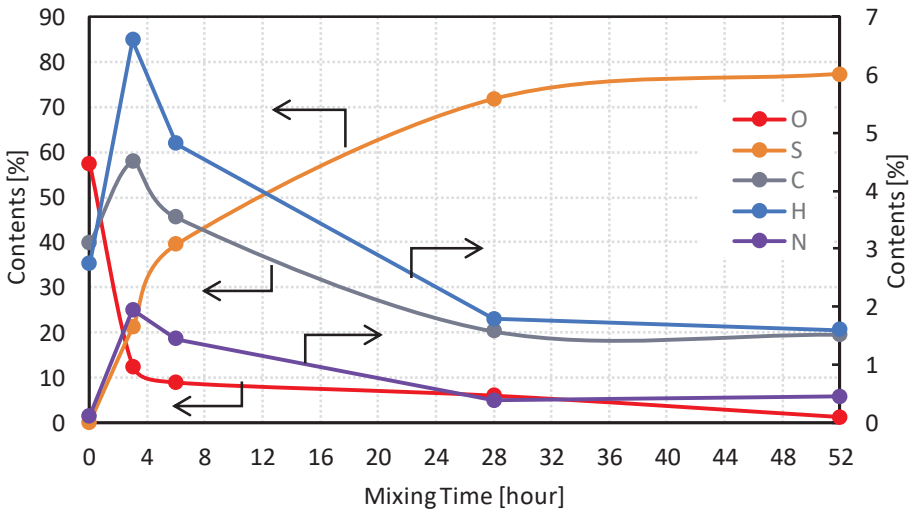


Figure 3-2. Contents of sulfur, carbon, hydrogen and nitrogen in SGO-Mx samples analyzed by CHNS elemental analysis.

The content of sulfur significantly increased with time until 28 hours and was gradually saturated until 52 hours. The content of sulfur was 77% at the point of 52 hours from starting. This means that sulfur could deposit without any additional acid. The oxygen content was 57% in the original GO. These oxygen sources were from adsorbed water and

oxygen containing surface functional groups [19]. The TGA result for GO also indicated corresponding weight loss of water and the oxygen-based functional groups as shown in Figure S1 [18]. These oxygen-based functional groups are known to generate protons by deoxygenation [19]. This is the reason why the GO suspension is acidic. As the content of oxygen is tracked in Figure 2, it dropped down from 57% to 12% just after beginning. Then the content gradually decreased from 5.8% at 28 hours to 1.1% at 52 hours. This means, after 52 hours, GO was almost completely reduced to graphene with some defects.

The pH was monitored during the mixing process. Figure 3-3 shows the pH change of the solution of $Na_2S_x$ and GO along with the contents of sulfur and oxygen. The initial pH of the polysulfide solution was 11.0. The pH of the original GO suspension was from 2.7 to 3.1. The pH reached 11 just after adding the polysulfide solution to the GO suspension, and then decreased to around 9.7 taking about 6 hours. Then the pH gradually decreased to around 9.0 over a period of about 40 hours. The pH started to drop drastically at the point of 48 hours after starting, and reached 7.0 at 52 hours after starting.

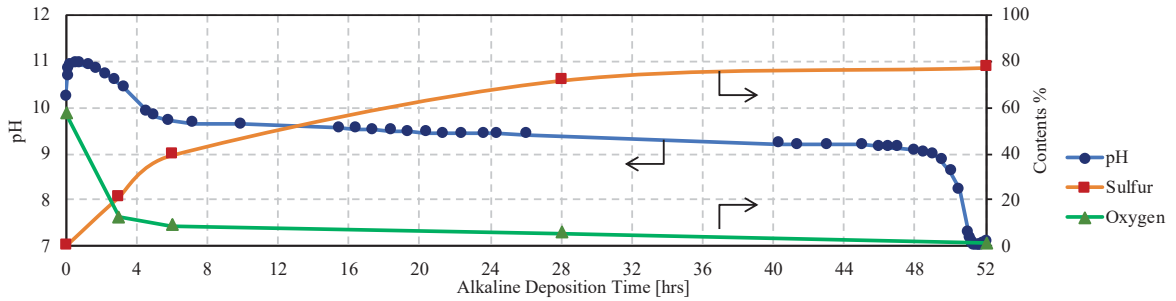


Figure 3-3. The contents of sulfur and oxygen in SGO-Mx (x is variable for the alkaline deposition time) samples and the pH change of the $Na_2S_x$-GO-CTAB mixture solution.

The color of the original polysulfide solution is dark orange. During the process, the color gradually became pale. Then it turned to colorless when the pH started to drop down to 7.0 at 48 hours.

All these results indicate that polysulfides are gradually converted to elemental sulfur

during the mixing time. All of the polysulfide in the solution is consumed at 52 hours after starting. It can be assumed that polysulfides are oxidized to sulfur by protons produced from deoxygenation of GO regarding the change of the oxygen content. This phenomenon demonstrates sulfur deposition in alkaline condition as represented in Equation (2). This phenomenon is named as alkaline deposition in contrast to the deposition under acidic conditions.

Figure 3-3 suggests that the deoxygenation rate of GO become slower after 6 hours. This result suggests that there are mainly two types of deoxygenation reactions on GO. One of them is fast and the other type is much slower. This is also supported by the literature presenting different deoxygenation reactions in strong alkaline condition and mild alkaline condition [19]. The model reactions in the literature are shown in Figure 3-4.

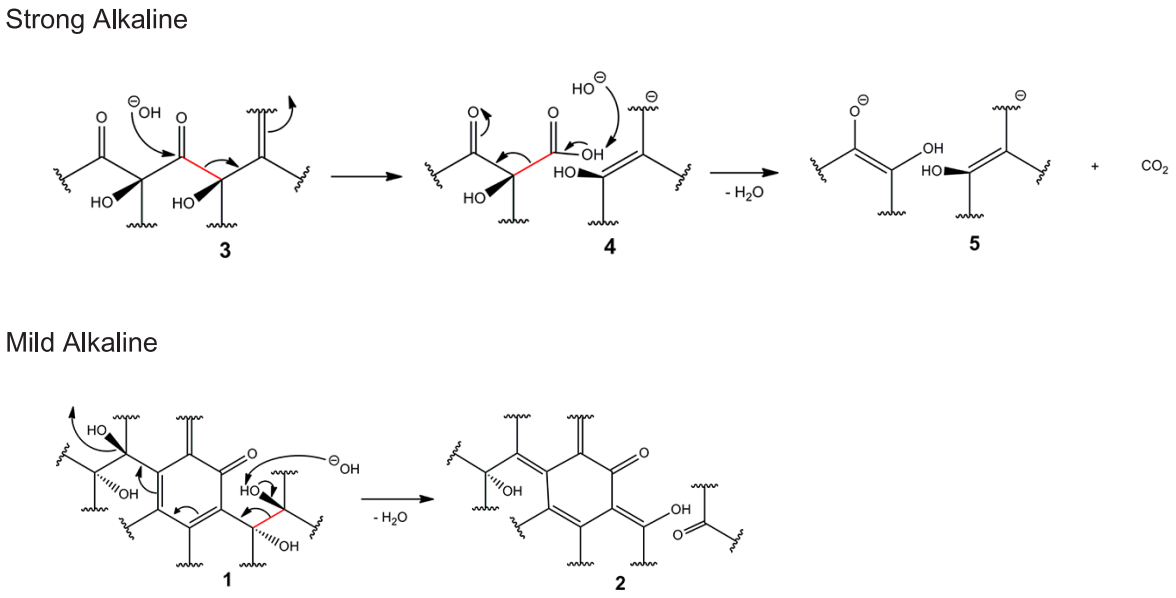


Figure 3-4 Two different deoxygenation reactions of the functional groups in GO under strong alkaline conditions and mild alkaline conditions from the literature 18.

It can be presumed that the conductivity of the SGO material increases as the reduction of GO proceeds with time.

From these experiments, it was found that alkaline deposition of sulfur occurred during the first step of the synthesis process, and a composite of sulfur and reduced GO was produced. The sulfur contents of those composites were different depending on the elapsed time of the mixing process.

### 3.2.4) Acidic deposition process

Acidification using formic acid was conducted after the alkaline deposition during the mixing process. The pH during the process was about constantly 2.4. The solution of polysulfide and GO was added dropwise to the formic acid solution. the remaining polysulfide in the solution is supposed to be acidified to produce elemental sulfur according to Equation (1) in this process. It is named acidic deposition in contrast to the alkaline deposition described above. The sulfur contents of all the samples after the acidic deposition were 84% from the results of elemental analysis. The color of the solution turned to milky blue gray immediately when the polysulfide mixture was added to the formic acid solution. Photos of the color change of the solution during the acidification are shown in Figure 3-5. The origin of the milky color is a colloid of liquid sulfur particles created by polysulfide which has not been converted to solid sulfur yet at this time [21]. Then the milky blue gray color gradually changed to more like milky black, and finally the milky solution became clear. The time from starting to the time at which the solution becomes clear is defined as the acidic deposition time.

Figure 3-5. Photos of color change of the solutions during the acidic deposition of SGO composite.

The acidic deposition times for samples prepared with different alkaline deposition times are presented in Figure 3-6 (a). The remaining amount of polysulfide was different depending on the alkaline deposition time, as expected from the result for the alkaline deposition. The acidic deposition time after shorter alkaline deposition time was longer since more polysulfide remained after the shorter alkaline deposition times. The acidic deposition time after 1 hour of alkaline deposition is about 5 hours. It is obvious that the acidic deposition is significantly faster than the alkaline deposition comparing with the total time required for alkaline deposition to be completed, which was 52 hours.

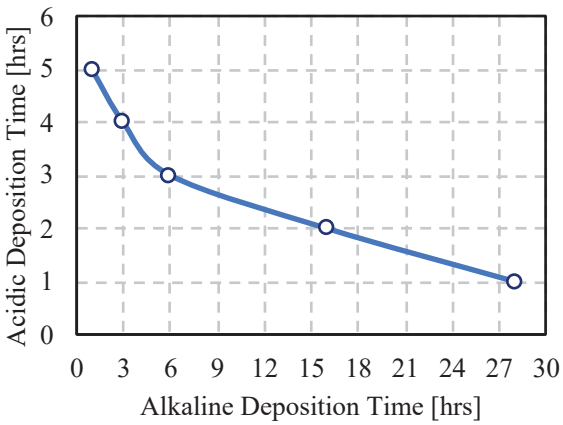


Figure 3-6. Acidic deposition times for different alkaline deposition times.

Upon a further investigation, it was found that the acidic deposition time was influenced significantly by other factors, too. Figure. 3-7 shows that the acidic deposition time increased linearly as more CTAB was added. When no CTAB was added, the deposition quickly went to completion since sulfur particles rapidly deposited onto the graphene oxide surface. This phenomenon is anticipated because liquid sulfur particles are expected to be more stabilized with increased CTAB concentration. Thus, it took a longer time to destabilize and deposit onto the graphene surface [20].

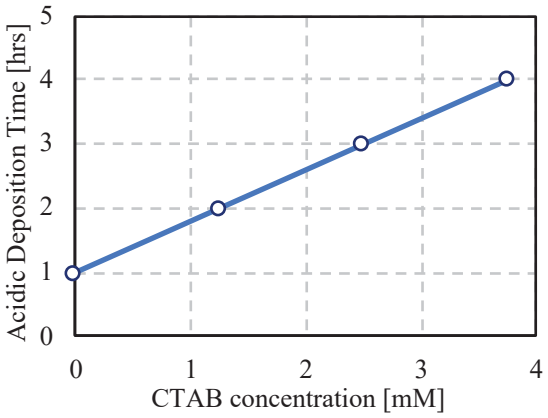


Figure 3-7. Acidic deposition times for different CTAB concentrations in the mixture solutions.

Furthermore, the temperature dependency of the acidic deposition time was investigated. The results are shown in Figure 3-8. The acidic deposition time is influenced strongly by temperature.

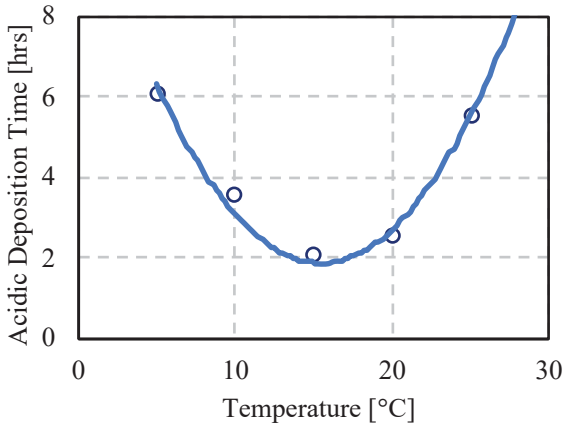


Figure 3-8. Temperature dependency of the acidic deposition time.

Considering that the solubility of CTAB is significantly influenced by temperature especially in the range from 10 °C to 50 °C [21], it is speculated that higher temperature increases CTAB solubility and thus better stabilize the liquid sulfur particles as a colloid. The speculation was correct only above 15 °C. The acidic deposition time at 15 °C was the shortest. The acidic deposition time increased at higher temperatures than 15 °C. The acidic deposition at 50 °C did not go to completion even after overnight. The existence of the minimum indicates that there are additional factors associated with temperature that affect the deposition of sulfur other than CTAB solubility. One of the possibilities is that an increase in temperature can increase the deposition reaction rate that counter balances the decreased deposition rate by CTAB-stabilized sulfur. This is reasonable with regard to the endothermic reaction of sulfur deposition reaction.

### 3.2.5) SEM for the samples prepared by alkaline deposition

The morphologies of the samples prepared using different alkaline deposition times

and associated different acidic deposition were studied. Also, the effect of different acidic deposition conditions on the morphologies was investigated. The SEM images of SGO-M6, SGO-M16 and SGO-M28, which are the samples obtained only by alkaline deposition, are shown in Fig. 3-9 (a), (c) and (e) respectively.

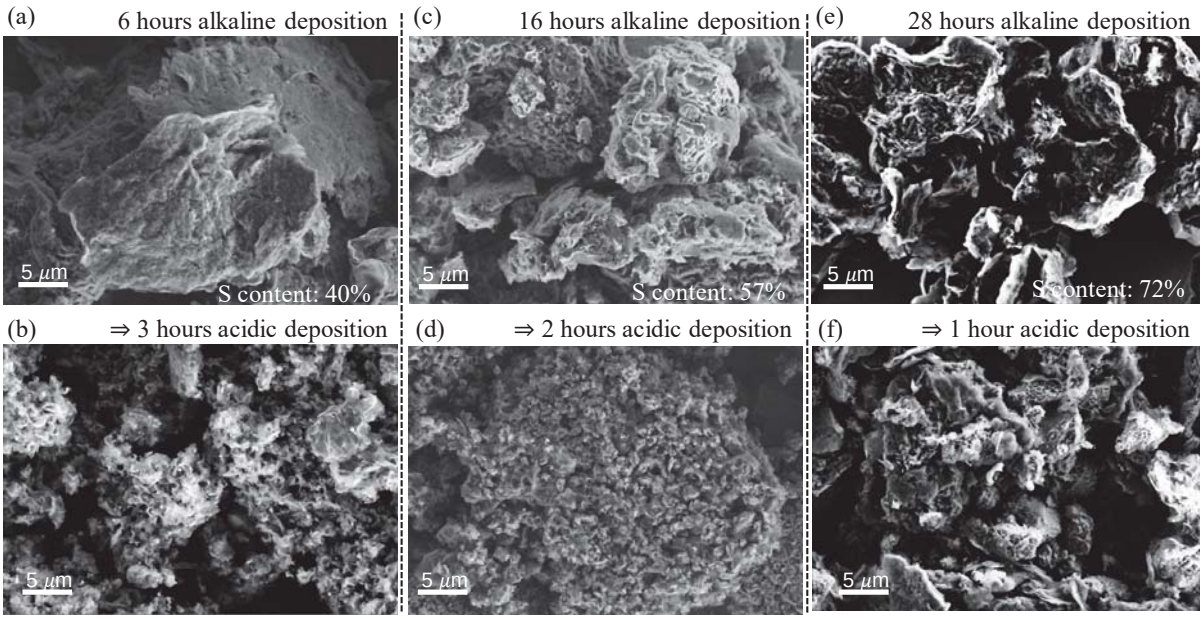


Figure 3-9. SEM images of SGO-M6 (a), SGO-M16 (c) and SGO-M28 (e), which were the samples obtained only by alkaline deposition, and SGO-M6-A15 (b), SGO-M16-A15 (d) and SGO-M28-A15 (f), which were obtained after subsequent acidic deposition for SGO-M6, SGO-M16 and SGO-M28 respectively.

The flake size of the original GO is 32.9 $\mu$m at D90, 16.6 $\mu$m at D50 and 6.63 $\mu$m at D10 from the information provided by the manufacturer of the GO. Regarding this information, the flake size of about 20 $\mu$m which can be observed in the middle of the image of SGO-M6 in Figure 3-9 (a) is one GO flake. Sulfur covers the surface of the GO flake judging from the EDX mapping for the magnified image of SGO-M6 as shown in Figure 3-10. SGO-M6 has about 40% sulfur content from the elemental analysis shown in Figure 3-2 and 3-3. Thus, the morphology of SGO-M6 keeps the shape of the GO flakes as sulfur

covers the surface of GO. The sulfur seemed not to be crystalized as independent particles in this sample.

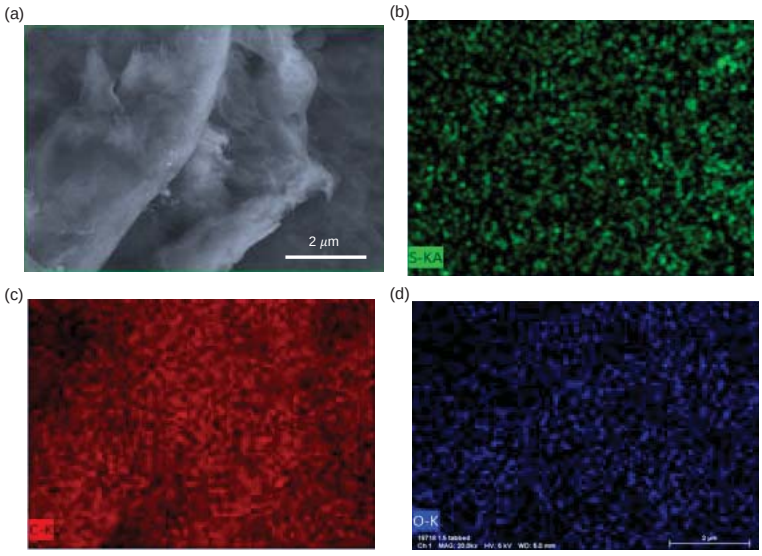


Figure 3-10. SEM image of SGO-M6 (a) and the corresponding EDX mapping for sulfur (b), carbon (c) and oxygen (d).

In Figure 3-9 (c) for the image of SGO-M16 having about 55% sulfur content, the reduced GO flakes are more wrinkled. In the image, a morphology like that of a honey comb can be seen among the GO flakes. These are the sulfur particles of which the surface was damaged by the electron beam of the SEM. The actual sulfur particles has a rough surface. It immediately started to become like a honey comb after focusing the SEM. Some damage could not be avoided to get clear images even though the parameters for the SEM measurement were adjusted. Considering this fact, in SGO-M16 in Figure 3-9 (c), sulfur crystalizing as bulk particles is observed in between the wrinkled reduced GO flakes. As for SGO-M28, the sulfur particles in between reduced GO flakes became much bigger and the reduced GO became less flaky as seen in Figure 3-9 (e). The images for SGO-M1 and SGO-M3 in Figure 3-11 (a) and (c) show similar morphology to that of SGO-M6. The image of SGO-M52 in Figure 3-11 (e) shows larger sulfur particles than SGO-M28 as expected.

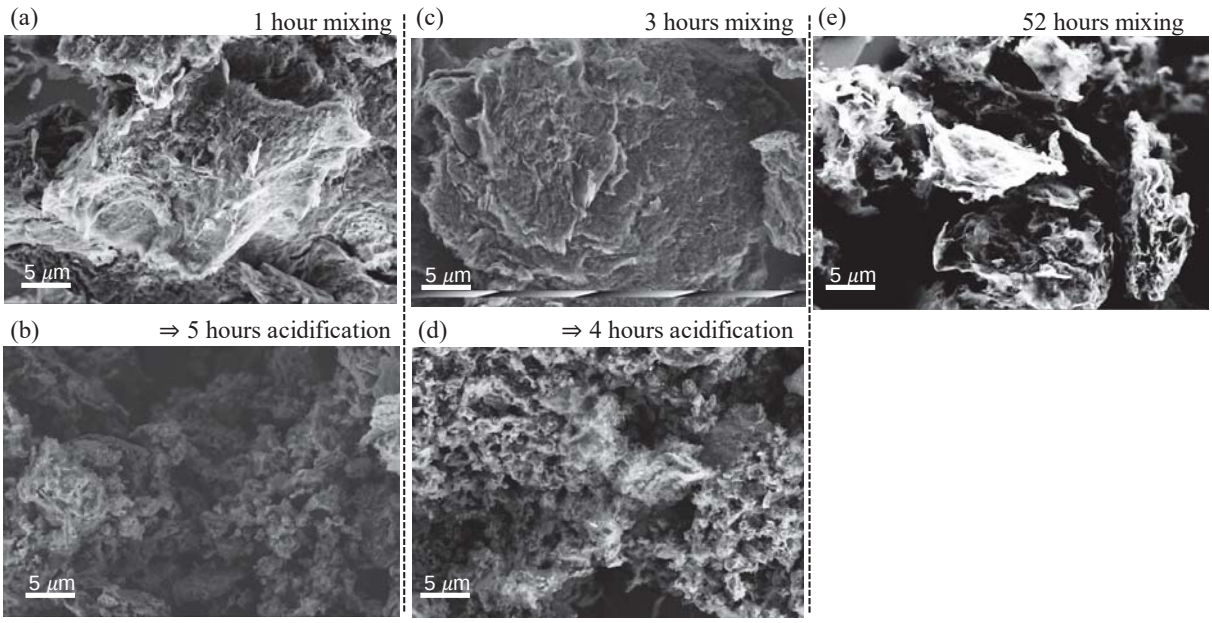


Figure 3-11. SEM images of SGO-M1 (a), SGO-M3 (c) and SGO-M52 (e), which were the samples obtained only by alkaline deposition, and the SGO-M1-A15 (b) and SGO-1M3-A15 (d), which were obtained after subsequent acidic deposition of SGO-M1, SGO-M3 respectively.

These SEM observations indicate that the following process occurred during the alkaline deposition. At the beginning, sulfur starts to deposit on the surface of GO flakes. As the sulfur content increases, sulfur starts to crystalize to produce independent sulfur particles making the GO flakes wrinkle. Then the independent sulfur particles grow to be bigger chunks during the extended time.

### 3.2.6) SEM for the samples prepared by both alkaline and acidic deposition

SGO-Mx-Ay (x: alkaline deposition time, y: acidic deposition temperature) samples were synthesized by acidic deposition following alkaline deposition for different times. The SEM images of SGO-M6-A15, SGO-M16-A15 and SGO-M28-A15 are shown in Figure 3-9 (b), (d) and (f). These correspond to SGO-M6 in Figure 3-9 (a), SGO-M16 in Figure 3-9 (c) and SGO-M28 in Figure 3-9 (e) respectively. The image of SGO-M1-A15

and SGO-M3-A15 are shown in Figure 3-11 as well. In the images of SGO-M1-A15, SGO-M3-A15 and SGO-M6-A15, very fine structures in the size range of 0.5 $\mu$m to 1.0 $\mu$m with wrinkled flaky shapes of GO without independent agglomeration of sulfur were observed. Judging from the EDX mapping results, these structures were confirmed to be composites of sulfur and GO. It is surprising that these morphologies are significantly different from the morphology before acidification, which means only with alkaline deposition such as SGO-M1, SGO-M3 and SGO-M6. Considering the fact that much of the polysulfide still remained in the mixture solution of polysulfide and GO before 6 hours mixing, those remaining polysulfides deposited as sulfur to create the fine structure in the acidification.

The reason for the structure difference between the samples resulting from alkaline deposition and from acidic deposition is assumed to be the reaction rate for sulfur deposition. The deposition rate in the alkaline deposition is much slower than that in the acidic deposition. Sulfur tends to deposit onto pre-existing crystals creating independent particles rather than distributed over the surface of the GO if the reaction rate is slow. Although sulfur deposits on the surface of GO at the beginning, once sulfur starts to crystalize by itself, the sulfur crystals grow as more sulfur deposits. On the other hand, when the deposition rate is fast under the acidic condition, the collision frequency can be more dominant than stabilization. As a result, sulfur deposits on the surface of GO homogeneously rather than agglomerating. When the alkaline deposition time is longer, more polysulfide is already crystalized as sulfur particles of around 10 $\mu$m, and a smaller amount of polysulfides remain in the solution before acidification. Although similar fine structures like SGO-M6-A15 are observed in the morphology of SGO-M16-A15 in Figure 3-9 (d), it seems to have secondary particles of around 10 $\mu$m. It is supposed that the remaining polysulfides deposit as fine composites with GO in a fast reaction during the acidic deposition and surrounded the pre-existing bigger sulfur particles. From this mechanism, it is understandable that big sulfur particles in SGO-M28-A15 are not surrounded by fine structures of GO as shown in Figure 3-9 (f) due to a smaller amount of

remaining polysulfide. From these observations, it can be concluded that the remaining polysulfides after alkaline deposition create fine composites with GO flakes and surround the pre-existing sulfur particles during acidic deposition.

### 3.2.7) SEM for the samples prepared by different acidic deposition temperature

Also, it was found that acidic deposition conditions affected the morphologies of the samples. SEM images of SGO-M16-Ay (y: acidic deposition temperature) synthesized by acidification at 5 °C, 15 °C and 25 °C are shown in Figure 3-12 (a), (c) and (e) respectively.

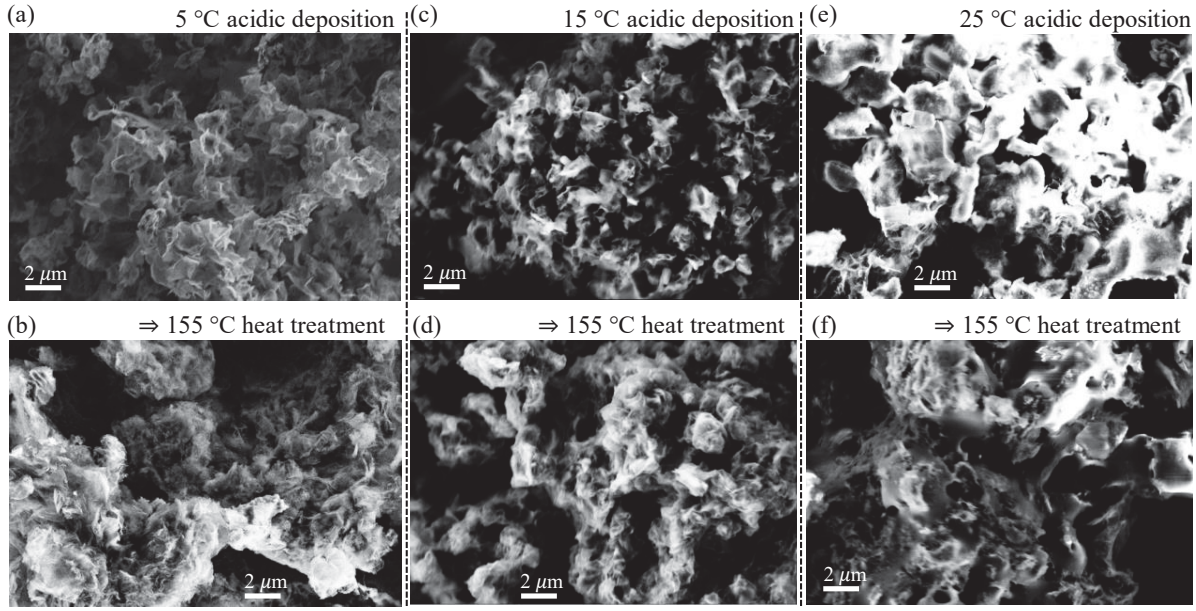


Figure 3-12. SEM images of SGO-M16-A5 (a), SGO-M16-A15 (c) and SGO-M16-A25 (e), which were the samples before the heat treatment, and SGO-M16-A5-H (b), SGO-M16-A15-H (d) and SGO-M16-A25-H (f), which were obtained after subsequent heat treatment of SGO-M16-A5, SGO-M16-A15 and SGO-M16-A25 respectively.

When the temperature during acidic deposition is 5 °C, the surfaces of the particles are covered by a very fine flaky structure as shown in Figure 3-12 (a). On the other hand, as the temperature increases, the surface becomes more solid and insulating judging from the

charging effects in SEM as shown in Figure 3-12 (c). These indicate that GO is more on the surface of the composite for the low temperature acidic deposition, and sulfur is more on the surface of the composite when the temperature is high during the process. Considering the influence of temperature on the acidic deposition time as seen in Figure 3-8, the deposition rate of sulfur is low as the acidic deposition temperature is low. From these results, it is assumed that the morphologies are affected by the reaction rate of sulfur deposition, which means that sulfur deposits more on the surface of the composite when the deposition rate is high at high temperature, and sulfur deposits inside the GO flaky structure when the deposition rate is low at low temperature. This phenomenon is understandable from the fact that SGO-M16-Ay has bulk sulfur cores inside the flaky structures observing the morphology before the acidic deposition as seen in Figure 3-9 (c). Then during the acidic deposition, polysulfides prefer to deposit as sulfur on the inner bulk sulfur surface rather than GO flakes at low temperature. As a result, sulfur deposition occurs inside the flaky structure at low temperatures. On the other hand, sulfur deposits on the surfaces which are easily reachable when the reaction rate is high at high temperature.

The summary of the relationship between the conditions of the process and the resulting morphology are shown in Figure 3-13 from these discussions. As the alkaline deposition time is longer, more bulk sulfur particles are created by the slow sulfur deposition rate. The sulfur deposits on GO to create a fine structure when sulfur is deposited by acidic deposition. However, even in acidic deposition, if the temperature is low and some sulfur bulk particles pre-exist because of the alkaline deposition process, sulfur deposits on the pre-existing sulfur particles rather than the GO surface.

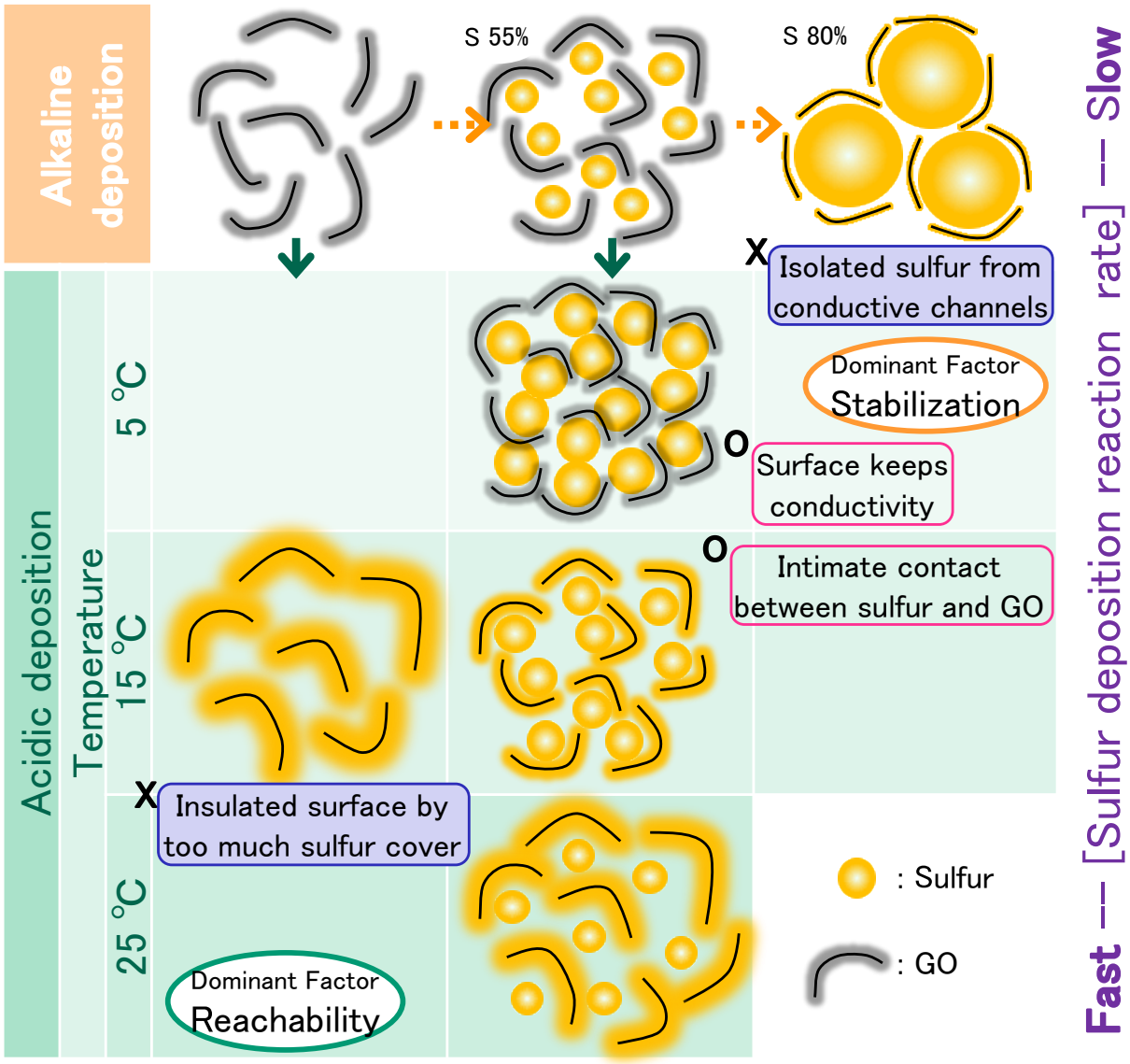


Figure 3-13. Summary of the relationship between the processing conditions and the resulting morphology.

### 3.2.8) SEM for the samples after the heat treatment

Heat treatment at 155 °C followed the acidic deposition. As checked by elemental analysis, the sulfur contents of all the samples after the heat-treatment were the same as before the heat-treatment, and was 84%. SEM images of the samples after the heat treatment, SGO-M16-A5-H, SGO-M16-A15-H and SGO-M16-A25-H, are shown in

Figure 3-12 (b), (d) and (f). These correspond to the samples before the heat treatment shown in Figure 3-12 (a), (c) and (e) respectively. Commonly it is expected that sulfur melts during the heat treatment and redistributes itself in the composite. The main features of the morphologies of the samples were, however, maintained even after the heat treatment at 155 °C for 18 hours. This means that the morphologies of the composites are largely determined by the alkaline deposition process and the acidic deposition process before the heat treatment.

### 3.2.9) Cell performance for the samples prepared by different alkaline deposition time

The electrochemical performance of the samples prepared using different conditions was obtained. The voltage profiles in the second cycle of SGO-M1-A15-H, SGO-M3-A15-H, SGO-M6-A15-H, SGO-M16-A15-H, SGO-M28-A15-H and SGO-M52-H, which are obtained using different alkaline deposition times, are shown in Figure 3-14. Only sample SGO-M52-H was without acidic deposition because all the polysulfide was converted to sulfur during the 52 hours alkaline deposition. All the other samples were acidified by taking different times for all the polysulfide to be converted to sulfur after the different alkaline deposition times. All the samples were heat-treated at 155 °C.

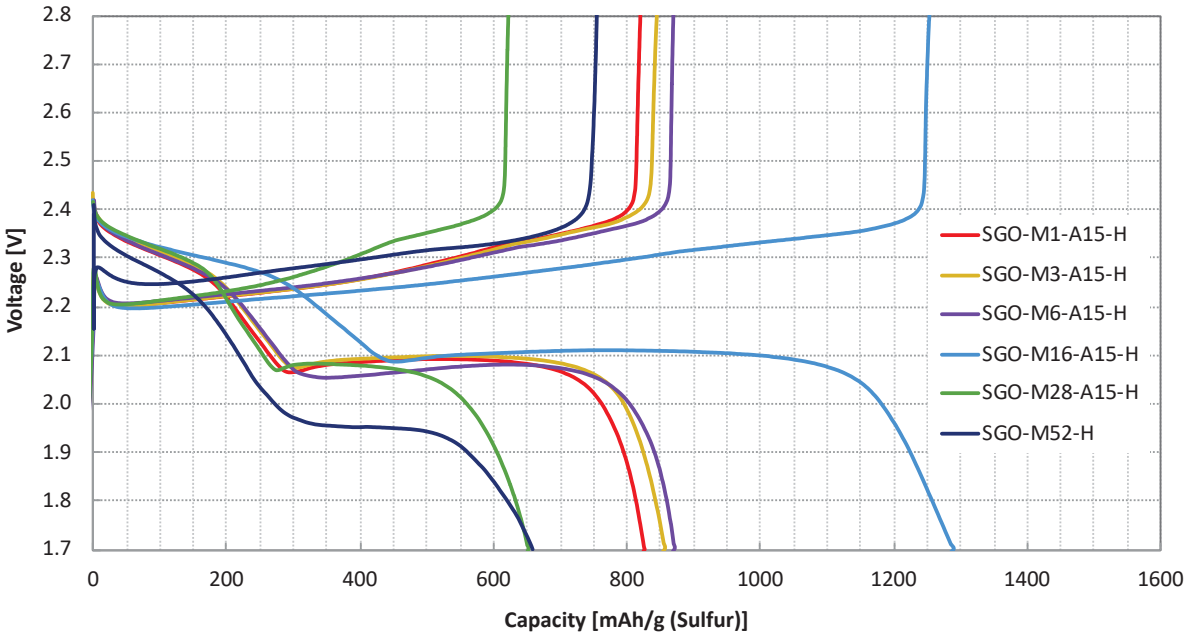


Figure 3-14. The voltage profiles in the second cycle of SGO-M1-A15-H, SGO-M3-A15-H, SGO-M6-A15-H, SGO-M16-A15-H, SGO-M28-A15-H and SGO-M52-H, which were obtained using different alkaline deposition times.

SGO-M1-A15-H, SGO-M3-A15-H and SGO-M6-A15-H show similar voltage profile and capacity. This is reasonable judging from the similar morphologies in these samples as shown in Figure 3-9 (b) and Figure 3-11 (b) and (d). These were prepared by using short alkaline deposition resulting more than 60% of sulfur deposited by acidic deposition. Meanwhile, SGO-M16-A15-H demonstrated the highest capacity among the samples. 57% of the sulfur deposited by the alkaline deposition and the rest of the sulfur deposited by the acidic deposition in this material. SGO-M28-A15-H and SGO-M52-H showed lower capacities than SGO-M16-A15-H. About 70% of sulfur deposited by the alkaline deposition in the case of SGO-M28-A15-H. 100% of the sulfur was accumulated by the alkaline deposition in the case of SGO-M52-H. As shown in Figure 3-9 (e) for SGO-M28 and Figure 3-11 (e) for SGO-M52, these materials have big agglomerations of sulfur because of the slow crystallization in the alkaline deposition.

From these results, it can be concluded that a specific combination of alkaline deposition and acidic deposition leads to high performance as the cathode active material in the cell. If too much sulfur deposits by acidic deposition, insulating sulfur covers the surface of GO as thick layers resulting in less conductivity of the materials as seen in SGO-M1-A15-H, SGO-M3-A15-H and SGO-M6-A15-H. Also, less reduced GO results in less conductivity. On the other hand, if too much sulfur is produced by alkaline deposition like SGO-M28-A15-H and SGO-M52-H, sulfur agglomerates in the slow reactions so that these big chunks of sulfur prevent the electron transfer to the inner sulfur in the particles.

### 3.2.10) Cell performance for the samples prepared by different acidic deposition temperature

Voltage profiles of SGO-M16-A5-H, SGO-M16-A10-H, SGO-M16-A15-H, SGO-M16-A20-H and SGO-M16-A25-H, prepared using different acidic deposition temperatures, are compared in Figure 3-15.

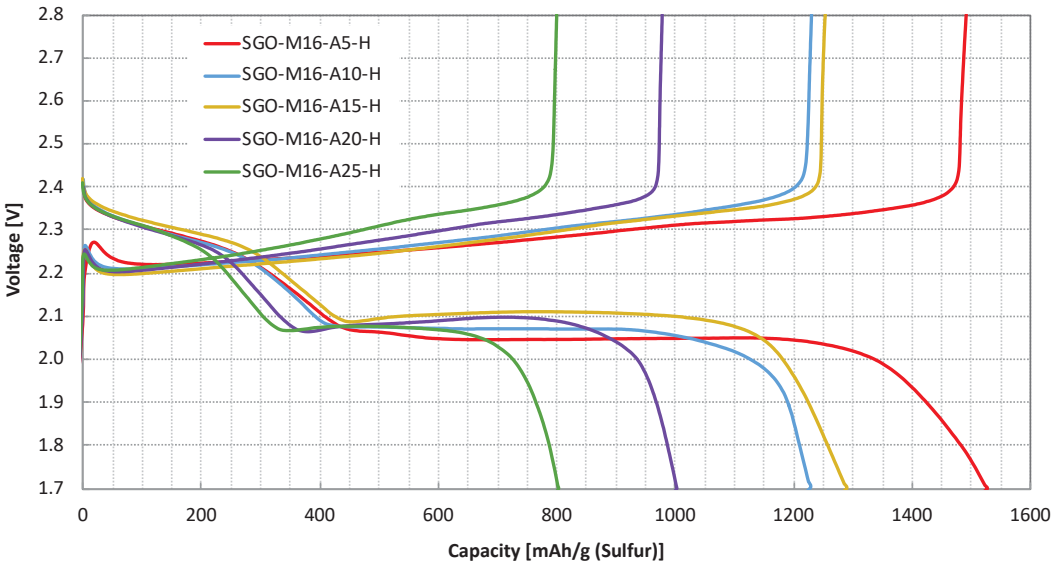


Figure 3-15. The voltage profiles of SGO-M16-A5-H, SGO-M16-A10-H, SGO-M16-A15-H, SGO-M16-A20-H and SGO-M16-A25-H, which were prepared using different acidic deposition temperatures.

SGO-M16-A5-H prepared at 5 °C acidic deposition exhibited a significantly higher capacity than the other samples. The capacity increased in the order of decrease in the acidic deposition temperature. It is surprising that the difference is critical. The voltage profiles for the first five cycles of SGO-M16-A5-H are shown in Figure 3-16.

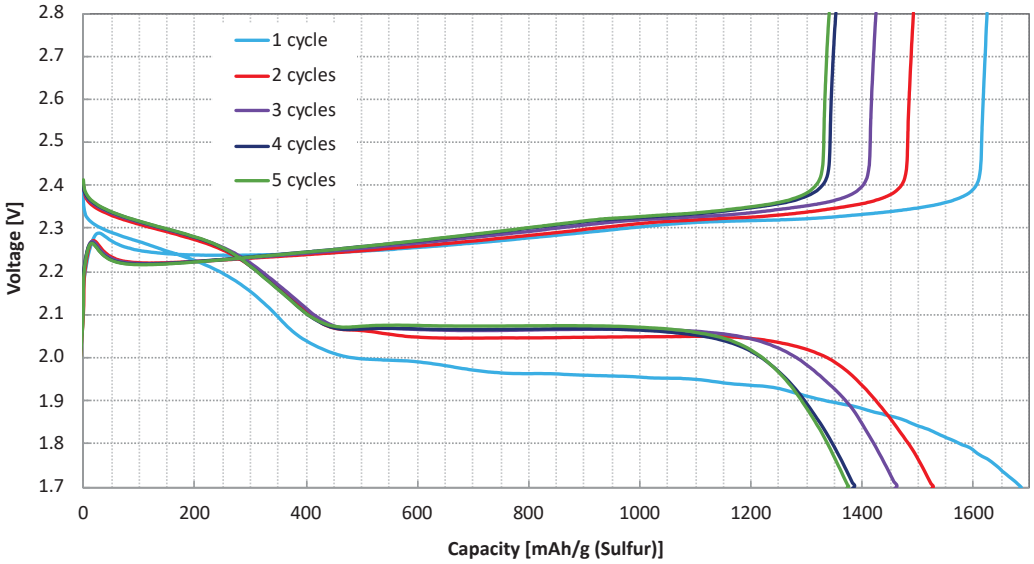


Figure 3-16. The voltage profiles of SGO-M16-A5-H for the first 5 cycles.

The rate capabilities of samples with different preparation conditions were examined and showed in Figure 3-17. SGO-M16-A5-H showed the highest capacity at different C rates. The voltage profiles for each C rate of SGO-M16-A5-H are shown in Figure 3-18. The voltage profile after 100 cycles is shown in Figure 3.-18 as well. The specific capacity remained at 800 mAh/g (sulfur) even after 150 cycles at 0.5 C discharge.

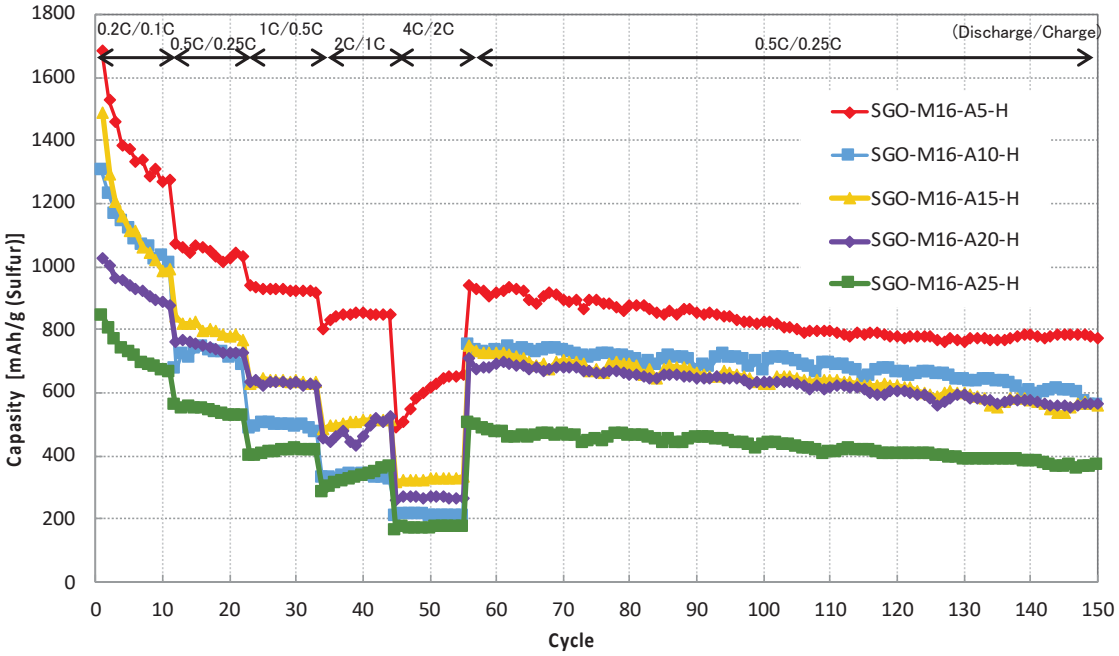


Figure 3-17. The rate capabilities and the cycle performance of SGO-M16-A5-H, SGO-M16-A10-H, SGO-M16-A15-H, SGO-M16-A20-H and SGO-M16-A25-H, which were prepared using different acidic deposition temperatures.

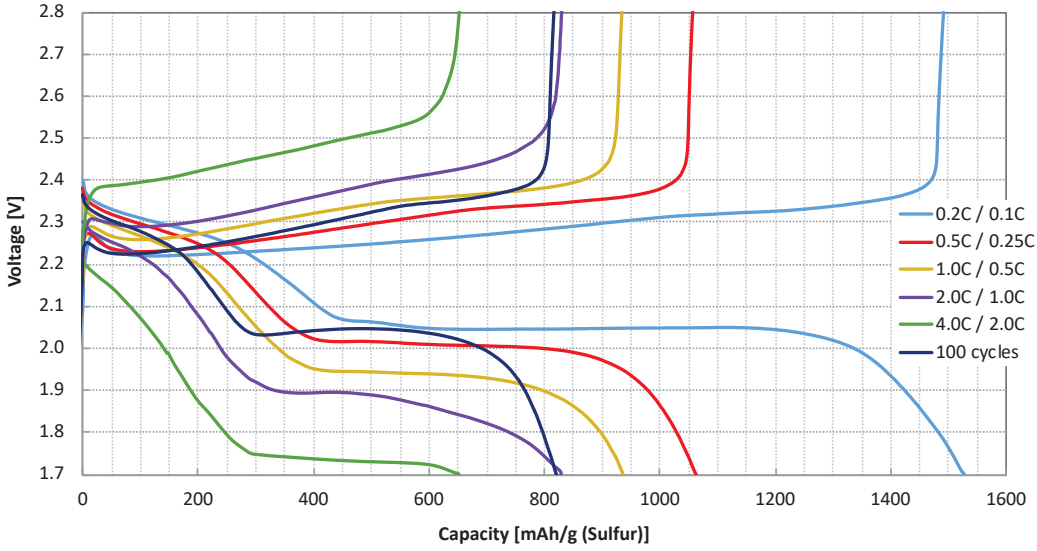


Figure 3-18. The voltage profile of SGO-M16-A5-H for different C rates and after 100 cycles.

Considering the morphologies in Figure 3-12, in SGO-M16-A5-H prepared at 5 °C acidic deposition temperature, better conductivity can be provided for most sulfur by the surrounding flaky layer of reduced GO, whereas too much sulfur accumulation on the surface of GO interfered with the conductivity among the particles for the composites prepared at higher acidic deposition temperatures. Thus, it is concluded that a lower acidification temperature i.e. 5 °C is preferable to obtain high capacity.

### 3.2.11) Relationship between the morphology and the cell performance

Considering these results together with the morphology of each sample, the relationships are illustrated in Figure 3-13. Too much sulfur agglomeration by too long alkaline deposition time causes loss of capacity due to isolation of inner sulfur deep inside the particles. On the other hand, if too much sulfur is deposited on the surface of GO only by acidic deposition without the alkaline deposition, or by high temperature acidic deposition even with the alkaline deposition, the conductivity on the surface of the composites is lost resulting in poor electronic conductivity among the particles. Thus, it is concluded that the specific combination of moderate alkaline deposition and acidic deposition at low temperatures lead to the highest capacity of the cells using the composite as the sulfur electrode active material.

### 3.2.12) Acidic deposition without Alkaline deposition

When the order of mixing three components, which are polysulfide, GO and formic acid, is changed, sulfur and graphene oxide composite created only with acidic deposition (SGO-A) can be obtained. The procedure is graphically shown in Figure 3-19 in comparison with SGO-Mx-Ay.

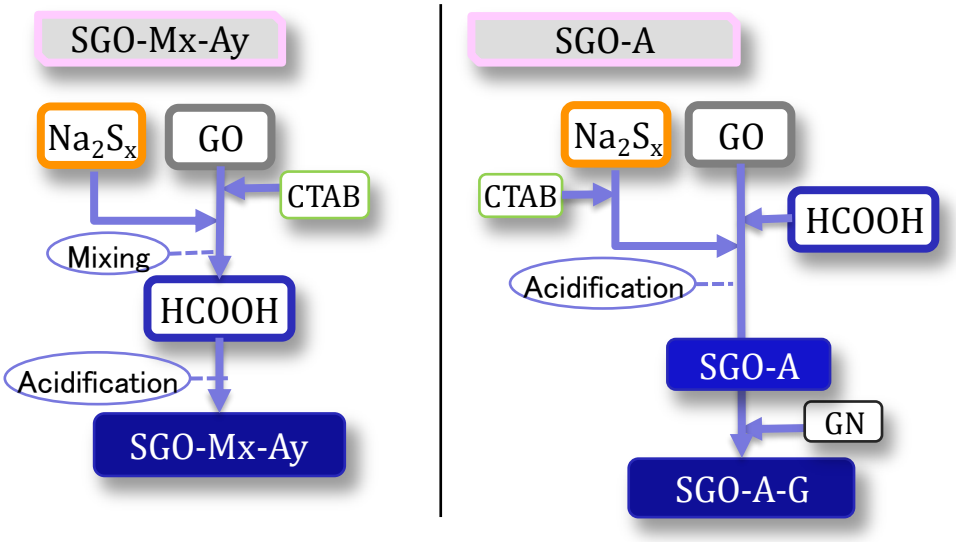


Figure 3-19. Diagram of the preparation of the SGO composite only with acidic deposition.

While the solution obtained in the procedure for SGO-Mx-Ay was powders in the solvent which could be filtered easily, the solution of SGO-A was like a mud with white gray fine particles which could not be filtered by common filter papers. As it has been described above, the morphology of SGO-Mx-Ay had flaky structure on the surface, and there were particles in the size range of 10 μm to 20 μm in random shapes. Figure 3-20 shows morphology of SGO-A.

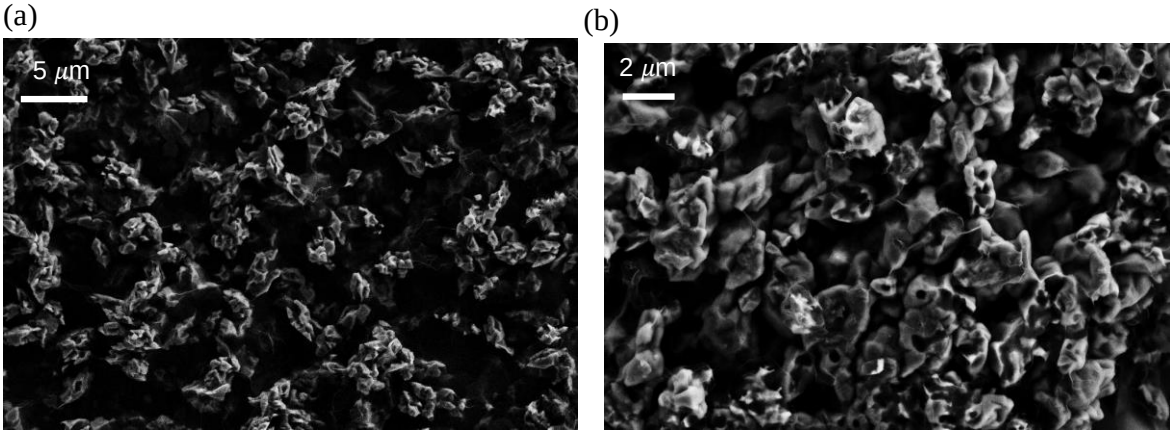


Figure 3-20. SEM images of SGO-A with 2000 magnification (a) and 5000 magnification (b).

The composite shapes uniform fine particles in the size range of 0.5 μm to 2 μm without big chunks of sulfur particles, which is shown in the zoomed-out image in Figure 3-20 (a). Judging from the round shape of those particles of SGO-A in contrast to the flaky surface of SGO-Mx-Ay, sulfur covered the surface of GO almost completely. An image illustrating the features of SGO-Mx-Ay and SGO-A is presented in Figure 3-21.

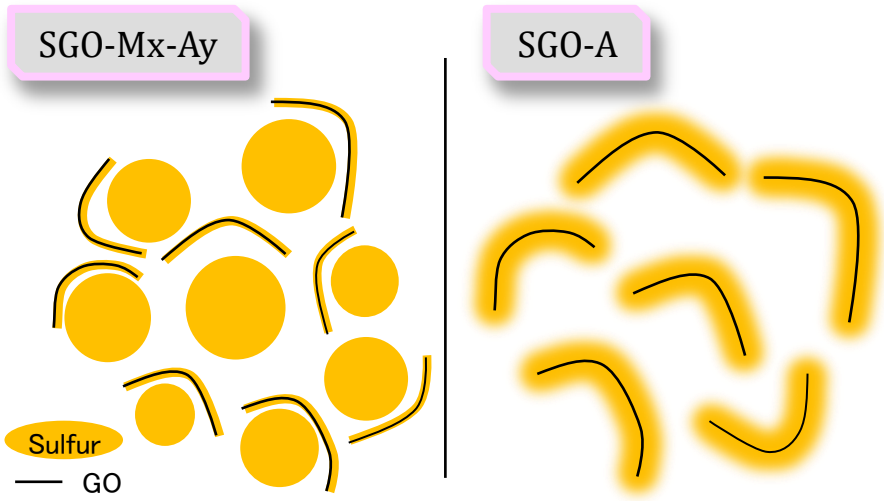


Figure 3-21. The graphical images illustrating the features in the morphologies of SGO-Mx-Ay and SGO-A.

The samples were analyzed by CHNS elemental analysis to check the contents of sulfur and oxygen. The contents of each element for GO, SGO-M16-A20 and SGO-A are shown in Table 3-2.

Table 3-2. The contents of carbon, hydrogen, nitrogen, sulfur and oxygen in GO, SGO-M16-A20 and SGO-A determined by CHNS elemental analysis.

| element | GO | SGO-M16-A20 | SGO-A |
|---|---|---|---|
| C | 39.78 | 15.45 | 10.43 |
| H | 2.73 | 1.63 | 0.41 |
| N | 0.11 | 0.42 | 0 |
| S | 4.02 | 82.51 | 79.52 |
| O | 53.36 | 0 | 9.64 |

The contents of each element are converted to the ratio vs. the content of carbon assuming the carbon in GO is stable enough so that the amount of carbon is not changed so much during the process. The ratios of sulfur and oxygen vs. carbon for GO, SGO-M16-A20 and SGO-A are listed in Table 3-3 and compared in Fig. 3. In the original GO, the ratio of oxygen to carbon is 1.3 which corresponds to an oxygen content of 54%. These oxygen sources are from adsorbed water and functional groups containing oxygen on the surface of GO. [18, 19] The FT-IR spectrum of GO also shows the existence of carboxyl groups, epoxy groups and hydroxyl groups as shown in Figure S3-2. As assumable from the results in Figure 3-2, SGO-M16-A20 does not contain oxygen. This means that almost all of the oxygen is consumed during the alkaline deposition. On the other hand, SGO-A maintains most of the oxygen even after the synthesis.

Table 3-3. The ratios vs. carbon of sulfur and oxygen in GO, SGO-M16-A20 and SGO-A to compare the amount change of oxygen.

| element | GO | SGO-M16-A20 | SGO-A |
|---|---|---|---|
| C | 1 | 1 | 1 |
| S | 0.10 | 5.3 | 7.6 |
| O | 1.3 | 0 | 0.92 |

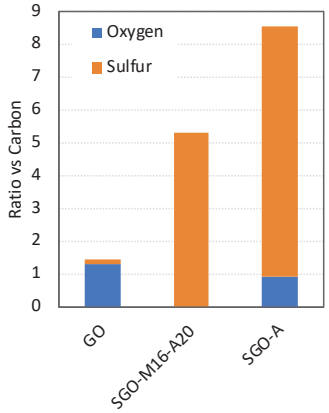

Figure 3-22. The ratios of sulfur and oxygen vs. carbon in GO, SGO-M16-A20 and SGO-A to compare the amount change of sulfur and oxygen during the synthesis.

Since there is no alkaline deposition in the synthesis for SGO-A, oxygen containing functional groups on GO keep staying during the synthesis. This means that the acidification process does not consume the oxygen in the reactions. It is predictable that the oxygen functional groups remains because there is plenty of acid from formic acid in the solution so that the acidic functional groups on GO are not used in the sulfur deposition reaction. The maintenance of the oxygen functional groups during the sulfur deposition supports the homogeneous deposition of sulfur on the surface of GO due to the interactions between polysulfide and the oxygen functional groups. [3] Also, the homogeneous deposition is encouraged by the fast deposition reaction. All polysulfide was converted to sulfur within 12 minutes as shown in TGA results of SGO-A samples taken from the solution at different times in Figure 3-22. The evaporation beginning at around 200 °C ending at 300 °C corresponds to evaporation of both sulfur and oxygen functional groups on GO. The sum of the contents of evaporated species is 90% which is consistent with the elemental analysis results. The contents reached to this number at 12 minutes after starting.

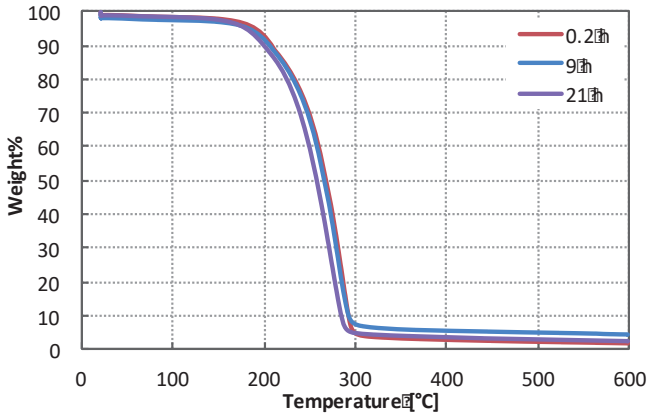


Figure 3-23. Weight loss of SGO-A at different acidic deposition times in TGA analysis corresponding to the evaporation of sulfur indicating the sulfur accumulation completed in 0.2 hours.

When the sulfur deposition is fast, accessibility is dominant rather than stabilization so that sulfur deposition occurrs on GO rather than creating sulfur particles.

### 3.2.13) Addition of conductivity to the sample prepared by acidic deposition

Since the surface of SGO-A seemed covered by sulfur, addition of electronic conductivity to SGO-A was attempted. Graphene nanomaterial (GN) consisting of graphene nano-flowers and multi-layer graphene flakes was introduced in order to enhance the conductivity. [22, 23] CTAB was introduced to the polysulfide solution before acidification and GN was introduced at the end of the synthesis. The modified SGO-A with GN is labeled as SGO-A-G. An SEM image of SGO-A-G before adding GN is shown in Figure 3-24 (a) and of SGO-A-G is shown in Figure 3-24 (b).

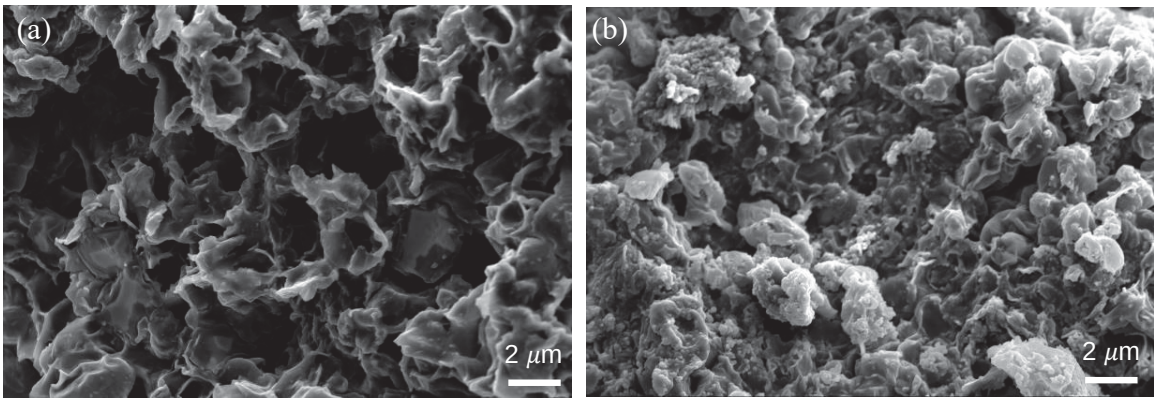


Figure 3-24. SEM images of SGO-A-G before adding GN (a) and SGO-A-G (b).

The size of multi-layer graphene flakes and graphene nano-flowers in GN is about 50 nm from the information in the literatures. [22, 23] It can be observed that the particles of SGO composite were surrounded by GN. To check the distribution of sulfur and carbon, EDS mapping was conducted for SGO-A-G as shown in Figure 3-25. It was verified that sulfur and carbon were distributed on the particles homogeneously. CTAB as the surfactant helped graphene additives to be dispersed so that it provided sufficient conductive networks.

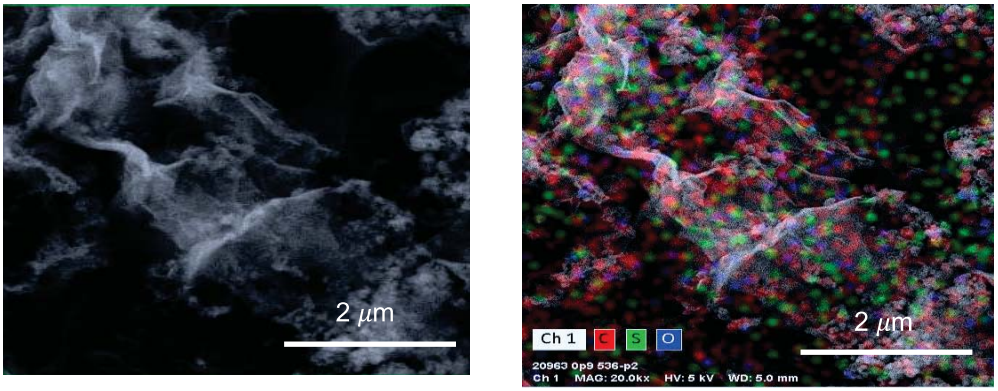


Figure 3-25. EDS mapping of SGO-A-G (right) with the corresponding SEM image without mapping (left).

### 3.2.14) Cell performance of the sample prepared by acidic deposition

The cell performance of SGO-A-G-H was examined. The results of rate capability tests and the following cycling performance are shown in Figure 3-26 in comparison with the results of SGO-M16-A15-H.

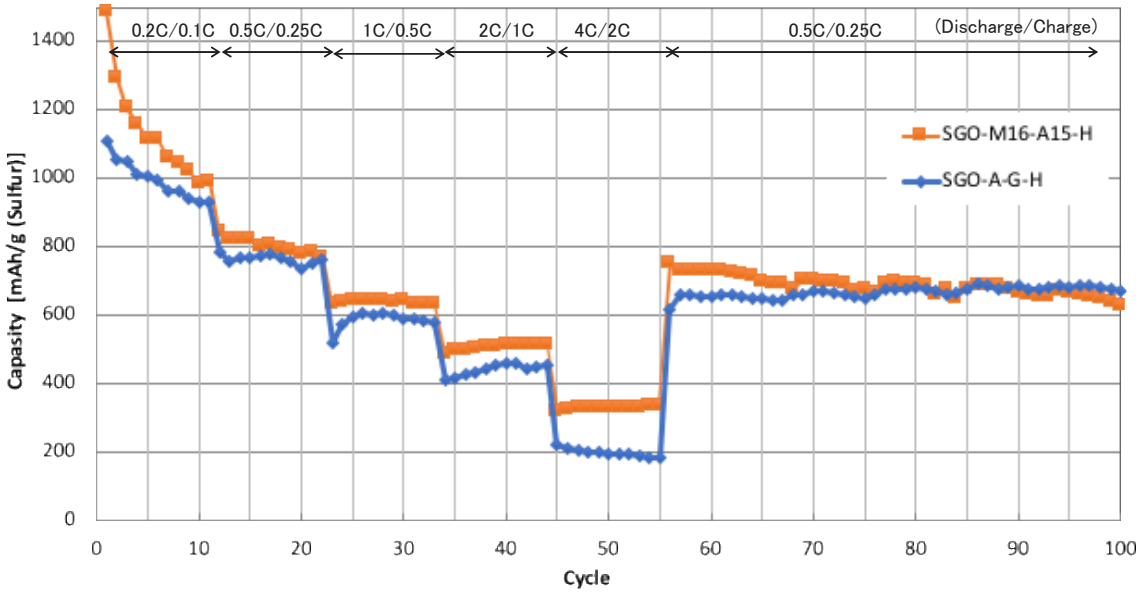


Figure 3-26. The rate capability tests and the following cycling performances of SGO-M16-A15 and SGO-A-G.

SGO-M16-A15-H showed higher initial capacity and better rate capability than SGO-A-G-H. Especially, the difference in the initial capacity is significant. SGO-M16-A15-H showed 1500 mAh/g while SGO-A-G-H showed 1100 mAh/g. However, when the cycling test was continued over 100 cycles, SGO-A-G-H showed better cycling stability than SGO-M16-A15-H as shown in Figure 3-27.

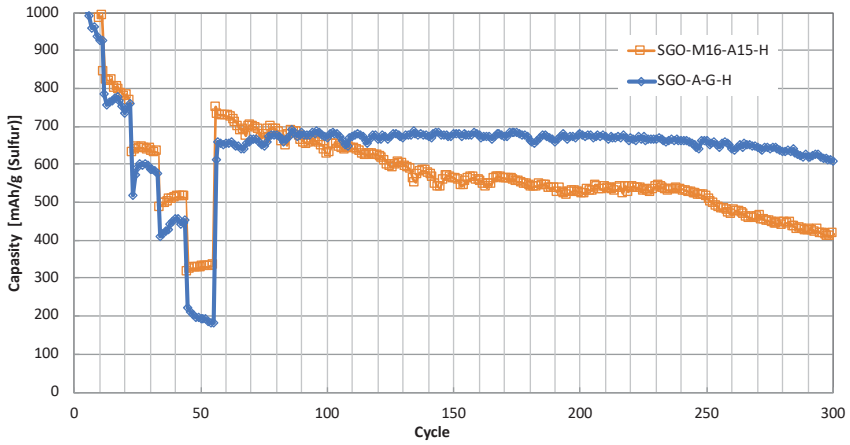


Figure 3-27. The cycling performance until 300 cycles of SGO-M16-A15-H and SGO-A-G-H.

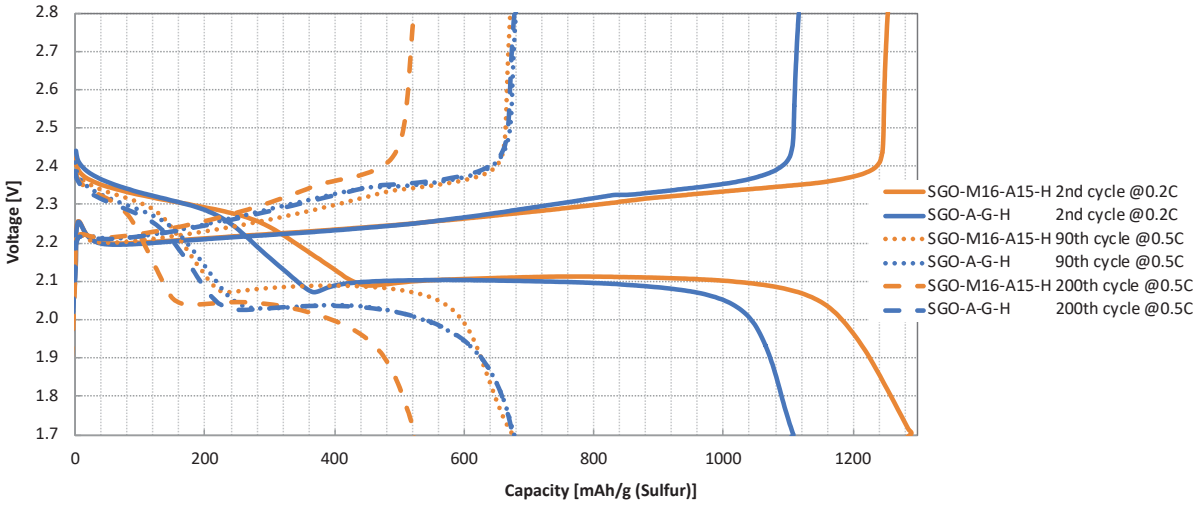


Figure 3-28. The voltage profiles of 2nd, 90th and 200th cycles for SGO-M16-A15-H and SGO-A-G-H

The voltage profiles of the second cycle, 90th cycle and 200th cycle for SGO-M16-A15-H and SGO-A-G-H are shown in Figure 3-28. At the second cycle, the overvoltage for SGO-M16-A15-H and SGO-A-G-H are almost same while the capacity for SGO-M16-A15-H is higher than SGO-A-G-H. This is explained from the observation of the morphology and the results of elemental analysis. SGO-M16-A15-H has a more flaky shape than SGO-A-G-H which means GO is more on the surface than SGO-A-G-H. Elemental analysis showed zero oxygen content in SGO-M16-A20 as shown in Figure 3-22, Table 3-2 and Table 3-3, which indicates that GO is converted to reduced GO, i.e. graphene with some defects, during the mixing process. Reduced GO is known to be more electron conductive than original GO. [6-8] As the results show, SGO-M16-A15-H has conductive reduced GO on the surface. This morphology enables the material to exhibit high sulfur utilization at the beginning. On the other hand, SGO-A has a morphology which has more sulfur on the surface. Although SGO-A-G has a more complicated morphology than SGO-A because it has CTAB and GN, it is supposed to have more sulfur on the surface than SGO-M16-A15 like as SGO-A. Furthermore, SGO-A retained some oxygen as shown by elemental analysis, that means GO retains the oxygen functional groups. SGO-A-G-H showed similar overvoltage to that of SGO-M16-A15-H thanks to the additional GN though, the initial sulfur utilization was limited by those features. These can be also the reason for the better rate capability of SGO-M16-A15-H than SGO-A-G-H. However, when the voltage profiles in 90th cycle and 200th cycle are compared, while these are almost exactly same for SGO-A-G, the 200th profile has more overvoltage and less capacity than the 90th cycle for SGO-M16-A15-H as shown in Figure 3-28. Although the overvoltage for SGO-A-G-H is higher than SGO-M16-A15-H, it remains at the same level between cycle 90 and cycle 200. The good retention of the capacity for SGO-A-G-H can be attributed to the maintenance of the oxygen containing functional groups on GO as seen in the result of elemental analysis. This result suggests that although the oxygen containing functional groups on GO may sacrifice electron conductivity, they can work to keep sulfur in the conductive matrix resulting high cycling stability.

This study showed the possibility of application of GO for capacity increase and cycling stability depending on the protocol in the synthesis process. Although the final aim is to obtain cycling stability with high capacity, understanding how the materials can be modified for different purposes gives important knowledge for future applications.

## 3.3) Summary

The sulfur deposition process in the preparation of SGO nano-composite active material was carefully investigated. It was found that just mixing of a polysulfide solution and a GO suspension produced a composite of sulfur and reduced GO by alkaline deposition. Also, the acidification of the polysulfide solution by formic acid, i.e. acidic deposition was influenced significantly by temperature. The sulfur deposition rate under different conditions influenced the morphology of the materials and their resulting cell performance. By controlling the synthesis condition such as the combination of moderate alkaline deposition for 60% of sulfur and the subsequent acidic deposition at a low temperature, specifically 5 °C, the preferred morphology of the sulfur/GO composite with high capacity was successfully synthesized. This work should allow the controlled synthesis of SGO active material for high-performance Li/S cells.

## 3.4) Experimental section

### 3.4.1) Synthesis

SGO-Mx (x is a variable representing the mixing time in hours) samples: 0.29 g sodium sulfide ($Na_2S$, anhydrous, Alfa Aesar) was dissolved in 12.5 mL distilled water to form a $Na_2S$ solution using 50 mL vial. 0.36 g elemental sulfur (99.5%, Alfa Aesar) was dissolved in the $Na_2S$ solution to form a sodium polysulfide ($Na_2S_x$) solution after stirring for 4 hours at 70 °C. 12 ml commercial GO-water dispersion (4 mg/mL, Graphenea) was diluted with water to form 78 ml of suspension and sonicated for 1.5 hours using 200 mL bottle. 82 mg CTAB (2.5 mM in the GO suspension, Sigma Aldrich) was dissolved in 3 mL water and added to the GO suspension drop-wise and stirred and sonicated for 1.5 hours. Then, the

$Na_2S_x$ solution was added to the as-prepared GO-CTAB suspension drop-wise. The $Na_2S_x$-GO-CTAB mixture was stirred for a different amount of time for each experiment. The mixing time, i. e. alkaline deposition time, for each sample is listed in Table 3-1. The powder was filtered and washed with acetone and water, and dried at 45 °C in a vacuum oven for 12 hours.

SGO-Mx-Ay (y is a variable representing the acidification temperature) samples: The same procedure was used before the filtration as for the SGO-Mx samples. The mixture was slowly added to 50 mL of 2 M formic acid solution (Aldrich) and the mixture was stirred until the solution phase became clear from a milky colloid suspension at different temperatures for each experiment. Then the powder was filtered and washed with acetone and water and dried at 45 °C in a vacuum oven for 12 hours.

SGO-Mx-Ay-H samples: After drying, the sample was heated (heat-treatment) in a tube furnace at 155 °C for 18 hours under Ar with a flow rate of 100 cc/min. An alumina boat containing the sample powders was wrapped with aluminum foil to prevent sulfur evaporation.

SGO-A samples: $Na_2S_x$ solution and 81 ml of GO suspension was prepared in the same method as for SGO-Mx-Ay. 50 mL of 2 M formic acid solution was added to the GO suspension and stirred. Then, the $Na_2S_x$ solution was added drop-wise to the as-prepared GO suspension in formic acid and stirred for 1 hours.

SGO-A-G samples: GO suspension in formic acid and $Na_2S_x$ solution were prepared according to the same process as described above. 82 mg CTAB (Sigma Aldrich) was added to the $Na_2S_x$ solution drop-wise and stirred for 30 min. Then, the $Na_2S_x$ solution with CTAB was added drop-wise to the as-prepared GO suspension in formic acid and stirred for 1 hour. Graphene nanomaterial (GN, carbon nano-flowers and multi-layer graphene flakes [22-23], provided by Jorma Jokiniemi) was added to the suspension of SGO-A-CTAB and stirred and sonicated. Then the powder was filtered and washed with acetone

and water, and dried at 45 °C in a vacuum oven for 12 hours.

SGO-A-G-H samples: After drying, SGO-A-G sample was heated (heat treatment) in a tube furnace at 155 °C for 18 hours under Ar with a flow rate of 100 cc/min.

The obtained samples are labeled as listed in Table 3-1.

### 3.4.2) Material characterization

Elemental analysis was performed using a Perkin Elmer 2400 CHNS/O series II analyzer. Combustion and reduction temperatures were 975 °C and 500 °C, respectively. The combustion parameters were 2, 10, 0, 0.

SEM observation was conducted using Zeiss Gemini Ultra-55 Analytical Field Emission Scanning Electron Microscope. A secondary electron detector was used. The EDS system was used for elemental X-ray analysis. The beam energy was 5 kV with 1 nm resolution.

### 3.4.3) Electrochemical Characterization

The sulfur electrodes were fabricated by mixing the samples after the heat treatment, carbon black (Super P C65) with a binder (SBR/CMC 1:1 by weight) at a weight ratio of 70:20:10 in isopropanol/water (1:3 by volume) solution to form a slurry. The resulting slurry was uniformly spread via a doctor blade onto pure aluminum foil. The solvent was allowed to evaporate at room temperature for 24 hours. The electrode was punched into circular pieces with a diameter of 12.7 mm for assembly into coin cells. The electrodes were then dried in a vacuum oven at 50 °C for 24 hours to eliminate any solvent residue. The sulfur content of the cathodes was 59% as a result of having 84% sulfur in the active materials and 70% active materials in the cathodes. The average sulfur loading of the electrodes was ~0.8mg/cm$^2$. For the electrolyte, 1 mol/kg lithium bis(trifluoromethylsulfonyl)imide (Sigma-Aldrich) in (N-methyl-(N-butyl) pyrrolidinium bis(trifluoromethanesulfonyl)imide (Sigma-Aldrich) / 1,3-dioxolane / 1,2-dimethoxyethane mixture (1:2:2, by volume) was prepared and used for evaluation of the

electrochemical performance. 0.5 mol/kg $LiNO_3$ was used as an additive in the electrolyte.

Type CR2032 coin cells were assembled with a separator (Celgard 2400) between a lithium metal foil (99.98%, Cyprus Foote Mineral) and a sulfur electrode fabricated with the SGO-Mx-Ay-H active material in a glove box filled with argon gas. Galvanostatic discharge and charge testing of the coin cells was performed using a battery cycler (Maccor Series 4000) at the 0.2 C rate (1 C = 1675 mA/g (sulfur)) for discharge and 0.1 C rate for charge between 1.7 and 2.8V. Then the current was changed accordingly. The cell capacity was normalized by the weight of sulfur. All electrochemical characterizations were performed at 30 °C. Before all electrochemical characterizations, the cells were held at open circuit at 30 °C for 12 h.

## 3.5) References

[1] G. Ji, J. Cao and Y. Shi, *Chem. Commun.* **2012**, *48*, 4106–4108.

[2] C. Jin, W. Zhang, Z. Zhuang, J. Wang, H. Huang, Y. Gan, Y. Xia, C. Liang, J. Zhanga, X. Tao, *J. Mater. Chem. A*, **2017**, *5*, 632.

[3] C. Zu and A. Manthiram, *Adv. Energy Mater.* **2013**, *3*, 1008.

[4] H. Wang, Y. Yang, Y. Liang, J. T. Robinson, Y. Li, A. Jackson, Y. Cui and H. Dai, *Nano Lett.* **2011**, *11* (7), 2644.

[5] Z. Wang, Y. Dong, H. Li, Z. Zhao, H. B. Wu, C. Hao, S. Liu, J. Qiu and X. W. (D.) Lou, *Nat. Commun.* **2014** doi: 10.1038/ncomms6002.

[6] L. Q. Lu, L. J. Lu and Y. Wang, *J. Mater. Chem. A*, **2013**, *1*, 9173.

[7] F. Zhang, X. Zhang, Y. Dong and L. Wang, *J. Mater. Chem.* **2012**, *22*, 11452.

[8] H. Sun, G. Xu, Y. Xu, S. Sun, X. Zhang, Y. Qiu and S. Yang, *Nano Res.* **2012**, *5*, (10), 726.

[9] J. Rong, M. Ge, X. Fang and C. Zhou, *Nano Lett.* **2014**, *14*, 473.

[10] M.-K. Song, Y. Zhang and E. J. Cairns, *Nano Lett.* **2013**, *13*, (12), 5891.

[11] L. Ji, M. Rao, H. Zheng, L. Zhang, Y. Li, W. Duan, J. Guo, E. J. Cairns and Y. Zhang, *J. Am. Chem. Soc*. **2011**, *133*, (46), 18522.

[12] L. Zhang, L. Ji, P.-A. Glans, Y. Zhang, J. Zhu and J. Guo, *Phys. Chem. Chem. Phys.* **2012**, *14*, (39), 13670.

[13] X. Feng, M.-K. Song, W. C. Stolte, D. Gardenghi, D. Zhang, X. Sun, J. Zhu, E. J. Cairns and J. Guo, *Phys. Chem. Chem. Phys.* **2014**, *16*, (32), 16931.

[14] Y. Ye, A. Kawase, M. Song, B. Feng, Y. Liu, M. A. Marcus, J. Feng, E. J. Cairns, J. Guo, J. Zhu, *Nanomaterials* **2016**, *6*, (14), doi:10.3390/nano6010014

[15] Y. Ye, A. Kawase, M. Song, B. Feng, Y. Liu, M. A. Marcus, J. Feng, H. Fang, E. J. Cairns, J. Guo, J. Zhu, *J. Phys. Chem. C* **2016**, *120*, 10111.

[16] A. Kawase, E. J. Cairns, *J. Mater. Chem. A,* **2017**, *5*, 23094

[17] A. Teder, *Acta Chem. Scand*. **1971**, *25*, 1722-1728.

[18] F. Barroso-Bujans, A. Alegrı´a, J. Colmenero, *J. Phys. Chem. C* **2010**, *114*, 21645–21651.

[19] A. M. Dimiev, L. B. Alemany, J. M. Tour, *ACS Nano* **2013,** *7,* 576-588.

[20] R. Steudel, *Ind. Eng. Chem. Res*. **1996,** *35*, 1417-1423.

[21] T. Warnheim, A. Jonsson, *J. Colloid Interface Sci*. **1988**, *125,* 627-633.

[22] M.Miettinen, J. Hokkinen, T. Karhunen, T. Torvela, C. Pfüller, M. Ramsteiner, U. Tapper, A. Auvinen, J. Jokiniemi, A. Lähde *J. Nanopart. Res*. **2014**, *16*, 2168.

[23] L. B. Modesto-López, M. Miettinen, J. Riikonen, T. Torvela, C. Pfüller, V.-P. Lehto, A. Lähde, J. Jokiniemi *Aerosol Sci. Technol.* **2015**, *49*, 45-56.

# CHAPTER 4

## The function of cetyltrimethyl ammonium bromide in lithium/sulfur cells

## 4.1) Introduction

### 4.1.1) Introduction of CTAB (cetyltrimethylammoniumbromide)

Utilization of a surfactant is important to disperse the conductive materials because many conductive materials such as various kinds of carbon are not easily dispersed in aqueous solution. CTAB is a widely used surfactant material in various fields such as medicine, household products, and nanoparticle synthesis like porous silica. In battery materials research, CTAB has also been introduced to the sulfur-carbon composite as a surfactant. [1-7] CTAB has hydrophilic quaternary ammonium and hydrophobic hydrocarbon chain so that it forms a micelle. A similar substitute such as tetradecyltrimethylammonium chloride has been used as a surfactant to wrap sulfur particles by GO as a battery material. [8]

### 4.1.2) Analysis of S-GO composite

As described in Chapter 3, S-GO (sulfur-graphene oxide) composites show high cell performance. To elucidate the reasons for such a high cell performance, several types of analyses of the materials have been conducted. [1-7] The presence of C-S bonds and O-S bonds in the S-GO composite have been observed by Raman spectroscopy, X-ray Photoelectron Spectroscopy, Near-edge X-ray Absorption Fine Structure, and X-ray Emission spectroscopy (XES). [3] In X-ray absorption spectroscopy (XAS) and XES, the information has been mostly obtained from C and O K-edge region, which are limited to the observations on the changes of GO. [3]

In recent work, it has been proposed that CTAB interacted with sulfur not only as a surfactant but also as a protection layer to enhance the cell performance because of the creation of C-S bonds between sulfur and CTAB as shown by Raman spectroscopy. [1]

Although it has been reported that several bonds like those mentioned above were created during the synthesis process and some effects enhanced the cycling stability of the

cell, the detailed effects of CTAB on the material preparation and the cell performance have not been elucidated. Not only for improvement of the cell performance of S-GO materials, but also for application of CTAB to various new sulfur cathode materials, a deeper understanding of the chemistry of CTAB in the materials is indispensable. Furthermore, the key factors for the high cell performance should be well understood for suitable scale-up of active material preparation and optimization of cell performance and lifetime.

In this chapter, a whole series of characterizations and cell performance tests are conducted for the S-GO composites. The chemical reactions in the synthesis procedure of the S-GO cathode material have been clarified by using TGA analysis, Raman spectroscopy, NMR spectroscopy mass spectroscopy and S K-edge XAS. In order to identify the peaks in the spectra, reference materials have been synthesized, and theoretical calculations are utilized. These results are used to clarify the effect of CTAB on the cell performance.

## 4.2) Results and Discussion

### 4.2.1) Synthesis Process

The flow chart of the preparation process of the S-GO-CTA is shown in Figure 4-1.

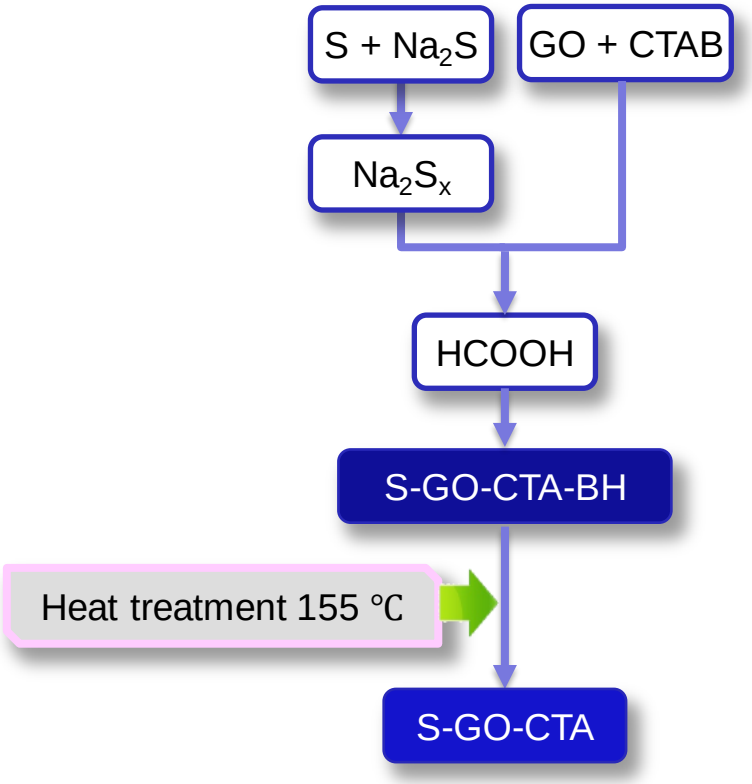


Figure 4-1. The flow chart of the synthesis process of the S-GO-CTA.

The reactions in the solutions during the synthesis are assumed to be as follows: First, polysulfide solutions are made by adding sulfur to a sodium sulfide aqueous solution.

$S_8 + Na_2S \rightarrow Na^+ + S_x^{2-}$ (x=3-8) (pH 11.6) (1)

Second, an aqueous solution of CTAB, which is ionized into bromine anion and cetyltrimethylammonium cation ($CTA^+$, $(C_{16}H_{33})(CH_3)_3N^+$), is combined with an aqueous suspension of GO.

$CTA^+ + Br^- + GO \rightarrow GO\text{-}CTA^+ + Br^{--}$ (pH 2.6) (2)

After mixing the GO-CTAB suspension with the polysulfide solution, the polysulfide is acidified by decreasing the pH using formic acid as shown in Equation 3.

$Na^+ + S_x^{2-} + GO\text{-}CTA^+ + Br^- + HCOOH \rightarrow Na^+ + S\text{-}GO\text{-}CTA + Br^- + COO^- + H_2S\uparrow$ (pH 10.8 → 2.4) (3)

Ions should be removed from the mixture during the filtering and washing process, and S-GO-CTA-BH (-BH: before the heat treatment) remained after the washing process. S-GO-CTA-BH is assumed to be a composite of sulfur, GO and CTA from Equation 3. However, the exact structure of S-GO-CTA-BH is not clear, as is the case for S-GO-CTA after the heat treatment.

Model samples were synthesized accordingly. The samples are labeled as listed in Table 4-1.

Table 4-1

| | GO | Additives | Heat Treatment |
|---|---|---|---|
| S-GO | | None | After the heat treatment |
| S-GO-BH | | None | Before the heat treatment |
| S-GO-CTA0.625 | | 0.625 mM CTAB | After the heat treatment |
| S-GO-CTA1.25 | | 1.25 mM CTAB | After the heat treatment |
| S-GO-CTA1 | | 1.0 mM CTAB | After the heat treatment |
| S-GO-CTA2 | | 2.0 mM CTAB | After the heat treatment |
| S-GO-CTA2.5 | | 2.5 mM CTAB | After the heat treatment |
| S-GO-CTA-BH | | 2.5 mM CTAB | Before the heat treatment |
| S-GO-CTA3 | | 3.0 mM CTAB | After the heat treatment |
| S-GO-CTA4 | | 4.0 mM CTAB | After the heat treatment |
| S-CTA | None | 2.5 mM CTAB | After the heat treatment |
| S-CTA-BH | None | 2.5 mM CTAB | Before the heat treatment |
| S-CA | None | CA | After the heat treatment |
| S-CMA | None | CMA | After the heat treatment |
| S-CDMA | None | CDMA | After the heat treatment |
| S-GO-CA | | CA | After the heat treatment |
| S-GO-CMA | | CMA | After the heat treatment |
| S-GO-CDMA | | CDMA | After the heat treatment |
| S2-GO-CTA | | 2.5 mM CTAB | After the heat treatment |
| S2-GO-CTA-BH | | 2.5 mM CTAB | Before the heat treatment |
| S/CTA-GO | | 2.5 mM CTAB | After the heat treatment |
| S/CTA-GO-BH | | 2.5 mM CTAB | Before the heat treatment |

### 4.2.2) TGA analysis

The TGA results of S-GO-CTA having different amounts of CTAB are shown in Figure 4-2. It is notable that S-GO-CTA having different amounts of CTAB showed different features in the TGA analysis.

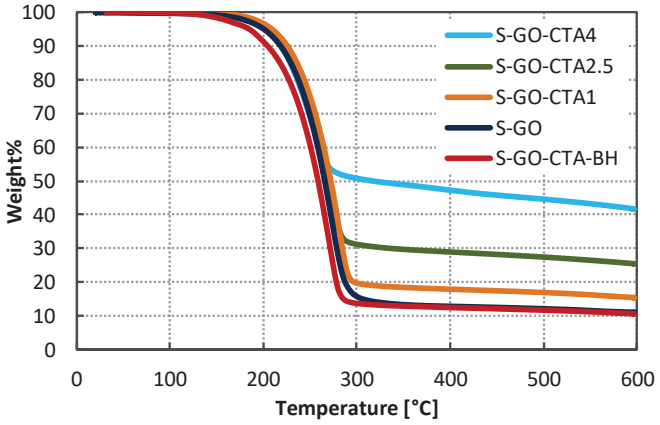


Figure 4-2. TGA results of S-GO-CTA containing different amounts of CTAB, S-GO and S-GO-CTA before the heat treatment.

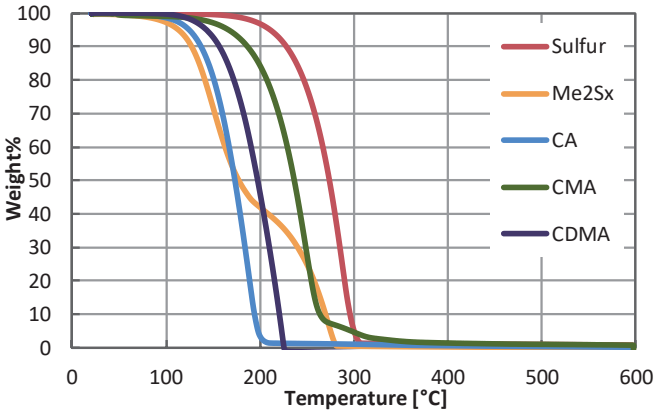


Figure 4-3. TGA results of sulfur, $Me_2S_x$, CA, CMA and CDMA as references.

Significant weight losses are observed from about 160 °C to 300 °C, which is the typical weight loss for the evaporation of elemental sulfur as shown in Figure 4-3. It can be noticed that the content of sulfur decreased as the amount of CTAB increased in the materials, and some portion remained even at 600 °C. At the same time, the TGA curve of S-GO-CTA-BH is almost the same as for S-GO. This result means that new reaction products were produced during the heat treatment of the S-GO-CTA. The new phases were still present even at 600 °C. The new phase is called as Phase X. The changes of the total weights of the samples before and after the heat treatment were measured. The contents of each component were calculated by the methods illustrated schematically in Figure 4-4.

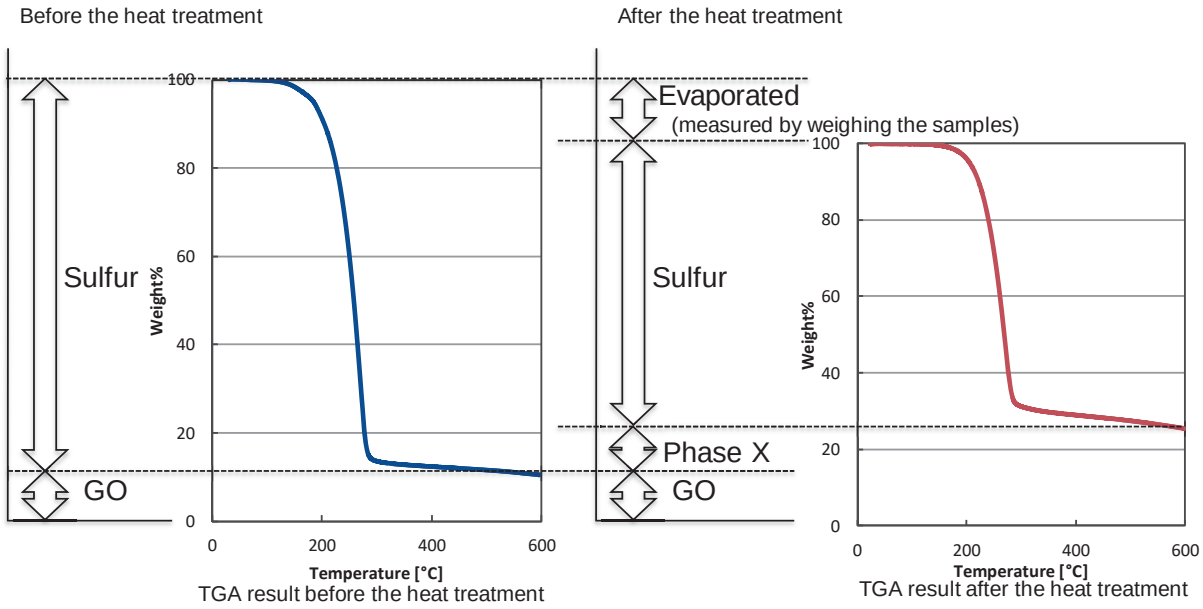


Figure 4-4. Graphical explanation of the method to calculate the contents of sulfur and Phase X produced during the heat treatment in S-GO-CTA using the TGA results and the measurement of the weight of the samples before and after the heat treatment.

The calculated contents of each component are shown in Figure 4-5. The contents of all the components are indicated as the percentage of the total weight of the materials before the heat treatment.

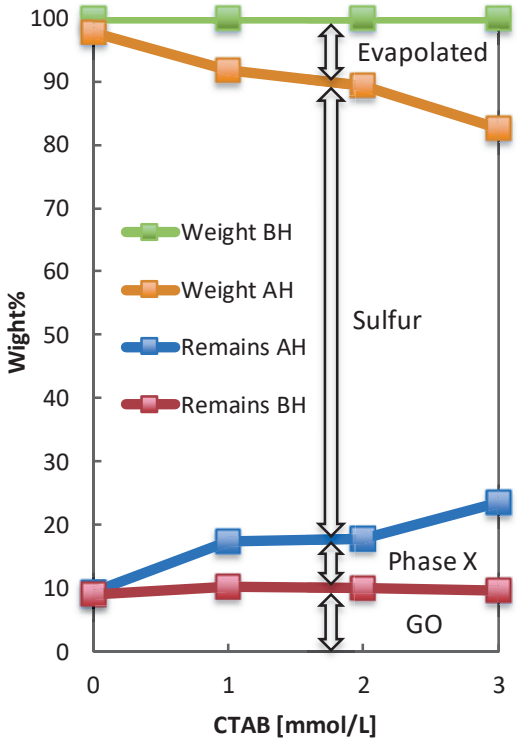


Figure 4-5. The change of the amount of each component in S-GO-CTA depending on the amount of CTAB calculated by the TGA results and the measurement of the weights of the samples before and after the heat treatment.

At first, it was noticed that the total weight after the heat treatment decreased from the weight before the heat treatment. This means that something must have evaporated during the heat treatment. Both the evaporated species and Phase X increased as the amount of CTAB increased, while the sulfur contents decreased. The amounts of GO were almost constant. These results indicate that Phase X was produced by reactions involving sulfur and CTAB, releasing some gaseous species.

### 4.2.3) ESI-MS spectrometry and NMR

S-CTA was synthesized as a model sample to examine the interaction between sulfur and CTAB without GO. In this case, the acidification process can be expressed by Equation 4.

$$Na^+ + S_x^{2-} + CTA^+ + Br^- + HCOOH \rightarrow Na^+ + S\text{-}CTA + Br^- + COO^- + H_2S\uparrow(pH\ 2.4) \quad (4)$$

S-CTA-BH can be a composite of sulfur and $CTA^+$. And S-CTA-BH can change its chemical structure during the heat treatment to S-CTA.

ESI-MS spectroscopy was performed for S-CTA to obtain information about the structure of S-CTA. The result showed only one set of peaks that corresponded to cetylmethylamine (CMA, $C_{16}H_{33}(CH_3)NH$) with a mass of 256.3 as shown in Figure 4-6.

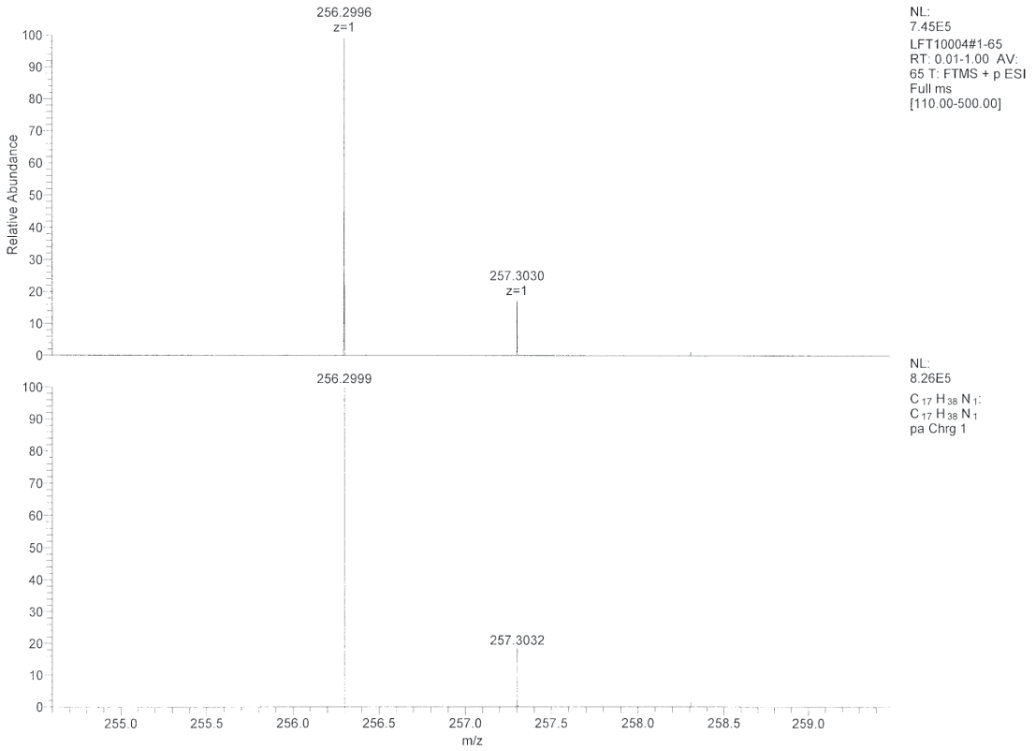


Fig. 4-6 ESI-MS spectrum of S-CTA model composite after the heat treatment with the theoretical isotope pattern to identify CMA.

Considering the mechanism of the ionization process in ESI MS spectroscopy, only easily polarized molecules were detected in this method. Then CMA was preferentially detected. There were possibilities for other species to be contained in S-CTA though, the presence of CMA was confirmed by this experiment. Considering the structure of $CTA^+$, CMA can be produced by removing two methyl cations from $CTA^+$ and adding one proton as in Equation 5.

$$(C_{16}H_{33})(CH_3)_3N^+ + H^+ \rightarrow C_{16}H_{33}(CH_3)NH + 2\ CH_3^+ \quad (5)$$

NMR spectra were obtained for S-CTA-BH and S-CTA to examine the reaction between sulfur and CTAB during the 155 °C heat treatment. Fig. 4-7 shows $^1$H NMR spectra of S-CTA-BH, S-CTA and CTAB as reference. In the spectrum of CTAB, peaks for H at the end of the chain of the cetyl group at 0.83 ppm, methylene H in the middle of the chain at 1.21 ppm, and methylene H adjacent to nitrogen in the chain appeared at 3.57 ppm. The strong peak at 3.43 ppm is attributed to the H in the three methyl groups bonded to the nitrogen atom which could deshield the methyl group. By comparing the spectra of CTAB and S-CTA-BH, it is noticed that the peak for H in the trimethyl groups for S-CTA-BH moves to a lower shift from 3.57 ppm to 3.28 ppm. This movement suggests that the deshielding of the nitrogen atom is weakened. Considering Equation 4, the sulfur atom might affect the chemical shift of the methyl H on the nitrogen by approaching the nitrogen atom. The peaks for H in the cetyl group at 0.83 ppm and 1.21 ppm moved slightly to 0.90 ppm and 1.27 ppm respectively. This movement can also be the result of interference of the sulfur atom near the nitrogen atom. The interaction between the sulfur atom and the nitrogen atom is also supported by the previous study which shows that the valence state of the sulfur is influenced by some interactions with CTAB in the sulfur-CTAB composite before the heat treatment. [5, 6] In the spectrum of S-CTA, the peaks for H in the cetyl group are maintained at 0.90 ppm and 1.27 ppm. But the peak for the trimethyl groups disappeared. Instead several small peaks appeared from 2.5 ppm to 2.8 ppm. Considering the results of mass spectroscopy which indicates the existence of CMA, the small triplet

peak at 2.75 ppm can be attributed to the methylene H next to the nitrogen in cetylmethylamine.

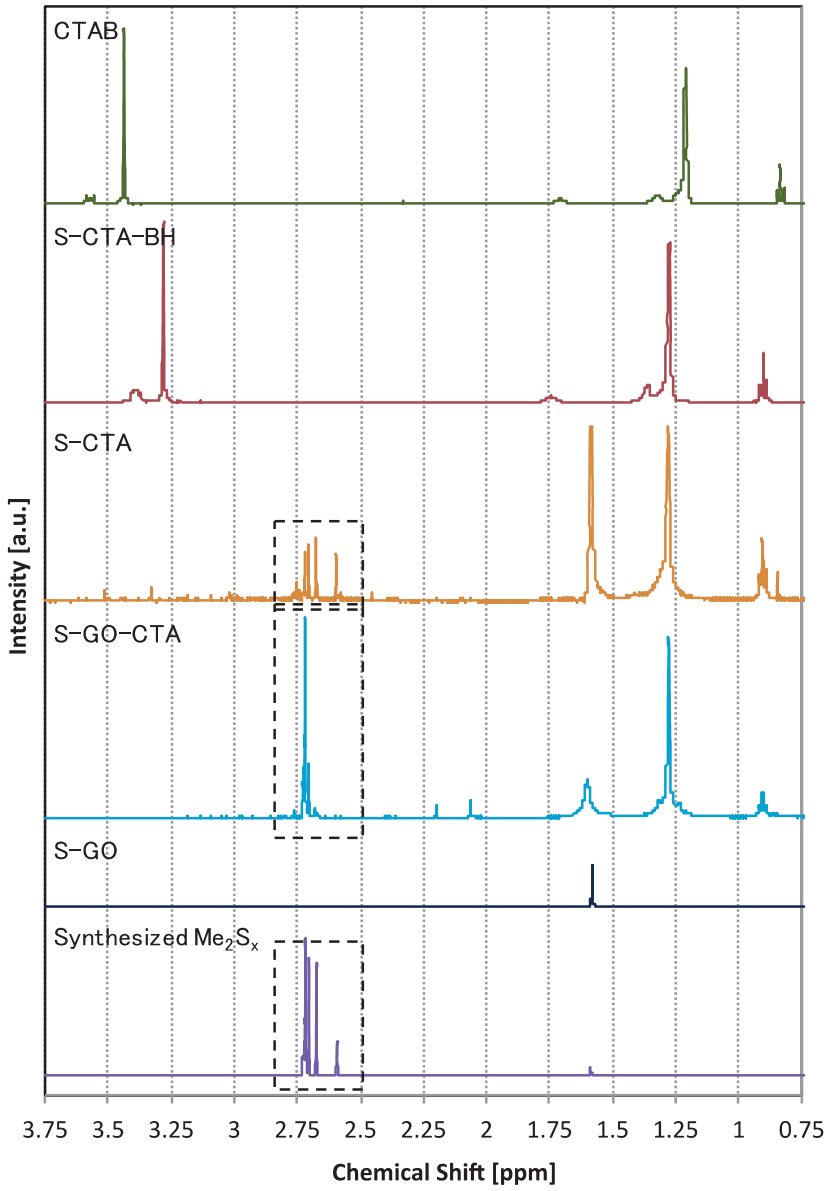


Fig. 4-7 $^{1}$H NMR spectra of S-GO composite with and without CTAB, S-CTA before and after the heat treatment as model materials, and the spectra of CTAB and $Me_2S_x$ as references.

In order to identify the other unknown peaks in this region, dimethylpolysulfides ($Me_2S_x$) was synthesized as reference materials. This experiment is based on an assumption that polysulfide might react with methyl cations removed from $CTA^+$ considering Equation 5. The $^1H$ NMR spectra of S-CTA and synthesized $Me_2S_x$ are shown in Figure 4-7. Figure 4-8 shows the magnified spectra from 2.55 ppm to 2.8 ppm. The peaks for synthesized $Me_2S_x$ at 2.59 ppm, 2.68 ppm, 2.717 ppm, 2.719 ppm, 2.721 ppm and 2.724 ppm are attributed to $Me_2S_3$, $Me_2S_4$, $Me_2S_5$, $Me_2S_6$, $Me_2S_7$ and $Me_2S_8$, respectively. [10]

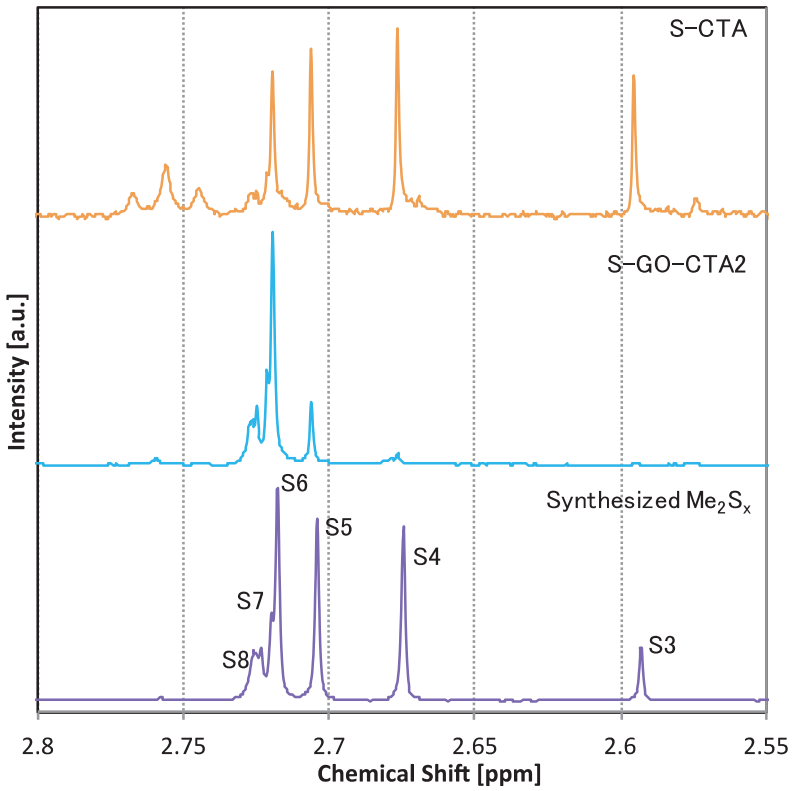


Figure 4-8. Enlarged $^1H$ NMR spectra of S-CTA-AH and $Me_2S_x$ to identify $Me_2S_x$ produced in S-CTA after the heat treatment.

Comparing these spectra, it can be clearly noticed that the peaks in the spectrum of S-CTA correspond exactly to the peaks of $Me_2S_x$. These data show that S-CTA contains $Me_2S_x$ as

a result of the 155 °C heat treatment. $^{13}C$ spectra for S-CTA and $Me_2S_x$ with the spectrum of CTAB are shown in Figure 4-9. The data show concurrence.

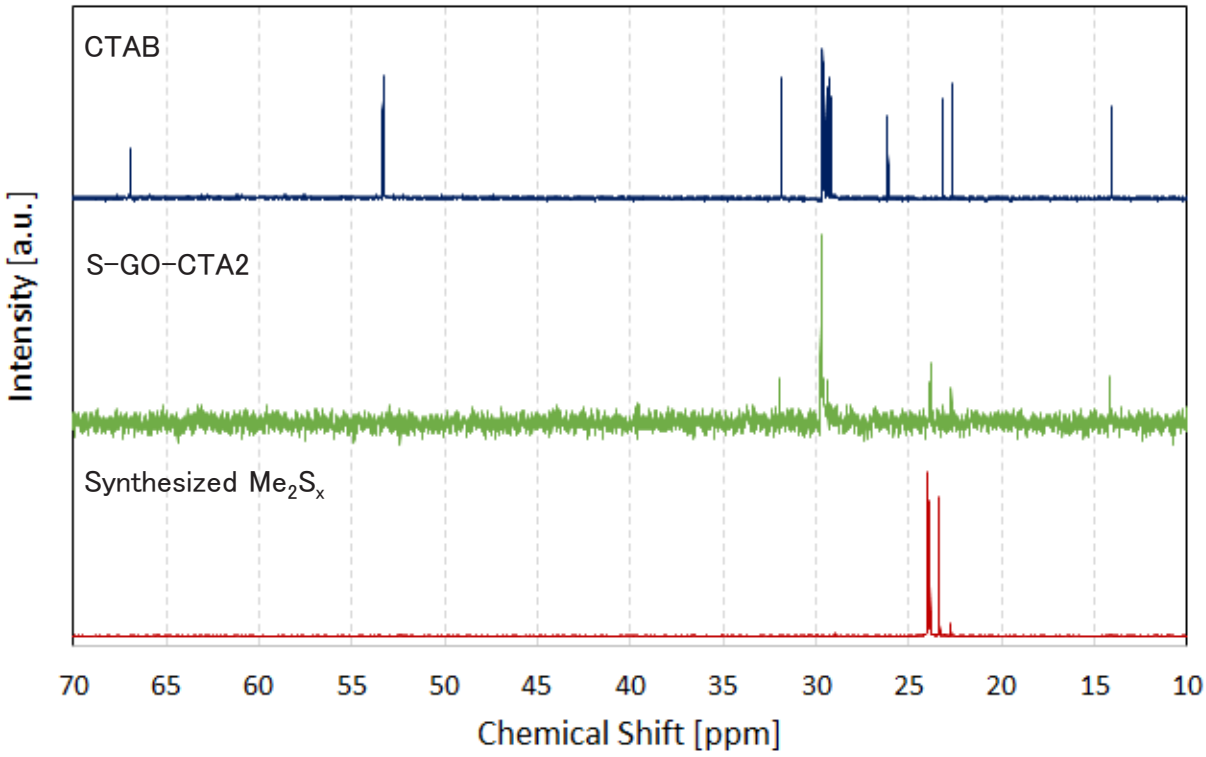


Figure 4-9. $^{13}C$ NMR spectrum of S-GO-CTA after the heat treatment, and the spectra of CTAB and $Me_2S_x$ as references.

Combining the results from ESI-Mass spectrometry and NMR spectroscopy, the presence of CMA and $Me_2S_x$ in S-CTA were confirmed. These findings allow to suggest the reaction during the heat treatment as Equation 6.

$$((C_{16}H_{33})(CH_3)_3N)(HS_x) \rightarrow (C_{16}H_{33})(CH_3)NH + (CH_3)_2S_x \quad (6)$$

The boiling points of dimethylsulfide ($Me_2S$), dimethyldisulfide ($Me_2S_2$) and dimethyltrisulfide ($Me_2S_3$) are 37.3 °C, 110 °C and 170°C, respectively. The boiling points of the other $Me_2S_x$ having more than three sulfur atoms are higher than 170 °C. $Me_2S$ and

$Me_2S_2$ should be evaporated during the heat treatment regarding the temperature for the heat treatment as 155 °C. This fact corresponds with the NMR results that showed only $Me_2S_x$ with more than three sulfur atoms. This result reminds that some gaseous species produced by the reaction of CTAB should be evaporated during the heat treatment as expected from Figure 4-5. The evaporated species are assumed to include $Me_2S$ and $Me_2S_2$ considering the boiling points and the temperature of the heat treatment.

Equation 6 helps to suggest the structure of S-CTA-BH. After one $CTA^+$ couples with one hydrogen polysulfide anion ($HS_x^-$), these two ions can be stabilized together in the solution and become S-CTA-BH. This assumption corresponds with the NMR result of S-CTA-BH, which shows the peaks for $CTA^+$ at shifted positions by the effect of polysulfide.

The NMR spectrum of S-GO-CTA containing GO is presented in Figure 4-7. S-GO-CTA showed the corresponding peaks to S-CTA at around 2.7 ppm for $Me_2S_x$, at 1.27 ppm for methylene H and at 0.9 ppm for methyl H in CMA. The results indicate that the same chemical reaction expressed as Equation 6 occurred in the process for S-GO-CTA as well as S-CTA. However, the peaks for $Me_2S_7$ and $Me_2S_8$ are intensified, while $Me_2S_3$ and $Me_2S_4$ disappear. Shorter polysulfides are pressumed to be oxidized to longer polysulfides by the surface functional groups on GO in the mixture of GO and the polysulfide solution considering the results in Chapter 3.

The peak at 1.58 ppm in the spectra of S-CTA, S-GO-CTA and S-GO is caused by the H in water as seen in Figure 4-10. [11] It was confirmed that there is no polysulfane ($H_2S_x$) in the material by checking the NMR spectra of synthesized $H_2S_x$ as shown in Figure 4-10. [12, 13]

The spectrum of S-GO without CTAB is shown in Figure 4-6. There is no peak other than the peak of water at 1.58 ppm in that spectrum. This absence of the peaks supports the fact that CTAB is necessary for the reactions producing CMA and $Me_2S_x$. The peak at 2.2 ppm is for the H in acetone, which remained after the washing process of the material as

seen in Figure 4-10. [11]

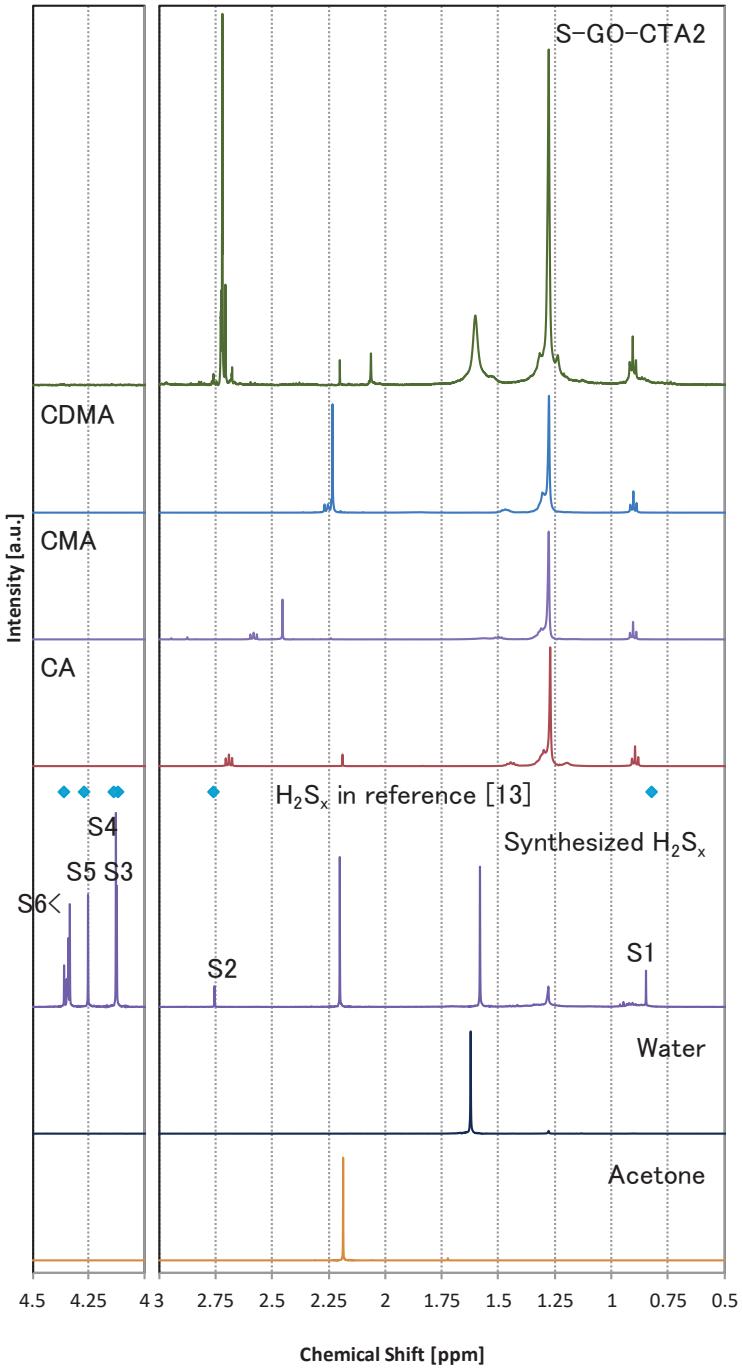


Figure 4-10. $^{1}$H NMR spectra of S-GO-CTA2-AH with reference spectra of three types of amines which can be produced by removing methyl group from $CTA^{+}$, $H_2S_x$, water and acetone.

### 4.2.4) TGA analysis 2

It was revealed that $Me_2S_x$ and CMA were produced by the chemical reactions between polysulfide and $CTA^+$ during the heat treatment. Considering the reaction between polysulfide and $CTA^+$ as described in Equation 6, it is highly possible for cetyldimethylamine (CDMA, $C_{16}H_{33}N(CH_3)_2$) and cetylamine (CA, $C_{16}H_{33}NH_2$) to be produced during the heat treatment as well as CMA. It is because the difference among those species is only the number of the methyl groups on the nitrogen atom. The assumption of production of CDMA is also supported by the literature. [14] Then candidates for Phase X are $Me_2S_x$, CA, CMA and CDMA. If some of them are Phase X, they should be stable above 300 °C in the TGA analysis. But none of them was stable above 300 °C as shown in Figure 4-3. This suggests that further reactions are required to produce Phase X. Assuming that Phase X materials are created by reactions involving sulfur and CA, CMA and CDMA, reference materials were prepared by the heat treatment of mixtures of sulfur and CA, CMA and CDMA. These are labeled as S-CA, S-CMA, and S-CDMA, respectively. Figure. 4-11 shows the TGA results for those model compounds. All of them show phases that remain even above 300 °C.

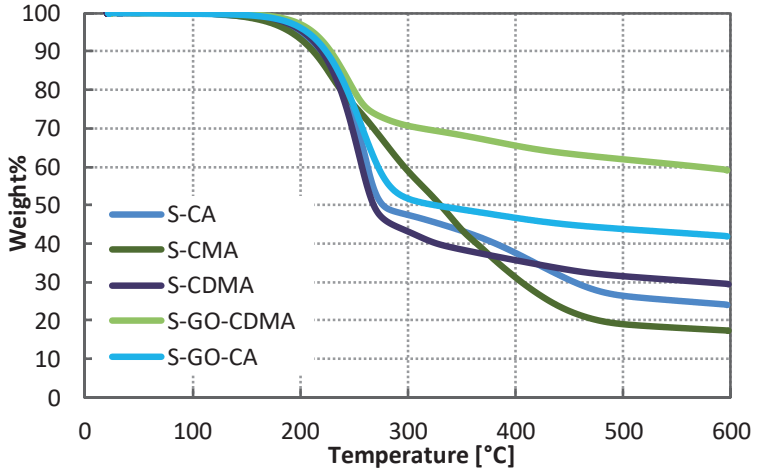


Figure 4-11. TGA results of reference samples prepared from sulfur and CA, CMA and CDMA.

This result strongly suggests the possibility that sulfur reacts with these cetylamine compounds that have been produced by reactions between $CTA^+$ and polysulfide during the heat treatment, and produces Phase X. Furthermore, model compounds were prepared by adding CA, CMA and CDMA to S-GO and by the same heat treatment. These compounds are labeled as S-GO-CA, S-GO-CMA and S-GO-CDMA as listed in Table 4-1. The TGA results of these model compounds are shown in Figure 4-11 as well. They exhibit stable features even above 300 °C, too.

### 4.2.5) Raman spectroscopy

In order to confirm whether some of S-CA, S-CMA, S-CDMA are Phase X, Raman spectroscopy was conducted. The spectra of S-GO-CTA and S-GO are compared as shown in Figure 4-12.

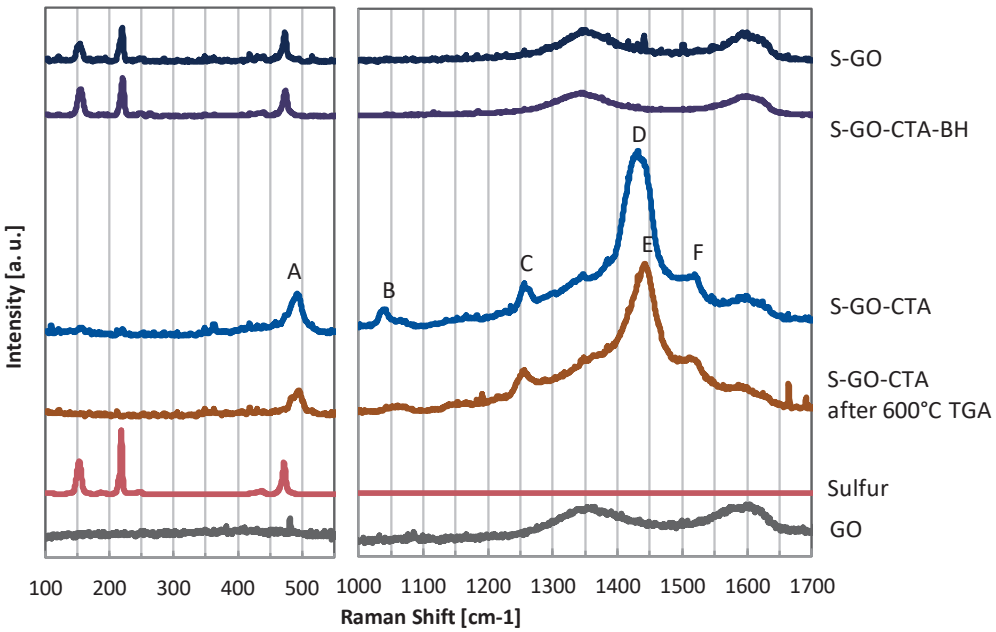


Figure 4-12. Raman spectra of the S-GO composite with and without CTAB, S-GO-CTA before and after the heat treatment, the powder remaining after TGA analysis of S-GO-CTA, and the spectra of sulfur and GO as references.

In the spectrum of S-GO, there are peaks attributed to sulfur at 150 $cm^{-1}$, 218 $cm^{-1}$ and 470 $cm^{-1}$. And there are two broad peaks for GO at 1330 $cm^{-1}$ and 1590 $cm^{-1}$, which are attributed to the D band and G band of carbon respectively. The spectrum of S-GO-CTA-BH is almost the same as that of S-GO. On the other hand, S-GO-CTA shows a quite different spectrum from those spectra. No peak is found for sulfur, and new peaks at 490 $cm^{-1}$, 1037 $cm^{-1}$, 1255 $cm^{-1}$, 1425 $cm^{-1}$ and 1520 $cm^{-1}$ appear instead. Those peaks are labeled as peak A, peak B, peak C, peak D and peak F respectively. The D band and G band of GO remain, overlapping with those new peaks. These results indicate that new phases having these peaks were produced during the heat treatment. Sulfur should be still inside the material of S-GO-CTA even after the heat treatment judging from the results of TGA in Figure 4-2 and XRD patterns in Figure 4-13.

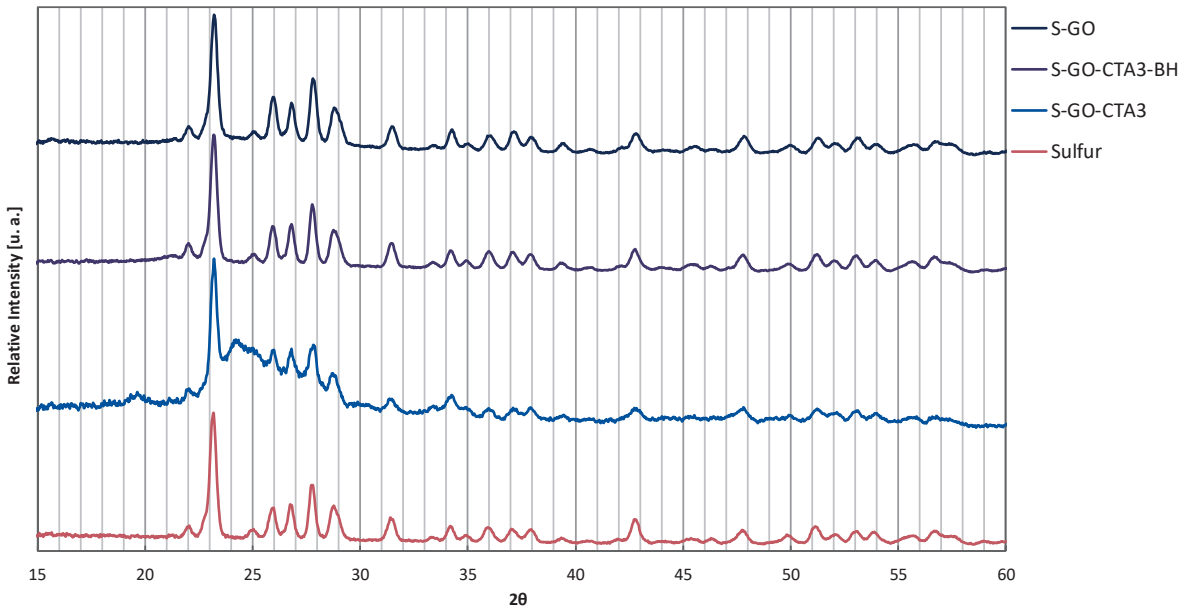


Figure 4-13. XRD patterns of S-GO-CTA with and without CTAB and before and after the heat treatment with reference of sulfur.

Therefore, the fact that peaks for sulfur disappear suggests that the newly produced phases covered the surface of sulfur in the composites. Although it was reported that a peak at 636

$cm^{-1}$ was evidence of C-S bonds in the previous study, [1] the peak at 636 $cm^{-1}$ was very small. In this study, it is better to focus on the more prominent peaks as represented by peaks from A to F rather than the peak at 636 $cm^{-1}$. The Raman spectrum of the powder remaining after TGA analysis is shown in Figure 4-12. Interestingly, this spectrum is almost the same as the spectrum before the TGA analysis. The only difference is that the peak position of peak D slightly changes to 1439 $cm^{-1}$. Observing carefully the spectrum of S-GO-CTA, peak D had a shoulder at 1439 $cm^{-1}$. It can be explained that peak D disappeared after TGA analysis, and then the peak at 1439 $cm^{-1}$, which existed even before TGA analysis, just became clear. This peak at 1439 $cm^{-1}$ is labeled as peak E. From these results, it can be concluded that the new phases having peaks A, B, C, D, E and F are produced during the heat treatment. Also, a part of the material having peaks A, B, C, E and F remains after TGA analysis as Phase X.

The Raman spectra of the model compounds, S-GO-CA, S-GO-CMA and S-GO-CDMA, were measured and are shown in Figure 4-14.

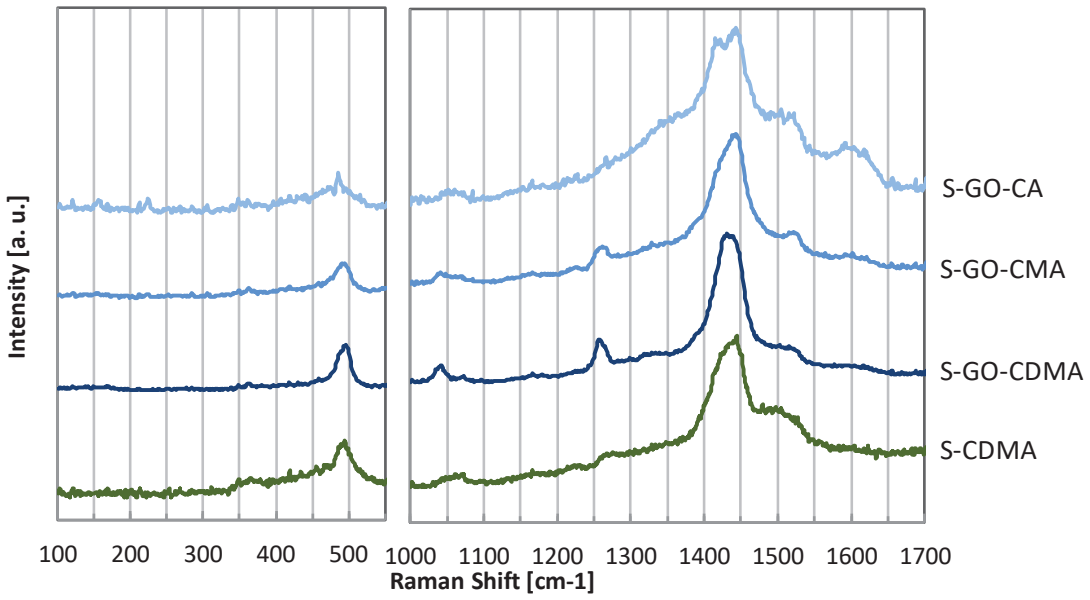


Figure 4-14. Raman spectra of the model compounds, S-GO-CA, S-GO-CMA, S-GO-CDMA and S-CDMA as references.

Comparing the spectra between Figure 4-12 and Figure 4-14, S-GO-CDMA exhibited exactly the same spectrum as S-GO-CTA. Although S-GO-CMA also shows quite a similar spectrum to those, peak D is not as clear as in the spectrum of S-GO-CTA. These results suggest that Phase X was created by the reaction between sulfur and CDMA during the heat treatment. The spectrum of S-CDMA, the model compound without GO, is shown in Figure 4-14 as well. Although the spectrum is almost the same as that of S-GO-CDMA, the existence of peaks B and C is not clear. Also, it was found that the samples were much more fragile under the laser beam for Raman spectroscopy than S-GO-CDMA. Actually, the spectra of S-CA and S-CMA could not be obtained easily due to unstablity under the laser beam. These results suggest that GO stabilizes these compounds made by the reactions between sulfur and CA, CMA, and CDMA. It is noticed that peaks B and C appeared as the result of the interactions with GO. Considering the fact that the spectrum of S-GO-CA does not show peaks B and C clearly, and that peaks B and C for S-GO-CMA are smaller than S-GO- CDMA, it can be said that CA and CMA have less interaction with GO than CDMA. This can be a reason why S-GO-CDMA was preferentially formed in the material.

### 4.2.6) ESI-Mass spectrometry

To identify the exact structure of Phase X, mass spectrometry was conducted for S-CDMA. The results indicated the existence of two molecules. One has a formula of C18H38NS with 300 m/z. The other one has a formula of C33H68NS with 510 m/z. The spectra and the corresponding isotope patterns are shown in Figure 4-15 and Figure 4-16. Considering the structure of CDMA, the highly possible structure for C18H38NS is $(C_{16}H_{33})(CH_3)NCH_2SH$, Cetylmethylaminomethanethiol (S-CDMA-1). This can be created by one sulfur atom addition to a methyl group on the nitrogen atom in CDMA as shown in Equation 7. The formula C33H68NS can be $(C_{16}H_{33})NH(CH_2SC_{16}H_{33})$, N-cethyl-1-cetylsulfanylmethanamine (S-CDMA-2). This can be produced by addition of the cetyl group to the sulfur atom in S-CDMA-1 and removal of a methyl group from the nitrogen

as shown in Equation 8.

$(C_{16}H_{33})(CH_3)_2N + S \rightarrow (C_{16}H_{33})(CH_3)NCH_2SH$ (7)

$(C_{16}H_{33})(CH_3)NCH_2SH + (C_{16}H_{33})(CH_3)_2N \rightarrow (C_{16}H_{33})NH(CH_2SC_{16}H_{33}) + (CH_3)_3N$ (8)

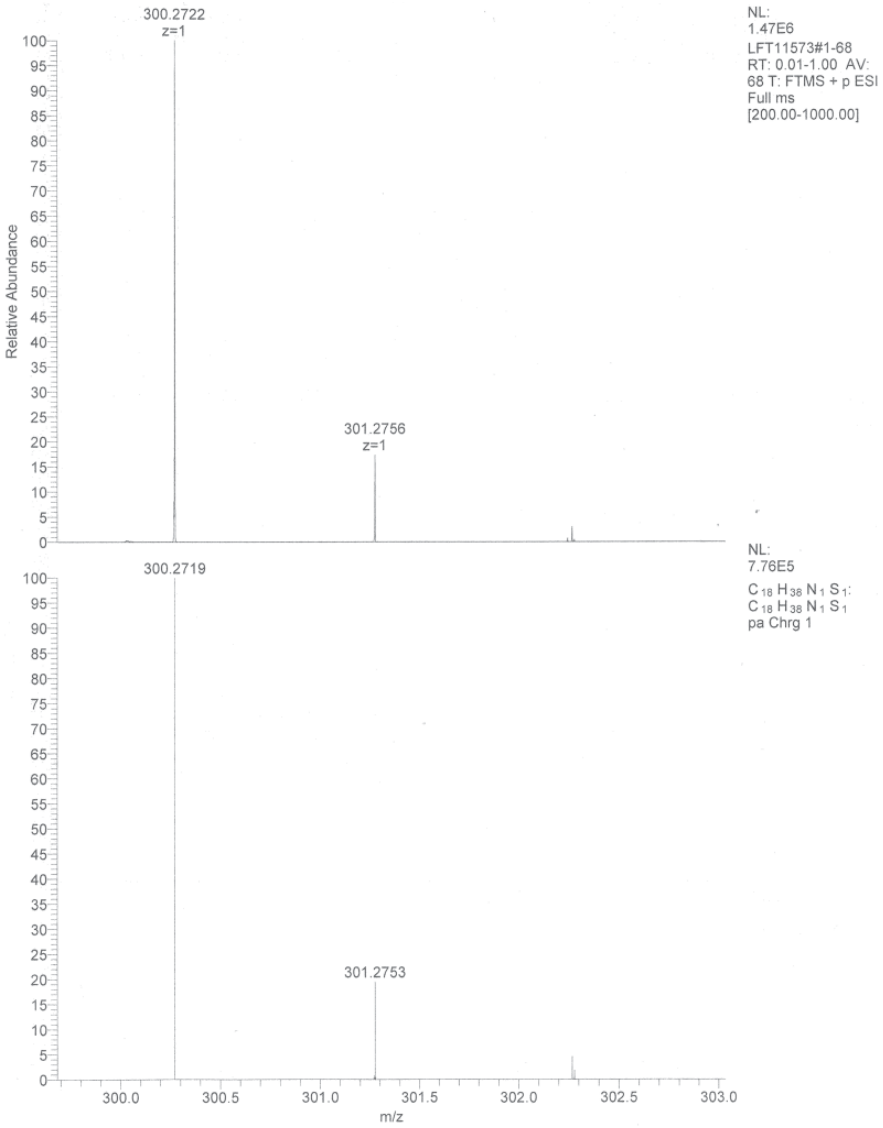


Figure 4-15. MS spectra of S-CDMA model composite after the heat treatment with the theoretical isotope pattern corresponding to the part to identify Cetylmethylaminomethanethiol (S-CDMA-1)

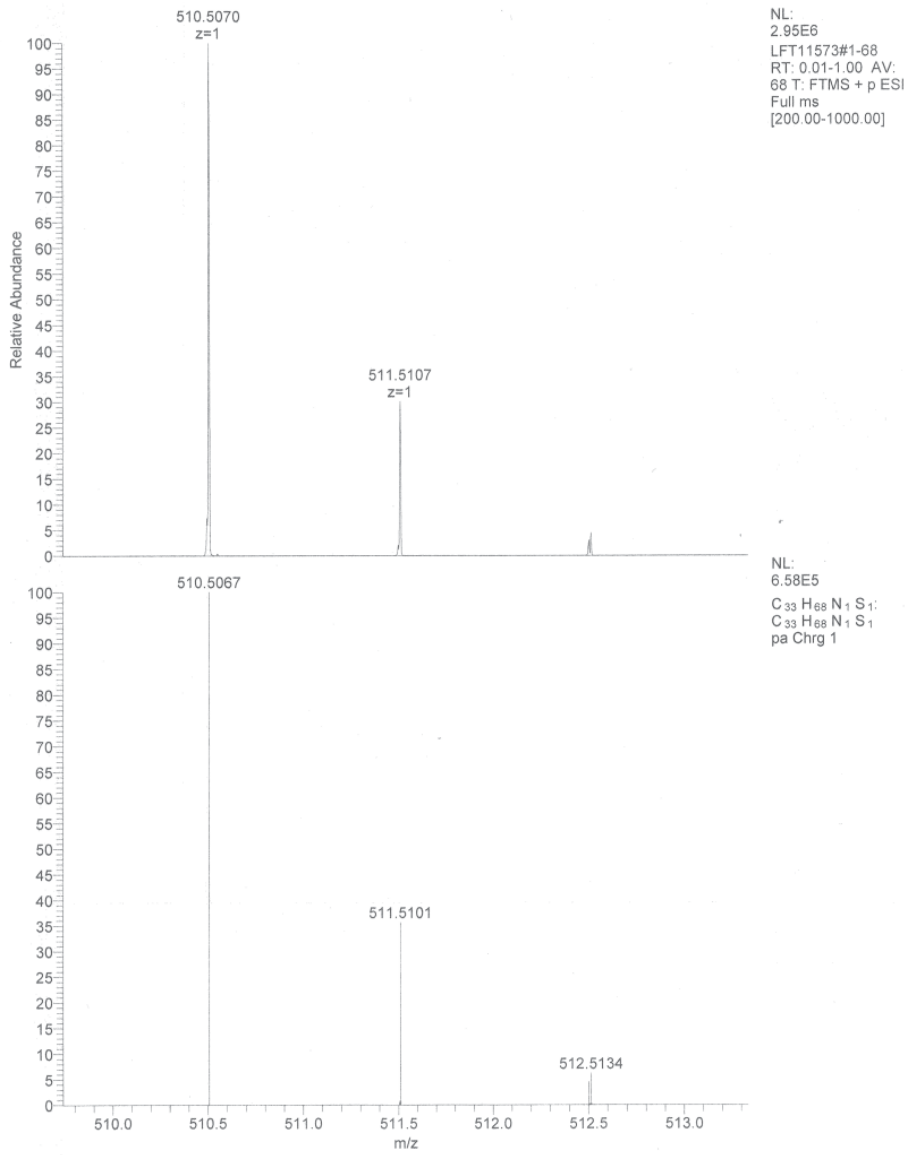


Figure 4-16. MS spectra of S-CDMA model composite after the heat treatment with the theoretical isotope pattern corresponding to the part to identify N-cethyl-1-cetylsulfanylmethanamine (S-CDMA-2).

It can be concluded that these big molecules were produced on the surface of the S-GO composite after the heat treatment and stayed even above 300 °C in the TGA analysis as Phase X.

### 4.2.7) Computational analysis for Raman spectroscopy

The Raman spectra were examined again by considering that S-CDMA-1 and S-CDMA-2 are the origins of specific Raman peaks. The spectra of the CTAB, CA, CMA and CDMA are collected in Figure 4-17 as reference. All of them show significant peaks around 1439 $cm^{-1}$ and 1462 $cm^{-1}$. These peaks become broader in the order of CTAB, CA, CMA and CDMA. The theoretical spectra of $CTA^{+}$, CA, CMA and CDMA were calculated by using optimized models. Figure 4-18 shows the theoretical spectra with their vibration modes. Most of the peaks in the experimental spectra correspond to the peaks in the calculated spectra, some differences between experimental and calculated spectra in the Raman shift were observed in the high wave number region though. The vibration modes of the peaks in the experimental spectra were analyzed by comparing with the calculated spectra.

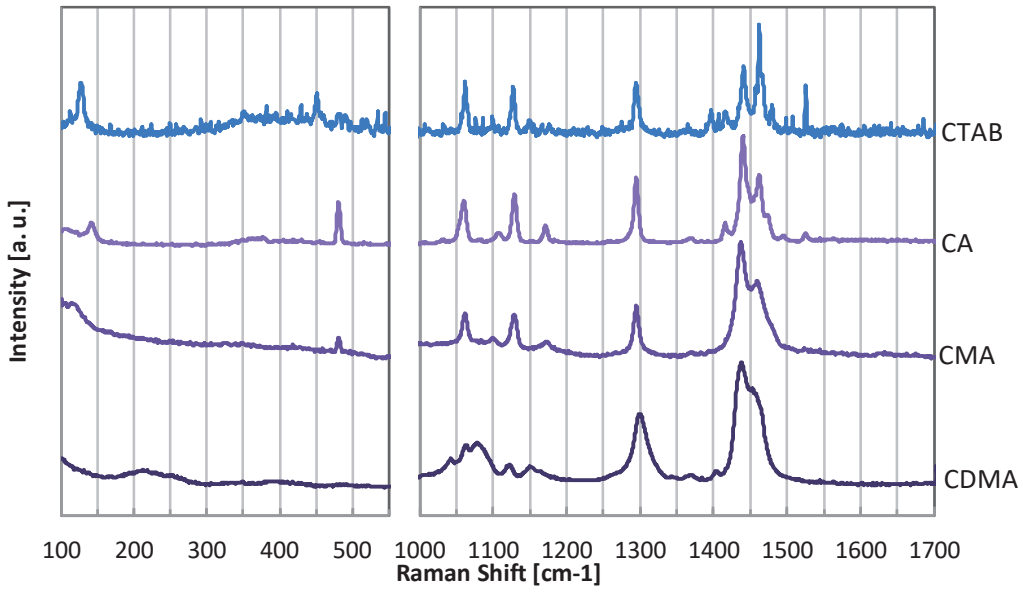


Figure 4-17. Raman spectra of CTAB, CA, CMA and CDMA as references.

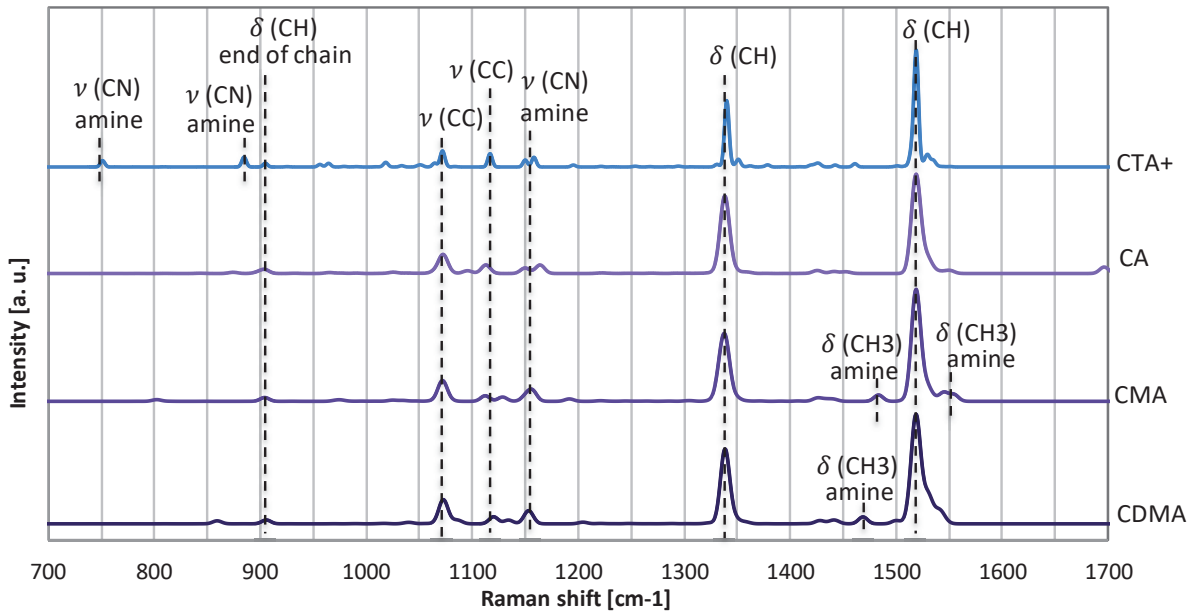


Figure 4-18. Theoretically calculated Raman spectra of CTA+, CA, CMA and CDMA with their vibration modes by using optimized models.

In all cases, the peaks centered at 1060 $cm^{-1}$ and 1127 $cm^{-1}$ correspond to C-C stretching vibrations; the small peak centered at 1170 $cm^{-1}$ represents a C-N stretching vibration in the amine group; the peaks centered 1295 $cm^{-1}$, 1439 $cm^{-1}$ are attributed to C-H bending vibrations; and the peak at 1462 $cm^{-1}$ corresponds to $CH_3$ bending vibrations in the amine group. Considering the fact that S-CDMA-1 and S-CDMA-2 also have a common structure with CA, CMA and CDMA, peak D can be attributed to a bending vibration of C-H bonds in the whole molecule. Peak E can be attributed to the bending vibration of $CH_3$ in the amine group. In the previous study, it was mentioned that the peaks centered at 748 $cm^{-1}$ and 1040 $cm^{-1}$ represented C-S and O-S bonds, and 1260 $cm^{-1}$ and 1440 $cm^{-1}$ corresponded to C-H stretch vibrations respectively. [3] From the knowledge gained from the calculated spectra and the results of mass spectroscopy, however, it can be said that the peaks at 748 $cm^{-1}$ and 1040 $cm^{-1}$ correspond to C-C or C-N stretching vibrations, and the peaks at 1260 $cm^{-1}$ and 1440 $cm^{-1}$ are for C-H bending vibrations.

### 4.2.8) XAS analysis

To investigate further details about the interaction between sulfur and $CTA^+$, XAS analysis was conducted. Figure 4-19 shows the S K-edge XAS data of $Na_2S_x$ solution and $Na_2S_x$ and CTAB mixture ($Na_2S_x$/CTAB) solutions. The spectra were collected with TFY mode. Judging from the shapes of the spectra, no self-absorption effect has been observed.

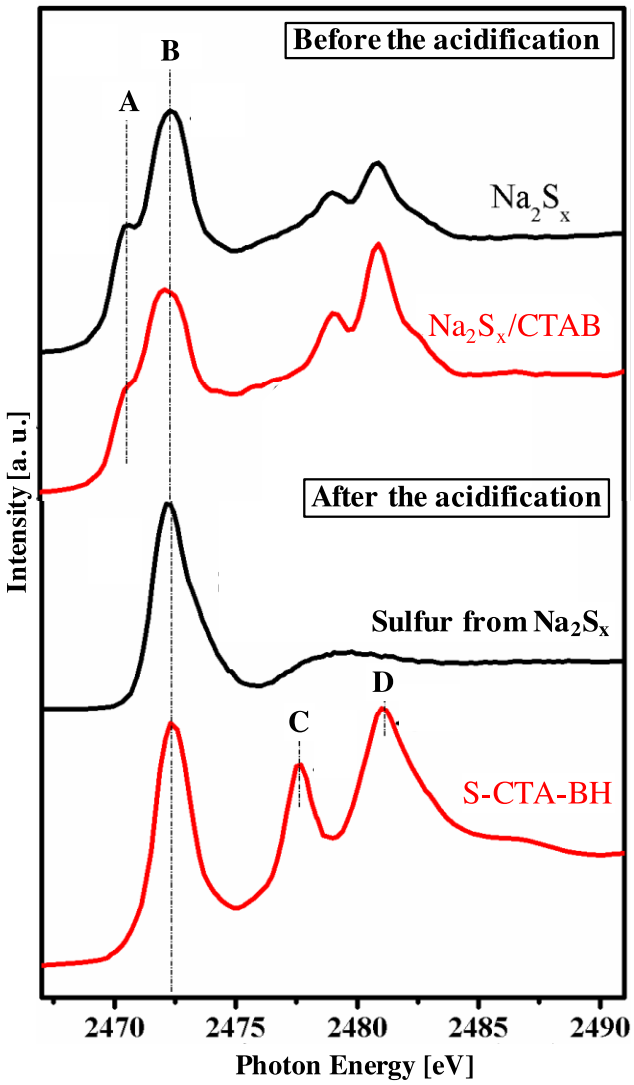


Figure 4-19. S K-edge XAS spectroscopy data of $Na_2S_x$ solution, $Na_2S_x$/CTAB mixture solution and the precipitates collected from the acidified $Na_2S_x$ solution and the $Na_2S_x$/CTAB solution labeled as S-CTA-BH.

Two peaks appeared at 2470.3 and 2472.2 eV close to the $S_8$ white line. These are labeled as Peak A and Peak B, respectively. The peaks in the energy range of 2468–2475 eV are features of the polysulfide chains. These are assigned to the transition from S 1s to the S−S π* states. [15-17] Specifically, peaks A and B arise from the differently coordinated S atoms in the polysulfide chains [18, 19]. A linear polysulfide chain, $S_x^{2-}$, is associated with each of the terminal S atoms with 1 $e^-$, and the internal S atoms formally uncharged. The accumulated electronic charge at the terminal S atoms red-shifts the absorption peak relative to the absorption peak of the internal S atoms [18]. Thus, Peak A and peak B are attributed to the terminal and internal S atoms, respectively. Figure 4-20 shows Peak A and Peak B together with the peak fittings and two Gaussian peaks after subtracting an arctangent edge jump.

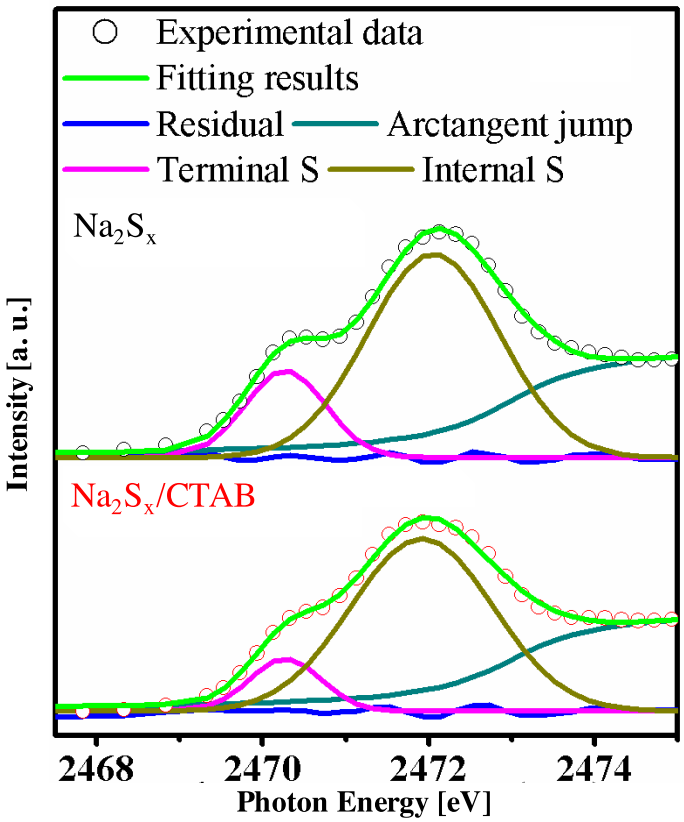


Figure 4-20. The peak fitting of the lower energy region of the spectra of $Na_2S_x$ solution and $Na_2S_x$/CTAB mixture solution.

Extracting from the fitting results shown in Figure 4-20, the ratio of the intensities of Peak A:Peak B, i.e. terminal S:internal S was determined. The peak intensities and the intensity ratio are summarized in Figure 4-21.

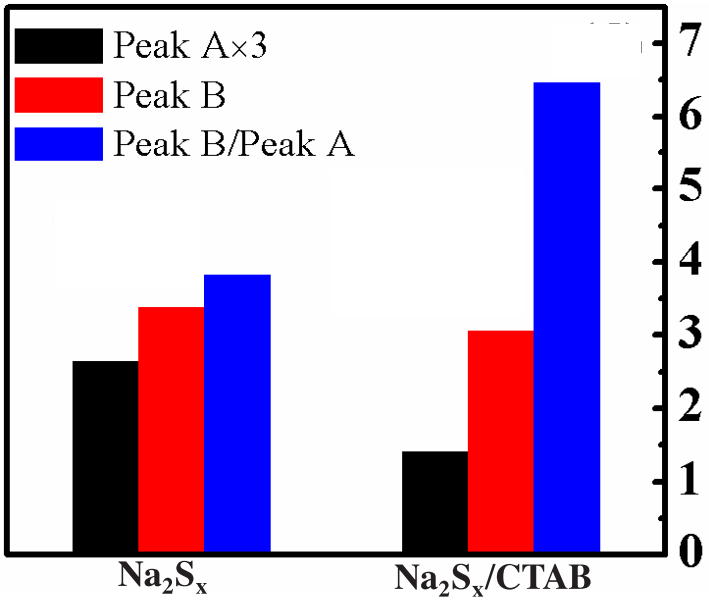


Figure 4-21. The intensities of Peak A and Peak B and the ratio of Peak B/Peak A.

Peak B/Peak A are 3.84 and 6.49 for the $Na_2S_x$ and $Na_2S_x$/CTAB solutions, respectively. In addition, a comparison of the spectra before and after introducing CTAB shows that the intensity of Peak A i.e. terminal S decreases up to 50% after introducing CTAB, while the intensity of Peak B i.e. internal S decreases just slightly to 90%. These results suggest that the terminal S was consumed by interacting with CTAB. Representing CTAB in solution as $CTA^+$ and $Br^-$, it can be proposed that $CTA^+$ attached to the terminal S atoms and influenced the accumulated charge on the terminal S atoms. Thus, it reduces the $S^-$ (ends) signal without much affecting the signal for the internal S.

Figure 4-19 shows the S K-edge XAS data of the samples obtained by the acidification of $Na_2S_x$ and $Na_2S_x$/CTAB i.e. synthesized sulfur and S-CTA-BH. The spectra were collected with TEY mode. Disappearance of Peak A is observed on both samples. This is

reasonable considering the reaction that the terminal S reacted with acid and evaporated as $H_2S$. On the other hand, two new peaks appeared at 2477.6 eV and 2481.1 eV only for S-CTA-BH. These are labeled as Peak C and Peak D respectively. These peaks have not been reported previously. It was further investigated by synthesizing and comparing the model samples S-GO-CTA-BH, S2-GO-CTA-BH, and S/CTA-GO-BH. S2-GO-CTA-BH was synthesized by using $Na_2S_x$ solution prepared decreasing the amount of $Na_2S$ by 10%. S/CTA-GO-BH was fabricated by adding CTAB to $Na_2S_x$ solution in advance of mixing with GO. The S K-edge spectra of samples S-GO-CTA-BH, S2-GO-CTA-BH and S/CTA-GO-BH are shown in Figure 4-22 on the left. The strong peak at 2472.2 eV which is identified as Peak B is observed for all the three samples, while corresponding peaks to Peak A did not appear. It shows the fact that elemental sulfur is the main component in the samples and there are no terminal S atoms. At the same time, two peaks appeared as the same position as Peak C and Peak D. Comparing the intensities of peaks B, C, and D, it is noticed that the intensity of peak B increased in the sequence of S-CTA-BH → S/CTA-GO-BH → S-GO-CTA-BH → S2-GO-CTA. On the contrary, the intensities of Peak C and D behave oppositely.

To investigate the effect of the heat treatment on the chemical interactions, S K-edge XAS spectra of the post heating samples have been recorded as shown in Figure 4-22 on the right. In comparison with the spectra on the left, significant changes are observed. A newly formed peak, labeled as peak E, centered at 2473.6 eV is evident. Peak E represents the transition from S 1s to the C−S σ* state. [4, 15] The appearance of this peak corresponds to the production of $Me_2S_x$, S-CDMA-1and S-CDMA-2 during the heat treatment. The spectrum of S/CTA-GO shows the strongest intensity of Peak E, while that of the S2-GO-CTA shows the weakest. Meanwhile, accompanying the appearance of Peak E, Peak C and D vanished during the heat treatment process.

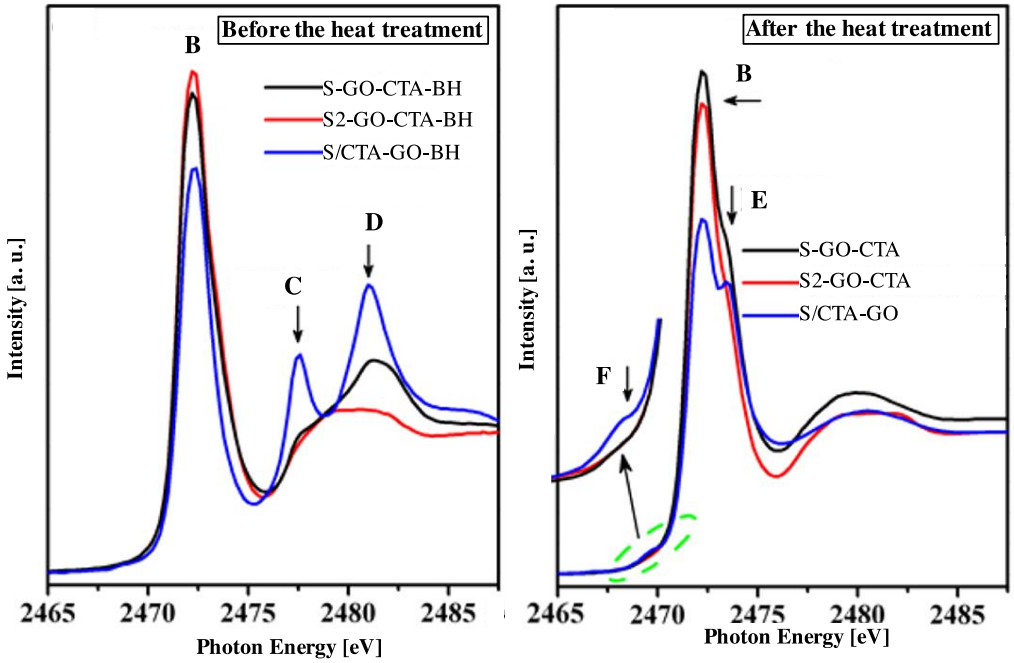


Figure 4-22. S K-edge XAS data of samples S-GO-CTA-BH, S2-GO-CTA-BH and S/CTA-GO-BH before the heat treatment on the left, S-GO-CTA, S2-GO-CTA and S/CTA-GO after the heat treatment on the right.

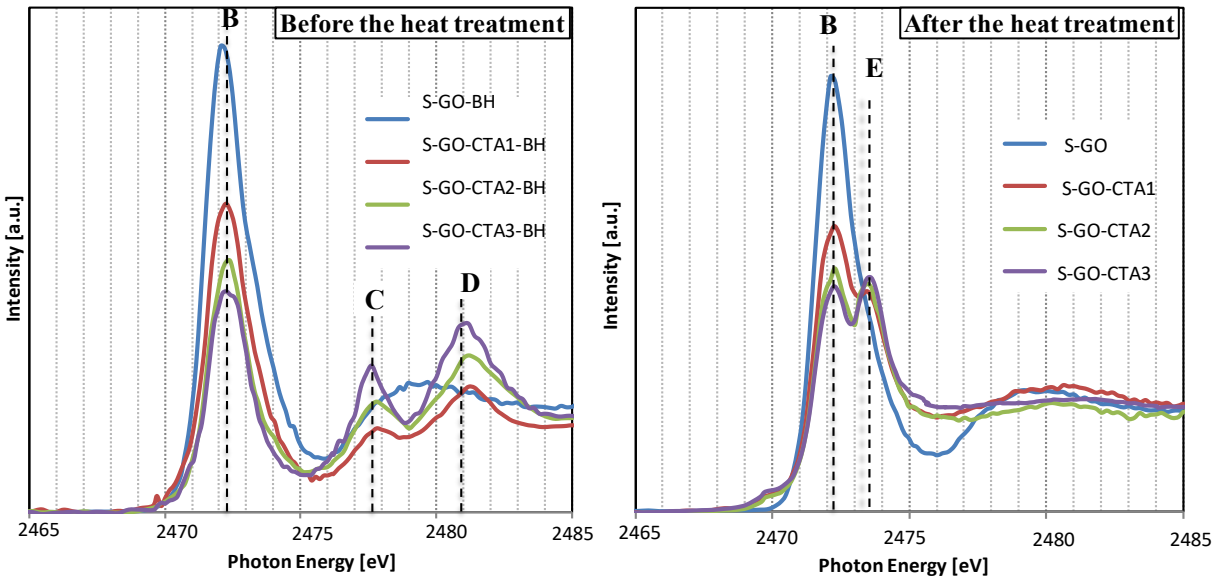


Figure 4-23. XAS spectra of S-GO-CTA composite having different amount of CTAB before the heat treatment (on the left) and after the heat treatment (on the right).

S K-edge XAS spectra of S-GO-CTA having different amount of CTAB are shown in Figure 4-23. It shows a decrease of Peak B and an increase of intensity of Peak C and Peak D for the samples before the heat treatment. An increase of Peak E attributed to C-S bonds for the samples after the heat treatment is seen as the amount of CTAB increases.

Summarizing these results, the species for Peak C and D were produced by consuming sulfur represented by Peak B. Then the species for Peak C and D formed the new species having C-S bonds showing Peak E after the heat treatment. Those reactions involved the interactions between sulfur and CTAB. Considering the sequence of the samples with regards to the intensity of those peaks, the interaction between sulfur and CTAB is more when CTAB is mixed with $Na_2S_x$ without GO, and less when the terminal S is less. It is suggested that the species for Peak C and D are the precursor for the further reaction products of sulfur and $CTA^+$ during the heat treatment. This assumption corresponds with the results from NMR analysis as shown in Figure 4-7.

Moreover, some detailed information can be noted as follows. The shoulder of Peak B is observed for the samples before the heat treatment at around 2473 eV in Figure 4-22. The shoulder is weaker for S/CTA-GO-BH compared to that for S-GO-CTA-BH and S2-GO-CTA-BH. The previous calculations show that this shoulder appears when the sulfur exist as rings. The internal atoms of liner chain of sulfur do not show the shoulder. [20] Thus, the weaker shoulder in S/CTA-GO-BH suggests that the sulfur atoms were more likely to be presented as liner chains in S/CTA-GO-BH, while more ring-structure $S_8$ existed in S-GO-CTA-BH and S2-GO-CTA-BH. This means that the sulfur in the precursor can be as liner chains.

Second, a 0.15 eV blue shift of peak B is observed for the S/CTA-GO-BH sample relative to the S-GO-CTA-BH and S2-GO-CTA-BH samples in Figure 4-22. It can be attributed to the charge transfer from S atoms to CTA. The charge transfer may not be

strong enough to change the valence states of S from a spectroscopic point of view. Instead, it can cause the blue shift of the peak B. The peak shift is not observed for S/CTA-GO after the heat treatment. This is due to the fact that the aforementioned charge transfer effect vanishes when the sample was heat-treated, where the mild interaction was converted to strong C−S chemical bonding.

Besides, a small shoulder, labeled as peak F, located at 2470.0 eV is visible in the spectra in Figure 4-22. The pre-edge region is enlarged for better clarity, as shown in the inset. Although the origin of peak F is still under discussion, [4] it may be due to the hybridization of S orbitals in S-CDMA-2.

A graphical summary of the reactions taking place during the heat treatment is shown in Figure 4-24.

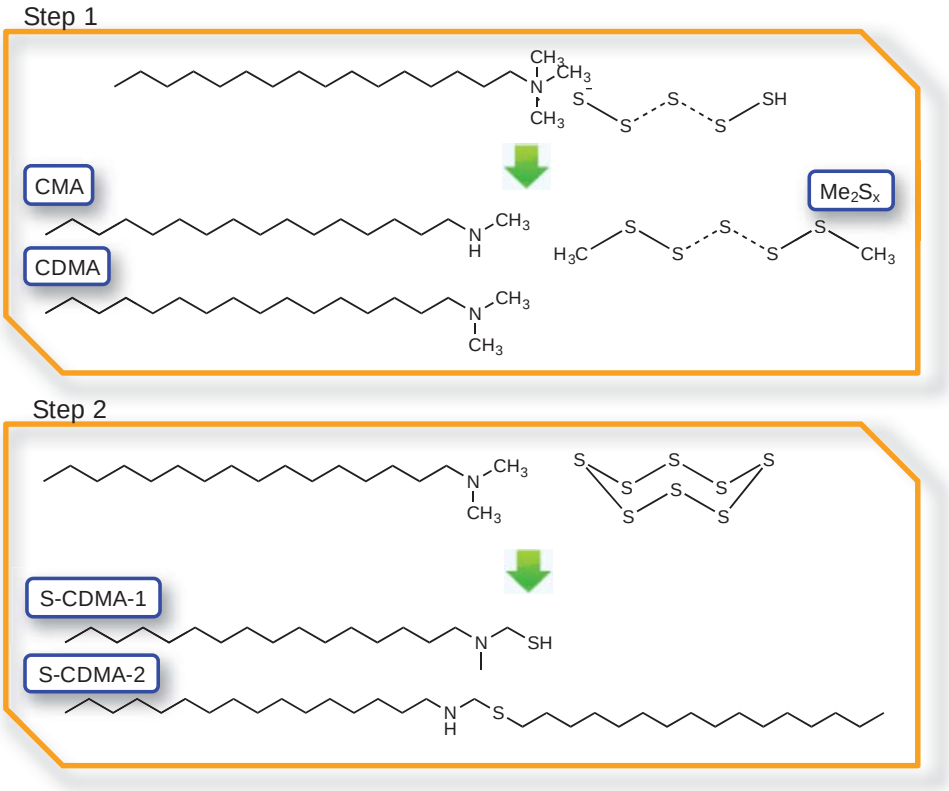


Figure 4-24. A graphical summary of the reactions taking place during the heat treatment.

### 4.2.9) SEM observation

The morphologies of S-GO, S-GO-CTA0.625, S-GO-CTA1.25 and S-GO-CTA2.5 were investigated. The SEM images are shown in Figure 4-25.

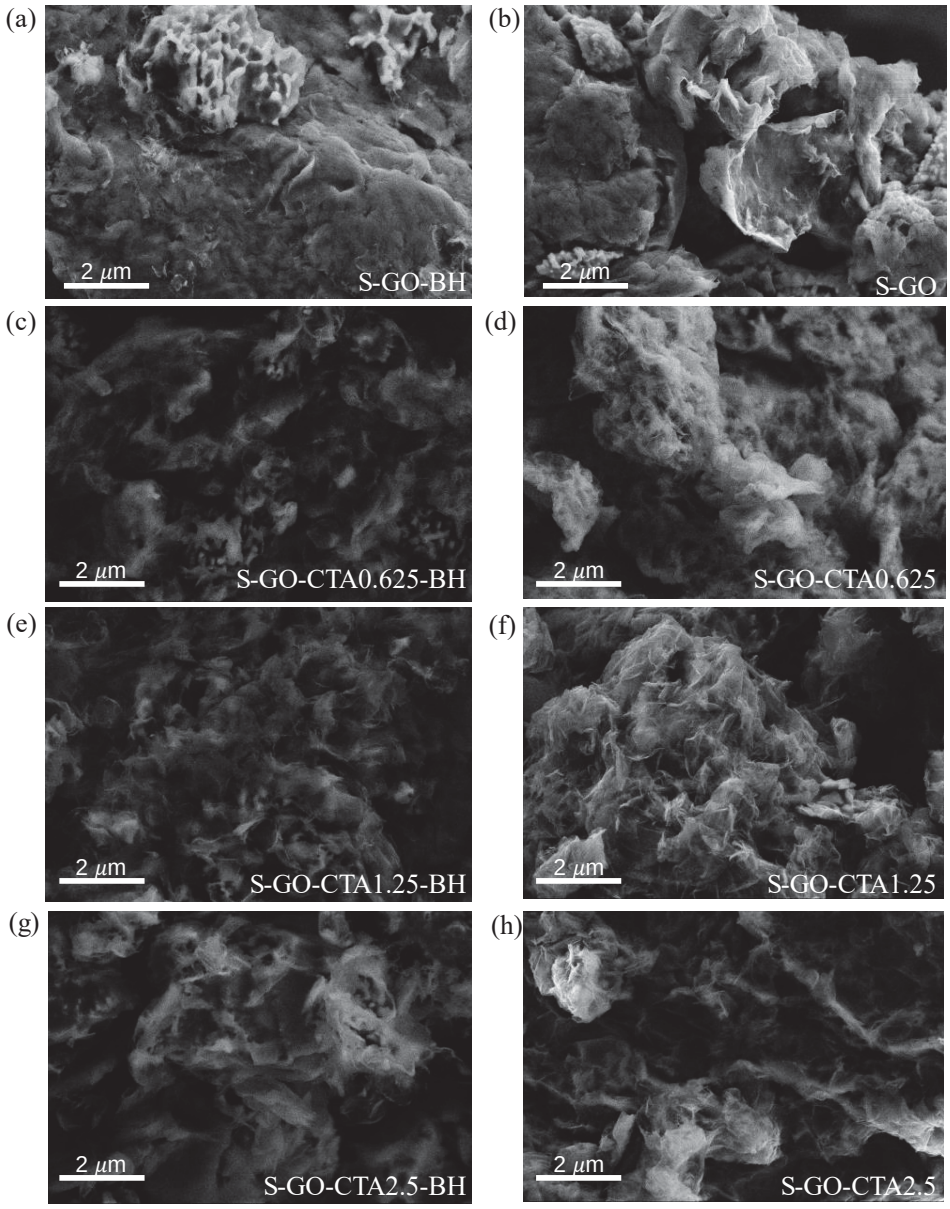


Figure 4-25. SEM images of S-GO-CTA composites having different amount of CTAB before and after the heat treatment.

As the amount of CTAB increased, the surface morphology of the materials become flaky structure, while bulky morphology is observed in S-GO. Comparing the morphologies before and after the heat treatment, the main features of the morphologies are maintained. This means that the morphologies of the composites are largely determined by the process before the heat treatment by the effect of CTAB. When attentions are focused on the morphology before the heat treatment, among the GO flakes, morphology like that of a honey comb can be seen. These are the sulfur particles of which the surface was damaged by the electron beam of the SEM as aforementioned in Chapter 3. Just what is noticed about the difference before and after the heat treatment is that the sulfur parts were not fragile against the electron beam for SEM observation after the heat treatment anymore. This is supposed that Phase X protected the sulfur against the electron beam. Thus, this result supports that Phase X was created on the surface of sulfur particles.

### 4.2.10) Electrochemical Test

To make clear the effects of Phase X in the materials on the electrochemical performance, cell tests were conducted using the materials with different amounts of CTAB and without CTAB. These samples were controlled to have the same sulfur content. Voltage profiles of S-GO, S-GO-CTA2.5, S-GO-CTA1.25 and S-GO-CTA0.625 in the 10th cycle at a C rate of 0.2 for discharge are shown in Figure 4-26. As shown in Figure 4-5, the content of Phase X in S-GO-CTA3 is almost 10%, which is so much that it sacrifices the sulfur content in the cathode resulting low energy density. Therefore, S-GO-CTA2.5 was compared as a cathode material as having the highest concentration of CTAB. It is noticeable that although the capacities of the first plateau are almost the same in all of them, the capacities corresponding to the second plateau shows differences among the materials. S-GO-CTA2.5 shows highest capacity and the capacity in the second plateau decreases as the amount of CTAB decreased. S-GO showed the least capacity among them. The reactions in the second plateau involve mainly reduction of $Li_2S_3$ to $Li_2S_2$ and $Li_2S$ as revealed in Chapter 2. [21]

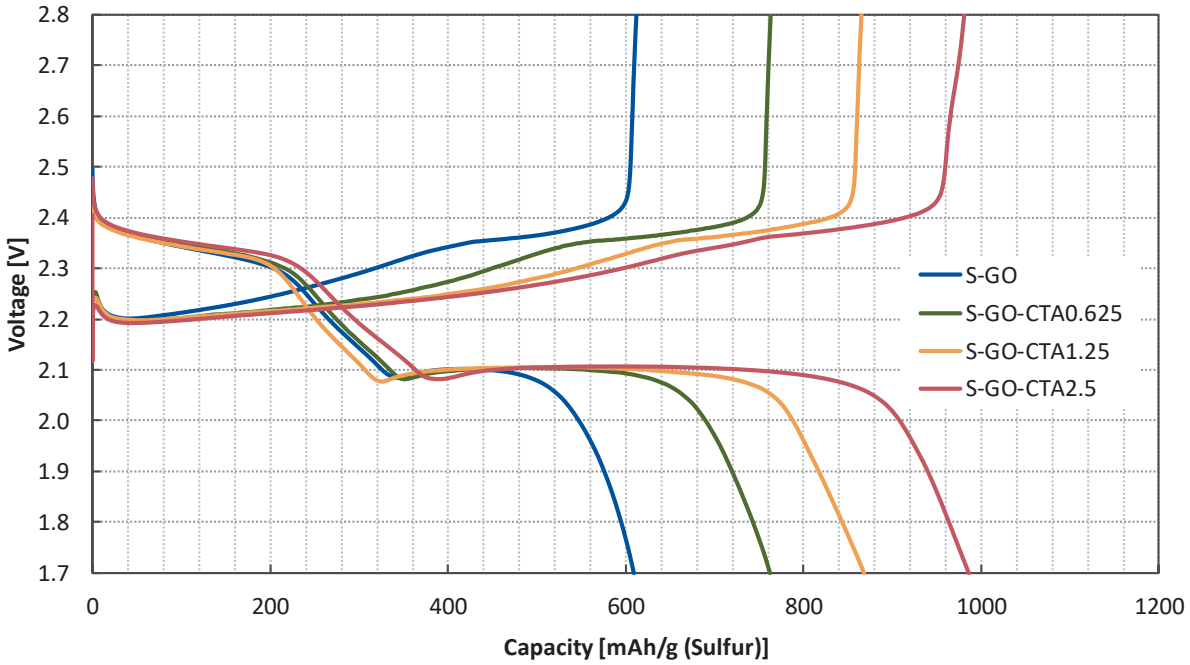


Figure 4-26. Voltage profiles of S-GO, S-GO-CTA0.625, S-GO-CTA1.25 and S-GO-CTA2.5 in the tenth cycle at a C rate of 0.2 for discharge.

Since the solubility of $Li_2S$ is quite low, solid $Li_2S$ deposits on the cathode during the discharge. The difference of the capacity in the second plateau among the materials having different amounts of CTAB suggests that Phase X encourages the uniform production of $Li_2S$ on the surface of GO by interacting with $Li_2S$.

Figure 4-27 shows the initial 10 cycles and the following rate capability tests and cycling tests. The capacity decreases from first cycle to 4th cycle and increases from 5th cycle to 10th cycle in S-GO- CTA2.5, S-GO-CTA1.25 and S-GO-CTA0.625. This phenomenon is considered to appear because the surface of the materials become wet more by the electrolyte solution after fifth cycle, while the amount of active sulfur is lost gradually. By considering that the phenomenon is more significant when CTAB concentration is high and it did not appear in S-GO, Phase X took more time to be wet than sulfur. This is understandable considering the result that Phase X has long hydrocarbon

chains. This suggest that the hydrocarbon part of Phase X is intimate with the carbon matrices. At the same time, Phase X has sulfide linkage which is expect to be intimate with $Li_2S$. Considering the enhancement of capacity in the second plateau of the cell having more Phase X, it is predictable that the layer of Phase X on the surface of the material provides sites for continuous $Li_2S$ formation by the intimate contact both to the electronic conductive carbon matrices and $Li_2S$ utilizing the hydrocarbon chain and the sulfide in Phase X which have affinity with carbon and sulfide respectively. This can prevent significant agglomeration of $Li_2S$ which can induce premature blocking of further conversion of polysulfide to $Li_2S$. Another possibility is that Phase X enhances the wettability of $Li_2S$ by the electrolyte solution so that the $Li_2S$ does not agglomerate. On the other hand, when there is no CTAB, $Li_2S$ deposits inhomogeneously or agglomerates. Then further reaction of polysulfide to form $Li_2S$ might be blocked due to a lack of electronic conductivity. It can be assumed that the cross-linked long molecule structure of S-CDMA-2 stabilizes the effects of Phase X as a facilitator of polysulfide reactions at the interface.

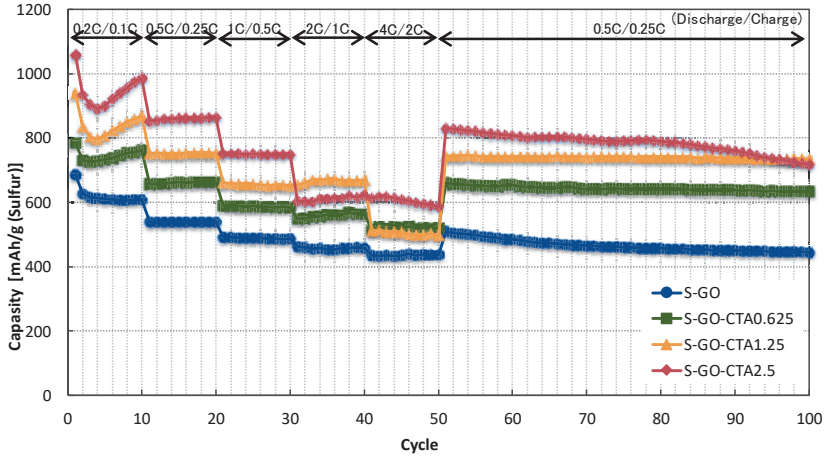


Figure 4-27. The results of rate capability tests of S-GO, S-GO-CTA0.625, S-GO-CTA1.25 and S-GO-CTA2.5.

As for the rate capability shown in Figure 4-27, all of the materials show high rate capability. The materials maintain the capacities in the same order of the amount of CTAB

except in 2C discharge and 4C discharge for S-GO-CTA1.25. The voltage profiles at different C rate for S-GO-CTA2.5, S-GO-CTA1.25, S-GO-CTA0.625 and S-GO are shown in Figure 4-28. The overvoltage becomes bigger in the same order with C rate in S-GO-CTA1.25, although the overvoltages are similar with those of S-GO-CTA0.625. These rate capability results suggest that Phase X does not contribute to the rate capability significantly because the materials having CTAB do not show a big advantage compared to S-GO without CTAB. Figure 4-28 shows the voltage profiles of S-GO-CTA2.5 at different C rates. The capacity loss induced by high C rates is caused by the capacity loss in both the first plateau and the second plateau.

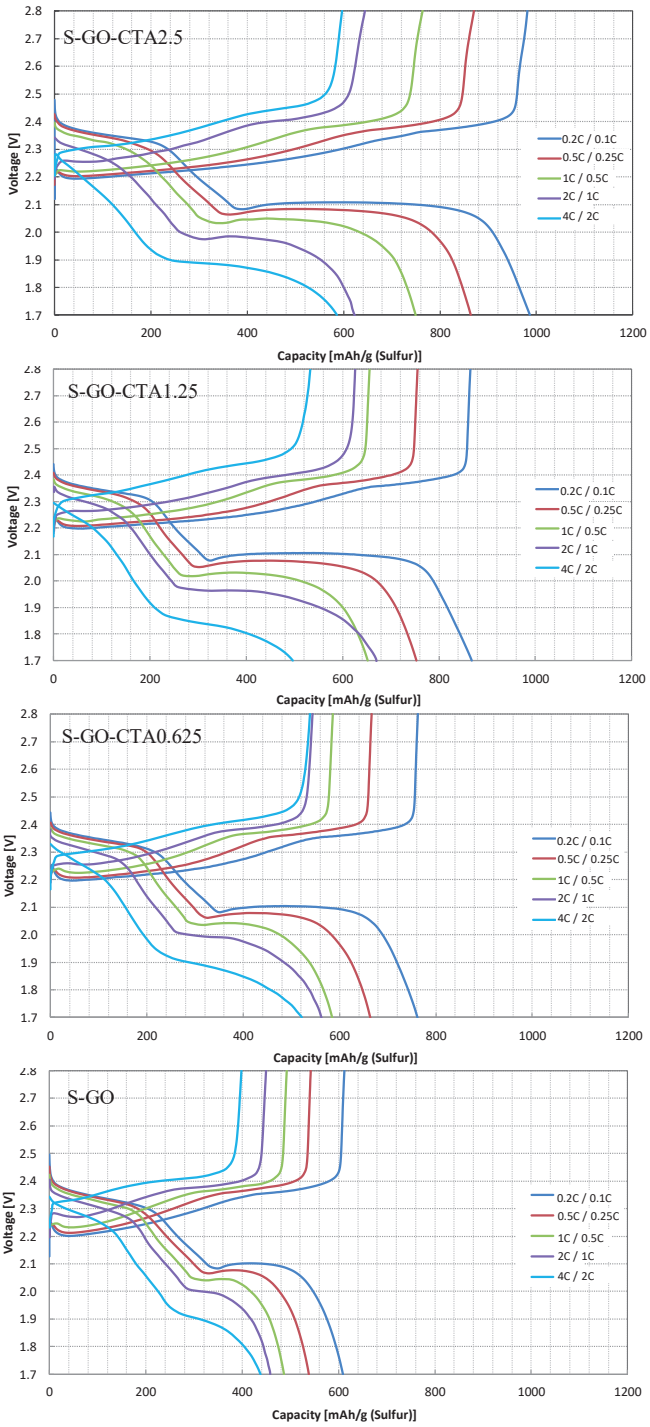


Figure 4-28. Voltage profiles of S-GO-CTA2.5, S-GO-CTA1.25, S-GO-CTA0.625 and S-GO at different C rates. The C rates for discharge and charge are indicated on left side and right side of the slash respectively.

As suggested in Figure 4-26, the advantage of having CTAB in the material is the capacity increase in the second plateau. Considering these results, the rate capabilities are apparently influenced by different factors than $Li_2S$ distribution for example ion conductivity. Then the similar performance at 4C discharge in S-GO-CTA1.25 and S-GO-CTA0.625 can be caused by the ion conductivity. The ion conductivity and the wettability of Phase X will be investigated in other studies.

## 4.3) Summary

The chemical reactions taking place during the synthesis process of S-GO-CTA and the key components for enhancing the capacity of cells using S-GO-CTA as a cathode material has been successfully identified. The CTAB added in the synthesis procedure of S-GO-CTA reacts with polysulfide composites during the 155 °C heat treatment and produces $Me_2S_x$, CA, CMA and CDMA. Furthermore, CDMA reacts with sulfur and creates S-CDMA-1 and S-CDMA-2 composing new stable materials, Phase X. The newly produced Phase X by the reaction of CTAB during the synthesis apparently worked as a promoter of the conversion reaction from polysulfide to $Li_2S$. Considering these effects of CTAB on the capacity enhancement, CTAB worked as both surfactant and the precursor of the functional layer. These new findings can be applied for various sulfur-carbon composites for cathode materials in sulfur cells. These findings can be applied to the control of the scaled-up production of the materials.

## 4.4) Experimental section

### 4.4.1) Synthesis

The same method was used to synthesize all of the samples: 0.29 g sodium sulfide ($Na_2S$, anhydrous, Alfa Aesar) was dissolved in 12.5 mL distilled water to form a $Na_2S$ solution. 0.36 g elemental sulfur (99.5%, Alfa Aesar) was dissolved in the $Na_2S$ solution to form a sodium polysulfide ($Na_2S_x$) solution after stirring for 4 hours at 70 °C. 12 ml GO-water dispersion (4 mg/mL, Graphenea) was diluted by water to form 75 ml of suspension

and sonicated for 1.5 hours. 82 mg CTAB (2.5 mM in the GO suspension, Sigma Aldrich) was dissolved in 3 mL water and added to the GO suspension drop-wise and stirred for 30 minutes and sonicated for 1 hour. Then, the $Na_2S_x$ solution was added to the as-prepared GO-CTAB suspension drop-wise. The $Na_2S_x$-GO-CTAB mixture was stirred for 16 hours. Finally, the mixture was slowly added to 50 mL of 2 M formic acid solution (Aldrich) and the mixture was stirred for 3 hours, filtered, and washed with acetone and water. After drying at 45 °C in a vacuum oven for 12 hours, the sample was heated (heat treatment) in a tube furnace at 155 °C for 18 hours under the flow of Ar with a flow rate of 100 cc/min.

The same procedure was performed to obtain S-GO composites containing different amounts of CTAB by changing the concentration of CTAB in the GO-CTAB suspension.

The obtained samples are labeled as listed in Table 4-1. The material labeled as S-CTA was synthesized using the same procedure by using only a CTAB solution instead of a GO-CTAB suspension. S2-GO-CTA was fabricated by decreasing the amount of $Na_2S$ by 10% in the $Na_2S_x$ solution. S/CTA-GO was fabricated by adding CTAB to $Na_2S_x$ solution before mixing with GO. Samples of the materials before the heat treatment are noted as –BH at the end of the sample label. The reference materials with amine species labeled as S-CA, S-CMA and S-CDMA were prepared by mixing sulfur and cetylamine (CA, $C_{16}H_{33}NH_2$), cetylmethylamine (CMA, $C_{16}H_{33}(CH_3)NH$) and cetyldimethylamine (CDMA, $C_{16}H_{33}(CH_3)_2NH$), and heat treated under the same conditions as the S-GO composites. The other reference materials labeled as S-GO-CA, S-GO-CMA and S-GO-CDMA were prepared by mixing S-GO and the amines and heat treated under the same conditions as the S-GO composites.

Dimethyl polysulfide ($Me_2S_x$) samples were synthesized as in the literature. [10] 25 ml $Na_2S_x$ aqueous solution was prepared using the same procedure as in the method for preparing the S-GO composite. The obtained solution was added into a mixture of methanol (35 mL) and methyl iodide (5 mL). The mixture reacted for 30 min at room

temperature. Methanol and any remaining methyl iodide were evaporated under vacuum at 70 °C. Then water (25 mL) and dichloromethane (25 mL) were added and the organic layer was separated. Dichloromethane was evaporated under vacuum from the separated organic layer. The remaining yellow oily liquid was used as the reference material. Hydrogen polysulfides ($H_2S_x$) were synthesized according to reference. [22] 7 mL of sodium polysulfide solution was prepared using the same method as for the synthesis of the S-GO composite. The polysulfide solutions were slowly added into 30 mL of 6 M hydrochloric acid while stirring. After cooling the reaction mixture at 4 °C, the separated yellow oil was dissolved in 6 mL of carbon disulfide. The carbon disulfide phase was separated and dried.

### 4.4.2) Material characterization

Thermogravimetric analysis (TGA, TA Instruments SDT Q600) was used to determine the content of sulfur and the newly formed phase. A heating rate of 10 °C/min was used under the flow of $N_2$ with a flow rate of 100 cc/min. To determine the contents of each component in the materials, the weights of each component were calculated using the weight of the powder before the heat treatment as a reference. The contents of GO were determined by the weight of the remaining material at 600 °C for the before heat treatment sample. The contents of sulfur and Phase X produced during the heat treatment were calculated using the method graphically explained in Fig. 3-4.

Raman spectroscopy (Horiba LabRAM ARAMIS) was used to investigate the interactions among GO, CTAB and sulfur. Mass spectroscopy was performed using a Fourier Transform Ion Cyclotron Mass Spectrometer coupled to a Linear Ion Trap (LTQ-FT) produced by Thermo Scientific. The solvent was a mixture of 20% dichloromethane and 80% acetonitrile with a flow rate of 5 μL/min.

For NMR measurements, samples were dissolved in deuterated chloroform and were analyzed using a Bruker Avance II900 MHz with TCI cryoprobe for 13C NMR, and a Bruker Avance 500 MHz for 1H NMR measurements.

X-ray diffraction (XRD) was conducted using Bruker AXS D8 Discover GADDS X-Ray Diffractometer equipped with a Vantec-500 area detector and was operated at 35 kV and 40 mA at a wavelength of Co Ka, 1.79A.

S K-edge X-ray absorption spectroscopy (XAS) was conducted on BL5.3.1, BL9.3.1 and BL10.3.2 at the Advanced Light Source (ALS), Lawrence Berkeley National Laboratory (LBNL). The samples were pressed onto indium foils for the XAS measurements. The solution samples were measured using a vacuum cell sealed with 100 nm $Si_3N_4$ window that allows nearly 100% transmission at the S K-edge. To eliminate the over-absorption effect, total electron yield (TEY) detection was used. The TEY signal was collected by monitoring the sample drain current. The energy ranges of the beamlines are from 2.4 keV to 12.5 keV, 2.4 keV to 5.0 keV and 2.1 keV to 17 keV, respectively. During the measurements, the energy scales for all XAS spectra were calibrated using elemental S spectra with a white line at 2472.20 eV.

SEM observation was conducted using Zeiss Gemini Ultra-55 Analytical Field Emission Scanning Electron Microscope. A secondary electron detector was used.

### 4.4.3) Theoretical calculation

The theoretical calculations were performed by preparing the models for $CTA^+$, CA, CMA and CDMA. The molecular geometries were first optimized and the Raman spectra were simulated for the geometries using density function theory (DFT) calculations. Each peak was represented by a Gaussian function with a maximum height proportional to the oscillator strength, using a full width at half maximum (FWHM) value of 5 $cm^{-1}$. The B3LYP exchange-correlation functional [23] was utilized for DFT and the 6-31+G (d) [24] basis sets were employed for the calculation. All calculations were performed using the Gaussian03 program. [25]

### 4.4.4) Electrochemical Characterization

The sulfur electrodes were fabricated by mixing the test materials, carbon black (Super C65) with a binder (SBR/CMC 1:1 by weight) at a weight ratio of 70:20:10 in isopropanol/water (1:3 by volume) solution to form a slurry. The resulting slurry was uniformly spread via a doctor blade onto pure aluminum foil. The solvent was allowed to evaporate at room temperature for 24 hours. The electrode was punched into circular pieces with a diameter of 12.7 mm for cell assembly. The electrodes were then dried in a vacuum oven at 50 °C for 24 hours to eliminate any solvent residue. The average sulfur loading of the electrodes was ~0.8mg/cm$^2$. For the electrolyte, 1 mol/kg lithium bis(trifluoromethylsulfonyl)imide (Sigma-Aldrich) in N-methyl-(N-butyl) pyrrolidinium bis(trifluoromethanesulfonyl)imide (Sigma-Aldrich) / 1,3-dioxolane / 1,2-dimethoxyethane mixture (2:3:3, by volume) was prepared and used for evaluation of the electrochemical performance. 0.5 mol/kg $LiNO_3$ was used as an additive in the electrolyte.

CR2325-type coin cells were assembled with a separator (Celgard 2400) between a lithium metal foil (99.98%, Cyprus Foote Mineral) and a sulfur electrode fabricated with the S-GO or S-GO-CTA active material in a glove box filled with argon gas. Galvanostatic discharge and charge testing of the coin cells was performed using a battery cycler (Maccor Series 4000) between 1.7V and 2.8V. The cell capacity was normalized by the weight of sulfur. All electrochemical characterizations were performed at 30 °C. Before all electrochemical characterizations, the cells were held at open circuit at 30 °C for 12 h.

## 4.5) References

[1] M.-K. Song, Y. Zhang and E. J. Cairns, *Nano Lett.* **2013**, *13*, (12), 5891.

[2] L. Ji, M. Rao, H. Zheng, L. Zhang, Y. Li, W. Duan, J. Guo, E. J. Cairns and Y. Zhang, *J. Am. Chem. Soc*. **2011**, *133*, (46), 18522.

[3] L. Zhang, L. Ji, P.-A. Glans, Y. Zhang, J. Zhu and J. Guo, *Phys. Chem. Chem. Phys.* **2012**, *14*, (39), 13670.

[4] X. Feng, M.-K. Song, W. C. Stolte, D. Gardenghi, D. Zhang, X. Sun, J. Zhu, E. J.

Cairns and J. Guo, *Phys. Chem. Chem. Phys.* **2014**, *16*, (32), 16931.

[5] Y. Ye, A. Kawase, M. Song, B. Feng, Y. Liu, M. A. Marcus, J. Feng, E. J. Cairns, J. Guo, J. Zhu, *Nanomaterials* **2016**, *6*, (14), doi:10.3390/nano6010014

[6] Y. Ye, A. Kawase, M. Song, B. Feng, Y. Liu, M. A. Marcus, J. Feng, H. Fang, E. J. Cairns, J. Guo, J. Zhu, *J. Phys. Chem. C* **2016**, *120*, 10111.

[7] A. Kawase, E. J. Cairns, *J. Mater. Chem. A,* **2017**, *5*, 23094

[8] J. Rong, M. Ge, X. Fang and C. Zhou, *Nano Lett.* **2014**, *14*, 473.

[9] M. Xiao, M. Huang, S. Zeng, D. Han, S. Wang, L. Sunb, Y. Meng, *RSC Adv.* **2013**, *3*, 4914-4916.

[10] D. Rizkov, O. Lev, J. Gun, B. Anisimov and I. Kuselman, *Accredit. Qual. Assur.* **2004**, *9*, 399.

[11] H. E. Gottlieb, V. Kotlyar, A. Nudelman, *J. Org. Chem.* **1997**, *62*, 7512.

[12] H. Schmidbaur, M. Schmidt and W. Siebert, *Chem. Ber.* **1964**, *97*, 3374.

[13] J. B. Hyne, E. Muller and T. K. Wiewiorowski, *J. Phys. Chem.* **1966**, *70*, (11), 3733.

[14] L. Huang, X. Chenb, Q. Lia, *J. Mater. Chem.* **2001**, *11*, 610- 615.

[15] F. Jalilehvand, *Chem. Soc. Rev.* **2006**, *35*, 1256−1268.

[16] H. Ota, T. Akai, H. Namita, S. Yamaguchi, M. Nomura, *J. Power Sources* **2003**, *119*, 567−571.

[17] A. Vairavamurthy, *Spectrochim. Acta, Part A* **1998**, *54*, 2009−2017.

[18] A. Braun, H. Wang, U. Bergmann, M. C. Tucker, W. Gu, S. P. Cramer, E. J. Cairns, *J. Power Sources* **2002**, *112*, 231−235.

[19] A. Braun, M. Janousch, J. Sfeir, J. Kiviaho, M. Noponen, F. E. Huggins, M. J. Smith, R. Steinberger-Wilckens, P. Holtappels, T. Graule, *J. Power Sources* **2008**, *183*, 564−570.

[20] T. A. Pascal, K. H. Wujcik, J. Velasco-Velez, C. Wu, A. A. Teran, M. Kapilashrami, J. Cabana, J. Guo, M. Salmeron, N. Balsara, et al. *J. Phys. Chem. Lett.* **2014**, *5*, 1547−1551.

[21] A. Kawase, S. Shirai, Y. Yamoto, R. Arakawa, T. Takata, *Phys. Chem. Chem. Phys.*

**2014**, *16*, (20), 9344

[22] E. Muller and J. B. Hyne, *Can. J. Chem.* **1968**, *46*, 2341.

[23] A. D. Becke, *J. Chem. Phys.*, **1993**, *98*, 5648; C. Lee, W. Yang and R. G. Parr, *Phys. Rev. B,* **1988**, *37*, 785.

[24] W. J. Hehre, R. Ditchfield and J. A. Pople, *J. Chem. Phys.,* **1972**, *56*, 2257; J. D. Dill and J.A. Pople, *J. Chem. Phys.*, **1975**, *62*, 2921; M.M. Francl, W. J. Pietro, W. J. Hehre, J. S. Binkley, M. S. Gordon, D. J. DeFrees and J. A. Pople, *J. Chem. Phys.,* **1982**, *77*, 3654.

[25] M. J. Frisch, et al., *Gaussian 03, Revision E.01* (Gaussian Inc., Wallingford, CT, 2004).

# CHAPTER 5

## Electrostatic polysulfides confinement to inhibit redox shuttle process in the lithium/sulfur batteries

## 5.1) Introduction

A binder has been considered as a component which keep the sulfur material and the carbon additive physically fixed to the current collector. For this purpose, polymeric materials are used as binders. Poly (ethylene-oxide), poly(tetrafluoro-etylene), poly(vinylidene fluoride), poly(vinyl pyrrolidone) and styrene-butadiene rubbers have been used in many research. Since divinyloxyhydroxyolysulphides was first developed by T. A. Skotheim et al. as an alternative binder to trap the polysulfide species to alleviate the redox shuttle phenomenon, [1] polymer including gelatin, polyacrylic acid, carboxyl methyl cellulose, gum Arabic, carbonyl-**β**-cyclodextrin, polyamidoamine dendrimer [2], polyacrylonitrile [3-5], polyfluorene derived polymers have been studied as promising binders to alleviate the polysulfide shuttle problem. The functional groups in binders are effective to immobilize the soluble lithium polysulfide through C−S, N−Li, or O−Li bonds. The polar amino groups were also investigated and reported to effectively reduce the polysulfide dissolution. [6]

Polyquaternium (PQ) is one of the typical cationic polymers which are commercially available and widely used in the personal care products. The most significant feature of PQ is the presence of quaternary ammonium cations in the polymer. Quaternary ammoniums can attract and immobilize the negative charges, such as $S_x^{2-}$ through electrostatic force with the positive charge on the nitrogen atom. If the PQ polymer is fixed in the electrode as a binder with carbon black, the attracted polysulfides ($S_x^{2-}$) to the quaternary ammoniums are immobilized and confined with the polymer. The confinement mechanism is graphically illustrated in Figure 5-1. The elemental sulfur form soluble polysulfide during initial discharge process. The negatively charged polysufide can be electrostatically absorbed by the quaternary ammonium cations on the PQ polymer binder. The electrostatic absorption alleviates the polysulfide diffusion into electrolyte and reduces the shuttle constant.

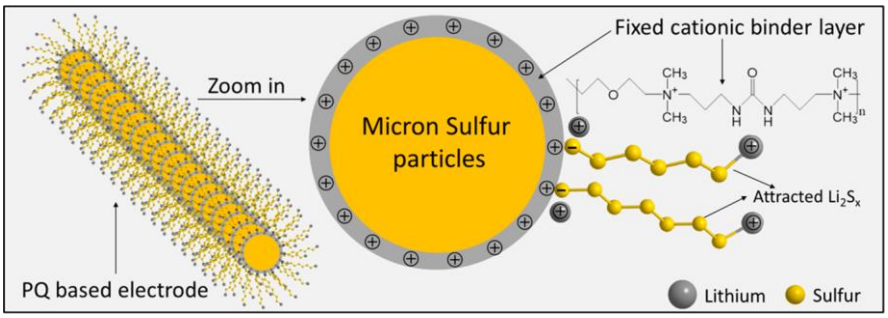


Figure 5-1. Polysulfides confinement through cationic polymer. The electrostatic attraction between the PQ quaternary ammonium cations and polysulfide anions.

## 5.2) Results and Discussion

### 5.2.1) Theoretical calculation

The electrostatic interaction with different ion species was simulated with density functional theory (DFT) prior to the electrochemical test. $Li_2S_6$ was used as a predominant polysulfide species in the simulation because of its high solubility in the electrolyte. [7] All the anions in the system, including bis-trifluoromethanesulfonimide anion (TFSI), are quantified through the simulation. The adsorption energy for 1,3-dioxolane (DOL)-$Li_2S_6$ and 1,2- dimethoxyethane (DME)-$Li_2S_6$ were 0.79 and 0.77 eV, respectively. The binding energy of PQ-TFSI anchoring system was 0.94 eV, which was higher than that of DOL-$Li_2S_6$ and DME-$Li_2S_6$. The binding energy for PQ-$Li_2S_6$ was 1.89 eV, which was the highest among the interactions calculated in this study. Although the adsorption energy of PQ-$Li_2S_6$ was the highest among all other absorption-based interactions calculated in the system, it was lower than the covalent bonding energy. The absorption binding energy between the polysulfides and various binders depends on the functional groups on the polymer backbone. The values of absorption binding energy for polysulfide and various functional groups of ester, ketone, amide, imine, ether, nitrile, fluoroalkane, chloroalkane, bromoalkane, alkane are 1.10, 0.96, 0.95, 0.88, 0.71, 0.60, 0.40, 0.26, 0.23, and 0.23 eV,

respectively. The calculation result of binding energy between ammonium cations and polysulfide is much higher than those for other functional groups reported in the literature.[8]

### 5.2.2) UV-vis spectroscopy

Besides the theoretical calculation, the binding capability was evaluated through in-situ Ultraviolet−visible spectroscopy (UV-vis). [9] The characterization was focused on PQ with quaternary ammonium groups, which was different from the chemically inert binders (i.e., PVDF). The 0.1 g of PQ polymer was soaked in 1 mL of electrolyte sample solution consisting of 1 M Bis(trifluoromethane) sulfonimide lithium salt (LiTFSI) in DOL/DME (1/1 vol) with existence of 3 mM lithium polysulfide (average formula $Li_2S_6$) for 22 h to track the polysulfide concentration evolution. In the in-situ UV-vis spectra shown in Figure 5-2, a significant absorption peak was observed at 427 nm. This absorption feature is attributed to adsorption by polysulfide. [10] A significant decrease of the absorbance at 427 nm was recorded for the solution with PQ polymer. The decrease of absorption is due to the concentration decrease of polysulfide in the solution, caused by the electrostatic attraction of polysulfide by PQ into solid polymer phase. In contrast, the absorption signals for polysulfide solution with PVDF stay at the original level during the exposure time, indicating no adsorption of polysulfide to PVDF.

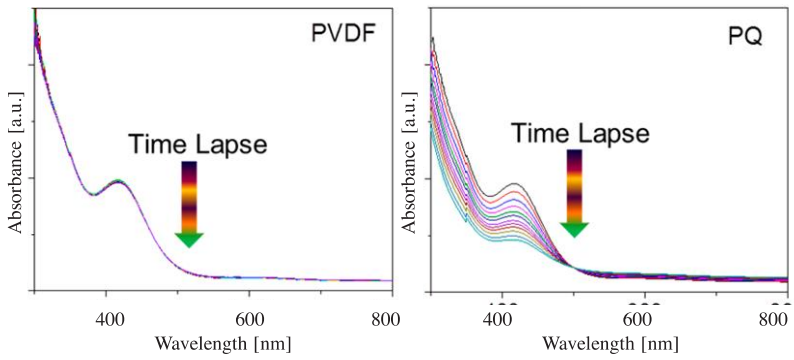


Figure 5-2. In situ UV−vis full spectra for PVDF (left) and PQ (right) in 3 mmol/L lithium polysulfide in DOL/DME.

To further illustrate the adsorption intensity evolution, the intensities of the absorbance peaks are plotted versus time as shown in Figure 5-3 on the left. This was differentiated and plotted in Figure 5-3 on the right.

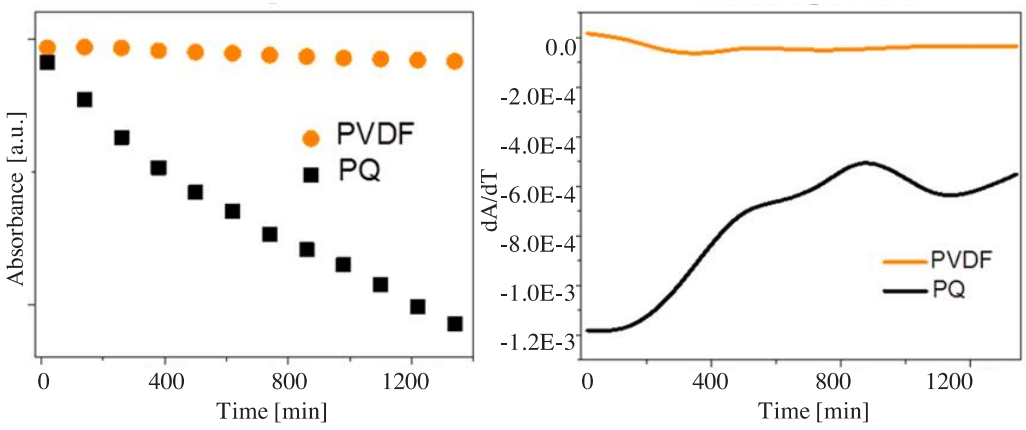


Figure 5-3. Absorption peak intensity change at 427 nm (left) and the calculated reaction kinetics (right) based on the UV−vis spectra.

PQ showed significant polysulfide capturing ability as shown in Figure 5-3 in the current experimental condition.

### 5.2.3) Electrochemical test

Regarding the calculations and UV−vis observation results, improved electrochemical performances are expected due to the electrostatic attraction. The electrochemical performances were all based on micron size sulfur particles and in high sulfur loading electrodes conditions. The electrodes are composed of 60 wt % micron size sulfur particles. The sulfur particle size varies from several microns to tens of microns as shown in Figure S5-1. The thermostability of PQ was compared with that of PVDF binder as shown in Figure S5-2. The water content in PQ binder is around 3 wt % from the isothermal test at 80 °C. The PQ polymer starts to decompose at around 150 °C during the temperature scan. It was confirmed that the thermal stability window of the PQ binder was well beyond the battery operational window. Galvanostatic studies were performed at a

constant current rate of 0.05C (based on sulfur mass in the electrode) and shown in Figure 5-4. A high initial areal capacity of 9.0 mAh/cm$^2$ was reached for PQ-based electrode, corresponding to a specific capacity of 1201.2 mAh/g. The sulfur utilization for the first cycle was 70.0% at the sulfur loading of 7.5 mg/cm$^2$. The capacity was stabilized at 885.1 mAh/g after 50 cycles.

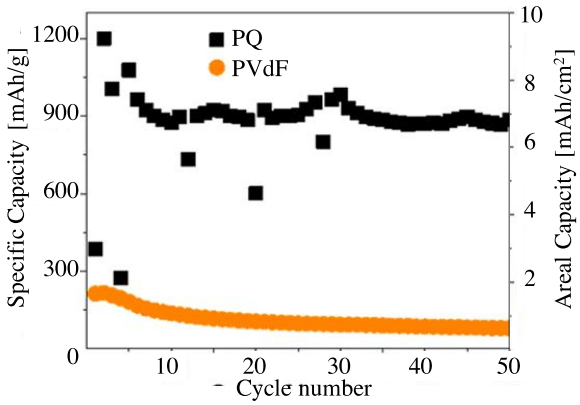


Figure 5-4. Cycling behavior of cathode using PQ polymer-based binder in contrast to conventional PVDF-based sulfur electrode.

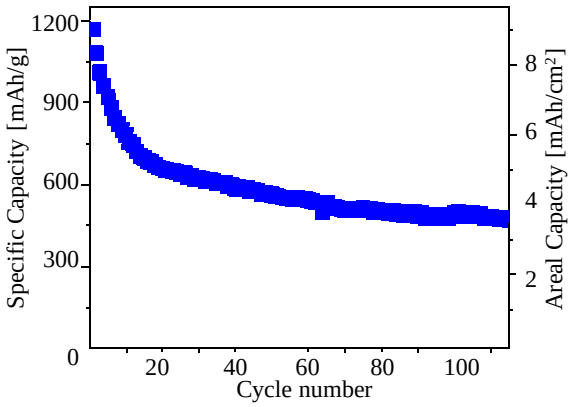


Figure 5-5. Cycling behavior of cathode using PQ polymer-based binder at C/3 rate.

The higher rate performance (C/3) at this loading (7.5 mg/cm$^2$) is plotted in Figure 5-5. The first two cycles are cycled at C/50. The initial specific and areal capacity was 1167.9 mAh/g and 8.8 mAh/cm$^2$ respectively. Good cycling stability was achieved for the thick

electrodes at C/3, with 40% capacity retention after more than 100 cycles.

For comparison, the PVDF-based high loading sulfur (7.5 mg/cm$^2$) electrode performance is also plotted in Figure 5-4. Because of the high loading and usage of micron size sulfur particles, the sulfur utilization was only 13% at the first cycle. And it drops down to 5% at the 30th cycle. The PVDF-binder-based sulfur electrode gave very poor cycling performance compared to the PQ-based binder for the high-loading electrode. Figure 5-6 shows voltage profile of PQ-based cell (left) and PVDF-based cell. It is observed that PQ-based electrodes exhibits well-defined two plateaus corresponding to the formation of soluble long chain polysulfides and their further dissociation into short chain polysulfides. In contrast, PVDF based electrode exhibits indistinguishable plateaus, which indicates disordered reaction process.

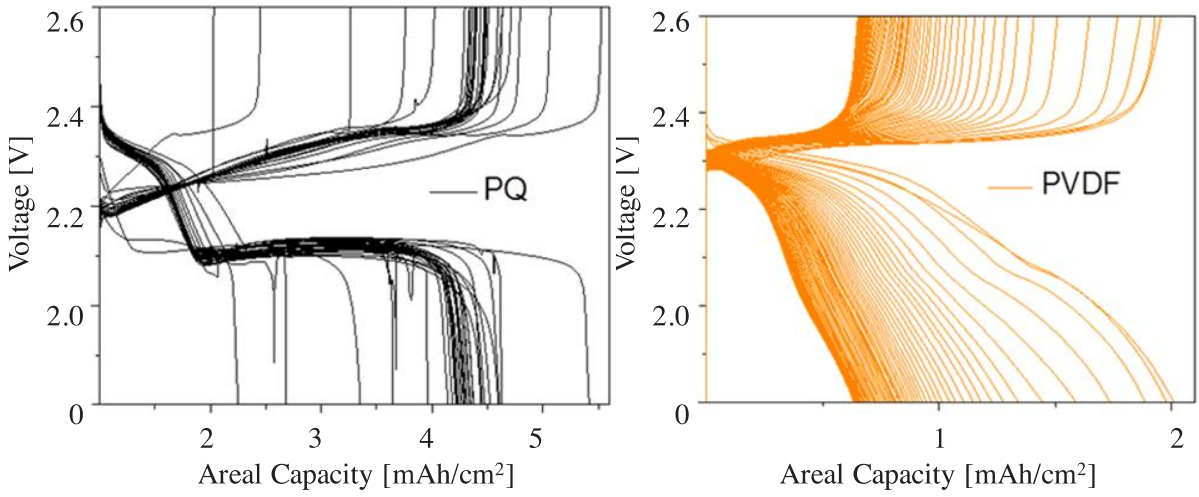


Figure 5-6. Voltage profiles for PQ-based (left) and PVDF-based (right) sulfur electrode.

### 5.2.4) Electrochemical analysis

To further analysis of the voltage profile, the shuttle factor is described in the equation

$$\frac{k_s q_H [S_{total}]}{I_d} = f_d$$

where $k_s$ is the shuttle constant, $q_H$ is the high plateau sulfur specific capacity, $[S_{total}]$ is the total sulfur concentration, $I_d$ is the delithiation current, $f_d$ is the delithiation-shuttle factor. [11] At $f_d < 1$, when the shuttle constant is low or the charge current is high enough, the cell can be fully delithiated i.e. charged, showing a sharp voltage increase. Rather, at $f_d > 1$, the cell never reaches complete delithiation and shows a voltage leveling. The larger the value of $f_d$, the lower the leveled voltage. The voltage profile in Figure 5-6 indicates an obvious sharp voltage increase in delithiation for PQ-based sulfur electrode. Hence, a low shuttle constant is assumed since the current is low, i.e. 0.05C. The PVDF-based sulfur electrodes showed only the higher voltage in the charge plateau. This indicates only long-chain polysulfides were involved in the charge process.

For the discharge profile, the experimental capacity for higher plateau $Q_L^H$ is not always equal to the accumulated capacity $Q_H^{acc}$. When the discharge process starts, two parallel paths exist for high polysulfide reduction: the first, simple electrochemical reduction due to the discharge current, and the second, reduction of polysulfides on the Li anode that depends on the shuttle constant.

$$Q_L^H = Q_H^{acc} \frac{\ln(1 + f_L)}{f_L}$$

where $f_L$ is the lithiation-shuttle factor. Analysis of the above equation shows that the capacity for higher plateau can reach its maximal value, which is equal to the lithiation

accumulated capacity, only when $f_L$ is close to zero. Experimentally, such conditions can be reached when the discharge current is high enough or at a low shuttle constant. In this study, the PQ-based sulfur electrodes were discharged at a very low current (0.05C) as shown in Figure 5-6 on the left. Hence, it can be said that a very low shuttle constant was achieved for the PQ-based sulfur cell, in stark contrast with the PVDF-based cell.

Thus, the immobilizing effect of PQ polymer in the cell was evaluated. The reason why the high sulfur utilization in the high sulfur loading electrode was achieved in the cell using PQ-based sulfur electrode can be explained from the point of this immobilizing effect. Although all the sulfur needs to access electron paths in order to achieve high sulfur utilization, it is difficult to distribute the carbon matrices in high sulfur loading electrodes. By immobilizing the produced polysulfide close to the carbon matrices thanks to PQ polymer having both quaternary ammoniums attracting polysulfide and hydrocarbon having a good contact with carbon, polysulfide was able to continue the electrochemical reactions resulting the big capacity in the second plateau. The absence of the lower plateau in the profile for PVDF-based electrode is due to the failure to immobilize high order lithium polysulfides on the sulfur electrode. Accordingly, the further reduction to lower order polysulfides could not be realized. It is also worth noticing that the voltage spikes are observed in Figure 5-6. These are caused by the growth of lithium dendrites on the surface of lithium foil due to the large amount of lithium being cycled, i.e. high lithium utilization. [12] The Coulombic efficiency for both sample electrodes are shown in Figure 5-7. In the first three cycles of PVDF-based electrode, the lithiation caused the dissolution of long chain polysulfide. Upon charging the dissolved polysulfides in the subsequent charge process, it leads to erratic Coulombic efficiency higher than 100%. In contrast, the initial Coulombic efficiency is 97.5% for the PQ-based electrode, and 98% efficiency after 30 cycles. The consistent Coulombic efficiency of the PQ-based sulfur electrode also supports the confinement of long-chain polysulfide by the cationic polymer. [13, 14]

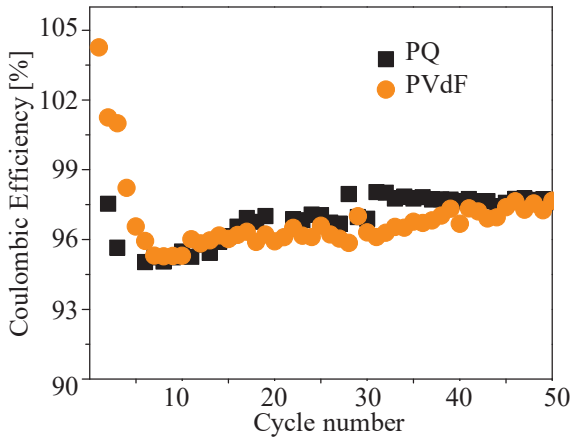


Figure 5-7. Coulombic efficiency of PVDF and PQ based sulfur electrode at 0.05 C.

### 5.2.5) SEM observation

To investigate the morphology evolution after cell cycling, SEM images of sulfur electrodes based on PQ at different state are investigated and shown in Figure 5-8.

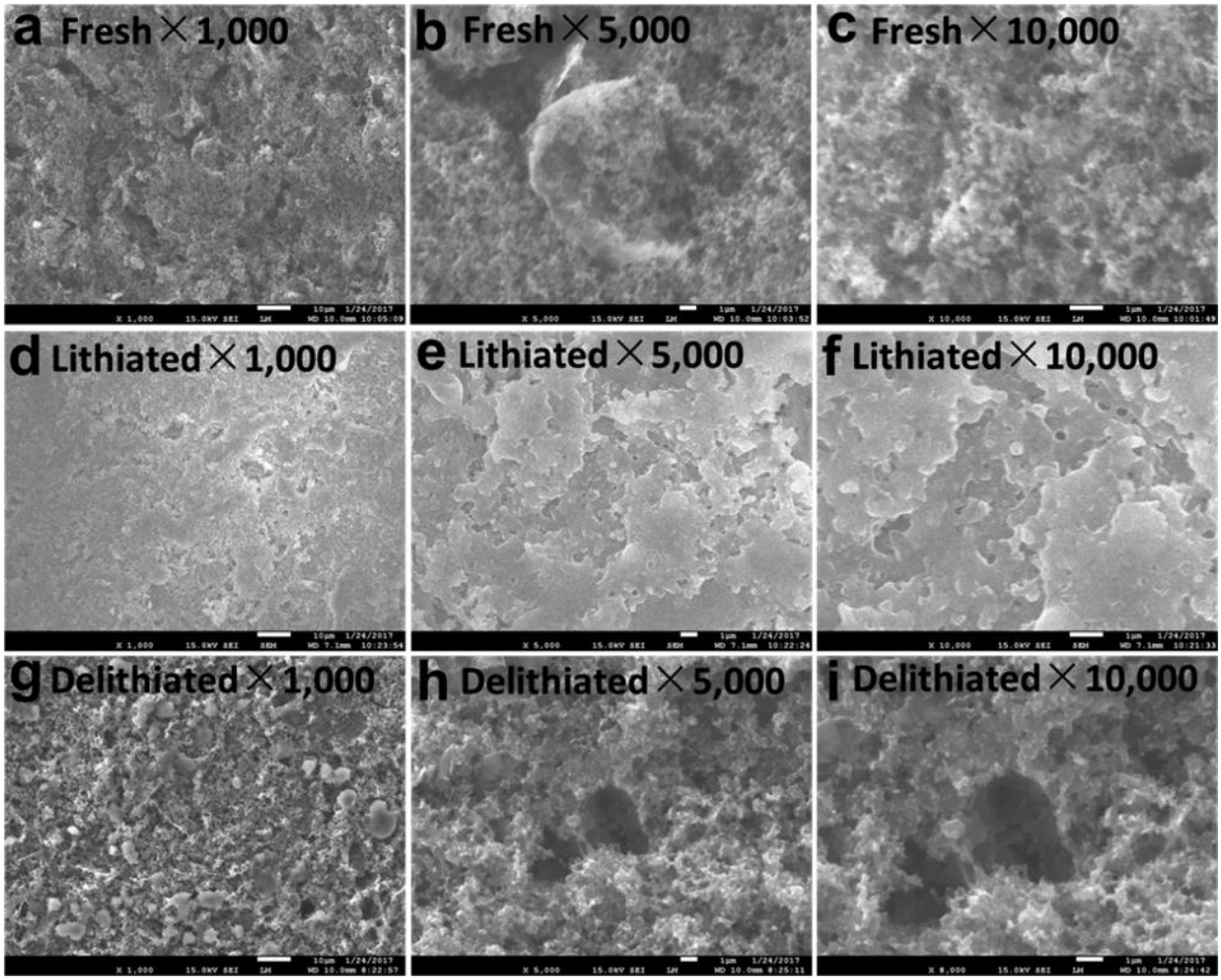


Figure 5-8. SEM images of PQ polymer-based sulfur electrodes. (a, b, c) fresh, (d, e, f) lithiated, and (g, h, i) delithiated images at different magnifications.

Bulk micron sulfur particles are found with carbon black covering on the surface. In fully discharged state, the porous surface is covered by flake-like lithiated product i.e. $Li_2S$. Meanwhile, the bulk sulfur particles are converted into sulfide species after lithiation. Fully charged cathode showed the similar porous surface structure as freshly prepared cathodes, which indicates the successful oxidization of the lithiated product. The good reversibility is in accordance with the electrochemical performance. The energy dispersive spectra (EDS) mapping of discharged and charged PQ-based sulfur cathodes are collected in Figure 5-9. Sulfur species were distributed homogeneously after discharge/charge in

contrast to the bulk micron sulfur particles in the freshly prepared electrode. The micron size sulfur particles were reduced and immobilized on the sulfur electrode side after cycling. [15]

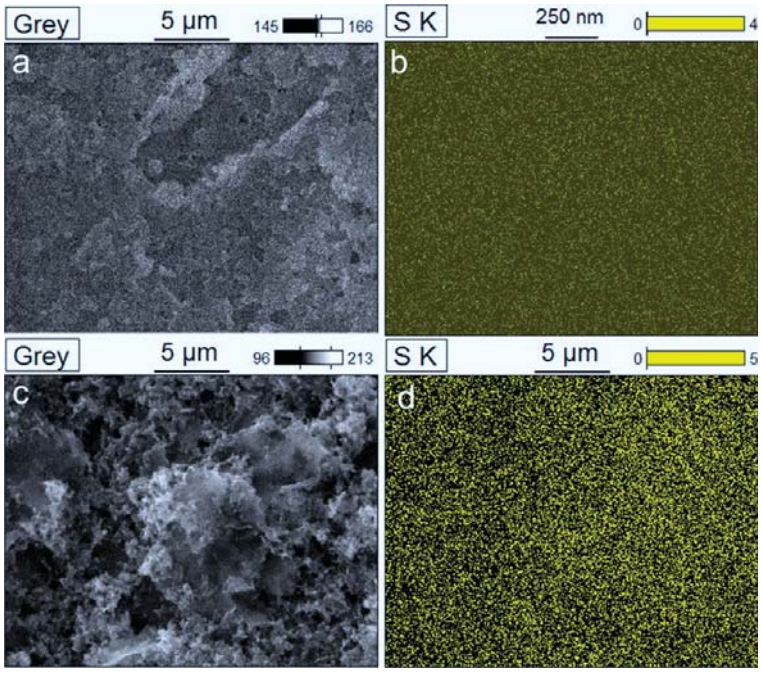


Figure 5-9. Energy dispersive spectra (EDS) mapping of (a, b) lithiated and (c, d) delithiated PQ-based sulfur electrodes.

The bulk sulfur particles were also observed in the fresh PVDF-based electrodes as shown in Figure 5-10. However, there is no flake-like lithiated product for PVDF based sulfur electrodes. For the charged electrodes, the intact sulfur particles are still seen in PVDF-based electrode, which indicates the sulfur particles are not utilized well in the initial cycle.

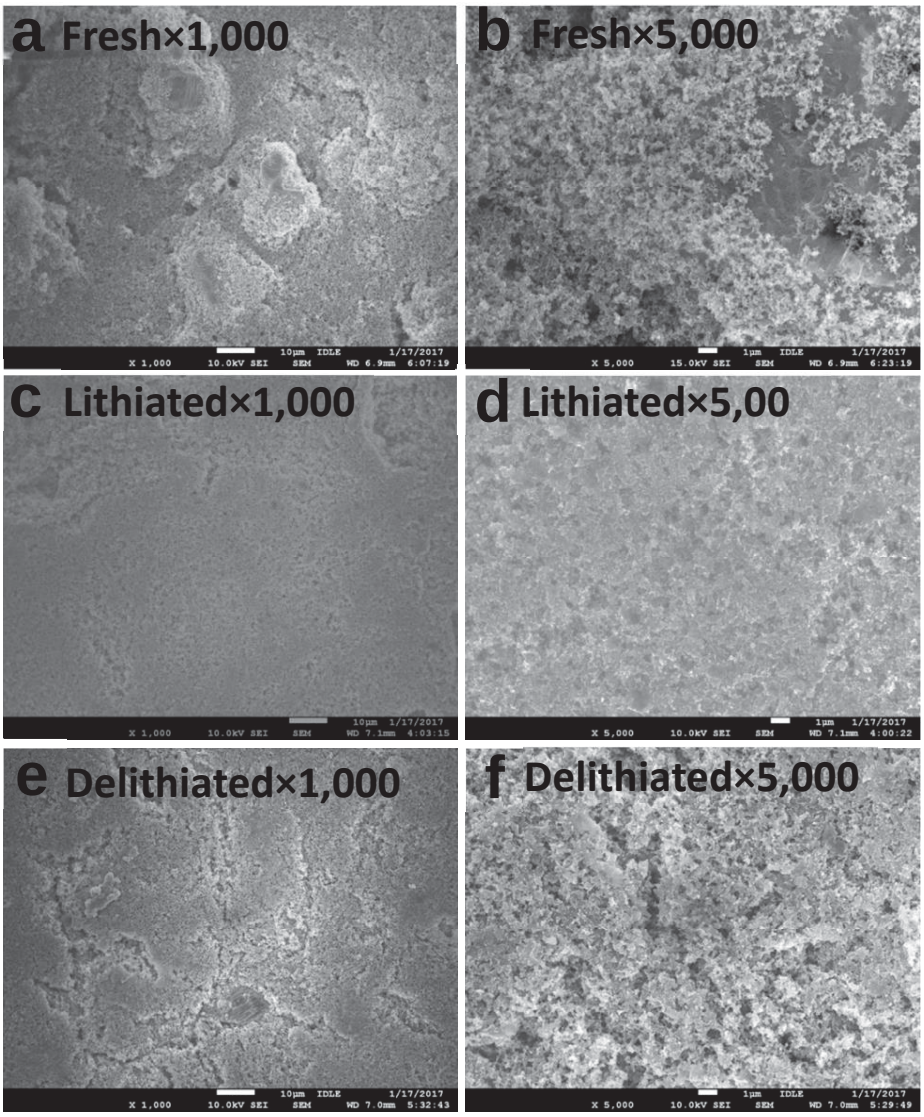


Figure 5-10. SEM images of PVDF polymer based sulfur electrodes. (a, b) fresh (c, d) lithiated and (e, f) delithiated microscopies under different scales.

## 5.3) Summary

Electrostatic absorption was used in the lithium sulfur battery system to control the polysulfides shuttle effect. Both the experimental and calculation results showed that quaternary ammonium cations could effectively bind polysulfides in the lithium sulfur system. The electrostatic absorption ability was also verified through UV−vis

spectroscopy. A high areal capacity of 9.0 mAh/cm$^2$ was achieved at high sulfur loading of 7.5 mg/cm$^2$. [5] Further optimization of the electrostatic confinement approach may lead to stable cycling of the high energy density Li/S rechargeable batteries.

## 5.4) Experimental section

### 5.4.1) Theoretical calculation

Gaussian 09 software1, with Density Functional Theory (DFT) method at the B3LYP/6-311++G(d, p) theory level was used to optimize conformations and calculate the adsorption energies. Mixed basis were used for I contained molecule, in which 6-311++G(d, p) basis was used for C, N, H, Li, S atoms, while LANL2DZ basis was used for I atom. A few initial configurations were tested in each case to obtain qualitative trends, and small variations were expected depending on the initial configuration thus giving rise to different local minima. The adsorption energies of $Li_2S_6$ on the substrates are defined by

$$E_{ads}=-[E(Sub\text{-}Li_2S_6)-E(Sub)-E(Li_2S_6)]$$

where E(Sub), E($Li_2S_6$) and E(Sub-$Li_2S_6$) stand for the calculated electronic energies of the bare substrates, $Li_2S_6$ and the anchoring systems, respectively [16]. Here, the higher values of $\Delta E_{ads}$ indicates the stronger anchoring interaction and vice versa.

### 5.4.2) Experimental detail

UV-Vis spectra

The concentration of lithium sulfide ($Li_2S_6$) applied in the in-situ UV-vis test was 3 mmol/L, in DOL/ DME (1:1 v/v). 0.1 g of the polymer binder was soaked in 1 mL of 3 mmol/L lithium polysulfide in DOL/DME electrolyte in a UV quartz container. A continuous spectra were collected through Cary 5000 UV-Vis-NIR during 22 hour period.

SEM Imaging

Morphology of the electrode surface was characterized with a JEOL JSM-7500F field

emission scanning electron microscope with an accelerating voltage of 15 kV using the high vacuum mode at room temperature. All electrodes were examined in different conditions, including fresh electrode, fully lithiated (in 10th cycle) and fully delithiated (in 10th cycle). The cycled electrodes were disassembled in the glove box and flushed with dimethyl carbonate repeatedly to remove electrolyte residue.

Cathode fabrication

The micron sulfur powder was purchased form Sigma-Aldrich, Super C45 was purchased from TIMCAL, and Graphene was from XG Sciences. All the other chemicals in this work were purchased from Sigma-Aldrich and used without further purification. Sulfur powder, Super C45 and Graphene were added into the binder solution according to a certain weight ratio. The mixture was stirred by a ball-milling method for 48 hours to obtain homogeneous slurry. Then the slurry was coated onto an aluminum current collector with a doctor blade using an Elecometer motorized film applicator. The coated slurry was allowed to air-dry overnight. Finally, 1.26 $cm^2$ cathodes were punched out and dried in a vacuum oven for 2 days at 50 ℃ before transferring into an argon-filled glove box for coin cell assembly. The typical mass loading of sulfur was 7.0 $mg/cm^2$. The composition of cathode was Sulfur:C45:Graphene:binder=6:2:1:1 (weight ratio).

Porosity calculation

The weight of the dried coating was 15.8 mg, which was composed of sulfur, super C45, graphene and binder. The weight ratio of each component was 6/2/1/1. The average dried coating thickness was 220 μm. The electrode area was 1.27 $cm^2$. The volume of the dried coating was $2.79\times10^{-2}$ $cm^3$. The bulk density of each component: $\rho_{sulfur}$=2.07 $g/cm^3$, $\rho_{superC45}$=0.56 $g/cm^3$, $\rho_{graphene}$=0.72 $g/cm^3$, $\rho_{binder}$=1.36 $g/cm^3$. Accordingly, the calculated volume of each component: $V_{sulfur}$=4.56×10-3 $cm^3$, $V_{super\ C45}$=5.62×10-3 $cm^3$, $V_{graphene}$=2.18×10-3 $cm^3$, $V_{binder}$=1.15×10-3 $cm^3$. Based on the calculated porosity, 14.3 μL void volume existed. The amount of the added electrolyte was fixed at 60 μL, which was

around four times of the void volume. The extra electrolyte was applied to guarantee a sufficient wetting of the electrodes and effective migration of lithium ions.

Cell assembly and testing

Coin cells (CR2325, National Research Council Canada) were assembled in an argon-filled glove box with $O_2$ and $H_2O$ content less than 0.5 ppm. Lithium metal foil was used as anode and polypropylene Celgard 2400 was used as separator. The electrolyte was 1M lithium bis(trifluoromethanesulfonyl)imide (LiTFSI) dissolved in a mixture of 1,3-dioxolane and dimethoxyethane (1:1 in volume) with 2% $LiNO_3$ added as an additive to help passive the surface of the lithium anode and reduce the shuttle effect. The electrochemical performance was measured Galvanostatically in a voltage range of 1.8 V - 2.6 V on a Maccor series 4000 cell tester at 30 ℃. The specific capacities were calculated based on the mass of S in the electrodes. Cells used for SEM characterization were tested at 0.05C for 10 cycles, and stopped at fully lithiated or fully delithiated state. Then these cells were disassembled in argon-filled glove box, finally the cathodes were flushed using DME/DOL (1:1) solvent and dried before SEM study.

## 5.5) References

[1] B.A. Trofimov, L.V. Morozova, M.V. Markova, A.I. Mikhaleva, G.F. Myachina, I.V. Tatarinova, T.A. Skotheim, *J. Appl. Polym. Sci.* **2006,** *101,* 4051–4055.

[2] P. Bhattacharya, M. Nandasiri, D. Lv, A. M. Schwarz, J. T. Darsell, W. A. Henderson, D. A. Tomalia, J. Liu, J.-G. Zhang, J. Xiao, *Nano Energy* **2016**, *19*, 176−186.

[3] S. Wei, L. Ma, K. E. Hendrickson, Z. Tu, L. A. Archer, *J. Am. Chem. Soc.* **2015**, *137*, 12143−12152.

[4] G. Ai, Y. Dai, Y. Ye, W. Mao, Z. Wang, H. Zhao, Y. Chen, J. Zhu, Y. Fu, V. Battaglia, J. Guo, V. Srinivasan, G. Liu, *Nano Energy* **2015**, *16*, 28−37.

[5] G. Li, M. Ling, Y. Ye, Z. Li, J. Guo, Y. Yao, J. Zhu, Z. Lin, S. Zhang, *Adv. Energy Mater.* **2015**, *5*, 1500878.

[6] W. Chen, T. Qian, J. Xiong, N. Xu, X. Liu, J. Liu, J. Zhou, X. Shen, T. Yang, Y. Chen, C. Yan, *Adv. Mater*. **2017**, *29*, 1605160.

[7] E. P. Kamphaus, P. B. Balbuena, *J. Phys. Chem. C* **2016**, *120*, 4296−4305.

[8] Z. W. Seh, Q. Zhang, W. Li, G. Zheng, H. Yao, Y. Cui, *Chem. Sci*. **2013**, *4*, 3673−3677.

[9] J. Lu, T. P. Wu, K. Amine, *Nat. Energy* **2017**, *2*, 17011.

[10] A. Kawase, S. Shirai, Y. Yamoto, R. Arakawa, T. Takata, *Phys. Chem. Chem. Phys.* **2014**, *16*, 9344−9350.

[11] Y. V. Mikhaylik, J. R. Akridge, *J. Electrochem. Soc*. **2004**, *151*, A1969−A1976.4

[12] H. Wu, D. Zhuo, D. S. Kong, Y. Cui, *Nat. Commun.* **2014**, *5*, 5193.

[13] S. H. Chung, P. Han, A. Manthiram, *ACS Appl. Mater. Interfaces* **2016**, *8*, 4709−4717.

[14] R. Elazari, G. Salitra, A. Garsuch, A. Panchenko, D. Aurbach, *Adv. Mater.* **2011**, *23*, 5641− 5644.

[15] C. Y. Fu, G. H. Li, J. Zhang, B. Cornejo, S. S. Piao, K. N. Bozhilov, R. C. Haddon, J. C. Guo, *ACS Energy Lett.* **2016**, *1*, 115−120.

[16] A. Manthiram, Y. Fu, S.-H. Chung, C. Zu, Y.-S. Su, Rechargeable Lithium−Sulfur Batteries. *Chem. Rev.* **2014**, *114*, 11751−11787.

# CHAPTER 6

# Degradation mechanism of lithium/sulfur cells using X-ray Absorption Spectroscopy

## 6.1) Introduction

### 6.1.1) Degradation during cycling

The short life time has been the significant obstacle for Li/S cells to be put into practical application for a long time. The cause of the degradation is assumed as mainly redox shuttle phenomenon of polysulfide species. Before 2005, the cycle performance was no more than 50 cycles. After lithium nitrate had been started to be employed as an additive in the electrolyte solution, the cycle number rose above 100 cycles quickly. The main role of lithium nitrate in the cells is creating some protection layers on the lithium anode. [1] In combination with the many other improvements of cathode materials and electrolyte components, the cycle retention has been improved up to 1500 cycles. The key factor for those improvements other than lithium nitrate is polysulfide confinement in the electron conductive network using chemical interaction.

In this chapter, in order to obtain a comprehensive picture on the whole process of a Li/S cell life cycle, the X-ray absorption spectroscopy (XAS) technique is applied. By employing two different detection modes, i.e. total electron yield (TEY) mode and total fluorescence yield (TFY) mode, during the XAS measurements, a detailed depth profile are obtained, providing direct structural information from the near surface (which contacts with the electrolyte) and bulk of the cathode. This will lead to better understand the degradation mechanism of the Li/S cells.

In comparison with the other characterization tools, such as transmission X-ray microscopy, X-ray diffraction, UV-visible spectroscopy and electron paramagnetic resonance, XAS has special advantages in the studies of Li/S cell materials because it is extremely sensitive to chemical and electronic structures of materials. The lack of the chemical and electronic state information of the Li/S cathode has become a serious impediment for the Li/S cell cathode optimization efforts. Therefore, it is aimed to solve this problem by introducing XAS technique to the application on the study of a Li/S cell.

### 6.1.2) Introduction of X-Ray Absorption Tools

XAS is a widely used technique for investigation of geometric and electronic structures of matter [2-6]. It is well established that XAS allows to determine chemical bonds, oxidation states, band structures and local symmetries of materials [5, 7]. To gain detailed information on applications of XAS, an X-ray absorption process is briefly described here.

When X-rays hit a sample, they will either be scattered or absorbed by the electrons in the sample [8]. In an X-ray absorption process, a core-hole is created at first when a core-electron is excited up to an unoccupied state above the Fermi energy. This transition is governed by the dipole-selection rules which limit the available final states. Thus the energy dependence of X-ray absorption depends on the distribution of unoccupied states which may be reached from the core-level via a dipole-allowed transition. The resulting core-hole can be refilled by the higher energy core-level electrons, valence electrons or previously excited electrons, with emission of photons (photon-in/photon-out process). A detector can be used to collect these photons as a TFY signal for XAS. The dominant channel for decay of the core-hole is Auger electron emission, rather than fluorescence [9]. Hence, a low energy secondary electron cascade can be induced by the inelastic electron scattering of the Auger electron. This provides the possibility of surface sensitive detection. Therefore, there are three methods for detecting X-ray absorption signals, each with a different probe depth: Auger electron yield (AEY) is measured by detecting primary Auger electrons which have not lost energy, thus is as surface-sensitive as X-ray photoelectron spectroscopy (XPS). TEY detection includes the secondary-electron cascade and has a probe depth of 5 nm (soft X-rays) to tens of nm (hard X-rays). The depth is limited by the depth from which electrons emerge with enough energy to overcome the work-function barrier [9]. In contrast, TFY detection probes the samples at depths of up to microns. These signals come from the different decay routes of refilling the core-hole, and can be collected simultaneously. However, in most cell investigations, sample preparation processes are

mostly conducted via wet-chemistry in the air, while the cycled cathode surfaces are highly influenced by possible remaining residues and adsorbed species in the air [10]. Then the surfaces of the samples may be complicated and highly influenced by the uncontrollable experimental environment. Therefore, AEY, as well as XPS, with its high surface sensitivity, may provide misleading information and is not suitable for in-situ/in-operando studies. Thus, TEY and TFY are mostly applied to get depth profiling information [2,3,10,11]. Hence, XAS can probe materials' chemical and electronic information ranging from several to hundreds of nanometers, leading to a deep insight into studies of Li/S cells.

## 6.2) Results and Discussion

### 6.2.1) Characterization of cycled cathode materials

S K-edge XAS has been applied to the study of the degradation mechanism of the cathode by observing the cathode samples before and after 500 and 1500 charge and discharge cycles, respectively. The cell was stopped at the fully charged state and the cathode were washed with DOL-DME (DOL: 1,3-Dioxolane, DME:1,2-Dimethoxyethane) solvents three times before the measurement. TEY and TFY signals were collected simultaneously to get depth profile information. Figure 6-1 shows the S K-edge XAS of the cycled cathode.

As shown in Figure 6-1, two peaks were observed in the initial cathode: the peak at 2472.2 eV representing the transition from S 1s to S–S π* state of $S_8$ and C–S-S–C, and the peak centered at 2473.7 eV which can be attributed to the transition from S 1s to the C–S σ* state [12-15]. These two peaks represent the active material that can contribute to the reaction during the charge / discharge cycles. After repeatedly cycling, several absorption peaks showed up in the higher photon energy region. The peaks are located at 2478.0, 2480.5 and 2482.3 eV corresponding to the transition from S 1s to the σ* state of S-O in $SO_3^{2-}$, $COSO_2^{-}$ and $SO_4^{2-}$ respectively. [12-14] These insulating species can come from the reactions between S and oxygen containing functional groups [10].

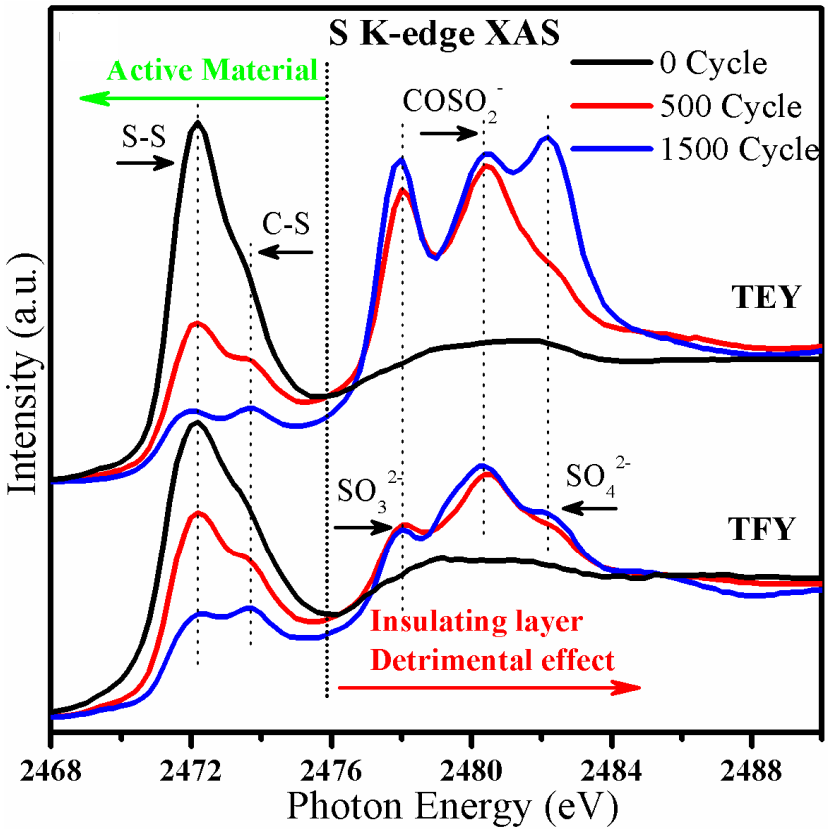


Figure 6-1. S K-edge XAS of cathode materials before cycling and after 500 cycles and 1500 cycles.

It can be observed from the spectra that the intensity of the S–S and C–S peaks decreases with increasing cycle number, indicating the loss of the active material. In addition, S–O species are formed and increased after cycling, at the expense of active S species. In comparison with the TFY signal, the ratio of peak intensities of S–S and C–S with respect to the S–O species is much lower in the TEY signals, which is surface sensitive. Thus, it can be assumed that the S–O species accumulated at the surface of the cathode, which is the interface of the cathode and the electrolyte in the cell. This layer is referred to as CEI (cathode-electrolyte interface) layer. The accumulation of this insulating CEI layer can block the diffusion of Li ions into and out of the cathode, leading progressive hindrance of the electrochemical reactions between Li and S, causing the cell performance to decay [2].

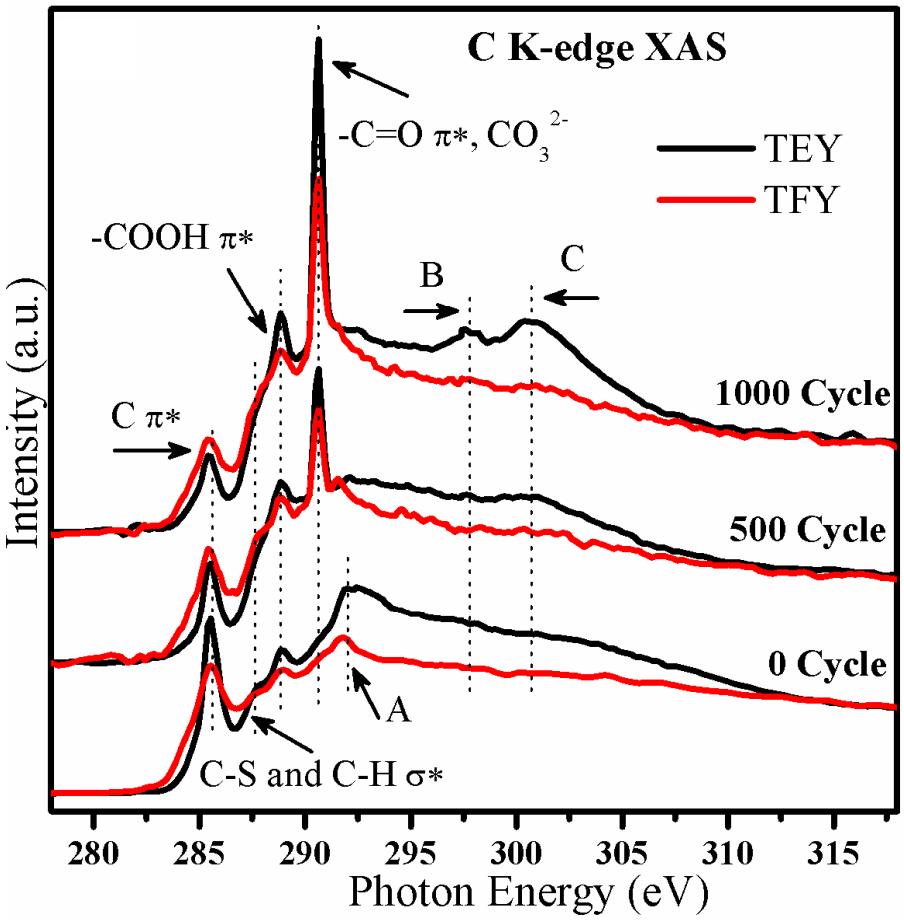


Figure 6-2. C K-edge XAS data of cathode materials before cycling and after 500 cycles and 1500 cycles.

Meanwhile, C K-edge XAS recorded species on the surface of the cycled cathode. Figure 6-2 shows C K-edge XAS of the cycled cathode. In the initial cathode, features at 285.5, 287.6, and 288.7 eV come from the transition from C 1s to the π* of GO and carbon black, C–S and C–H σ* and –COOH π*, respectively [2, 3, 16, 17]. Moreover, Peak A located at 292.0 eV is attributed to the transition from C 1s to the σ* state at the Γ point of graphene Brillouin zone [2, 3]. On cycling, (1) vanishing of Peak A, i. e. the σ* peak of GO at 292.0 eV; (2) increase of the peak at 290.6 eV and Peak B and C at higher photon energies, were found. The peak around 290.6 eV arises from the transition from C 1s to the –C=O π* state [18], while Peak B and C are associated with the appearance of $CO_3^{2-}$ [19].

Therefore, it can be assumed that, with cycling, the carbon and graphene structures are highly influenced while the $CO_3^{2-}$ species accumulates. Moreover, similar to what are observed on the S K-edge XAS, depth profile information can be obtained by a comparison between C K-edge TEY and TFY signals. The intensity ratio of $CO_3^{2-}$ peak relative to the peak of graphene π* state is higher for the TEY signal than for TFY. This observation indicates that the accumulation of the $CO_3^{2-}$ species took place at the surface of the cycled cathode. The accumulation of this layer can contribute to the cell capacity decay.

Note that the intensities of the signals of S–O species, $SO_3^{2-}$, $SO_4^{2-}$ and $COSO_2^{-}$, increased significantly from the initial condition to 500th cycles, and the difference is not that significant from 500th cycle and 1500th cycle. It is assumed that the insulating layer accumulated during the first several hundreds of cycles, slowing down thereafter. On the other hand, the intensity of the peaks of S-S and C-S representing active sulfur species decreased and the peak of $CO_3^{2-}$ increased at a roughly constant rate during the whole cycling. Thus, there are at least two components contributing to the overall observed capacity fade: the accumulation of insulating layer and loss of active sulfur.

The application of XAS technique provides both near-surface and bulk information at a range from several to hundreds of nanometers concerning the speciation of different elements on the cathode. This comprehensive picture can benefit the understanding of the Li/S cell degradation mechanism.

## 6.3) Summary

In this chapter, the degradation mechanisms in a lithium/sulfur cell was investigated in detail utilizing X-ray spectroscopic techniques. The results from S K-edge and C K-edge XAS revealed that some oxidized products of sulfur and carbon on the surface of the cathode increased over the long cycling process. Loss of sulfur as the active material was also confirmed. These results and the technique will be applied to further investigations and modifications of long-life lithium/sulfur cells.

## 6.4) Experimental section

### 6.4.1) Sample preparation

A detailed description of the sample preparation is in Chapter 3. Basically, 0.58 g $Na_2S$ and 0.72 g S were dissolved in 25 mL distilled water to form a sodium polysulfide ($Na_2S_x$) solution after stirring with a magnetic stirrer for 2 h. 164 mg CTAB (Sigma Aldrich, St. Louis, MO, USA) was added to the $Na_2S_x$ solution and stirred for 2 h to make a $Na_2S_x$ and CTAB mixture solution. Then, the $Na_2S_x$ solutions with and without CTAB were slowly added to 100 mL 2 M formic acid solution (HCOOH, Sigma Aldrich, St. Louis, MO, USA), resulting in the precipitation of S species. The obtained nano-composites have been applied as active material. SBR/CMC were used as binders and the electrolyte was (2:1:1, v/v/v) PYR14TFSI/DOL/DME/0.1 M $LiNO_3$ (PYR14TFSI: 1-butyl-1-methylpyrrolidinium bis(trifluoromethanesulfonyl)imide). The cell was cycled at discharge/charge rates of 1 C/0.25 C (1 C = 1675 mA/g S).

### 6.4.2) Analysis

All the XAS data were taken at the Advanced Light Source, Lawrence Berkeley National Laboratory, CA, USA. For S K-edge XAS measurement, three beamlines (BLs) were used: 9.3.1, 10.3.2 and 5.3.1. BL 9.3.1 has a vacuum-chamber end-station with a beam size of 1 × 0.7 $mm^2$ and energy range 2.4–5.8 keV. BL 10.3.2 has a spot size variable from 2 × 2–10 × 6 $\mu m^2$ and energy range 2.1–17 keV, and BL 5.3.1, with a spot of around 80 × 100 $\mu m^2$ and energy range 2.1–12 keV. For the soft X-ray, the experiment can also be performed at two vacuum based beamlines: the undulator BL 8.0.1 offers the focused high flux beam at 100 × 35 $\mu m^2$ with energy region of 80–1200 eV, while the bend magnet BL 6.3.1.2 offers the focused beam at 50 × 500 $\mu m^2$ with energy region of 250–2000 eV. All the beamlines allow us to measure samples using TEY and TFY modes, and BL 6.3.1.2 has the ability to record the PFY (partial fluorescence yield) signal using a Vortex (Hitachi High-Technologies Science America, Northridge, CA, USA) silicon drift detector.

## 6.5) References

[1] D. Aurbach, E. Pollak, R. Elazari, G. Salitra, J. Electrochem. Soc. **2009**, *156* A694-A702.

[2] X. Feng, M.-K. Song, W.C. Stolte, D. Gardenghi, D. Zhang, X. Sun, J. Zhu, E. J. Cairns, J. Guo, *Phys. Chem. Chem. Phys.* **2014**, *16*, 16931–16940.10

[3] L. Zhang, L. Ji, P.-A. Glans, Y. Zhang, J. Zhu, J. Guo, *Phys. Chem. Chem. Phys.* **2012**, *14*, 13670–13675.11

[4]. F. Jalilehvand, *Chem. Soc. Rev.* **2006**, *35*, 1256–1268.12

[5] A. Vairavamurthy, *Spectrochim. Acta A* **1998**, *54*, 2009–2017.13

[6] Y.-S. Liu, P.-A. Glans, C.-H. Chuang, M. Kapilashrami, J. Guo, *J. Electron Spectrosc. Relat. Phenom.* **2015**, *200*, 282–292. 14

[7] F. De Groot, *Chem. Rev*. **2001**, *101*, 1779–1808.15

[8] M. Giorgetti, *ISRN Mater. Sci*. **2013**, *2013*, 1–22.16

[9] B.H. Frazer, B. Gilbert, B.R. Sonderegger, G. de Stasio, *Surf. Sci.* **2003**, *537*, 161–167. 17

[10] Z. Lin, C. Nan, Y. Ye, J. Guo, J. Zhu, E. J. Cairns, *Nano Energy* **2014**, *9*, 408–416.18

[11] G. Ai, Y. Dai, Y. Ye, W. Mao, Z. Wang, H. Zhao, Y. Chen, J. Zhu, Y. Fu, V. Battaglia, et al. *Nano Energy* **2015**, *16*, 28–37.19

[12] M.-K. Song, Y. Zhang, E. J. Cairns, *Nano Lett*. **2013**, *13*, 5891–5899.2

[13] X. Ji, L. F. Nazar, *J. Mater. Chem*. **2010**, *20*, 9821–9826.3

[14] A. Manthiram, Y. Fu, S.-H. Chung, C. Zu, Y.-S. Su, *Chem. Rev*. **2014**, *114*, 11751–11787.4

[15] A. Manthiram, Y. Fu, Y.-S. Su, *Acc. Chem. Res*. **2013**, *46*, 1125–1134.5

[16] H. Yabuta, M. Uesugi, H. Naraoka, M. Ito, A. Kilcoyne, S. Sandford, F. Kitajima, H. Mita, Y. Takano, T. Yada, et al. *Earth Planet Sp*. **2014**, *66*, 1–8.23

[17] J. Kikuma, B.P. Tonner, *J. Electron Spectrosc. Relat. Phenom*. **1996**, *82*, 53–60.24

[18] Y. Kebukawa, M.E. Zolensky, A.L.D. Kilcoyne, Z. Rahman, P. Jenniskens, G.D.

Cody, *Meteorit. Planet. Sci*. **2014**, *49*, 2095–2103.25

[19] J. A. Brandes, S. Wirick, C. Jacobsen, *J. Synchrotron Radiat*. **2010**, *17*, 676–682. 26

CHAPTER 7

# Conclusion

In this thesis, the author describes the analysis and the development of sulfur electrode technologies for lithium/sulfur cells for practical applications as next generation batteries. Establishment of the technologies for lithium/sulfur cells which can be scaled-up with high performance and high reproducibility is aimed. In order to achieve this goal, the technologies need to be understood well and sulfur loading in the cathode sheet need to be high while keeping a high performance. All studies were conducted from these points of view.

In Chapter 1, the author addressed the motivation of the research of lithium/sulfur cells by emphasizing the high theoretical capacity of the cell which shows its potential to achieve a cell with high specific energy. At the same time, the developments made in the history to enhance the cell performance were described. While the main components of the electrolyte have been established, sulfur electrode technologies have not reached to the point of the practical use due to complication in the fabrication process. Considering these facts, the purpose of this thesis was set up to develop technologies of sulfur electrode for practical applications.

In Chapter 2, the lithium polysulfide species generated in a lithium/sulfur cell were analyzed by LC/MS and NMR combined with an organic conversion technique. The results suggested that electrochemical reactions in the cell proceeded through four distinct stages. It is of particular interest that the second plateau in the discharge profile, which is the most important reaction state in practical use because of its constant voltage, is dominated by the reduction of $Li_2S_3$. Meanwhile the first plateau and the transition state, in which the voltage varies with the capacity, are associated with multiple reactions. The graphical images of electrochemical reactions of sulfur species is shown in figure 7-1. It also revealed that longer polysulfides, $Li_2S_x$ (x = 6 to 8), are responsible for the redox shuttle phenomenon, which causes serious capacity degradation. This work is the first step of understanding the influence of components on the reaction scheme, which is connected with cell performances.

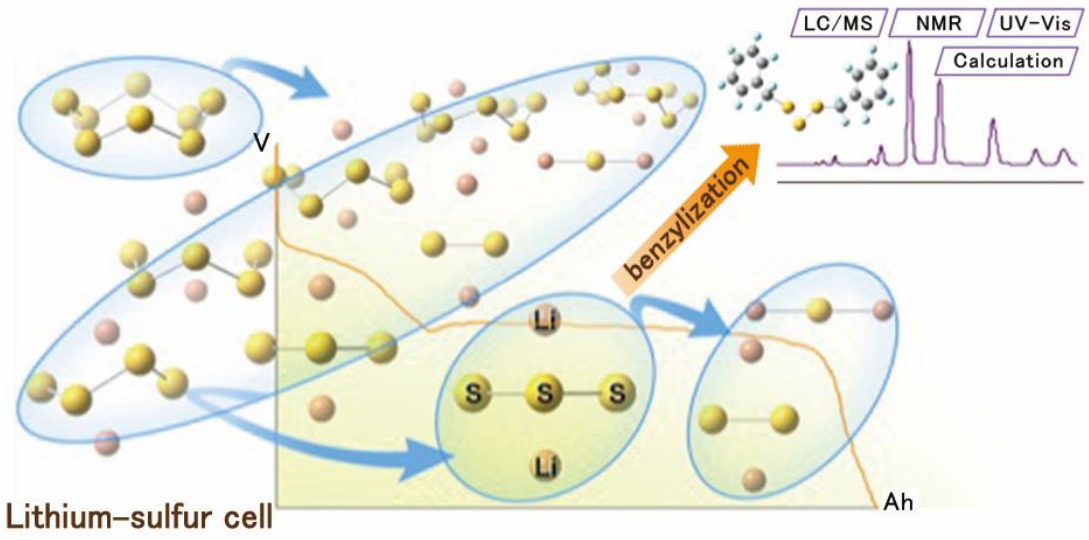


Figure 7-1. The graphical images of electrochemical reactions of sulfur species.

In Chapter 3, the sulfur deposition process in the preparation of sulfur-GO composite active material for sulfur electrode was carefully investigated. It was found that just mixing of a polysulfide solution and a GO suspension produced a composite of sulfur and reduced GO by alkaline deposition. Also, the acidification of the polysulfide solution, i.e. acidic deposition was influenced significantly by temperature. The sulfur deposition rate under different conditions influenced the morphology of the materials and their resulting cell performance. The graphical images illustrating the features in the morphologies of sulfur-GO composite depending on the synthesis conditions is shown in Figure 7-2. By controlling the synthesis condition such as the combination of moderate alkaline deposition for 60% of sulfur and the subsequent acidic deposition at a low temperature, specifically 5 °C, the preferred morphology of the sulfur/GO composite with high capacity was successfully synthesized.

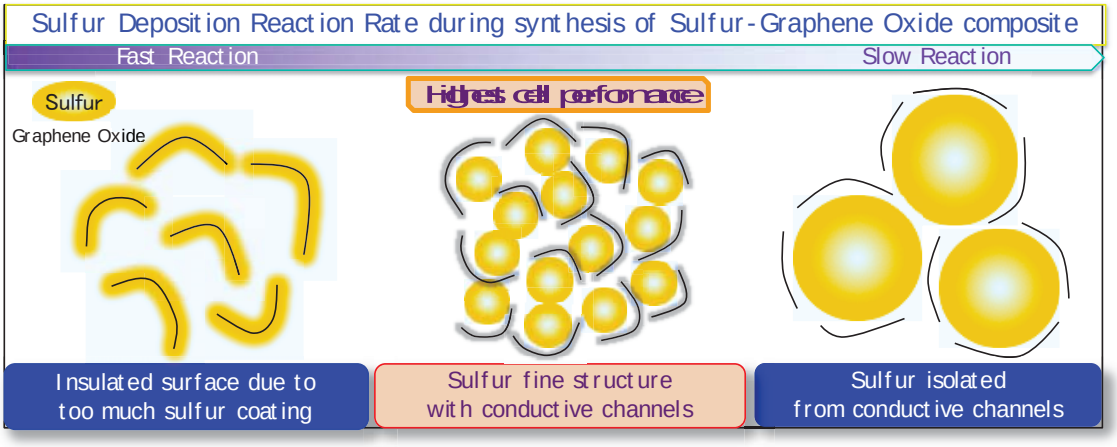


Figure 7-2. The graphical images illustrating the features in the morphologies of sulfur-GO composite depending on the synthesis conditions.

In Chapter 4, the author has identified the key components for enhancing the capacity of cells using S-GO-CTA as a cathode material. The CTAB added in the synthesis procedure of S-GO-CTA reacts with polysulfide composites during the 155 °C heat treatment and produces $Me_2S_x$, CA, CMA and CDMA. Furthermore, CDMA reacts with sulfur and creates S-CDMA-1 and S-CDMA-2 composing new stable materials, Phase X. A graphical summary of the reactions taking place during the heat treatment is shown in Figure 7-3. The newly produced Phase X by the reaction of CTAB during the synthesis apparently worked as a promoter of the conversion reaction from polysulfide to $Li_2S$. Considering these effects of CTAB on the capacity enhancement, CTAB worked as both surfactant and the precursor of the functional layer. These findings can be applied for various sulfur-carbon composites for cathode materials in sulfur cells. These findings can be applied to the control of the scaled-up production of the materials.

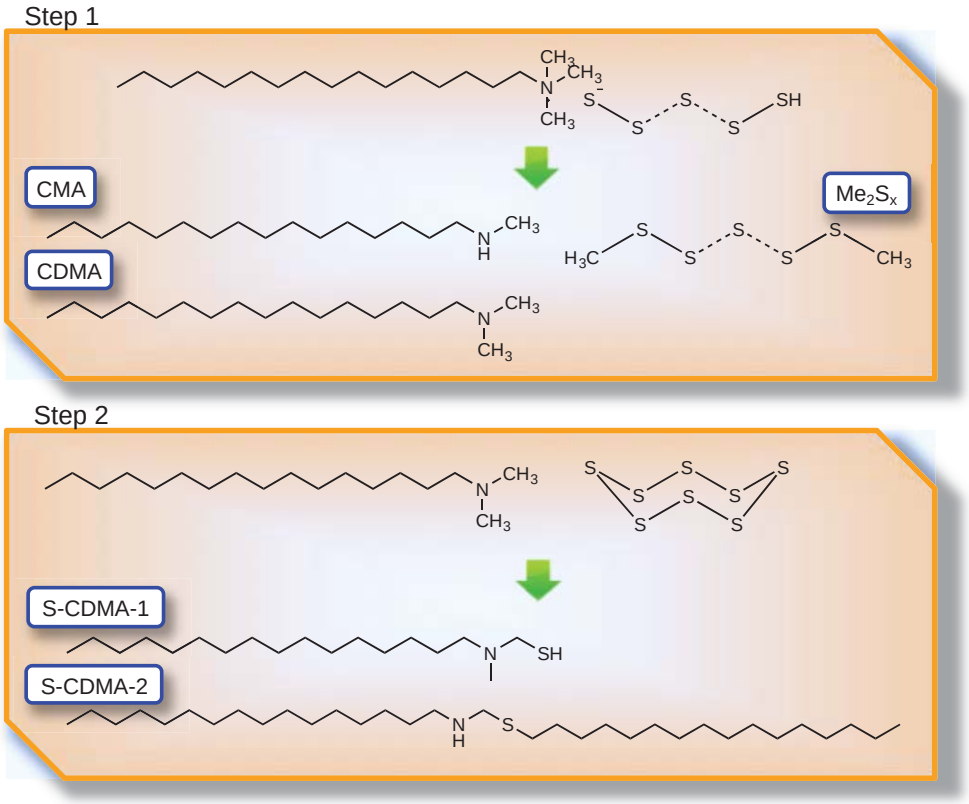


Figure 7-3. A graphical summary of the reactions taking place during the heat treatment in the synthesis process of sulfur-GO composite.

In Chapter 5, electrostatic absorption was used in the cathode sheet of lithium/sulfur cells to control the polysulfides shuttle effect in high sulfur loading electrodes. Both the experimental and calculation results showed that quaternary ammonium cations could effectively bind polysulfides in the lithium/sulfur cells. A graphical image of polysulfides confinement through cationic polymer and the electrostatic attraction between the PQ quaternary ammonium cations and polysulfide anions is shown in Figure 7-4. The electrostatic absorption ability was also verified through UV−vis spectroscopy. A high areal capacity of 9.0 mAh/cm$^2$ was achieved at high sulfur loading of 7.5 mg/cm$^2$.

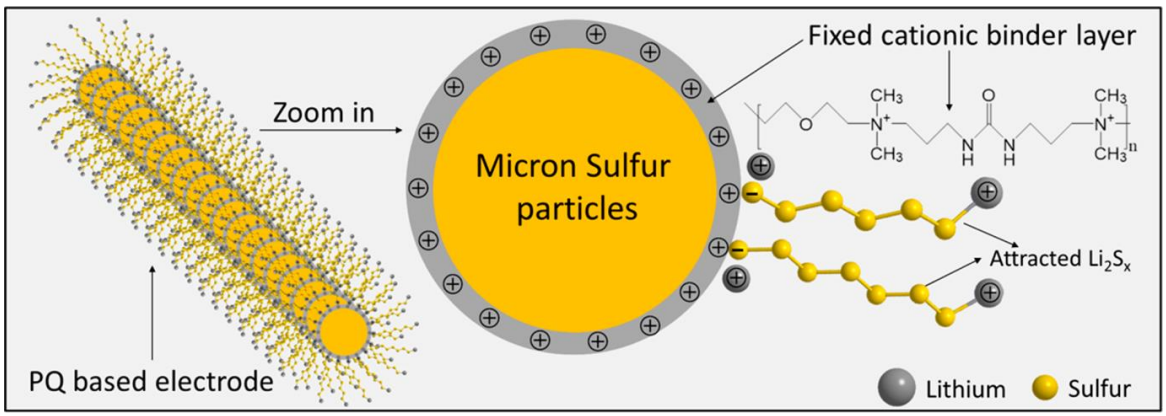


Figure 7-4. A graphical image of polysulfides confinement through cationic polymer and the electrostatic attraction between the PQ quaternary ammonium cations and polysulfide anions.

In Chapter 6, the degradation mechanisms in a lithium/sulfur cell was investigated in detail utilizing X-ray spectroscopic techniques. The results from S K-edge and C K-edge XAS revealed that some oxidized products of sulfur and carbon on the surface of the cathode increased over the long cycling process. Loss of sulfur as the active material was also confirmed. These results and the technique will be applied to further investigations and modifications of long-life lithium/sulfur cells.

Although author believes whole these studies are valuable to realize the practical application of lithium/sulfur cells, still some challenges are to be solved in the future works, which are enhancement of the cell cycle life as noted in Chapter 6. Thus, electrolyte additives and separators which influence the polysulfide shuttling and/or lithium dendrite should be developed further. Prevention of decomposition of the cell components is also necessary to realize a practical cell.

# Supporting Information

## Chapter 3

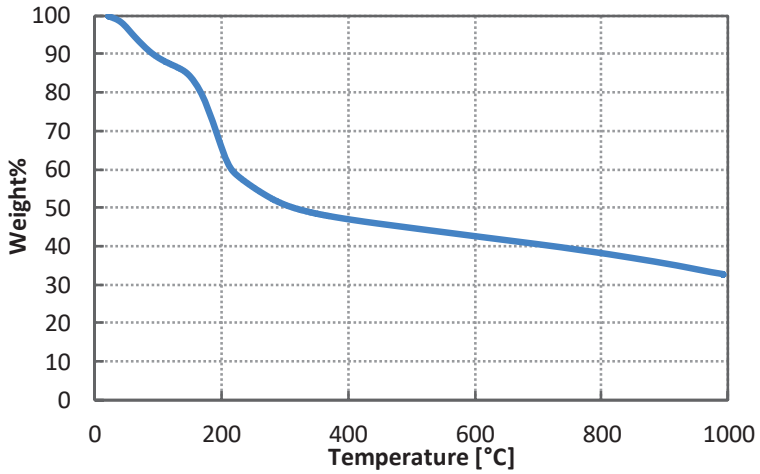


Figure S3-1. Weight loss in TGA analysis for GO corresponding to the evaporation of water and the functional groups.

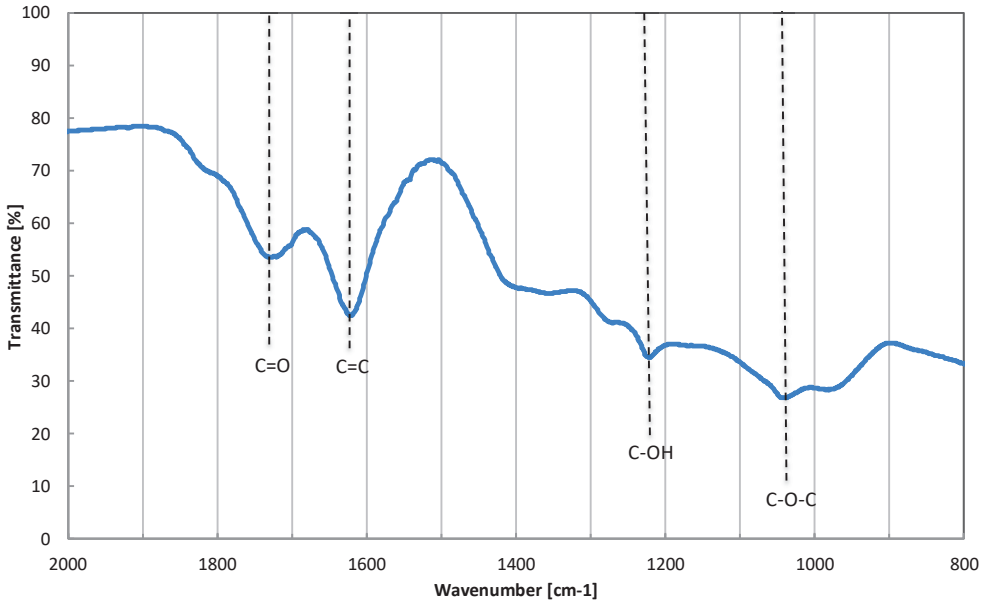


Figure S3-2. FT-IR spectrum of GO showing the existence of carboxyl groups, epoxy groups and hydroxyl groups.

# Chapter 4

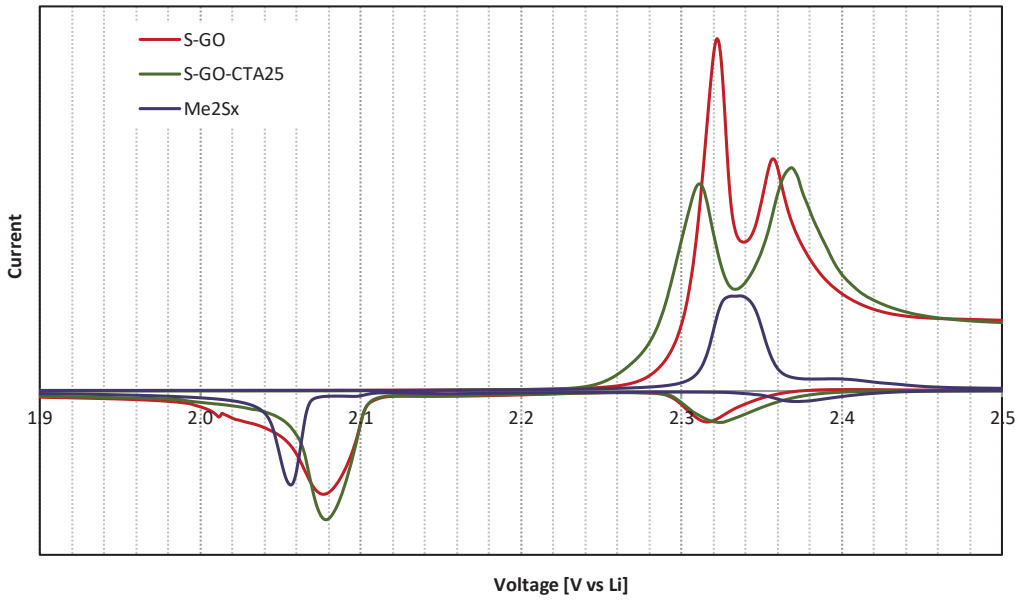


Figure S4-1. Cyclic voltammetry of S-GO-CTA composites having CTAB and no CTAB and dimethylpolysulfide.

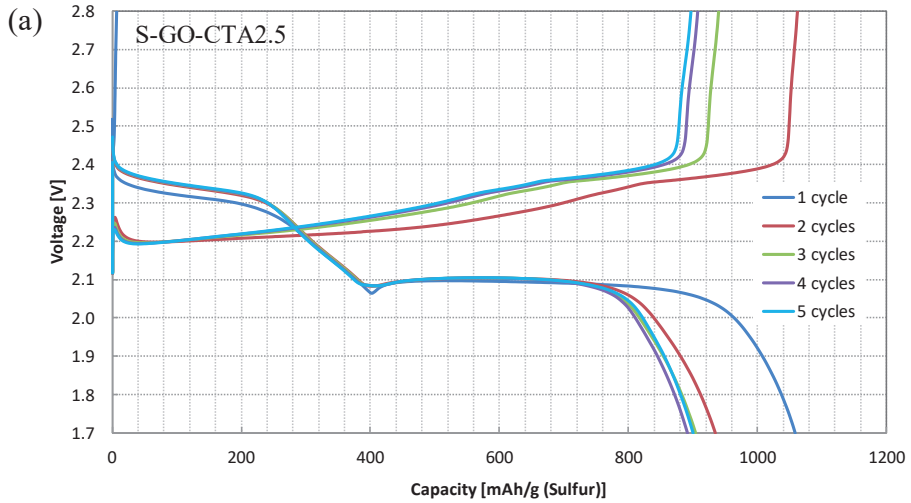

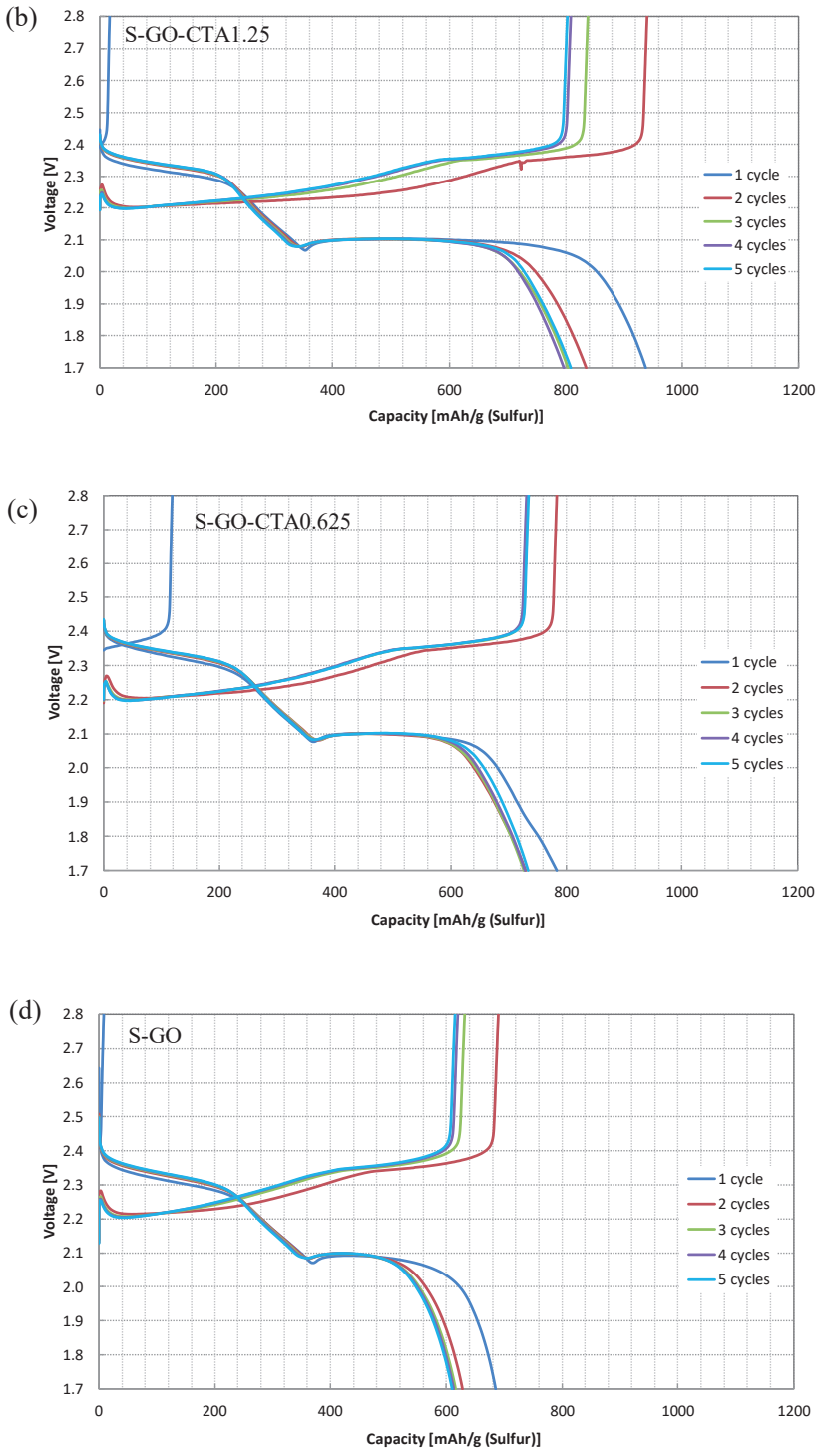


Figure S4-2. Voltage profiles of (a) S-GO-CTA2.5, (b) S-GO-CTA1.25, (c) S-GO-CTA0.625 and (d) S-GO for the first 5 cycles.

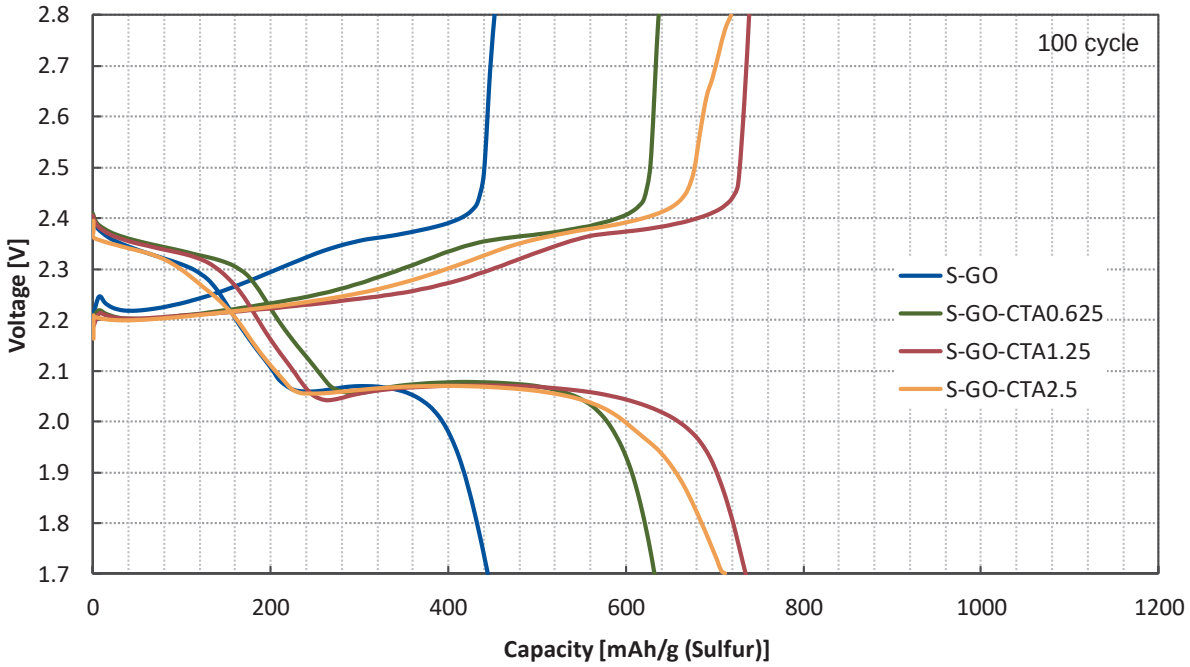


Figure S4-3. Voltage profiles of S-GO-CTA2.5, S-GO-CTA1.25, S-GO-CTA0.625 and S-GO after 100 cycles.

# Chapter 5

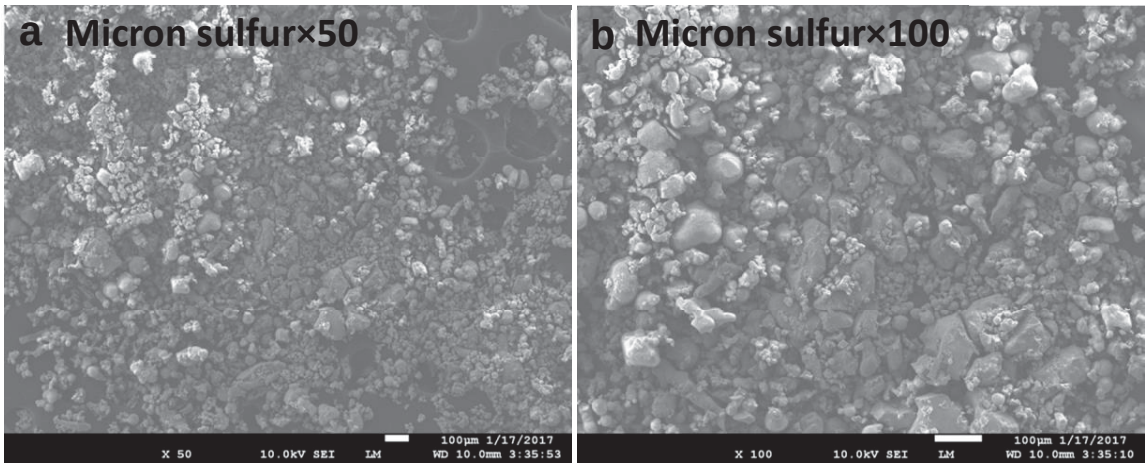


Figure S5-1. SEM images of commercial available micron sulfur particles. The particle size varies from several microns to tens of microns.

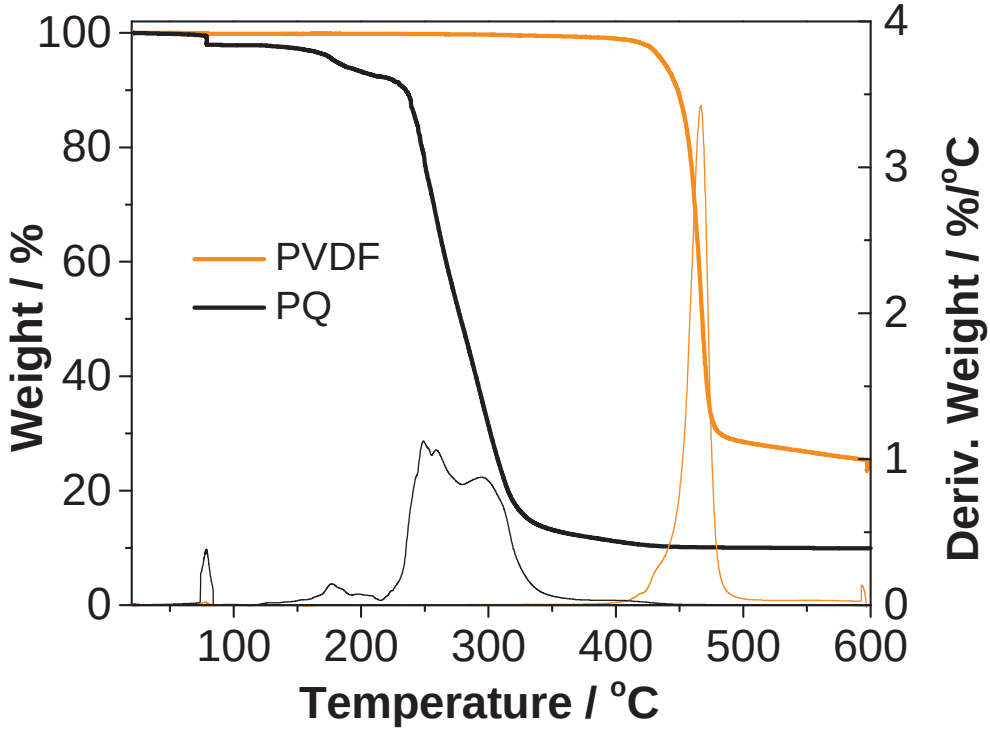


Figure S5-2. Thermalgravimetric analysis (TGA) of PVDF and PQ is conducted. The temperature is ramping from room temperature to 600 °C in nitrogen at the rate of 5 °C/min.

# List of Measurement Equipment and Chemical Reagents

LC/MS spectrometry

Dionex Ultimate 3000 LC system

Thermo Scientific Exactive mass spectrometer

Thermo Scientific Fourier Transform Ion Cyclotron Mass Spectrometer coupled to a Linear Ion Trap (LTQ-FT)

$^{1}$H NMR and $^{13}$C NMR

JEOL AL-400 spectrometers for $^{1}$H NMR

Bruker Avance II 900 MHz with TCI cryoprobe for $^{13}$C NMR

Bruker Avance 500 MHz for $^{1}$H NMR

UV-Vis spectroscopy

Shimadzu UV-3100PC

Cary 5000 UV-Vis-NIR

Elemental analysis

Perkin Elmer 2400 CHNS/O series II analyzer

Thermogravimetric Analysis

TA Instruments SDT Q600

TA Instruments Q5000

Raman spectroscopy

Horiba LabRAM ARAMIS

SEM

Zeiss Gemini Ultra-55

JEOL JSM-7500F

X-ray diffraction

Bruker AXS D8 Discover GADDS X-ray diffractometer equipped with a Vantec-500 area detector

X-ray absorption spectroscopy

Advanced Light Source, Lawrence Berkeley National Laboratory, BL9.3.1, BL5.3.1 and BL10.3.2 for S K-edge

Cell test

Maccor series 4000

# List of Publication

## Original Paper

1) "Electrochemical reactions of lithium–sulfur batteries: an analytical study using the organic conversion technique"
Ayako Kawase, Soichi Shirai, Yoshinari Yamoto, Ryuichi Arakawa, Toshikazu Takata
*Physical Chemistry Chemical Physics* **2014**, *16, (20), 9344*, doi: 0.1039/c4cp00958d
(included in Chapter 2)

2) "Low temperature sulfur deposition for high-performance Lithium/Sulfur Cells"
Ayako Kawase, Don Donghyeok Han, Elton J. Cairns
*Journal of the Electrochemical Society* **2018**, *165,* (9) A1805-A1812,
doi:10.1149/2.1051809jes
(included in Chapter 3)

3) "Method for creation of fine sulfur particles with graphene oxide for Lithium/Sulfur Cells"
Ayako Kawase, Elton J. Cairns
*Journal of the Electrochemical Society* **2018**, *165,* (14) A3257-A3262,
doi:10.1149/2.0181814jes
(included in Chapter 3)

4) "Understanding the function of cetyltrimethyl ammonium bromide in Lithium/Sulfur Cells"
Ayako Kawase, Elton J. Cairns
*Journal of Material Chemistry A*, **2017**, *5*, 23094–23102, doi: 10.1039/C7TA07522G
(included in Chapter 4)

5) "X-ray Absorption Spectroscopic Characterization of the Synthesis Process: Revealing the Interactions in Cetyltrimethylammonium Bromide-Modified Sulfur–Graphene Oxide Nanocomposites"
Yifan Ye, Ayako Kawase, Min-Kyu Song, Bingmei Feng, Yi-Sheng Liu, Matthew A. Marcus,

Jun Feng, Haitao Fang, Elton J. Cairns, Junfa Zhu, Jinghua Guo
*Journal of Physical Chemistry C* **2016**, *120*, 10111-10117, doi: 10.1021/acs.jpcc.6b05127
(included in Chapter 4)

6) "Electrostatic Polysulfides Confinement to Inhibit Redox Shuttle Process in the Lithium Sulfur Batteries"
Min Ling, Wenjun Yan, Ayako Kawase, Hui Zhao, Yanbao Fu, Vincent Battaglia, Gao Liu
*ACS Applied Materials & Interfaces* **2017**, *9*, 31741−31745, doi: 10.1021/acsami.7b06485
(included in Chapter 5)

7) "X-ray Absorption Spectroscopy Characterization of a Li/S Cell"
Yifan Ye, Ayako Kawase, Min-Kyu Song, Bingmei Feng, Yi-Sheng Liu, Matthew A. Marcus, Jun Feng, Elton J. Cairns, Jinghua Guo, Junfa Zhu
*Nanomaterials* **2016**, *6*, (14), doi:10.3390/nano6010014
(included in Chapter 4 & 6)

## Patent

1)「二次電池システムおよび充電制御方法」
繁綾子,
特開2014-229512.

2)「リチウム−硫黄電池」
繁綾子,
特開2013-229279.

3)「電池の処理方法」
繁綾子,
特開2013-206593.

4)「リチウム−硫黄二次電池用電極およびリチウム−硫黄二次電池」

繁綾子,

特開2013-206593.

5)「二次電池」

繁綾子,

特開2012-069412.

6)「二次電池用電極および二次電池」

繁綾子,

特開2011-198550.

7)「電極活物質、二次電池および電極活物質の製造方法」

繁綾子,

特開2010-232085.

## International Conference

1) “Electrochemical reactions of lithium–sulfur batteries: an analytical study using the organic conversion technique”
Ayako Kawase, Soichi Shirai, Yoshinari Yamoto, Ryuichi Arakawa, Toshikazu Takata *Li-SM3conference*, London, UK, February **2016** (Invited Key Speaker).

2) “Reaction analysis of lithium-sulfur cell using UV-vis spectra, 1H NMR, and DFT calculation”
Ayako Kawase,
The 15th International Symposium on Batteries,Fuel Cells and Capacitors, Tokyo, November **2011** (Oral, International Section)

## Domestic Conference

1) “Electrochemical Reactions of Lithium-sulfur Batteries:

an Analytical Study Using the Organic Conversion Technique”
Ayako Kawase, Soichi Shirai, Yoshinari Yamoto, Ryuichi Arakawa, Toshikazu Takata
第54回電池討論会, 大阪, **2013**年10月(Oral)

# Acknowledgement

I would like to express my cordial gratitude to Professor Toshikazu Takata in Tokyo Institute of Technology for his guidance for my research, his suggestion for the analysis, and all his support for this doctoral dissertation. Even though he was not my direct supervisor when I was in the college, he did not hesitate at all to provide his guidance on my research on Li/S cells in Daihatsu Motor. Moreover, his support continued until this thesis finally.

I deeply appreciate to Professor Manabu Ihara, Professor Takeo Yamaguchi, Associate Professor Izumi Taniguchi, Associate Professor Shinsuke Inagi in Tokyo Institute of Technology for reviewing this thesis and their precious comments and suggestions.

I would like to express my sincere gratitude to Professor Elton Cairns in Lawrence Berkeley National Laboratory for all his supervision on my research there. He not only gave precious advice on my research, but also encouraged me as a role model of an admirable scientist.

I would like to express my deep gratitude to Dr. Soichi Sirai in Toyota Central R&D Laboratories not only for his precious suggestion on my research but also for his gentle guidance on writing my first publication.

I am grateful to Mr Hirotoshi, Fujikawa, Mr Akihisa Kuruma and Dr Hirohisa Tanaka of Daihatsu Motor, for their support and encouragement during the work related to this thesis.

I appreciate Professor Ryuichi Arakawa (now retired) and Mr. Yoshinari Yamoto in Kansai University for their generous support on the experimental analysis and the encouragement.

I would like to express my profound gratitude to Dr. Jiro Sakata (now retired) in Toyota Central R&D Laboratories for the helpful discussion. His scientific attitude of mind encouraged me to continue the science.

I would like to express my gratitude to Professor Ralf Steudel (now retired) in Technical University Berlin for his helpful advice on my research related to sulfur chemistry. I admire him as one of the authorities of sulfur chemistry.

I appreciate the experimental support for the analyses from Dr. Jeffrey Pelton of the 900 MHz NMR Facility, Dr. Rita V. Nichiporuk of the Quantitative Biosciences (QB3) institute, Dr. Elena Kreimer of the Microanalytical Facility at Univerisity of California, Berkeley.

Acknowledgement

I appreciate Dr. Min Ling (now at Suzhou University) in Lawrence Berkeley National Laboratory for his encouragement. I also appreciate the experimental support from Dr. Yifan Ye, Dr. Liang Zhang, Mr. Hsiao-Tsu Wang and Dr. Jinghua Guo at Advanced Light Source in Lawrence Berkeley National Laboratory. Also, I thank Dr. Tevye Kuykendall of the Molecular Foundry of LBNL for his support.

I appreciate the meaningful discussion with Dr. Zachary Favor at ZAF Energy Systems (now NexTech Batteries). Also, I appreciate helpful discussions with Dr. Yoon Hwa, Dr. Dan Sun (now at Tokyo University), Dr. Min-Kyu Song (now at Washington State University) of Lawrence Berkeley National Laboratory.

I express my gratitude to Mr. Bill Burger at ZAF Energy Systems (now NexTech Batteries) for his financial support on the works in Lawrence Berkeley National Laboratory.

I appreciate Daihatsu Motor company for the support on the works there.

I would like to express my special gratitude to Dr. Shingo Urata for his hearty encouragement.

Finally, I would like to express my deepest gratitude to my parents for their warm support and encouragement throughout my life.

March 2019

Ayako Kawase